

**SCANNING NEAR-FIELD PHOTON EMISSION  
MICROSCOPY**

**ISAKOV DMITRY VLADIMIROVICH**  
*Master of Science Degree (Moscow State University)*

**A THESIS SUBMITTED  
FOR THE DEGREE OF DOCTOR OF PHILOSOPHY  
DEPARTMENT OF ELECTRICAL AND COMPUTER  
ENGINEERING  
NATIONAL UNIVERSITY OF SINGAPORE**

**2010**

I dedicate this thesis  
in memory of my father,  
VLADIMIR ALEKSEEVICH ISAKOV

## **Acknowledgements**

I am thankful to my supervisor, Professor Jacob C.H. Phang, whose encouragement, guidance and support throughout my research enabled me to develop a keener understanding of the subject.

I also owe my deepest gratitude to my co-supervisors, Professor Ludwig J. Balk (University of Wuppertal) and Doctor Ying Zhang (Singapore Institute of Manufacturing Technology) for their advice that helped me execute this work efficiently. I was very lucky to work with a team, abundant with ideas and different points of view, which allowed me to focus my research. In this regard, I also want to thank Thomas Geinzer for our many in-depth discussions and his help with the system development.

This thesis would not have been possible without the efficient and timely support from Center of Integrated Circuit Failure Analysis and Reliability (CICFAR) and SEMICAPS Pte Ltd.

Lastly, I would like to express my gratitude to all those who supported me in any aspect of the project.

## Content:

Summary .....	1
List of Tables .....	3
List of Figures .....	4
List of Symbols .....	9
Chapter 1.	
Far-field Photon Emission Microscopy .....	12
1.1 Semiconductor device miniaturization .....	12
1.2 Failure Analysis of Integrated Circuits .....	15
1.3 PEM analysis of technologies beyond 50 nm .....	19
1.3.1 Resolution enhancement using immersion lenses.....	23
1.3.2 Resolution enhancement using near-field detection .....	26
1.4 Thesis goals and lay-out.....	27
Scheme of Argumentation for SNPEM implementation .....	30
Chapter 2.	
Near-field optical detection.....	31
2.1 Introduction into near-field optics .....	31
2.2 Near-field optical probes.....	35
2.2.1 Probe based on sub-wavelength aperture.....	36
2.2.2 Probe based on the uncoated dielectric tip.....	40
2.2.3 Protrusion type probe .....	42
2.2.4 Probe based on a scattering metallic tip.....	43
2.2.5 Probe based on metallic nanoparticle attached to dielectric tip .....	45
2.3 Near-field interaction of scattering probes .....	46
2.3.1 Scattering by a homogeneous isotropic sphere .....	47
2.3.2 Dielectric function of the scatterer .....	48
2.3.3 Engineering of the dielectric function.....	51
2.4 Detection of the scattered signal .....	54
2.4.1 Collection efficiency of the taper for dielectric uncoated probe.....	54
2.4.2 Near-field interaction of the probe body.....	56
Chapter 3.	
SNPEM functional blocks and discussion on near-field condition .....	59
3.1 SNPEM system set-up .....	59
3.2 Probe nanometric positioning and coarse navigation .....	60
3.3 Probe-sample distance regulation .....	62
3.3.1 Excitation method of the TF .....	63
3.3.2 Probe-sample distance regulation in SNPEM.....	65
3.3.3 Linearity of SNPEM scanning stage.....	67
3.4 Impact of sample structure on the near-field condition .....	69
3.4.1 Front-side analysis .....	71
3.4.2 Back-side analysis.....	72
3.5 Light sensitive detectors for SNPEM .....	76
Summary.....	79

Chapter 4.	
Near-field probe for SNPEM .....	81
4.1 Requirements for SNPEM probe .....	81
4.2 Evaluation of existing near-field probes .....	83
4.2.1 Probes with sub-wavelength aperture .....	84
4.2.2 Dielectric probes .....	86
4.2.3 Protrusion type probe .....	87
4.2.4 Scattering metallic probes.....	88
4.2.5 Probes based on metallic nanoparticle attached to the dielectric probe....	89
4.2.6 Ranking of existing probes .....	91
4.3 Applications of dielectric tips for SNPEM analysis .....	93
4.3.1 Dependence of intensity distribution on probe geometry and on emission source location below the surface .....	93
4.3.2 Application of dielectric probe to emission source placed below the surface .....	99
4.3.3 Application of dielectric probe to MOSFET with a short channel .....	103
4.3.4 Applications of dielectric probe to MOSFET with a long channel .....	108
Summary .....	111
Chapter 5.	
Scattering dielectric probe with embedded metallic scatterer .....	112
5.1 Considerations for SNPEM probe optimization .....	112
5.2 Tapering of the optical fiber by three step process .....	117
5.2.1 Reduction of fiber diameter using heat-drawing method .....	117
5.2.2 Sharpening the tip down to nanometric dimensions .....	123
5.3 Dielectric probe with embedded gallium scattering center.....	128
5.4 Optical characterization of the probe with embedded Ga.....	133
5.4.1 Optical properties of Ga.....	133
5.4.2 Characterization of Ga impact on the probe scattering efficiency.....	135
Summary .....	139
Chapter 6	
Photon emission detection with Ga-SDP .....	140
6.1 Estimation of lateral resolution for Ga-SDP .....	140
6.2 Sensitivity of SNPEM system.....	148
6.2.1 Detection efficiency of the Ga-SDP for an SNPEM application.....	150
6.3 Impact of the detection condition on SNPEM analysis .....	156
6.3.1 Impact of emission source location below the surface .....	156
6.3.2 Impact of probe positioning above the surface .....	166
Summary .....	169
Chapter 7.	
Conclusions and future work .....	171
7.1 Conclusions.....	171
7.2 Future work.....	176
Appendix A	
Photon Emission mechanisms.....	179
A.1 Radiative transitions.....	179

A.2	Photon emission from silicon based ICs .....	180
A.2.1	Photon emission from forward biased silicon p-n junction .....	182
A.2.2	Photon emission from reverse biased silicon p-n junction .....	183
A.2.3	Photon emission from MOSFET .....	185
A.3	Confusion on the origin of hot carrier emission .....	186
Appendix B		
	Quasi-static approximation (QSA) .....	188
B.1	Influence of the sample on QSA .....	189
B.2	Influence of the near-field of the emission source on QSA .....	191
References:	.....	196
Publication list:	.....	211

## Summary

The resolution of fault isolation techniques, like far-field photon emission microscopy (FFPEM), is grossly inadequate for advanced semiconductor technology nodes beyond 65 nm. The fundamental limit on spatial resolution of FFPEM is approximately half the wavelength of the detected photons. The practical limit is slightly less than 1  $\mu\text{m}$ . FFPEM with such a resolution is not only incapable of identifying the faulty transistor but it also cannot identify the faulty functional block in the integrated circuit (IC). Near-field optical detection using scanning near-field photon emission microscopy (SNPEM) promises resolution capabilities below 100 nm. However, existing implementations of SNPEM have serious limitations in terms of photon emission detection efficiency, repeatability and applicability to different samples. The quality of near-field detection is mainly determined by the properties of a near-field probe. Different near-field probe designs are available but they have certain disadvantages that can limit their application in SNPEM. To overcome these, eight requirements are formulated in this thesis to rank the existing probes. Using this ranking the uncoated dielectric probes are chosen and applied for SNPEM detection from a variety of test structures. A detection efficiency level of 10  $\mu\text{A}$  in terms of variation of the biasing current through the transistor is demonstrated. However, such detection efficiency is achieved through the compromise in resolution to approximately 200 nm.

In order to improve the SNPEM imaging quality, a novel concept of a scattering dielectric probe with embedded metallic scatterers is proposed. In this concept, a metallic nano-particle is embedded into the nanometric tip of the tapered dielectric waveguide. In

order to fabricate such a probe, an implantation of gallium (Ga) atoms using a focused ion beam is implemented. A unique fabrication method allows us to perform the implantation simultaneously with the formation of the nanometric tip, making this method simple and repeatable. The performance of such a Ga-based scattering dielectric probe (Ga-SDP) is evaluated. A theoretical prediction of the scattering efficiency for a Ga nanoparticle shows that an enhancement of approximately 20 times can be expected in comparison with a similar sized nanoparticle made of silica. The experimental comparison of Ga-SDP and silica tips shows that the enhancement can reach a value of 37. It is suggested that such a high value originates from the modified dielectric function of the Ga-silica composite in comparison with pure Ga used for the theoretical evaluation. The application of Ga-SDP for SNPEM shows that a resolution capability in the order of 50 nm is achievable. The lowest detected variation in the biasing current is below 1  $\mu$ A. This makes SNPEM with Ga-SDP suitable for the detection of the leakage currents in current and future technologies. Wavelength dependent SNPEM measurements show the possibility for distinguishing different photon emission phenomena within the single emission spot. It is also shown that the position of the emission source below the surface, as well as the probe-sample distance regulation, have a strong influence on the recorded images. Reduction of these two parameters leads to substantial benefits in terms of both spatial resolution and detection efficiency.



## List of Tables

Table #	Table caption	Page #
<b>1.1</b>	Key parameters defining the FA success at each technology node.	<b>13</b>
<b>4.1</b>	Ranking of the existing probe designs.	<b>91</b>
<b>B.1</b>	Validity of QSA for SiO <sub>2</sub> and Au nanoparticles with radii of 30 nm. <b>n'</b> and <b>k'</b> are real and imaginary parts of the refractive indexes of SiO <sub>2</sub> and Au at particular wavelength.	<b>189</b>

## List of Figures

Figure #	Figure caption	Page #
1.1	Overlay of the laser beam size on the layout of the SRAM built in 65 nm technology node [19].	17
1.2	Comparison of demonstrated capabilities of FL methods with the requirements on spatial resolution and detection efficiency to the corresponding leakage currents for the selected technology nodes [17].	18
1.3	Intensity distribution in the image plane of the objective collecting light from a point source. Insert shows the 3D representation of the distribution [13].	20
1.4	Comparison of the SRAM cell area (yellow rectangle) at 22 nm technology node [24] with the area covered by diffraction limited PE spot with diameter of 1 $\mu\text{m}$ .	22
2.1	Original idea of near-field optical microscope by E.H.Synge [37].	33
2.2	The scattering model for collection near-field probe [48].	35
2.3	Application of a-SNOM for photon emission detection. a) Schematic representation [34]. b) SEM image of the 100 nm aperture [50].	36
2.4	Difference between a) PSTM and b) SNOM illumination schemes [47].	40
2.5	Schematic representation of protrusion-type probe [94].	42
2.6	Illumination and collection optics for application of metallic scattering SNOM tips [102].	44
2.7	Scattering SNOM with metal particle attached to the dielectric tip [46].	45
2.8	Small dielectric homogeneous isotropic sphere scattering the uniform electric field [104].	47
2.9	Comparison of theoretical and experimental values of dielectric function of copper [108] with dielectric function of silica (red line) taken from Ref. 109.	49
2.10	The dependence of the scattering amplitude on the $\text{Re}(\epsilon)$ at 633 nm for different values of $\text{Im}(\epsilon)$ . The corresponding values of dielectric functions of different materials are indicated [102].	50
2.11	Distribution of metallic nanoparticles implanted into dielectric [114].	53
2.12	Scattering capture fraction as a function of the transmitting fiber critical angle $\theta_c$ [47].	55
2.13	Approximation of the probe with two spheres with different diameters [39].	57
3.1	The schematic representation of the main components of the system.	60

3.2	Probe positioning capabilities: a) photo of the SNPEM system during operation; b) coarse positioning stage shown without the piezo stage and the sample holder.	61
3.3	Excitation methods used for TF vibration: a) mechanical driving; b) direct driving [129].	64
3.4	Dependence of the feedback signal on the tip-sample distance. The red cross indicates the distance when the tip starts to sense the surface.	66
3.5	Calibration of SNPEM using polystyrene spheres with diameter of 350 nm: a) topography image; b) topography profile across the line <b>AA'</b> . Red ( <b>R</b> ) and Blue ( <b>B</b> ) lines identify the borders of the five spheres under consideration.	68
3.6	a) SEM image of calibration grid TGX1 from NT-MDT [134]; b) SNPEM topography image of TGX1 sample.	69
3.7	Illustration of the NF condition in case of SNPEM application.	70
3.8	Schematic representation of SNPEM analysis applied to the sample from front-side.	71
3.9	Schematic representation of the bulk silicon sample thinned down to nanometric level for back-side SNPEM analysis using FIB.	73
3.10	Schematic representation of the SOI sample thinned down to nanometric level for back-side SNPEM analysis using chemical etching.	74
3.11	SOI sample deprocessing for back-side SNPEM analysis: a) front-side image of SOI device before deprocessing; b) back-side image of the device after substrate etching with TMAH solution.	75
3.12	Spectral response of Hamamatsu H5783-20 [142].	76
3.13	Connection between the bare end of the fiber and visible PMT.	77
3.14	Spectral response of Hamamatsu R5509-42 [143].	78
3.15	Connection between the bare end of the fiber and NIR PMT.	78
4.1	Schematic representation of existing probe designs based on: a) sub-wavelength aperture; b) uncoated dielectric tip; c) protrusion type probe (PTP); d) metal tip; e) metallic nanoparticle attached to the dielectric tip.	83
4.2	Schematic representation of SNPEM analysis with a metallic probe demonstrating the limitations due to external collection as well as danger to cause a short-circuit between the probe and the sample or between adjacent metal lines.	89
4.3	Point source emission profile detected with uncoated probe. Situation i) $\mathbf{a_s} = 0$ and $\mathbf{a_p} = 10\text{nm}$ . a) $2\theta=20^\circ$ and b) $2\theta=90^\circ$ .	94
4.4	Point source emission profile detected with uncoated probe. Situation ii) $\mathbf{a_s} = \mathbf{a_p} = 10\text{nm}$ . a) $2\theta=20^\circ$ and b) $2\theta=90^\circ$ .	95
4.5	Point source emission profile detected with uncoated probe. Situation iii) $\mathbf{a_s} = 10\text{nm}; \mathbf{a_p} = 50\text{nm}$ . a) $2\theta=20^\circ$ and b) $2\theta=90^\circ$ .	97
4.6	Point source emission profile detected with uncoated probe.	98

	Situation iii) $a_s = 100\text{nm}$ ; $a_p = 50\text{nm}$ . a) $2\theta = 20^\circ$ and b) $2\theta = 90^\circ$ .	
<b>4.7</b>	SEM image of PTP with large base aperture fabricated using FIB.	<b>99</b>
<b>4.8</b>	I-V characteristics of the good and stressed (damaged) device.	<b>100</b>
<b>4.9</b>	a) FFPEM of the leaking silicon p-n junction; b) SNPEM analysis of the same junction with PTP. Passivation layer thickness: $\sim 1.5 \mu\text{m}$ ; avalanche current of $50 \mu\text{A}$ .	<b>101</b>
<b>4.10</b>	3D representations of the a) FFPEM and b) SNPEM results in Fig.4.9.	<b>102</b>
<b>4.11</b>	Schematic representation of the MOSFET test structure investigated by SNPEM	<b>103</b>
<b>4.12</b>	Low magnification images of the test MOSFET: a) (i) FF reflection and (ii) FFPEM; b) low magnification (i) topography and (ii) SNPEM images recorded with PTP.	<b>105</b>
<b>4.13</b>	a) Digitally magnified (i) 2D and (ii) 3D FFPEM images of the test MOSFET (ii); b) High magnification (i) 2D and (ii) 3D SNPEM images of the test MOSFET recorded with PTP.	<b>106</b>
<b>4.14</b>	Emission intensity profile across the line marked in Fig.5.12b(i).	<b>107</b>
<b>4.15</b>	Investigation of PE distribution for n-MOSFET with $5\mu\text{m}$ gate length by a) FFPEM and b) SNPEM.	<b>108</b>
<b>4.16</b>	(i) Topography and (ii) SNPEM images recorded at a) $I_d = 30\mu\text{A}$ , $V_d = 4.5\text{V}$ , $V_g = 2.5\text{V}$ drain current and b) $I_d = 40\mu\text{A}$ , $V_d = 5.2\text{V}$ , $V_g = 2.5\text{V}$ .	<b>110</b>
<b>5.1</b>	Schematic representation of proposed dielectric probe with embedded metallic scatterer.	<b>115</b>
<b>5.2</b>	The design of the taper optimum for SNPEM application.	<b>118</b>
<b>5.3</b>	Probes tapered by heat-drawing method: a) SMF; b) MMF.	<b>119</b>
<b>5.4</b>	Heat-drawing method applied to MMF: a) heating and simultaneous pulling of MMF; b) hard pull.	<b>120</b>
<b>5.5</b>	The effect of hard pull on the probe shape: a) parabolic shape achieved with heating; b) shape after hard pull.	<b>121</b>
<b>5.6</b>	Tip quality after hard pull: a) side view; b) facet view; c) tip after FIB cut.	<b>122</b>
<b>5.7</b>	The effect of the defective primary surface on the final result of FIB based sharpening.	<b>124</b>
<b>5.8</b>	Formation of the sharp dielectric tip: a) shape of the probe after heat and pull method; b) shape of the probe tip before application of FIB; c) tip shape after 30 sec of FIB illumination; d) tip shape after 60 sec of FIB illumination.	<b>125</b>
<b>5.9</b>	Evaluation of the core/cladding profile using EDX characterization at different regions of the probe: a) SEM image; b) region A; c) region B; d) region C.	<b>126</b>
<b>5.10</b>	Confirmation of repeatability of the sharpening process for two different probes. a) and b) are SEM images of the probes at different points of time: i) starting point; ii) 15 sec; iii) 30 sec; iv) 45 sec; v) 60 sec.	<b>127</b>

<b>5.11</b>	Formation of embedded scatterer by Ga ion implantation using FIB.	<b>129</b>
<b>5.12</b>	Implantation of 2000 Ga ions into silica at normal incidence with energy of 30keV: a) Trajectories inside the target; b) distribution of implanted Ga below silica surface.	<b>130</b>
<b>5.13</b>	Sputtering yield at different incidence angles: a) normal incidence 0°; b) 80°.	<b>131</b>
<b>5.14</b>	Observation of Ga “drop” in the tip: a) SEM image of the probe tip; b) visualization of the material density by measuring the number of transmitted electrons when 30 keV electron beam is scanning across the tip.	<b>132</b>
<b>5.15</b>	Comparison of scattering efficiencies for Ga vs. Au and SiO <sub>2</sub> nanoparticles.	<b>135</b>
<b>5.16</b>	Overlaid optical and topography images of the polished waveguide recorded with different probes: a) Ga-SDP; b) simple tapered glass tip.	<b>136</b>
<b>5.17</b>	Line profiles of the waveguide across with different tips: a) line AA’ shown in Fig.5.16a; b) line BB’ shown in Fig.5.16b. For the simple glass tip the amplified line profiles are also presented for comparison.	<b>137</b>
<b>5.18</b>	Dust build up on Ga-SDP probe after SNPEM measurements.	<b>138</b>
<b>6.1</b>	FinFET test structure: a) FFPEM image; b) SEM image of the drain metal contact area.	<b>141</b>
<b>6.2</b>	Images of the Fin-FET test structure at different magnifications: a) topography and b) SNPEM.	<b>142</b>
<b>6.3</b>	High magnification (a) topography and (b) SNPEM images of the PE spot in the location of highest intensities.	<b>144</b>
<b>6.4</b>	Topography and intensity profiles across AA’ lines in Fig.6.4.	<b>144</b>
<b>6.5</b>	Curve fitting of the intensity profile in Fig.6.5 with two Gaussian curves corresponding to NF and FF interactions of the emission source and the probe.	<b>146</b>
<b>6.6</b>	Localization of photon emission spot with 50 nm resolution. Highest 20% of PE intensities in Fig.6.4b is overlaid with the topography image in Fig.6.4a.	<b>148</b>
<b>6.7</b>	Visible emission distribution in the NF of the sample surface at different reverse bias of the p-n junction: a) 5.5, 1.6μA; b) 5.52V, 2.3 μA; c) 5.54V, 7.5μA; d) 5.56V, 27μA; e) 5.58V, 60μA; f) 5.60V, 100μA.	<b>151</b>
<b>6.8</b>	NIR emission distribution in the NF of the sample surface at different reverse bias of the p-n junction: a) 5.58, 60μA; b) 5.62V, 123 μA; c) 5.66V, 186μA; d) 5.68V, 218μA; e) 5.72V, 281μA; f) 5.76V, 345μA.	<b>153</b>
<b>6.9</b>	Comparison of I-V characteristic of the p-n junction at reverse bias with SNR dependence on supplied voltage in Visible and NIR spectral ranges. The dependence of NIR signal is fitted with a	<b>154</b>

	parabolic function.	
<b>6.10</b>	Comparison of SNR dependences on supplied current in Visible and NIR spectral ranges. The corresponding fitting functions for both spectral ranges are provided.	<b>155</b>
<b>6.11</b>	Schematic representation of the base-emitter junction [57].	<b>157</b>
<b>6.12</b>	Reflection images of the leakage area of the p-n junction a) before and b) after passivation is removed.	<b>157</b>
<b>6.13</b>	FFPEM images of the p-n junction at a) reverse and b) forward bias	<b>158</b>
<b>6.14</b>	a) Topography and b ) SNPEM images of a leaking p-n junction at reverse and forward biasing conditions: i) -5.56V, -50 $\mu$ A; ii) 0.89V, 9 mA.	<b>160</b>
<b>6.15</b>	Difference in current paths (indicated by arrows) for a) forward and b) reverse biased junction with defect.	<b>161</b>
<b>6.16</b>	Degradation of the oxide layer on top of the leakage site of the junction.	<b>162</b>
<b>6.17</b>	a) Topography and b) NIR SNPEM images of reverse biased p-n junction with locally removed SiO <sub>2</sub> layer.	<b>163</b>
<b>6.18</b>	Variation of the intensity profiles of the emission spot recorded at different <b>d</b> .	<b>164</b>
<b>6.19</b>	Expansion of the emission spot due to the refraction at Si-SiO <sub>2</sub> interface.	<b>165</b>
<b>6.20</b>	Images of the leakage site in the silicon p-n junction acquired with Ga-SDP at different distances <b>h</b> from the sample surface: a) topography; b) <b>h</b> = 4 $\mu$ m; c) <b>h</b> = 2.6 $\mu$ m; d) <b>h</b> = 1.5 $\mu$ m; e) <b>h</b> = 1 $\mu$ m; f) <b>h</b> = 0.5 $\mu$ m; g) <b>h</b> $\approx$ 10 nm; h) image g) overlaid on image a).	<b>167</b>
<b>6.21</b>	Corresponding of profiles across line AA' for a) Fig.6.19a; b) Fig.6.19c; c) Fig.6.19b.	<b>169</b>
<b>A.1</b>	a) Radiative transition processes in silicon devices [12]; b) Distinction of various radiation transition mechanisms in a realistic band structure of silicon [14].	<b>179</b>
<b>A.2</b>	Qualitative spectral range comparison of black body and PEM detectors [adopted from 161].	<b>181</b>
<b>A.3</b>	Emission spectrum of forward biased p-n junction [169].	<b>183</b>
<b>A.4</b>	Emission spectrum of reverse biased p-n junction a) visible and b) NIR spectral range [169].	<b>184</b>
<b>A.5</b>	Occurrence of photon emissions in MOSFETs: a) hot electron effects; b) junction leakage; c) contact spiking; d) junction avalanche; e) latch-up; f) oxide current leakage.	<b>186</b>
<b>B.1</b>	The mirror-dipole induced by the tip in the proximity of the sample surface [206].	<b>190</b>

## List of Symbols

$\lambda$  - wavelength

**NA** - numerical aperture

**n** - refractive index

$\theta$  - semi-collection angle of the objective lens or the semi-cone angle of the probe

**R** - lateral resolution

**a** - characteristic dimension of the probe, sphere radius

**h** - separation distance between the probe and the sample

$\epsilon$  - dielectric function of the probe tip or sphere

$\epsilon_m$  - dielectric function of the surrounding medium

$E_0$  - uniform electric field

$\vec{E}_0$  - vector form of the uniform electric field

**r** - distance from the sphere

$\varphi$  - angle between field and the scattering direction

$\Phi_{out}$  - potential of the field outside the sphere

$\Phi_d$  - potential of the ideal dipole

$\bar{p}_d$  - dipole moment induced in the sphere

$\alpha$  - sphere or scatterer polarizability

$g = \frac{\epsilon - \epsilon_m}{\epsilon + 2\epsilon_m}$  - coefficient in Eqn.3.4

**Re( $\epsilon$ )** - real part of the dielectric function

$\text{Im}(\epsilon)$  - imaginary part of the dielectric function

$m$  - electron mass

$q_e$  - electron charge

$\Gamma$  - dumping constant

$\omega$  - field oscillation frequency

$x$  - electron displacement under the effect of external field

$x_0$  - displacement amplitude

$\bar{E}$  - external field

$\bar{P}$  - polarization of the medium

$N$  - the number of oscillators per unit volume

$\epsilon_0$  - vacuum permittivity

$\omega_p$  - plasma frequency of the electron cloud

$\mu_S$  - signal mean value

$\sigma_n$  - background noise standard deviation

$k = 2\pi/\lambda = \omega/c$  - wave number

$n = n' + ik'$  - complex refractive index of the sphere

$c$  - speed of light

$\tau^*$  - time required for the field to propagate across the sphere

$\tau$  - characteristic time of the field

$\epsilon_{\text{sub}}$  - dielectric function of the substrate

$\alpha_{\text{eff}}$  - effective polarizability of the tip at the sample or substrate surface

$\beta = (\epsilon_{\text{sub}} - \epsilon_m) / (\epsilon_{\text{sub}} + \epsilon_m)$  - coefficient in Eqn.3.13



$\vec{H}$  - vector of the dipole magnetic field

$\vec{n}$  - field propagation direction

$L$  - characteristic dipole dimension

$\vec{k}$  - wavevector

$k_t, k_z$  - transverse and longitudinal wavenumbers

$\theta$  - incident angle of the light beam at the interface

$\gamma$  - decay constant

$I_d$  - signal detected at the bare end of the fiber

$I_0$  - signal incident on the probe

$S$  - capture fraction for scattered radiation

$\sigma$  - scattering coefficient

$\theta_c$  - internal critical angle

$\Delta$  - coefficient in Eqn.3.25

$a_P$  - radius of Sphere P in Fig.3.16

$a_T$  - radius of Sphere T in Fig.3.16

$a_S$  - radius of Sphere S in Fig.3.16

$r_P$  - distance from dipole within Sphere S to the induced dipole in Sphere P

$r_T$  - distance from dipole within Sphere S to the induced dipole in Sphere T

$I_P(\mathbf{x})$  - signal due to scattering with Sphere P

$I_T(\mathbf{x})$  - signal due to scattering with Sphere T

$\mathbf{e}_{\text{eff}}$  - effective dielectric function

$f$  - metal fraction in the metal-dielectric composite

## **Chapter 1.**

### **Far-field Photon Emission Microscopy**

The resolution and detection efficiency of fault isolation techniques for an integrated circuit failure analysis are grossly inadequate for advanced semiconductor technology nodes beyond 65 nm. Far-Field Photon Emission Microscopy (FFPEM) is a common non-invasive technique that is used for the fault isolation. The practical spatial resolution for a conventional FFPEM is slightly less than 1  $\mu\text{m}$ . A FFPEM with such a resolution is not only incapable of identifying the faulty transistor but it also cannot identify the faulty functional block in the integrated circuit (IC). Resolution enhancement techniques, like an immersion lens, can theoretically bring the resolution down to 140 nm. But even a theoretically achievable resolution cannot satisfy the requirements of the current and future technology nodes. An alternative approach to improve the spatial resolution is to use the capabilities of near-field detection. Unfortunately, the gain in resolution for existing near-field optical techniques is compromised by its low detection efficiency in terms of the minimum biasing currents detectable by the system. A substantial modification of the technique is required to improve the detection efficiency.

#### **1.1 Semiconductor device miniaturization**

Following the demonstration of the first laboratory transistors in 1960, the semiconductor industry has, over the years, become a global business with rapid technological advances. These advances contributed significantly to the global economic growth in the late 20th-

century. The rate of progress of the semiconductor industry far surpassed nearly all other industries [1]. This success has been driven by Moore's Law [2], which states that the number of transistors that can be placed inexpensively on an IC doubles every year. Since 1975, this has been revised to every two years [3]. The pursuit of Moore's Law has facilitated an increase in the number of transistors by five orders of magnitude within the last four decades [4]. According to the 2007 International Technology Roadmap for Semiconductors (ITRS 2007) [5], such a scale of integration will lead to the technology node corresponding to 22 nm by 2016 (Table 1.1). However, changes in favor of a less aggressive trend are expected in the next decades due to the limitations of power consumption, which are in turn due to a tremendous increase in lithography cost, and the expected large variations in the electrical characteristics of transistors with smaller geometry [6].

In Table 1.1 some critical parameters for the different technology nodes are highlighted.

**Table 1.1:** Key parameters critical for FA success at each technology node.

<b>Year of Production</b>	<b>2007</b>	<b>2010</b>	<b>2013</b>	<b>2016</b>
Technology node (nm)	65	45	32	22
SRAM cell area, $\mu\text{m}^2$ [5]	0.73	0.35	0.17	0.08
No of transistors per $\mu\text{m}^2$ for SRAM*	8	17	35	75
Leakage current of one cell, $\mu\text{A}$ [7]	< 1	< 1	< 1	-
Maximum number of wiring levels [5]	11	12	13	13

\* Derived from ITRS 2007 Data [5]

Historically, the technology node has been defined through the smallest half-pitch of contacted metal lines on any product. However, lately, the functional density has become a clearer indicator of technology development. That is why an example of static random access memory (SRAM) is also provided in Table 1.1. It is shown that the SRAM cell with six transistors will occupy an area smaller than  $0.1 \mu\text{m}^2$  by the year 2016. Such integration leads to the density of 75 transistors per  $\mu\text{m}^2$  (Table 1.1). This value is important for a comparison with the spatial resolution capabilities of different failure analysis (FA) techniques. Another critical value is the leakage current. In Table 1.1 the example of leakage current level for one SRAM cell is given. The analysis of three advanced technological nodes shows that the value should not exceed  $1 \mu\text{A}$  [7]. This value provides a benchmark for the evaluation of the detection efficiency of FA techniques.

Although there are solutions for manufacturing such small devices [4], the semiconductor industry currently lacks the means to efficiently test and characterize them. This presents a critical hurdle because characterization plays the role of a feedback loop for understanding the underlying defect mechanisms and process marginalities. The Characterization also enables rapid fabrication yield learning and continuous improvement of manufacturing processes. The above-mentioned reduction of the feature size, caused a tremendous drop in the characterization efficiency due to inadequate resolution and detection efficiency of the applied tools [8,9]. The number of wiring levels, provided in Table 1.1, puts an additional pressure on the FA efficiency because these layers make certain conventional tools inapplicable. The overall efficiency drop has

serious economic consequences for the industry due to the lowering of the asymptotic maximum achievable yields per die size on the new process technologies [5]. Substantial improvements and innovations to existing tools and techniques are therefore required to keep pace with the technology advancement.

## **1.2 Failure Analysis of Integrated Circuits**

The importance of FA of ICs is derived from the critical role that the semiconductor industry plays in the world today as was described in sub-section 1.1. The semiconductor FA is a process that focuses on the determination of the root cause for device failures [8]. The success rate of FA depends on five steps executed in the following order [10]: i) verification of the failure mode; ii) fault localization (FL); iii) sample preparation and defect tracing; iv) physical and chemical characterization; and v) root cause determination. The second step of FL is used to isolate the defective regions in the failed units. This is the most critical step that largely determines the success rate of FA procedure [9].

FL techniques are usually divided into passive and active techniques. Passive techniques can boast of being non-invasive [11], meaning that the characteristics of the device under test (DUT) are not altered during the analysis. The most common passive technique is Far-Field Photon Emission Microscopy (FFPEM) [12]. FFPEM uses photon emission from active semiconductor elements within the IC [11]. It is based on the far-field detection through the objective of an optical microscope equipped with a very sensitive

camera. Such a far-field optical system is subject to a natural limitation in resolution due to diffraction [13]. The practical resolution limit for FFPEM with an air-gap objective lens is slightly less than 1  $\mu\text{m}$  [13]. The main advantages of FFPEM are the ease of use and interpretation of the data. By imaging the active layers through the back-side of the silicon substrate, it also overcomes the problem of the increased number of wiring layers, highlighted in Table 1.1. Additionally, the advantage of FFPEM lies in its capability to perform spectral [12] and time-resolved analysis [14], which in turn provides unique information about the processes within the biased IC.

A Superconducting Quantum Interference Device (SQUID) is another passive technique that allows the detection of currents within the packaged sample without the need for sample deprocessing [15]. Unfortunately, its resolution capabilities cannot exceed 1  $\mu\text{m}$  due to its geometrical constraints [16], while its detection efficiency is two orders of magnitude lower in comparison to FFPEM [17].

Further, active techniques are those that are based either on optical or on particle beams for carriers or thermal stimulation. These techniques are quite powerful especially for the localization of failures in interconnects [18]. The optical beam techniques employ a laser beam to stimulate the failing components of an IC and identify the defects by measuring the changes of electrical or optical parameters. Similar to FFPEM, laser beam techniques are mainly used from the back-side of the substrate for the analysis of advanced technologies with multiple metal layers. For this purpose, lasers with working

wavelengths above 1  $\mu\text{m}$  are implemented, in order to prevent the absorption in silicon.

Such long wavelengths lead to values of spatial resolution close to 1  $\mu\text{m}$ .

In Fig.1.1 a comparison between the beam size and the layout of a SRAM is provided. The layout in Fig.1.1 is given for the 65 nm technology node [19] with a single SRAM cell of 6 transistors confined to the area of 0.7  $\mu\text{m}^2$ . Figure 1.1 shows that the interaction area of the beam with the DUT is larger than the area occupied by several active elements. Due to this it is hard to distinguish which of the elements is affected. Therefore it becomes hard to draw a reliable conclusion from the test [20]. Another problem with active techniques is that they alter the characteristics of the DUT, making it difficult to directly investigate the actual performance of the device.

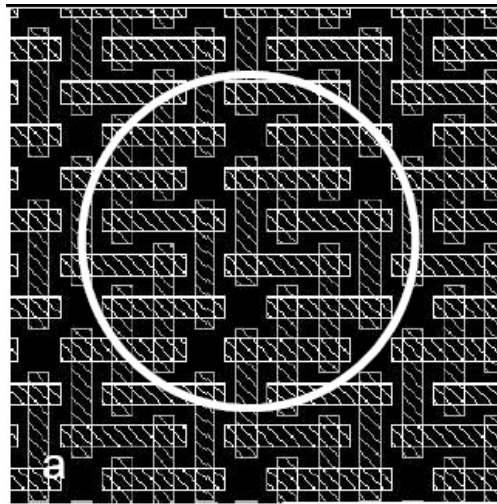


**Figure 1.1:** Overlay of the laser beam size of 1  $\mu\text{m}$  on the layout of the SRAM built in 65 nm technology node [19].

Active techniques based on particle beams can achieve a higher resolution in comparison to laser beam techniques. The reason is that the de Broglie wavelength of highly energetic particles is approximately two orders of magnitude shorter than near-infrared

wavelengths. The disadvantage of particle-based techniques is that its superior resolution is limited to an interaction with only the top surface layers of the sample [11]. The introduction of the multiple wiring layers (Table 1.1) makes these techniques less powerful and they are not applicable from the back-side of the substrate. Additionally, particle beam techniques are operated in a vacuum, which puts considerable constrain on the DUT properties.

In Fig.1.2, the capabilities of some FL techniques are compared to the lateral dimensions of different technology nodes. These techniques are also compared in terms of the detection efficiency of leakage currents that are critical for each technology. It is clear that the capabilities of most of these techniques are not satisfactory, even for a 130 nm technology node (Fig.1.2).

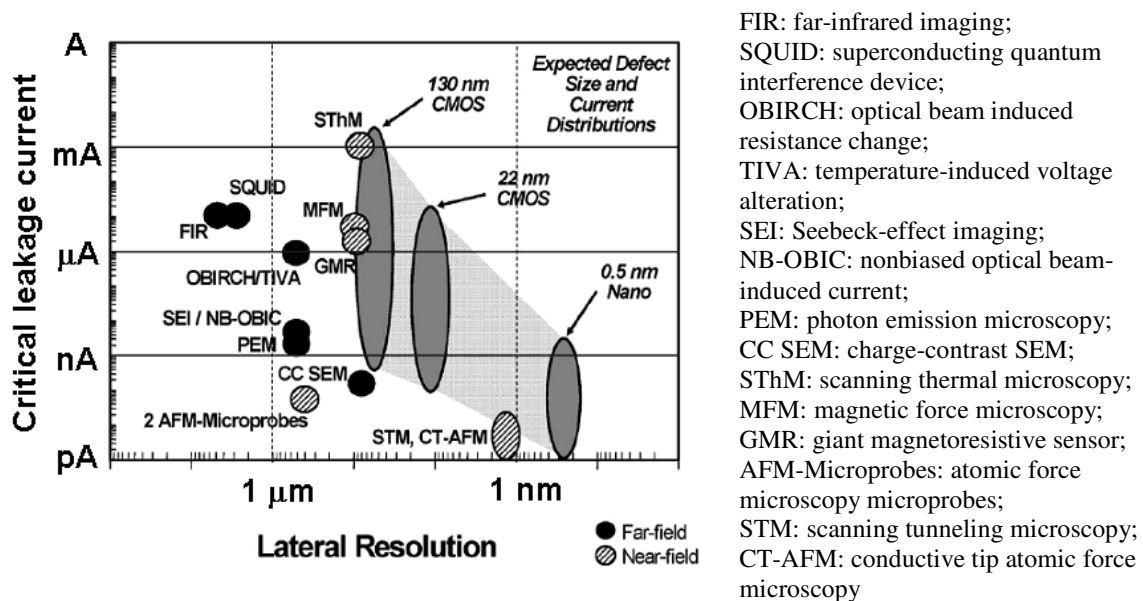


**Figure 1.2:** Comparison of demonstrated capabilities of fault isolation methods with requirements on spatial resolution and detection efficiency to the corresponding leakage currents for selected technology nodes [17].



The inadequate precision of FL techniques requires a substantial investment into the analysis during the post-localization steps iii-v (mentioned in the beginning of this subsection) of the FA procedure sequence. Such poor precision will dramatically increase the cost of FA and at the same time reduce its success rate. There is therefore a need to improve the resolution and detection efficiency of the actual localization. At the same time, there is also an increasing demand from the industry to develop FL tools that can perform the characterization of devices while they are still an integral part of the IC [10]. This puts even more stringent requirements on such tools.

Promising resolution capabilities are provided by the techniques marked as near-field (NF) in Fig.1.2. These techniques are generally based on the principles of Scanning Probe Microscopy (SPM). In SPM, a mechanical probe interacts with the signal source at a distance from the source much smaller than the characteristic length of the field responsible for the interaction [17]. Such a condition is usually referred to as a NF condition. If the mechanical probe is scanned within the NF condition from the source, then it is possible to resolve this source with a lateral resolution determined mainly by the size of the probe and independent of the characteristic length of the field.

### **1.3 PEM analysis of technologies beyond 50 nm**

This thesis mainly focuses on the resolution enhancement of PEM. An investigation of the origins of Photon Emission (PE) in semiconductor devices is not critical for the purpose of the thesis and thus, the discussion on the origin is provided in Appendix A. It is known that multiple mechanisms of PE contribute throughout the spectral range of

interest from 400 nm to 1700 nm. These mechanisms include recombination, hot carrier effects and even Joule heating of the current path. However, it is worth noting that there is an on-going debate in literature regarding the exact mechanism for different samples or set of biasing conditions. This is discussed in Appendix A. The enhancement in resolution proposed in this thesis can help resolve the arguments.

For the purpose of this thesis, it is sufficient to discuss the imaging of a single self-luminous point source. The image formation in conventional far-field optical systems is governed by Abbe's theory of diffraction. According to Abbe's theory, the image contrast formed in the image plane of the objective is determined by the interference of rays from the different points in the object [21]. For the case of a single self-luminous point object, the image formed by the objective consists of a central spot surrounded by diffraction rings, as shown in Fig.1.3.

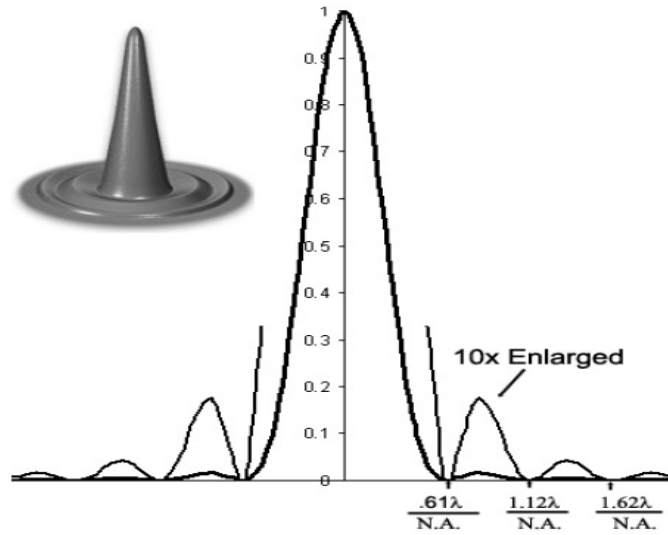


**Figure 1.3:** Intensity distribution in the image plane of the objective collecting light from a point source. Insert shows the 3D representation of the distribution. [13].

The position of minima in the intensity distribution shown in Fig.1.3 is determined by the wavelength  $\lambda$  and numerical aperture  $\mathbf{NA} = n \sin \theta$ .  $\mathbf{NA}$  is determined by the refractive index  $n$  of the media between the object and the objective lens and by the semi collection angle  $\theta$ . From Fig.1.3, it can be concluded that two point sources are resolved by the optical system if the image maximum of the intensity distribution for one of the point sources coincides with the first minimum for the second point source. Such a resolution capability  $\mathbf{R}$  of far-field systems is usually referred to as the Raleigh Criterion and given by the formula:

$$\mathbf{R} = \frac{0.61\lambda}{\mathbf{NA}} = \frac{0.61\lambda}{n \sin \theta} \quad (1.1)$$

It is clear from Eqn.1.1 that  $\mathbf{R}$  can be improved if one uses smaller  $\lambda$  or increases the  $\mathbf{NA}$ . For the case of the air-gap objective lens, the refractive index is fixed at  $n = 1$ . In this case,  $\mathbf{NA}$  can be thought of as the collection cone of the objective and it approaches the limit as the collecting half angle  $\theta$  approaches  $90^\circ$ . So for an air-gap objective, the maximum  $\mathbf{NA}$  is limited to unity and in practice rarely exceeds 0.95. This means that the best resolution for an air-gap objective lens is not better than  $\lambda/2$ . An improvement of resolution through the use of a smaller  $\lambda$  is not applicable for FFPEM because most of the photons generated by silicon devices have a wavelength close to 1170 nm corresponding to the silicon bandgap [12]. It is clear that for air-gap objectives, the theoretical limit of spatial resolution is above 500 nm. The actual value is closer to 1  $\mu\text{m}$  due to spherical and chromatic aberrations present in any far-field optical system [13].

A spatial resolution of  $1\text{ }\mu\text{m}$  was sufficient for older technologies, in which a considerable distance separates transistors or other active elements. For example, in the year 1994 the SRAM cell occupied approximately  $20\text{ }\mu\text{m}^2$  [22] and it was possible to pinpoint a transistor demonstrating the anomalous emission of photons. In the year 2009, SRAM cells fabricated at 22 nm technology node were revealed [23]. Each cell was confined to an area smaller than  $0.1\text{ }\mu\text{m}^2$ , as shown by the yellow broken rectangle in Fig. 1.4. For comparison the red broken circle represents a diffraction limited emission spot with a diameter of  $1\text{ }\mu\text{m}$ . It is clear that one diffraction-limited spot can cover up to 9 cells or 54 transistors. Hence, FFPEM is not only incapable of identifying the faulty transistor but also cannot identify the faulty functional block.

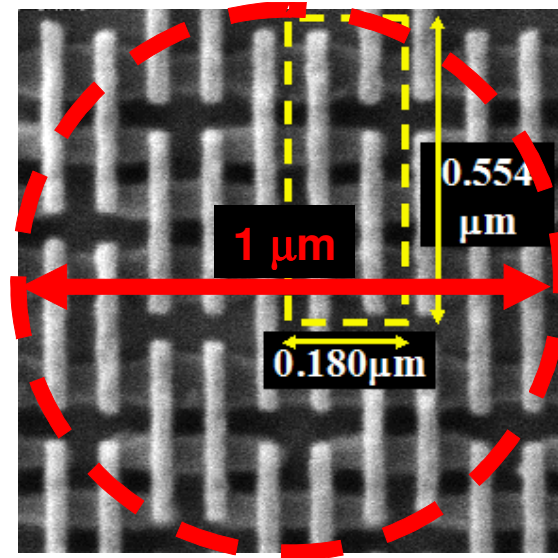


**Figure 1.4:** Comparison of the SRAM cell area at 22 nm technology node [24] with the area covered by diffraction limited PE spot with diameter of  $1\text{ }\mu\text{m}$ .

### 1.3.1 Resolution enhancement using immersion lenses

Various approaches have been undertaken to improve the spatial resolution of far-field optical systems. One popular approach for resolution enhancement in optical-based FL techniques is the use of liquid or solid immersion lens (SIL) [25]. The idea is to place a medium with a refractive index higher than that of air. The presence of such a medium in the gap between the sample and the objective improves the value of the **NA** , which leads to a proportionally better resolving power,.

The liquid immersion lens was first implemented in laser scanning imaging and optical probing. The resolution of 0.5  $\mu\text{m}$  for a 1064 nm laser beam was achieved [26]. An additional advantage of the immersion lens is its ability to investigate sub-surface objects with higher detection efficiency as compared to the air-gap objective lens. The sub-surface imaging implies that the object is placed within the medium with a higher refractive index. The transmission of light through such an interface is described by Snell's Law,

$$\frac{n_i}{n_t} = \frac{\sin(\theta_t)}{\sin(\theta_i)} \quad (1.2)$$

where indexes **i** and **t** correspond to the incident and transmitted rays at the interface, respectively.

Following Eqn.1.2, it is possible to state that the rays passing from the medium with higher refractive **n<sub>i</sub>** index to the medium with lower refractive index **n<sub>t</sub>** will propagate at a larger angle  **$\theta_t$**  from the normal to the interface in comparison to the incident angle  **$\theta_i$**

[27]. At a certain critical angle, the incident ray is totally reflected back into the medium. This effect is known as the condition of Total Internal Reflection (TIR). For the air-gap objective, the rays subjected to TIR at the sample interface will never reach the objective, thus limiting the effective collection angle. The presence of oil that can match the refractive index of the sample eliminates the TIR and thus, restores the collection angle and improves the **NA**.

Liquid immersion microscopy, when it is applied to the front-side analysis, has two major disadvantages. These are a) contamination of the sample by the liquid and b) a short working distance. In the case of a back-side analysis, the disadvantage is that it is not possible to find a liquid, with a refractive index high enough to match that of silicon. As a result, the TIR of light at the liquid-silicon interface still limits the collection angle.

In order to overcome the limitations of liquid immersion lens for back-side analysis, the approach of silicon SIL was introduced [25]. For silicon substrates, the refractive index is approximately equal to 3.5 in NIR spectral range, which can increase the **NA** proportionally to the same value [28]. However, due to refraction at the interface the maximum  $\theta_i$  that does not undergo TIR is limited. According to Snell's Law (Eqn.1.2) the maximum  $\sin(\theta_i)$  reduces by the same value of  $n_i = n_{Si}$  and thus, the final **NA** remains the same.

Ideally, the angular semi-collection angle in the object space  $\theta_t$  can be maximized by the surface geometry [29]. The introduction of SIL is intended to perform this action. The

two main types of SIL technologies that are applicable to backside sub-surface imaging are Refractive SIL (RSIL) [30] and Diffractive SIL (DSIL) [31]. The RSIL is a truncated spherical silicon lens placed on the back surface of the substrate.

The introduction of RSIL allows for improving the value of  $\sin(\theta_i)$ , but the value of  $\sin(\theta)$  cannot be more than unity and thus, the best theoretical resolution is  $\sim \lambda / 2n$ . For  $\lambda = 1000$  nm and  $n = 3.5$  Eqn.1.1 gives the value of  $R \sim 143$  nm. Hence, even the theoretically achievable value cannot satisfy the requirements for the current and future technology nodes (Table. 1.1). Also, chromatic aberrations will degrade the resolution enhancement for photon emissions with panchromatic wavelengths [29].

In addition, the performance of the proposed RSIL designs is strongly affected by the surface finishing of both the silicon substrate and the lens. The presence of a gap or surface features at the interface causes the scattering and reflections, which degrade the signals [32]. One approach to overcome this problem is the use of DSIL, which is formed by concentric rings at the polished substrate [30]. The DSIL is based on the principles of interference. However, this implies monochromatic rays not suitable for applications with the polychromatic emissions encountered in PEM [30].

Another very interesting approach is to form a silicon substrate into SIL [33] or FOSSIL. The mechanical milling with a computer-controlled lathe [33] forms the FOSSIL. The application of FOSSIL allowed us to distinguish PE from neighboring transistors separated by 560 nm. Conventional FFPEM was not able to distinguish the emissions

from these two transistors. However, it is clear that even smaller separations will not be resolved by FOSSIL. The value of 560 nm is at least one order of magnitude larger than the required spatial resolution highlighted in Table 1.1. From this example it is clear that for advanced technologies with a much denser packing of active elements (Fig.1.4), the resolution capabilities of any SIL are not sufficient. The reason of the insufficient resolution is that SIL is still based on the far-field approach and thus, limited by diffraction. In order to overcome this limitation an alternative approach is necessary.

### 1.3.2 Resolution enhancement using near-field detection

An alternative approach to improve the spatial resolution is to use the capabilities of the Near-Field (NF) detection. In Fig.1.2, several techniques based on NF detection were highlighted. However, none of them are capable to detect optical information. The technique that is capable to detect PEs with sub-100 nm resolution has been proposed in Ref.34. This technique is based on the capabilities of aperture based Scanning Near-Field Optical Microscopy (a-SNOM). In a-SNOM, an image is formed by scanning a sub-wavelength probe at a constant sub-wavelength distance from the sample surface [35]. The signal is recorded at each point of the scan. The recorded image represents the distribution of the PE intensity within the scanned area. The a-SNOM resolution is defined by the size of the aperture and the distance between this aperture and the emission source [35]. This makes it possible to avoid the wavelength dependence and overcome the diffraction limit imposed on conventional FF optical techniques (Eqn.1.1). Unfortunately, the gain in resolution for the proposed a-SNOM approach [34] is



compromised by low detection efficiency in terms of the minimum biasing currents detectable by the system. All the results using a-SNOM were achieved so far at drive current levels of tens of milliamperes [36]. A direct implementation of a-SNOM is not practical for the detection of PEs from leaking sites in the micro and nano-ampere regimes. This drawback is a possible reason for SNOM not being included in Fig.1.2. A substantial modification of the SNOM concept is required in order to improve detection efficiency of this technique. The proposed modification requires substantial understanding of the principle and evaluation of the current developments in the field of near-field optics. That is why Chapter 2 is devoted to the discussion on near-field optical detection.

#### **1.4 Thesis goals and lay-out**

This thesis is devoted to the development of a technique for the local detection of PEs with a sub-100 nm spatial resolution and a detection efficiency at sub- $\mu$ A drive currents through silicon devices. The proposed new technique is named Scanning Near-Field Photon Emission Microscopy (SNPEM), which is intended to achieve the following goals:

- i. Near-field detection of photon emissions from biased semiconductor devices with sub-100 nm resolution for its compatibility with advanced technology nodes.
- ii. Near-field detection of photon emissions with a detection efficiency sufficient for the detection of sub- $\mu$ A currents for compatibility with the biasing conditions of advanced technology nodes.

- iii. Compatibility with the requirements of failure analysis applications including the need for a routine operation with high level of repeatability.

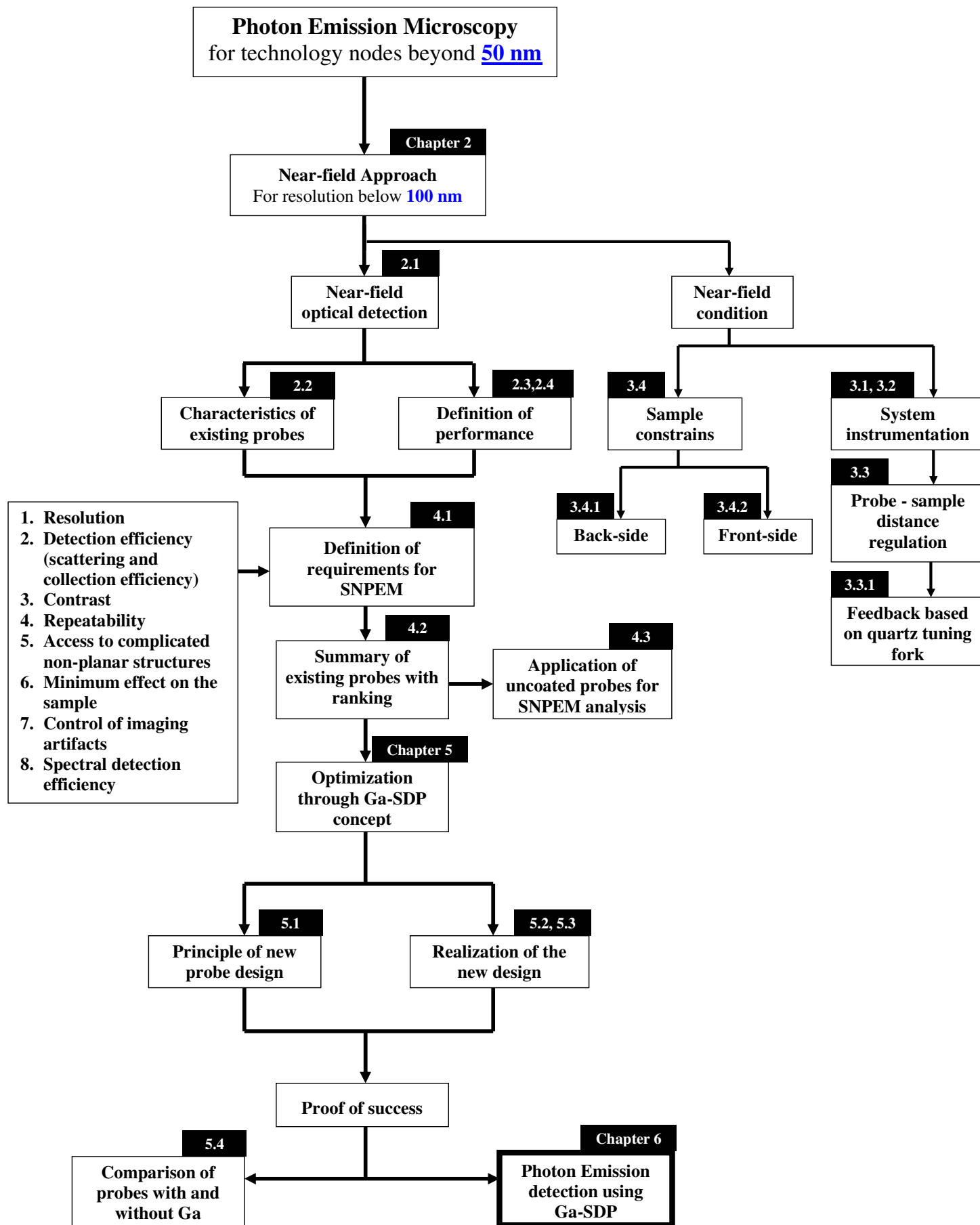
The basis and outline of the thesis are schematically presented in a diagram at the end of this Chapter. This diagram is summarized as follows:

- i. Chapter 2 introduces the concept of near-field optical detection as a means to enhance the optical lateral resolution below 100 nm. The origin of the near-field optical interaction and the critical parameters of the near-field optical probes are discussed. The description and performance of existing near-field optical probes are compared.
- ii. Chapter 3 describes the actual SNPEM set-up with a particular focus on the near-field condition. The near-field condition demands a precise positioning of the probe within a nanometric distance from the sample surface. It also required that the emission source is placed at a nanometric distance below the surface. The distance regulation and sample preparation methods required for achieving this condition are demonstrated.
- iii. Chapter 4 formulates the requirements for the near-field probe that is suitable for SNPEM analysis. Based on these requirements, existing probe designs are summarized and ranked. The uncoated dielectric probe is found to satisfy most of the requirements. SNPEM results using uncoated dielectric probe show resolution capabilities at the level of 200 nm, which are still insufficient for SNPEM application. At the same time, a detection efficiency of 10  $\mu$ A in terms of minimum

drive current variation is demonstrated. This result shows an improvement of three orders of magnitude when compared to the results achieved with a-SNOM.

- iv. Chapter 5 presents a novel scattering dielectric probe with an embedded gallium nanoparticle (Ga-SDP). This probe is designed to improve the resolution, detection efficiency and the contrast of near-field imaging. The fabrication method is also proposed and implemented. The method allows repeatedly creating a scattering Ga center at the nanometric tip of the tapered glass fiber. The performance of such a probe is compared to that of a probe without Ga and an enhancement of up to 37 times is demonstrated.
- v. Chapter 6 demonstrates a resolution capability of 50 nm and a detection efficiency below 1  $\mu\text{A}$  when Ga-SDP is implemented for SNPEM analysis of different semiconductor test structures. Wavelength dependent imaging is demonstrated which is capable of identifying the different emission mechanisms within a single emission spot. Also a possibility for the sub-surface localization of the emission source is demonstrated.
- vi. The last Chapter provides the conclusions and suggestion for future work.

## Scheme of Argumentation for SNPEM implementation



## **Chapter 2.**

### **Near-field optical detection**

The general idea for overcoming the diffraction limit is to convolute the spatial frequencies of the sample with the spatial frequencies of a nanometric probe placed into the near-field of the emission source. The near-field is scattered by the probe and collected in the far-field. Different near-field probe designs are available but they have certain disadvantages that can limit their applications for a SNPEM analysis. The efficiency of scattering is determined mainly by the polarizability of the final tip, which can reach high levels if the tip is metallic. The engineering of the tip dielectric function can also be considered as a means for improving the scattering efficiency. One promising design consists of the metallic scatterer attached to the transparent dielectric tip. The dielectric tip is required to capture a considerable section of the scattered light. A proper design for the final taper of such a dielectric tip is required in order to optimize the capture fraction of the probe.

#### **2.1 Introduction into near-field optics**

The resolution limit imposed on FFPEM (Eqn.1.1) can be overcome if the analysis is brought into the near-field of the emission source. With a similar purpose, the SNOM has already established itself as a powerful tool capable of performing optical measurements with spatial resolution far beyond the diffraction limit. This technique is based on the interaction between a nanometric mechanical probe and optical near-fields of the object. Optical near-fields can be found either at the source region of the optical radiation or at the secondary sources that appear on the boundary of the materials subjected to the

external radiation [37]. The interaction with these near-fields is non-linear and, unlike in the case of conventional far-fields, the spatial resolution is closely correlated with the actual properties of a sub-wavelength emission source as well as the near-field probe.

In general, the major difference between the Far-Field (FF) and Near-Field (NF) interactions is that the former is a complex product of field and distance. The latter allows the measuring of these parameters separately due to the strong impact of the source [38]. To put it simply, the NF interaction between two objects is confined to a region where the distance between these objects is smaller than the characteristic length of the field responsible for the interaction.

There are many different NF interactions in the various techniques and there are also many phenomena that are normally not correlated to the NF but, nevertheless, imply NF conditions [38]. One good example is the stethoscope, in which a diaphragm of several centimeters in diameter is used to locally detect sound waves from internal organs. These waves have characteristic wavelengths in the range from hundreds of centimeters to several meters. Such detection is possible only in the NF of the object, which explains why the diaphragm has to touch the body.

These observations can be used for the formulation of the main principle of the NF imaging, which is often referred to as the NF condition. This condition can be summarized in the following way: when a probe with a characteristic dimension of the

scattering center **a** is raster scanned at a constant distance **h** above the object, it is possible to achieve spatial resolution on the order of **a** [39] if

$$\mathbf{h} \leq \mathbf{a} \ll \lambda \quad (2.1)$$

where  $\lambda$  is the wavelength of light used for imaging.

When the NF condition is achieved, the detection efficiency depends on the geometric and material properties of the probe. Two types of probes are mainly used: aperture and aperturless or scattering probes. It is commonly accepted that the aperture-based probe was first proposed by E.H. Synge [40]. However, originally he had proposed a different idea formulated a few months before his journal publication in a letter written to A. Einstein [37]. In this letter, Synge described a microscopic method in which a sub-wavelength source is formed not by the field penetrating through a tiny aperture but by the field scattered from a tiny particle. A schematic representation of this idea is shown in Fig.2.1.

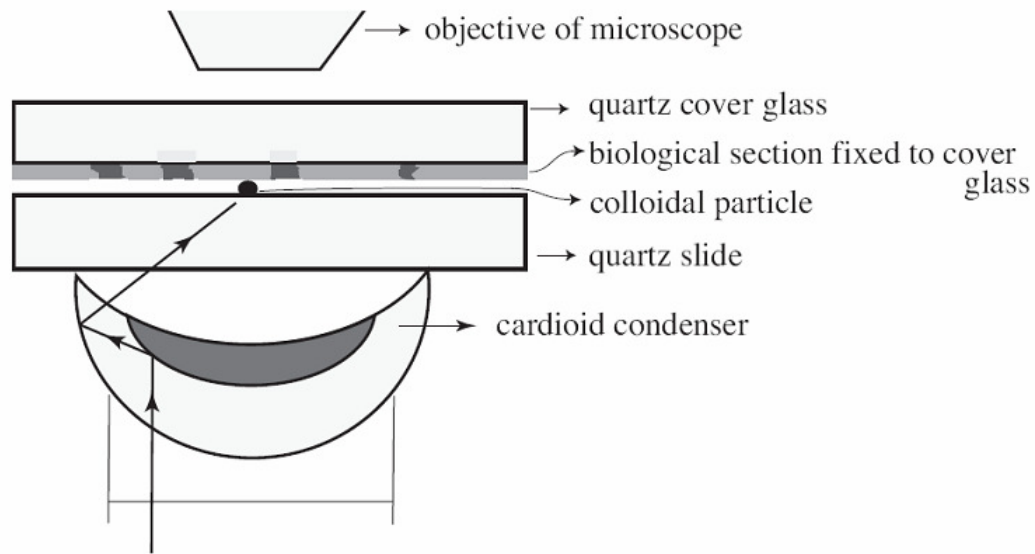


**Figure 2.1:** Original idea of near-field optical microscope by E.H.Synge [37].

In this method the particle is attached to a glass slide and illuminated from below by a light beam that undergoes Total Internal Reflection (TIR). According to Synge's proposal, most of the light should be reflected back except for a small fraction that would reach the surface at the base of the particle. This portion would be scattered into the upper space of the glass slide. To this, if one was to place another slide with a sample of interest at a close distance above the particle (Fig. 2.1) and scan it in raster parallel to the first glass, then the signal collected by the objective (Fig. 2.1) should depend upon the relative opacity of the different parts of the sample.

However, such an implementation was impractical and reasonably dismissed by Einstein because at such short distances the frustrated TIR will cause a considerable leakage of the original beam into the second glass slide. In his response to Synge, Einstein suggested the use of a tiny hole in an opaque layer as the light source [37].

It is important to understand that the general idea of overcoming the diffraction limit is to convolute the spatial frequencies of the sample with the spatial frequencies of the probe [41]. As long as the probe object is capable of providing the necessary high spatial frequencies, it does not really matter whether a particle or an aperture is scanned over the surface [42,43]. When it comes to scattering, the sub-wavelength aperture and the sub-wavelength non-transparent object are equivalent [44]. Today it is well established and experimentally verified that a tiny particle can serve as a local sub-wavelength source of radiation [45,46]. Such scattering near-field probes have an advantage of enhanced near-



field excitation [41] and in principle; they have no limitation with respect to the minimum effective size of the field confinement volume or resolving power [47].

A considerable part of this thesis is devoted to the identification of the optimum near-field probe for the specific application of SNPEM. The optimization of the design will focus on three parts of the probe (Fig.2.2): the near-field interaction volume, the collection part and the guiding part.

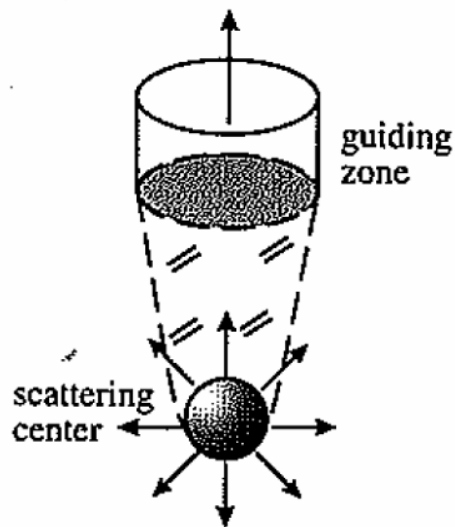


**Figure 2.2:** The scattering model for collection near-field probe [48]

## 2.2 Near-field optical probes

A number of SNOM systems have been proposed in the last 30 years, which vary with regards to the type of NF probes, illumination and detection optics and their applicability to different samples. The description of different schemes can be found in Ref. 49. In this thesis, the detection principle is defined as the detection of emissions in the NF of biased

semiconductor devices. Hence, the research is mainly focused on the applicability of different probes to such devices. In the following sub-sections, the different NF probes will be summarized.

### 2.2.1 Probe based on sub-wavelength aperture

It has already been described in Section 2.1 on how the idea of using the sub-wavelength aperture for optical measurements beyond the diffraction limit came to be used. To simplify the issue, in the aperture based SNOM (a-SNOM) the imaging beyond the diffraction limit is achieved by raster scanning a tiny aperture with diameter  $a \ll \lambda$  at a distance  $h$  as defined by the NF condition (Eqn.2.1). The simple representation of a-SNOM is shown in Fig.2.3a, which is redrawn from a patent where a-SNOM was proposed for NF detection of photon emissions from semiconductor devices [34].

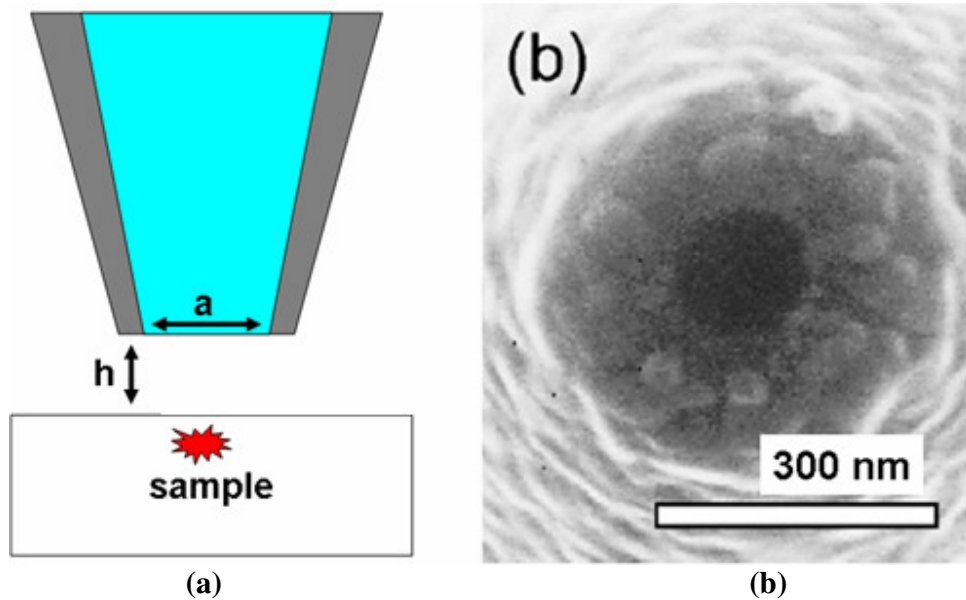


**Figure 2.3:** Application of a-SNOM for photon emission detection. a) Schematic representation [34]. b) SEM image of the 100 nm aperture [50].

The scanning electron micrograph of one of such apertures is shown in Fig.2.3b. The a-SNOM was applied by many groups for the detection of electroluminescence from semiconductor lasers [36,51-56], as well as of photon emission from silicon p-n junctions [57]. In all these attempts, the detection was performed at drive currents in the mA range, while the nanometric resolution was not demonstrated. A SNPEM application targets the detection of leakage currents in the sub- $\mu$ A range critical for modern devices (Fig.1.2). Hence, it is likely that the poor detection efficiency of a-SNOM in collection mode is the main reason why NF photon emission detection did not attract much of attention so far.

The reason behind the poor detection efficiency is a strong attenuation of light transmitted through the sub-wavelength aperture. The behavior of such an aperture in an infinitely thin screen made of an ideal metal has been known for quite a long time. It is described by Bethe-Bauwkamp Theory [58-60]. The transmission  $\mathbf{T}$  of the aperture with diameter  $\mathbf{a}$  illuminated with a plane wave at wavelength  $\lambda$  is given by

$$\mathbf{T} \propto \left( \frac{\mathbf{a}}{\lambda} \right)^4 \quad (2.2)$$

Equation 2.2 shows that in order to improve the resolution by one order of magnitude (from 1  $\mu$ m to 100 nm), it will be necessary to improve the sensitivity of the photon detector by  $10^4$  times in order to detect the same signal. And there will be a need for at least another order of magnitude improvement of detector sensitivity if one wants to shift the analysis from the visible to the near-infrared part of the spectrum. The attenuation factor described in Eqn.2.2 is an underestimation because real apertures are not made of infinitely thin metal [61]. Another assumption for Eqn.2.2 is that an ideal metal is used

for coating. However, this assumption ignores the fact that a considerable portion of light power will be transferred to heat [62,63], further increasing the attenuation. The non-ideality of the metal also puts a limit on the achievable resolution. The most common design of the aperture probe is a tapered optical fiber coated with aluminium or gold. Real metals have a finite skin depth of 6-10 nm [64] where the electric field can penetrate. This means that for an aperture with physical diameter of 10 nm the uncertainty of the effective optical diameter can reach 100% [64,65].

The attenuation due to the sub-wavelength aperture is strong and unavoidable but attenuation within the taper region is also considerable. That is why so far all the improvements of aperture-based probes have clearly gone towards the multi-taper geometries [66-68] or the ultimate geometry of parabolic tapers [69,70]. Such geometries naturally minimize the length of the taper region where the light is propagating beyond the cut-off diameter [66,70]. However, it is likely that the reason of this improvement is due to the optimum collimation property of the parabolic mirror in collection mode (for an illumination mode the parabolic mirror is an ideal geometry for focusing the collimated light from the optical fiber into the single spot). If the aperture is placed at the focal point of that mirror, then all the light passing through the aperture will be collimated into a parallel beam. Such a beam can easily be within the acceptance angle of the optical fiber waveguide and thus, maximum light passing the aperture will be guided towards the detector at the bare end of the fiber. Parabolic tapers can be realized by forming a tip inside a light-sensitive polymer drop placed on the cleaved surface of the conventional single mode optical fiber (SMF) [71,72]. The parabolic shape is achieved

due to the natural Gaussian beam of the fundamental mode of the SMF. It is specified to provide at least one order of magnitude improvement in comparison with conventional conical tapers. Unfortunately, the optimization of the taper will never be sufficient because the actual aperture still has a finite thickness causing attenuation [61].

Along with the poor transmission of the sub-wavelength aperture, there are also no reliable methods for nanometric aperture fabrication. Such unreliable fabrication is a serious road-block for SNOM adoption for FA. The most popular method is capitalizing on the shadowing effect [73] when the probe is simply pointing away from the metal evaporation source during film deposition. This allows a portion of the tip to remain uncoated and thus, form an aperture. By rotating the tip during coating one can expect an even metal coating around the sides of the tip [61]. However, the aperture size is not reproducible [74,75]. Also the grainy structure at the tip, as shown in Fig.2.3b, is causing longer distances between the aperture and the sample. Longer distances degrade resolution and detection efficiency [76,77]. Additionally, such grains introduce an unpredictable shift between the topographic and optical images [78], which strongly complicate the interpretation of the recorded information. Focused Ion Beam (FIB) can be used to make a smooth ending surface on the probe [79,80]. However, the usual coating thickness is from 100 to 200 nm [61], which makes such probes blunt with a low aspect ratio and thus, low topography resolution [81]. Even for probes treated with FIB, the benefit of superior resolution is achieved only on very flat samples and with perfect alignment between the probe and the sample.

### 2.2.2 Probe based on the uncoated dielectric tip

Another notable variation of a NF probe is a sharp uncoated dielectric tip. Most commonly it is used in Photon Scanning Tunneling Microscopy (PSTM), also called Scanning Tunneling Optical Microscopy (STOM). This approach was developed simultaneously by three different groups [82-84]. In PSTM, the probe tip acts as a transducer that couples energy out of an evanescent field at the sample surface into a homogeneous propagating field within the probe body [47], as shown in Fig.2.4a.

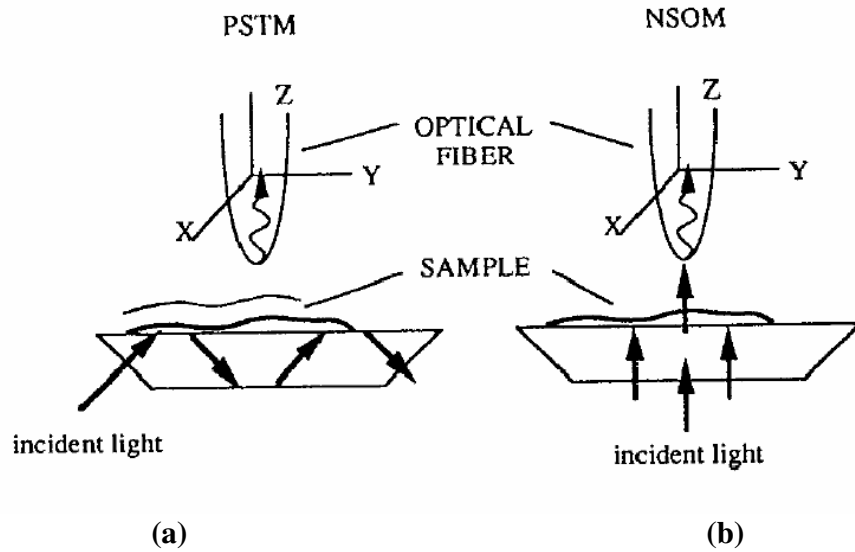


**Figure 2.4:** Difference between a) PSTM and b) SNOM illumination schemes [47].

The most common arrangement for exciting evanescence field is using Total Internal Reflection (TIR) at a dielectric-air interface of the glass prism as shown in Fig. 2.4a. For comparison, Fig. 2.4b shows the SNOM in collection mode with such a probe. In both cases, the excited field is modulated by a thin sample placed on the illuminated surface of the prism and it is collected by the PSTM probe [82].

Some interesting applications of PSTM are found in optoelectronics and optical waveguide analysis. PSTM allows the measuring of the evanescence tail of a waveguide mode and also allows us to directly visualize the electromagnetic field associated with an optical pulse [85,86]. Extensive theoretical studies of the PSTM method were performed by several groups [87-89], but the interpretation of the recorded images is still a challenging task [90,91]. It is also likely that for uncoated dielectric tips, the effective detection plane does not coincide with the final tip position but it is situated within the probe [91]. A comparison of the theoretical and experimental results allowed an estimation for the detection plane height at 140 nm for the heat-drawn probe with 20 nm apex and 8° taper angle **20** [91]. However, such distances mean that the resolution will be degraded to a similar value. The best resolution predicted for such probes, when only directly coupled into local bound modes of the probe are taken into account, is no better than 150 nm [89].

In addition to the bound modes excited in the probe, there are independent excitations or scattering events, which can lead to a secondary coupling [43,47,60]. This scattering is caused by edge effects and inhomogeneities. Some fraction of the scattered light can couple into the propagation modes of the probe. The intrinsic molecular scattering of silica glass was proposed as a source of the scattering caused by local fluctuations of the permittivity [47]. The scattering in various grades of telecommunication fibers is a well-known phenomenon [92]. It is also known that an addition of dopants increases the scattering [47]. For such probes, the effective scattering volume of the tip determines the

resolution. The resolution can thus be improved as long as the tip size can be reduced [47].

### 2.2.3 Protrusion type probe

The disadvantage of uncoated tips is that the direct coupling to the fiber is comparable or even higher than the coupling induced by tip the scattering. It is practical to apply a coating above the tip in order to limit the impact of this coupling. Such a probe is schematically shown in Fig.2.5.

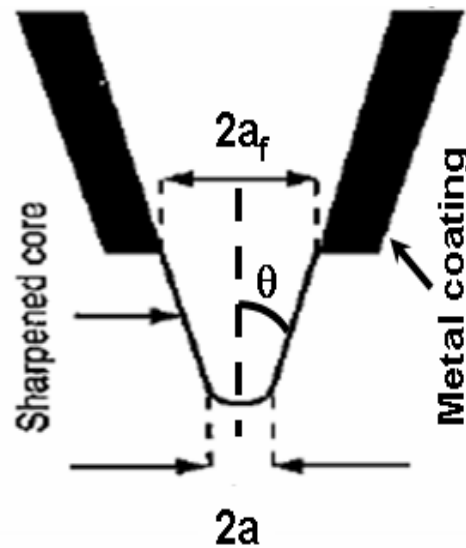


**Figure 2.5:** Schematic representation of protrusion-type probe [94].

The dielectric sharp tip can be seen as protruding through the metal film. That is why such a probe is usually called a Protrusion Type Probe (PTP). The tip of the protrusion defines the highest spatial frequency recovered by the system from the optical images



[93]. The final image contains all the frequencies within the interval corresponding to sizes between the tip diameter and the diameter of the base aperture [94].

A few self-terminating processes can be applied in order to fabricate a PTP [95,96]. The self-terminating nature of those methods allows a high level of control of the aperture parameters with a minimal human interference in the process. Such probes can ensure that the topography and optical images always coincide because they are related to the interaction of the same point on the probe with the sample [95]. Also they protect the aperture from wearing out [96]. However, the base aperture diameter in such a probe is still kept at sub-wavelength levels. According to Eqn.2.2, such a small base aperture limits the detection efficiency.

#### 2.2.4 Probe based on a scattering metallic tip

In comparison with aperture probes and dielectric tips, metallic tips have the advantage of higher NF excitation for a given incident intensity. Also, at least in principle, metallic tips have no limitation with respect to the minimum effective size of the field confinement volume or resolving power [41]. The basic idea is to choose a metal that demonstrates the resonant scattering at the wavelength of interest [97, 98]. A detailed discussion on the origin of the resonance will be provided in Section 2.3.

A disadvantage of metallic tips is the background due to the reflections from the probe shaft. This disadvantage is usually avoided by dithering the tip in the vertical direction

followed by demodulation of the signal using lock-in [99] or heterodyne detection [100]. An additional way to suppress the background and improve the contrast is to create a discontinuity of material at the end of the tip [101]. Such a tip should not only provide a better contrast between the action of the tip and the action of the probe body but it is also predicted to provide one order of magnitude higher field enhancement in comparison with all metal tips of similar dimensions [101].

Another problem with the metallic tips is that the collection of the signal is performed by external optics at an angle to the probe axis, as shown in Fig.2.6, or below the sample if the sample is transparent. This puts considerable constraints on the sample properties. For example, the light scattered within the structures with a high aspect ratio, like metal contacts of the DUT, will only be partly detected by the distant objective shown in Fig.2.6.

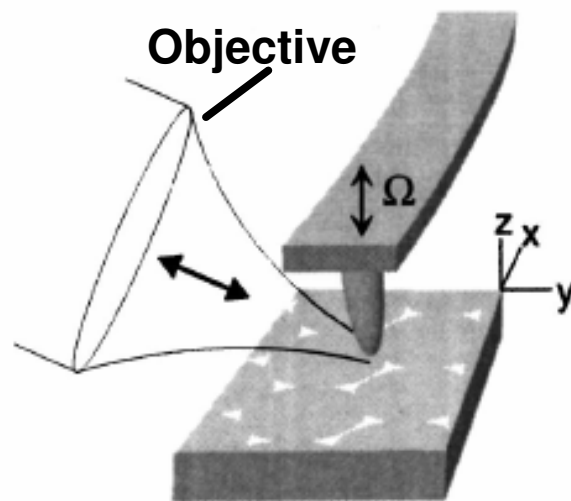


**Figure 2.6:** Illumination and collection optics for application of metallic scattering SNOM tips [102].

### 2.2.5 Probe based on metallic nanoparticle attached to dielectric tip

In the previous sub-sections, it was suggested to introduce a concept of discontinuity of material at the end of the tip, in order to achieve enhanced scattering. Such a probe can be achieved by attaching a metallic nanoparticle at the end of the dielectric probe [45,46]. Surprisingly, this most recent idea in NF optics brought the discussion back to Synge's original idea discussed in Section 2.1, except that now the particle is attached not to the glass slide but to the tiny glass probe, as shown in Fig.2.7. Such an arrangement considerably reduces the tunneling of light due to a frustrated TIR and thus, overcomes Einstein's concern.

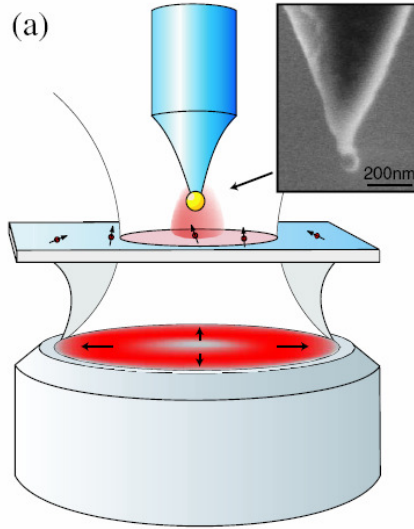


**Figure 2.7:** Scattering SNOM with metal particle attached to the dielectric tip. Inset: SEM image of a gold particle attached to the end of a pointed optical fiber. [46].

The particle is attached by glue to the end of the tapered glass fiber [45,46]. Such a particle will be a much stronger scatterer than the glass fiber tip due to its inherent

capability of a higher scattering efficiency. Such a difference in the scattering efficiency improves the contrast of the recorded image due to the lower background from the probe shaft. Particles of different metals and sizes can be attached to the glass tip [103] and these properties will define the spectral detection efficiency of the probes

The disadvantage of such probes is that the collection of scattered light is still performed by external optics [45,46]. In Fig.2.7, the scattered light is collected by an objective placed below the transparent sample. The detection of the scattered signal through the same optical fiber, to which the particle is attached, is usually not considered. A possible reason is the misalignment between the particle position and the optical axis of the fiber that makes the fiber an inefficient collector of the scattered NF signal [98].

A discussion of the advantages and disadvantages of the different probes for applications in SNPEM is provided in Chapter 4.

### **2.3 Near-field interaction of scattering probes**

From the description of near-field probes proposed in literature, it is clear that the choice of the scattering center (Fig.2.2) is the most critical parameter determining the final detection efficiency. The scattering efficiency of the center depends on geometry and material properties of the probe tip. Below these properties are discussed in detail.

### 2.3.1 Scattering by a homogeneous isotropic sphere

The simplest geometry of a scatterer is a sphere. Before discussing the interaction of such a sphere with the NF, it is important to consider the conventional scattering of the uniform electrical field. For this purpose, let's look at a small homogeneous isotropic sphere of radius  $a$  with dielectric function  $\epsilon$ . This particle is placed into the uniform electric field  $\mathbf{E}_0$  inside the medium with dielectric function  $\epsilon_m$  (Fig. 2.8).

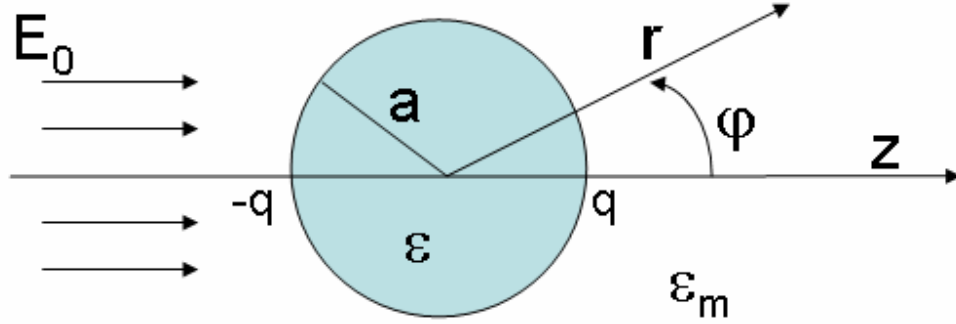


**Figure 2.8:** Small dielectric homogeneous isotropic sphere scattering the uniform electric field [104]

The scattered field is related to the potential induced by the sphere, which is calculated by Laplace equation [104]. The potential of the field outside the sphere at distance  $r$  scattered into direction, which is defined by an angle  $\phi$ , is given by

$$\Phi_{\text{out}} = -E_0 r \cos \phi + E_0 a^3 \cos \phi \frac{\epsilon - \epsilon_m}{\epsilon + \epsilon_m} = -E_0 r \cos \phi + \Phi_d \quad (2.3)$$

The potential  $\Phi_d$  is a potential of the ideal dipole  $\bar{p}_d$  induced by the external field  $\bar{E}_0$  and given by [105]

$$\bar{p}_d = 4\pi\epsilon_m a^3 \frac{\epsilon - \epsilon_m}{\epsilon + 2\epsilon_m} \bar{E}_0 = \epsilon_m \alpha \bar{E}_0 \quad (2.4)$$

where the ease of polarizing the sphere is determined by polarizability  $\alpha$ , given by

$$\alpha = 4\pi a^3 \frac{\epsilon - \epsilon_m}{\epsilon + 2\epsilon_m} = 4\pi a^3 g \quad (2.5)$$

where  $g = \frac{\epsilon - \epsilon_m}{\epsilon + 2\epsilon_m}$ .

The definition of polarizability in Eqn.2.5 is valid not only for the uniform field but also when the particle is illuminated by a plane wave, with a condition that the size of the particle  $a$  is much smaller than that of the wavelength  $\lambda$ . For the visible and NIR spectral ranges such a particle has nanometric dimensions and it will be referred as nanoparticle later in the thesis. The condition proposed above is usually referred to as Quasi-Static Approximation (QSA), which requires the field to be uniform within the sphere [104]. The issue of applicability of this approximation for qualitative estimation of efficiency of nanoparticles to scatter near-field of the emission source is discussed in Appendix B.

### 2.3.2 Dielectric function of the scatterer

The overall intensity of light scattered by a nanoparticle is proportional to the square modulus of the dipole moment  $\bar{p}_d$  induced inside the particle [39]. Then using Eqn.2.4, it can be concluded that for the fixed illumination source, the intensity is proportional to the square modulus of polarizability  $\alpha$ . Assuming that only the nanometric tip of the NF probe determines the scattering, it is possible to approximate this tip with a nanoparticle. Hence, the optimization of the probe can be done by the maximization of the value of  $|\alpha|^2$  for a nanoparticle made of the same material as the tip.

For a sphere with a fixed diameter the maximum  $\alpha$  is achieved when the denominator in Eqn.2.5 is equal to zero or when  $\epsilon = -2\epsilon_m$ . Assuming that the surrounding medium is air with  $\epsilon_m \approx 1$ , the maximum  $\alpha$  is achieved when the real part of the dielectric function of the sphere  $\text{Re}(\epsilon)$  is negative. This negative value is observed in metals because of the presence of free carriers. The behavior of such carriers is quantitatively described by the Drude Model [106]. In Fig.2.9 the theoretical values of the copper dielectric function are compared to experimentally measured values retrieved from the Handbook of Optical Constants [107].

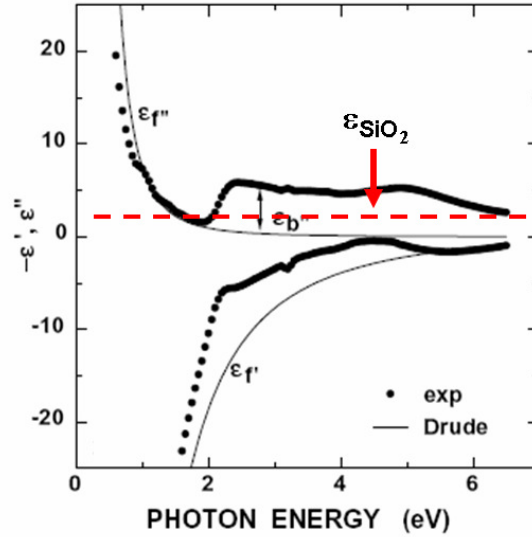


**Figure 2.9:** Comparison of theoretical and experimental values of dielectric function of copper [108] with dielectric function of silica (red line) taken from Ref.109.

The discrepancy for the real part of the dielectric function of copper  $\text{Re}(\epsilon_{\text{Cu}})$  observed in Fig.2.9 is due to the contribution of bound electrons in the material [108,110]. However,

the most important observation here is that  $\text{Re}(\epsilon_{\text{Cu}})$  is negative and approaches the resonance value of -2 (assuming  $\epsilon_m = 1$ ) for certain photon energies. The non-zero imaginary part  $\text{Im}(\epsilon_{\text{Cu}})$  is responsible for a damping in the system and it will not allow the resonance to reach infinity. For comparison, the values of dielectric function of silica are also indicated in Fig.2.9. This function is always positive, varying from 2 to 2.25 throughout this range of wavelengths and does not have any imaginary part [109].

The impact of the sign in front of  $\text{Re}(\epsilon)$  can be estimated using the value of polarizability as shown in Fig.2.10.

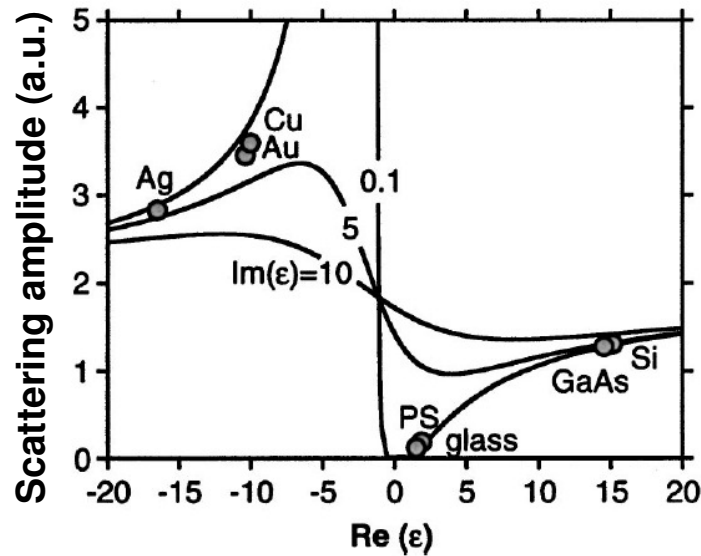


**Figure 2.10:** The dependence of the scattering amplitude on the  $\text{Re}(\epsilon)$  at 633 nm for different values of  $\text{Im}(\epsilon)$ . The corresponding values of dielectric functions of different materials are indicated [102].

From Fig.2.10 it is clear that for dielectric or semiconductor materials, which have a positive value of  $\text{Re}(\epsilon)$ , the scattering efficiency is always lower than that for metallic materials, which have negative  $\text{Re}(\epsilon)$ . It is also clear that for  $\text{Re}(\epsilon) = -2$  the scattering



efficiency is maximum and in the case of negligible  $\text{Im}(\epsilon)$  it can increase infinitely. In Fig.2.9 it was shown that for certain wavelengths the  $\text{Re}(\epsilon)$  can indeed reach such a resonance condition.

It follows from Fig. 2.9 and 2.10 that for the enhancement of the scattering, it is preferable to use metallic particles instead of dielectric ones. The qualitative confirmation of this conclusion in the near-field zone is given, for example, in Ref.111. There it is shown that light scattered from metallic (gold) particles is 5 times higher than light scattered by dielectric (latex) particles of a similar diameter. This result confirms the conclusion of Appendix B that QSA is applicable for the qualitative estimation of scattering efficiency in the near-field. The quantitative analysis is complicated by the dependence of the scattering efficiency on the sample and by non-uniformity of the field (see discussion in Appendix B).

### 2.3.3 Engineering of the dielectric function

In sub-section 2.2.5, it was shown that improved performance can be achieved by attaching the metallic nanoparticle to the dielectric probe. However, such an approach limits the applicability of the probe to a relatively narrow wavelength range where this metallic nanoparticle is an efficient scatterer. Most of such particles are efficient in the ultraviolet or visible spectral ranges but not in the NIR spectral range of interest for PEM. In order to have better control of the dielectric function of the scattering center, an alternative method can be adopted. This method implies an implantation of metallic ions

into the dielectric tip of the probe. The implantation of metals like Cu, Au, Ag, Ta, W, Ni and Ga has already showed the possibility of altering the optical properties of silica and other materials [108,112-116]. Modified resonances of metallic nanoparticles implanted into the dielectric medium are shifted in relation to pure metal resonances [116]. The modification of scattering properties is related to the change of effective dielectric function of the composite materials in relation to both, the dielectric and the metal. The effective dielectric function  $\epsilon_{\text{eff}}$  of the composite material can be described by Maxwell-Garnett Theory (MGT) if the metal fraction  $f$  is small [117], and given by

$$\epsilon_{\text{eff}} = \epsilon_m \frac{\epsilon + 2\epsilon_m + 2f(\epsilon - \epsilon_m)}{\epsilon + 2\epsilon_m - f(\epsilon - \epsilon_m)} \quad (2.6)$$

For large metal fractions effective medium theory can be used [117,118]:

$$f \frac{\epsilon - \epsilon_{\text{eff}}}{\epsilon + 2\epsilon_{\text{eff}}} + (1 - f) \frac{\epsilon_m - \epsilon_{\text{eff}}}{\epsilon_m + 2\epsilon_{\text{eff}}} = 0 \quad (2.7)$$

After implantation, the metal atoms tend to form colloids with diameters in the range of 1 nm to 20 nm, as shown in Fig.2.11. The distribution of these colloids is dependent on the metal used, ion flux, accelerating voltage and post implantation annealing. If one can implant such nano-colloids into the nanometric glass tip, it will be possible to tune the scattering properties of the NF tip by optimizing the implantation parameters and with the proper choice of metals.

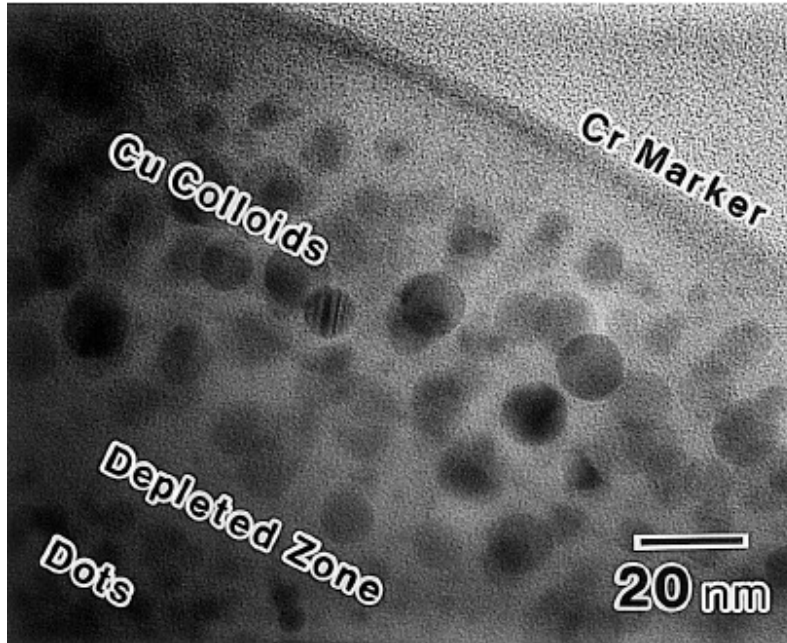


**Figure 2.11:** Distribution of metallic nanoparticles implanted into dielectric [114].

For particular SNPEM application it is necessary to cover a broad spectral range. Hence, several strategies can be proposed. For example, implantation of different metals into the same tip can be considered. Different metals are responsible for scattering at different spectral ranges, as was shown in Ref.115. And if different metals are mixed than the overall mixture can be expected to respond to a broader spectral range. An alternative approach is to use a metal, which has enhancement capabilities in a broader spectral range in comparison with conventional methods. Such metal is Ga, which is characterized by  $\text{Re}(\epsilon_{\text{Ga}})$  of approximately -9 within a broad range from 500 nm to 1300 nm [119]. Hence, by the proper mixing with silica the optimum value of -2 can be achieved throughout the considerable part of the spectral range of interest for PEM (400 – 1700 nm). The second approach will be attempted in this thesis.

## 2.4 Detection of the scattered signal

Detection of the signal scattered by the probe tip is determined by the efficiency of the collection optics used in the system. It was already mentioned in sub-section 2.2.5 that it is advantageous to perform the collection of the signal scattered by the tip through the body of the same probe. Hence, the properties of the last taper play a critical role in the ability of the NF optical probe to collect the maximum signal scattered. The collected signal can be described through the capture fraction **S** for scattered radiation used in Ref.47.

### 2.4.1 Collection efficiency of the taper for dielectric uncoated probe

Many methods have been developed to obtain efficient and reproducible tapered glass fiber tips. The two most popular approaches are heat-drawing [76,120] and chemical etching in aqueous hydrofluoric (HF) acid solution [95,121]. The first approach produces a tip with a very smooth surface, but with a long taper length. Consequently, it has a small cone angle at the tip apex that would lead to low light transmission of the system [122,123]. The value of **S** for the heat-drawn tip is a function of internal critical angle  $\theta_c$  given by [47]

$$\theta_c = \sqrt{(n_1^2 - n_2^2)/(2n_1^2)} = \sqrt{2\Delta} \quad (2.8)$$

where  $n_1$  and  $n_2$  are refractive indexes of fiber core and cladding respectively.

The dependence of **S** on  $\theta_c$  is shown in Fig.2.12.

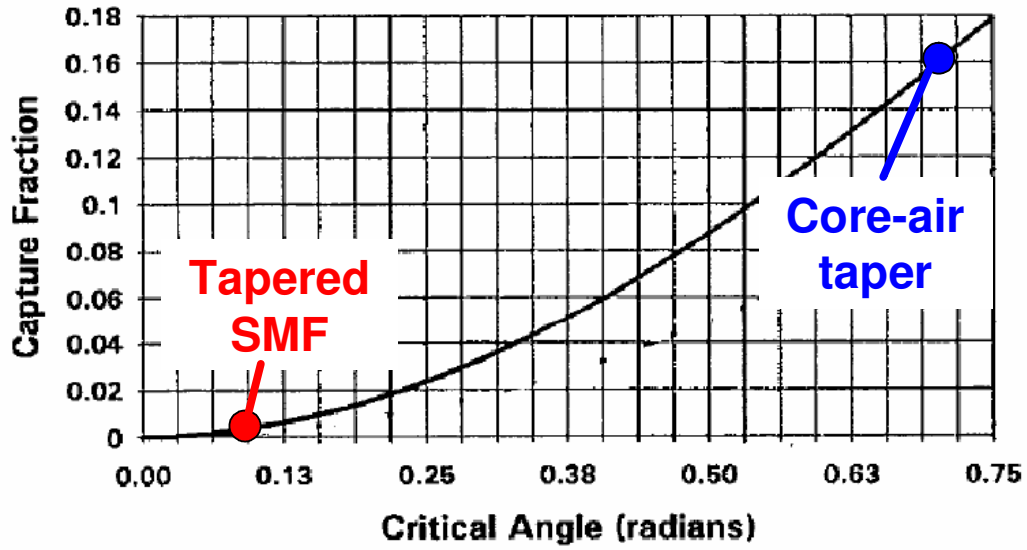


**Figure 2.12:** Scattering capture fraction as a function of the transmitting fiber critical angle  $\theta_c$  [47].

When a standard SMF with  $\Delta \approx 0.003$  and  $\theta_c \approx 0.08$  radians is considered, the capture efficiency is not lower than  $3 \times 10^{-3}$ . However, if the waveguide is formed by glass as a core and air as a cladding then  $\Delta \approx 0.27$  and  $\theta_c \approx 0.7$ , leading to  $S > 10^{-1}$ . Hence, for the same taper angle, an improvement of two orders of magnitude in the collection efficiency can be achieved if the cladding of the final tip is removed, leaving a waveguide made of glass core and air cladding [47].

High values of  $\Delta$  also allow 10 times smaller taper diameters that can still efficiently couple the scattered light in comparison with tapers made of SMF [47]. However, the all-glass waveguide structure above the final tip should be retained, in order to facilitate low loss guiding towards the detector.

From Fig.2.12 it is clear that **S** improves as long as the taper consists of only core material and the taper angle is increased. Such a tip is achieved by chemical etching. This is partly the reason why the chemically etched probes outperform heat-drawn probes in terms of optical efficiency [66,95]. Using the chemical etching method, cone angles **2θ** up to 120° are achievable [124]. The main drawback of this method is the instability of the tip shape and the poor surface quality due to environmental influences [122].

The ultimate probe angle **2θ** of ~180° is also achievable if parabolic-like tapers are implemented. It is expected that such tapers should provide better collection efficiencies in comparison with conical shapes [48,124]. And it was already mentioned in sub-section 2.2.1 that parabolic-like tapers provide order of magnitude improvement for transmission efficiency in aperture-based probes in comparison with conically shaped probes [69-71]. However, in the case when the probe is uncoated a parabolic shape or conical shape with a large opening angle will deteriorate the contrast due to NF interaction between the sample and the tapered body of the probe [39].

#### 2.4.2 Near-field interaction of the probe body

In addition to the function of collecting the scattered light from the tip, the taper of the probe can also undesirably interact with the NF of the emission source. The presence of this interaction degrades the contrast of the final image. In order to consider the NF interaction of the taper, one can approximate the profile of the probe with two spheres [39]. In Fig.2.13, Sphere P with a radius of **a<sub>P</sub>** represents the effective volume of the tip

that is closest to the emission source represented by Sphere S. Sphere T of a larger radius  $a_T$  placed above the Sphere P represents the body of the probe (Fig.2.13).

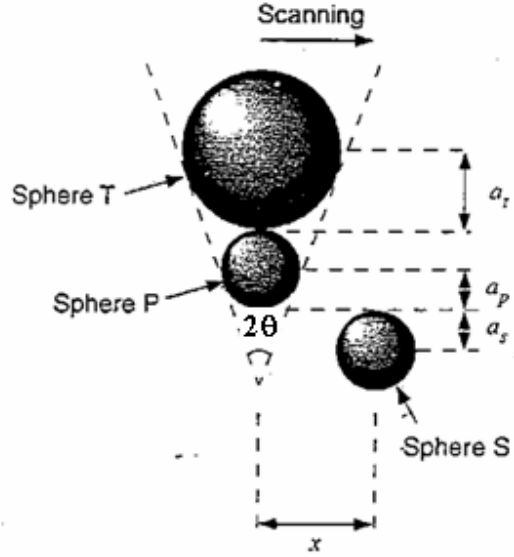


**Figure 2.13:** Approximation of the probe with two spheres at different diameters [39].

The radius  $a_T$  can be expressed in terms of the semi-cone angle of the probe  $\theta$  [39]

$$a_T = \frac{1 + \sin(\theta)}{1 - \sin(\theta)} a_P \quad (2.9)$$

For simplicity, let's consider Sphere S in Fig.2.13 with a radius of  $a_S$  as a source of light with a radiation pattern corresponding to a dipole placed in the center of the sphere. The dependence of the dipole electric field on the distance from the dipole is given by  $\frac{1}{r^3}$

(see Appendix B). In a situation when the probe is scanning along the  $x$  axis above Sphere S, the corresponding distances to the induced dipoles in Sphere P and Sphere T are  $r_P = \sqrt{x^2 + (a_S + a_P)^2}$  and  $r_T = \sqrt{x^2 + (a_S + 2a_P + a_T)^2}$ . The scattering intensity

is proportional to the square modulus of the dipole moment given by Eqn.2.4. The corresponding intensities scattered by two spheres are given by

$$I_P \propto |\alpha_P|^2 E^2(r_P) \propto |g_P|^2 \frac{a_P^6}{r_P^6} = |g_P|^2 \frac{a_P^6}{(x^2 + (a_S + a_P)^2)^3} \quad (2.10)$$

$$I_T \propto |\alpha_T|^2 E^2(r_T) \propto |g_T|^2 \frac{a_T^6}{r_T^6} = |g_T|^2 \frac{a_T^6}{(x^2 + (a_S + 2a_P + a_T)^2)^3} \quad (2.11)$$

where  $g_i = \frac{\epsilon_i - \epsilon_m}{\epsilon_i + 2\epsilon_m}$  for i representing either P or T and  $\epsilon_m$  is the dielectric function of

the surrounding medium.

Using Eqn. 2.10-2.11 it is possible to investigate how the detected signal depends on the opening angle  $2\theta$ ,  $a_S$  and  $a_P$  as well as the probe material properties given by  $g_P, g_T$ . Although the influence of Sphere T and the whole body of the probe can be considerable, the NF signal  $I_P$  due to the scattering with Sphere P should still be present in the image [39]. Hence, the resolution will improve as long as some part of the probe is placed in the NF of the emission source. In addition to resolution improvement, bringing the probe into the near-field enhances the amount of signal collected by the probe. An improvement of up to 30% was observed when an uncoated probe approached the emitting sample from a starting distance of 3  $\mu\text{m}$  down to the distance below 100 nm [125].



## **Chapter 3.**

### **SNPEM functional blocks and discussion on near-field condition**

This chapter describes the main components of the system involved in SNPEM imaging. The system is designed to perform a scanning of the probe, while the sample remains static. The preferred distance regulation is based on a quartz tuning fork sensing the shear force between the probe and the sample. This regulation allows us to maintain the probe within a 10 nm distance from the sample surface. Such a distance satisfies the near-field condition from the sample surface. The near-field condition in the SNPEM application additionally requires that the emission source is also placed sufficiently close to the sample surface. The development of sample preparation techniques is proposed in order to bring the emission source close enough to the sample surface. The available photon detectors allow the detection of the SNPEM signal in the spectral range from 300 nm to 1400 nm.

#### **3.1 SNPEM system set-up**

The SNPEM system is modified from an Atomic Force Microscope (AFM) with a large sample stage [126]. The schematic representation of the main components of the system involved in SNPEM imaging is shown in Fig.3.1. The diagram in Fig.3.1 is divided into five functional blocks:

- i. probe positioning
- ii. feedback loop for a distance regulation between the probe and the sample
- iii. sample or device under test (DUT)

iv. photon sensitive detector

v. SNPEM probe

The first four blocks are described in this chapter, while the SNPEM probe is discussed in Chapters 4 and 5.

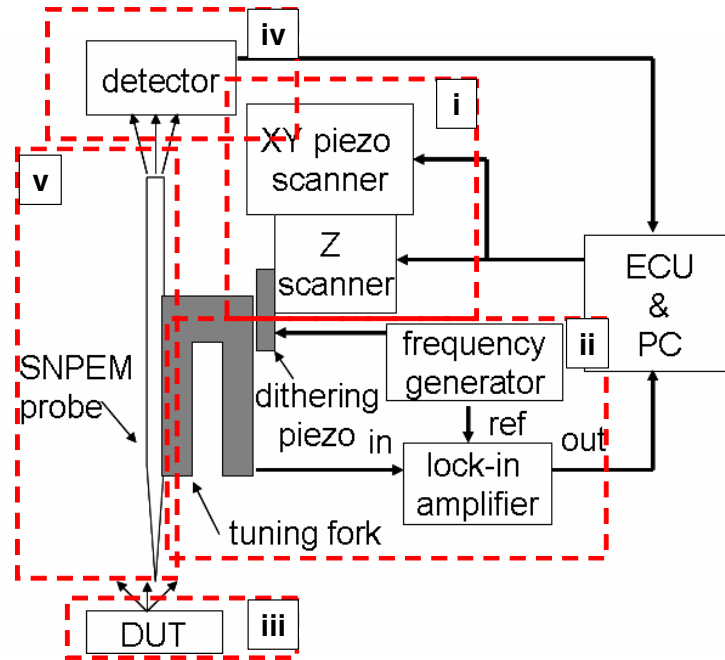


**Figure 3.1:** The schematic representation of the main components of the system.

### 3.2 Probe nanometric positioning and coarse navigation

The system is designed in such a way that the probe can be moved during the scan in all three directions while the sample itself remains static. The scanning of the probe is preferred because the mechanical scanning of large samples would give rise to mechanical vibrations. This arrangement is also more convenient for the investigation of ICs with arbitrary package configurations and electrical connections.

The image of the system ready to perform SNPEM measurements is shown in Fig.3.2a. The scanning of the probe in a horizontal direction is done with a XY nano-positioning stage from Physik Instrumente with a scan range of  $60 \times 60 \mu\text{m}^2$  and a resolution of 0.3 nm. The feedback control based on the capacitive position sensor ensures the linear movement of the lateral positioning system [126]. The scanning in the orthogonal direction is done by a Z piezo stage with a scanning range of 12  $\mu\text{m}$  and resolution of 0.05 nm also equipped with the capacitive position sensor.

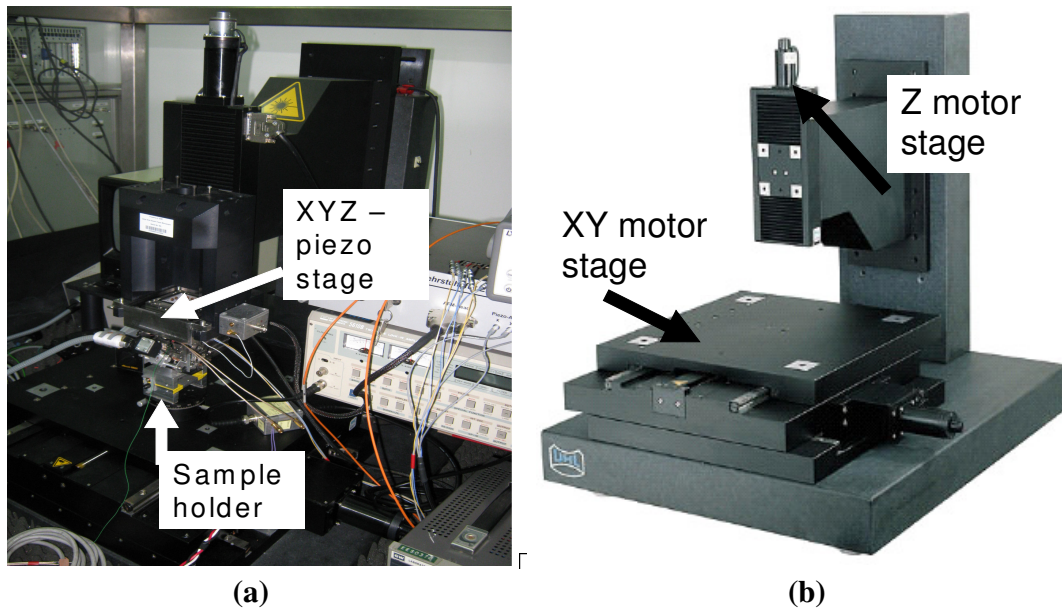


**Figure 3.2:** Probe positioning capabilities: a) photo of the SNPEM system during operation; b) coarse positioning stage shown without the piezo stage and the sample holder.

In Fig.3.2b, the system is described in terms of its capability to position the probe relative to the sample and perform their coarse movement. For the coarse navigation, the sample is moved using a 3-axis positioning system. For the lateral movement of the sample, the system is equipped with a stepping motor stage with a traverse of 300 mm in the X and Y directions. For the vertical coarse movement, the piezo scanner is placed on a Z-motor

that can traverse 50 mm. Such an arrangement allows the easy exchange of the probe or the sample.

### **3.3 Probe-sample distance regulation**

The overall idea of the SNPEM is to apply NF optics for the characterization of PE sources in semiconductor devices with the spatial resolution surpassing the diffraction limit. In order to achieve this, it is important to bring a sub-wavelength probe within the NF of the emission source. The NF condition is described by Eqn.2.1, which states that the sub-wavelength probe with characteristic size  $\mathbf{a}$  has to be placed at distance  $\mathbf{h} < \mathbf{a}$  in order to achieve resolution on the order of  $\mathbf{a}$ . The probe size for SNPEM imaging is expected to be below 100 nm and thus,  $\mathbf{h}$  should be less than 10 nm. In order to bring the probe to such a short distance from the sample surface and to keep it at this distance during the scan, a feedback regulation is needed.

In the SNPEM system, a feedback mechanism based on a quartz tuning fork (TF) is used to maintain the tip of the SNPEM probe at a constant distance of 5-10 nm above the sample. Quartz is a material with low internal mechanical losses ensuring very high quality factor, which makes quartz TF to be one of the best mechanical oscillators [127]. For quartz TFs, this Q-factor can reach values of several tens of thousands in air. The advantages of TFs lie in their standardized properties and their low prices due to large-scale production. For NF imaging, the optical probe can be rigidly attached to one of the arms of the TF. When the driving frequency of the dithering piezo (Fig. 3.1) is equal to the resonance frequency of the assembly composed of the TF and the probe, the

piezoelectric signal generated by the TF reaches its maximum value [128]. Even a weak interaction of the probe apex with the sample will disturb the oscillatory motion of the assembly. This disturbance can then be easily detected using the lock-in technique in the following manner. A signal from a function generator, which is driving the dithering piezo (Fig.3.1), is used as a reference for the lock-in amplifier. The amplified signal is later used as the feedback signal to control the voltage from Electronic Control Unit (ECU) applied to the Z scanner (Fig.3.1). In this way, the probe is kept at a constant distance from the sample surface during the scan. The expansion of the Z scanner at each point of scan is used to generate the topography image. Simultaneous recording of the PE signal intensity at each point of scan is used to generate an image of PE distribution or SNPEM image. This SNPEM image can be overlaid with the topography image and provide information on the emission location in the device.

### 3.3.1 Excitation method of the TF

One of the issues considered in the SNPEM application, is the method of TF excitation. The oscillations of the TF can be excited using two approaches. The first approach is based on a mechanical driving of the TF with a dithering piezo, as shown in Fig.3.3a. In this case, the TF acts as a mechanical-electrical converter. The mechanical oscillation of the TF arm with a glued probe induces surface charges that create an alternating potential between the arms. The on-resonance piezoelectric voltage induced between two arms of the TF excited by the dithering piezo in Fig.3.3a is three orders of magnitude smaller than the theoretically predicted value [128,129].

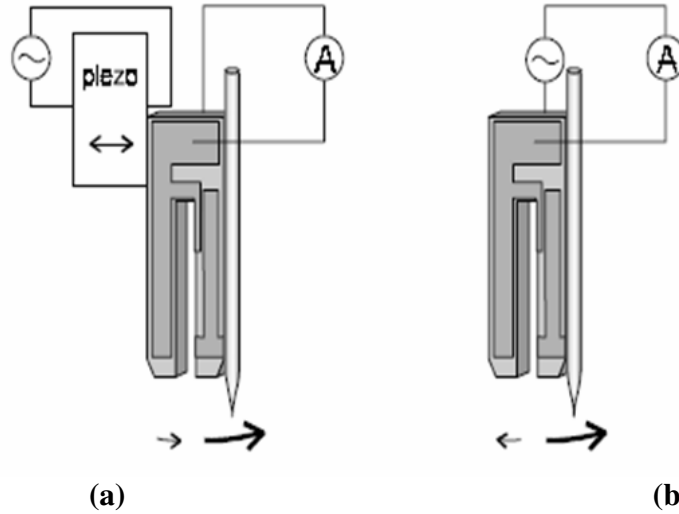


**Figure 3.3:** Excitation methods used for TF vibration: a) mechanical driving; b) direct driving [130].

This discrepancy is attributed to the fact that commercial TFs have contact pads designed to excite the mode of oscillation, in which both arms oscillate in opposite directions (mirror fashion) [131]. During the mirror fashion oscillations, when the center of mass of the TF is fixed in space, opposite charges are generated at different electrodes amplifying the signal. When the TF is excited with the dither piezo the arms are moving in one direction (Fig.3.3a). For ideal TF with identical arms, this method should result in a zero net electrical signal. However, the presence of the probe on one of the arms disbalances the TF and allows the generation of the finite signal. This signal is much smaller in comparison to a signal from an ideal TF. It can also be desirable to redesign the TF electrodes to optimize the signal for this mode of oscillation.

There is an alternative approach that is based on the direct driving with an AC voltage source, as shown in Fig.3.3b. This method corresponds to the designed application of the

TF and thus the fundamental mode of mirror fashion oscillation can be excited. For TF with glued golden wire, the direct driving demonstrates signals comparable to the theoretical results [132]. Therefore, direct driving has the potential to provide higher sensitivity. However, the NF probe based on a glass optical fiber has a larger mass and bulkier geometry in comparison with a golden wire. Hence, it can be expected to disbalance the TF severely, causing lower sensitivities. Thus, the advantage of the direct driving for SNOM applications is still debatable.

Both schemes are implemented in a SNPEM system but both of them suffer from poor repeatability due to a shared disadvantage -manually gluing the probe to the TF, which is never repeatable. Hence, it is hard to provide a conclusive summary of the comparison between the two methods. The process of gluing the probe is also problematic since the adhesive tends to form a thin cushion between the probe and the TF. This “soft” connection is caused by a difference in the elastic properties of quartz and epoxy [133]. The elastic modulus of the epoxy is 20 times smaller than that of quartz. Also the epoxy has an appreciable loss at the typical TF frequencies [133]. The losses generate damping and result in reduced Q-factor values. To minimize the resulting damping, the gluing process has to be carefully controlled requiring considerable skill and experience. Once glued, a probe cannot be removed or readjusted after curing of the epoxy.

### 3.3.2 Probe-sample distance regulation in SNPEM

In order to satisfy Eqn.3.1, it is important to ensure that the distance regulation based on TF feedback signals is capable of keeping the probe at a nanometric distance from the

sample surface. In Fig.3.4, the dependence of the feedback signal on the tip-sample distance is shown. This dependence is recorded by the SNPEM system during the approach of the probe towards the flat sample.

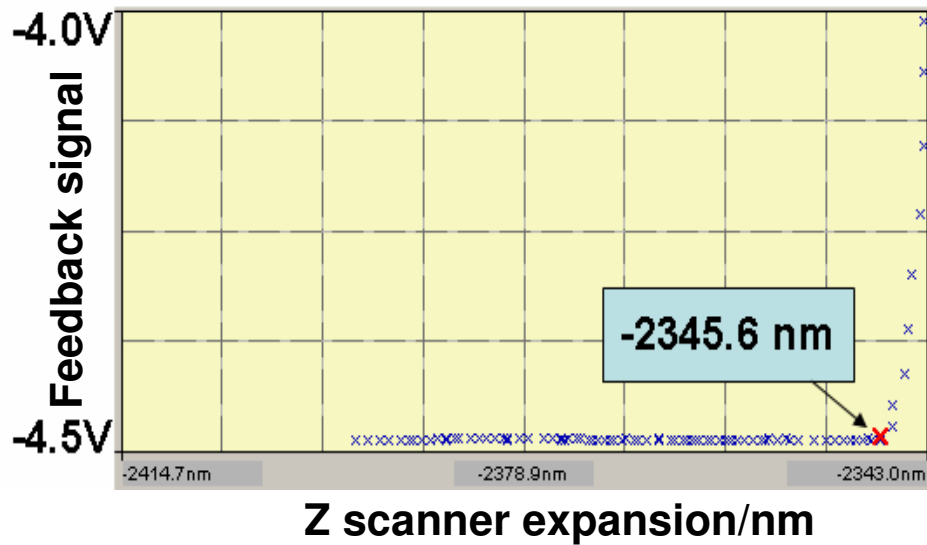


**Figure 3.4:** Dependence of the feedback signal on the tip-sample distance. The red cross indicates the distance when the tip starts to sense the surface.

The negative values for the feedback should be explained. The system is based on an AFM platform (see Section 3.1), in which the software was originally designed for a feedback signal that is supposed to increase at the surface. For TF based regulation, the feedback signal drops when the probe is close to the sample. In order to avoid modifications to the existing software, the signal is adjusted to the negative value using lock-in phase parameter. Hence, the interaction with the sample will cause a reduction of the absolute signal but in the case of the software, the signal will appear to increase.

In Fig.3.4, it is shown that when the probe is far from the sample the feedback signal is adjusted to the value of -4.5V, while the value of -4 V is chosen as a set point for distance regulation during the scan. The red cross in Fig.3.4 indicates the start of the decrease in



the absolute value of the feedback signal. This decrease indicates that the probe begins to feel the presence of the surface. Comparing the expansion of the z-piezo at the red cross with the final value of expansion at the set point, it is possible to conclude that the absolute signal drops to a set-point value within a distance of approximately 3 nm. Unfortunately, such control can be achieved only on a flat sample and in the case of a nicely glued probe. For other probes and samples, values up to 50 nm can be observed. Numerous factors, such as the probe properties or ambient conditions, can be responsible for such poor regulation. . As a rule of thumb, the SNPEM measurements are performed only for those probes that demonstrate a distance control within 10 nm. However, it should be noted that the value can vary during the measurement process due to the attachment of dust particles during the scan or the breakage of the probe.

### 3.3.3 Linearity of SNPEM scanning stage

The distance regulation is required to perform not only at one spot but also during the movement of the probe in lateral directions. It is also important to ensure that the X-Y piezo stage is linear and relays the correct values of displacement to ECU.

The system's scanning capabilities are calibrated by imaging the topography of two samples. The first sample consists of polystyrene spheres with diameter of 350 nm. Fig.3.5a shows a topographic image of the surface with closely packed spheres.

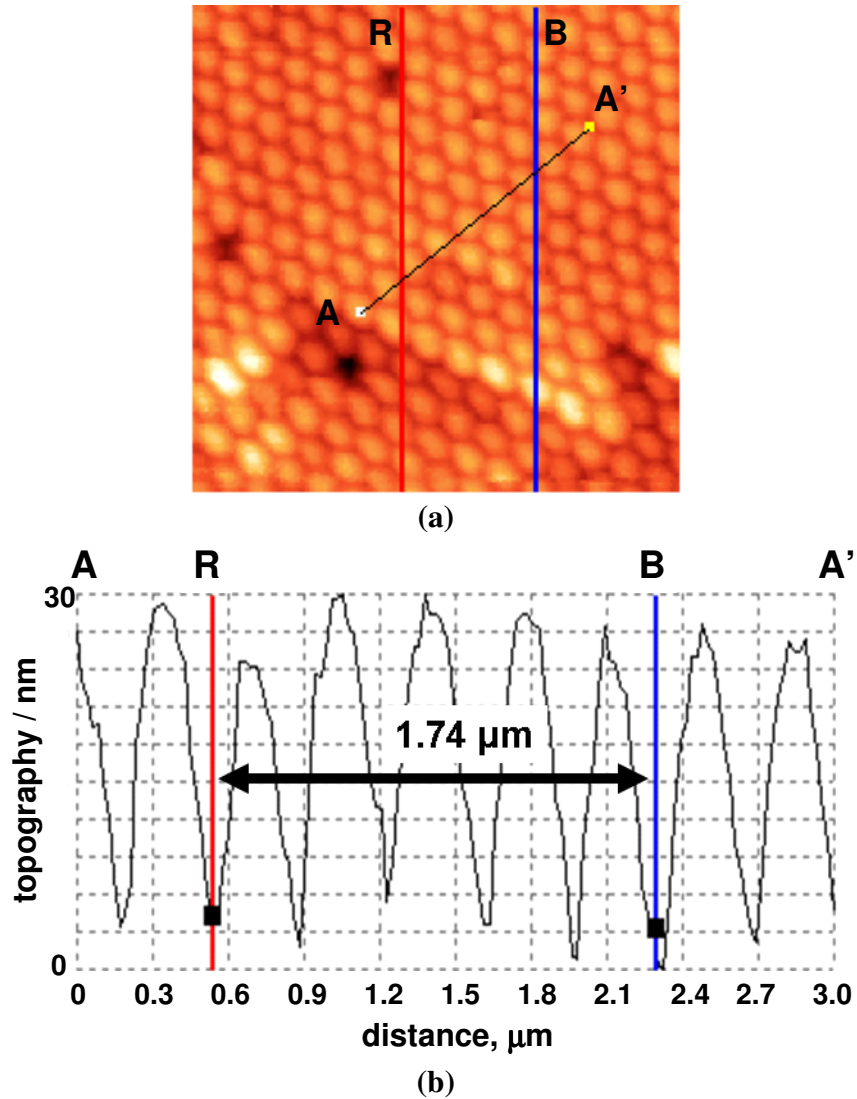


**Figure 3.5:** Calibration of SNPEM using polystyrene spheres with diameter of 350 nm: a) topography image; b) topography profile across the line **AA'**. Red (**R**) and Blue (**B**) lines identify the borders of the five spheres under consideration.

The image size is  $8 \text{ by } 8 \mu\text{m}^2$  and image resolution is 200 by 200 pixels. Each pixel corresponds to 40 nm and represents the accuracy of the measurement. The topography profile across the line **AA'** marked in Fig.3.5a is shown in Fig.3.5b. One can see that five spheres are within a distance of  $1.74 \mu\text{m}$ . This result is close to the expected distance of  $350 \times 5 = 1750 \text{ nm}$ . It shows that the actual accuracy of the measurement can be within one pixel.

The second sample is a calibration grid TGX1 from NT-MDT with a period of 3  $\mu\text{m}$  [134], as shown in Fig.3.6a.

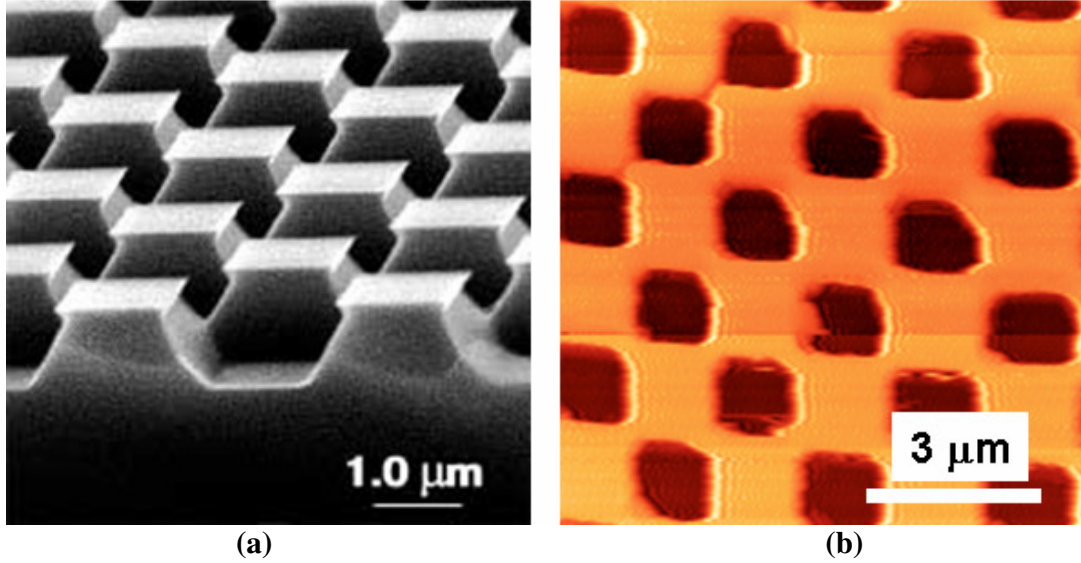


**Figure 3.6** a) SEM image of calibration grid TGX1 from NT-MDT [134]; b) SNPEM topography image of TGX1 sample.

The topography image of the same grid is shown in Fig.3.6b. The image size is 9 by 9  $\mu\text{m}^2$  and contains three periods in both horizontal and vertical directions. In Fig.3.6a, the square structures are disconnected, while in Fig.3.6b they seem to be connected. This result is observed due to the finite size of the probe tip leading to the interaction of the probe body with the edges of the top squares shown in Fig.3.6a.

### 3.4 Impact of sample structure on the near-field condition

The NF condition that was defined in Eqn.3.1 assumes that the emission source is placed at the surface of the sample. For the case of SNPEM, a modified near-field condition is

introduced in this thesis. It has to be modified because the emission source is generally placed at a finite distance **d** below the surface, as schematically shown in Fig.3.7.

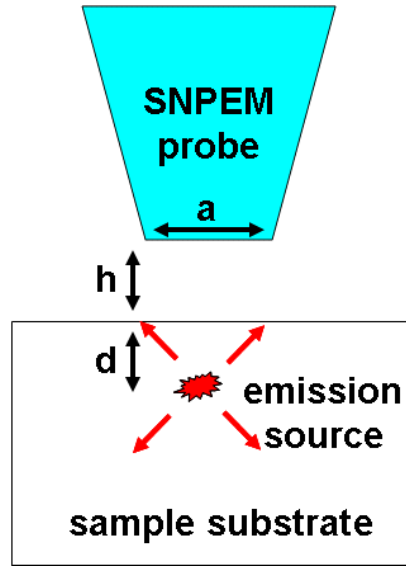


**Figure 3.7:** Illustration of the NF condition in case of SNPEM application.

The modified NF condition is given by

$$\mathbf{h} + \mathbf{d} \leq \mathbf{a} \ll \lambda \quad (3.1)$$

From Eqn 3.1, it is clear that in order to achieve the desired resolution capability it is important to minimize not only the probe sample separation **h** but also the **d**. At the same time, the minimization of **d** should not influence the electrical biasing of DUT. It will be shown below that **d** is not negligible for both front-side and back-side approaches in semiconductor failure analyses.

### 3.4.1 Front-side analysis

An example of the SNPEM analysis from a front-side of a single planarized MOSFET with one metal layer is shown in Fig. 3.8.

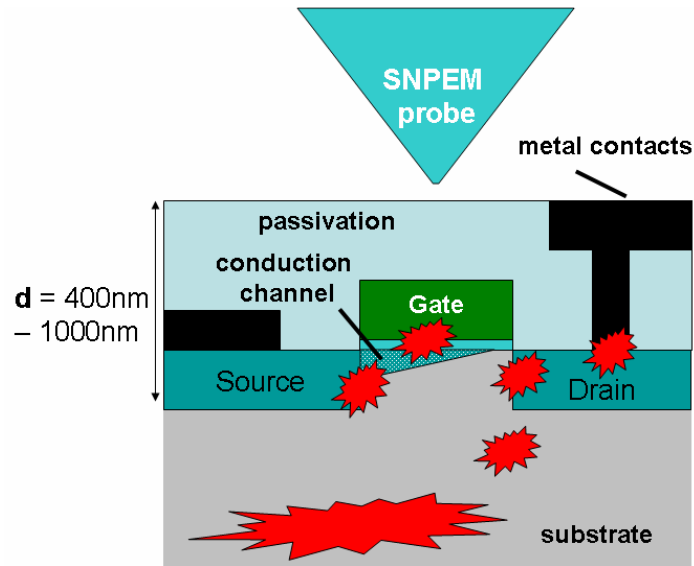


**Figure 3.8:** Schematic representation of SNPEM analysis applied to the sample from front-side.

The description of different photon emission phenomena highlighted in Fig.3.8 is given in Fig.A.7 of Appendix A. Even for such a simple structure, the SNPEM will never reach a NF condition of the emission source given by Eqn.3.1. However, the emission distribution in-between the metal lines satisfies the NF condition. And it can still be correlated to the particular device with a lateral resolution better than what FF microscopy is capable of providing. Hence, SNPEM can be useful for the analysis of test structures with minimal number of metallization layers. For more sophisticated devices,

the number of metal layers is more than 10 (Table 1.1), making it impossible to obtain any valuable information by neither SNPEM nor FFPEM.

### 3.4.2 Back-side analysis

In SNPEM analysis, a biasing of the sample is required. Hence, the sample preparation technique should preserve the original circuitry of the device. In order to satisfy this requirement for technology nodes with multiple metal layers, a back-side analysis is commonly implemented in FFPEM. Back-side analysis capitalizes on the transparency of the silicon substrate to the wavelengths above the silicon bandgap [12]. The substrate is usually thinned down to 50-100  $\mu\text{m}$  by mechanical polishing [17]. It is clear that this approach alone is not capable of bringing the SNPEM anywhere close to the NF condition (Eqn.3.1). In order to reduce the thickness of the substrate, a process of physical or chemical etching can be employed. Recently two supplementary methods were developed to reduce  $d$  down to hundreds or even tens of nanometers: i) the thinning of bulk silicon substrates with the use of Focused Ion Beam (FIB) [135]; ii) the selective chemical etching of Silicon on Insulator (SOI) substrates [136]. These two methods were first proposed for SNPEM in Ref [137].

#### 3.4.2.1. Thinning of bulk silicon substrates with FIB.

For standard bulk substrates, chemical etching is not applicable because the chemical reaction will not distinguish the substrate from the active layers. Hence, physical etching

is implemented where the FIB performs the etching in a controllable manner [135]. The expected final structure for a SNPEM analysis after FIB back-side preparation is shown in Fig. 3.9. Using this technique, the thickness of the remaining silicon can be controlled and reduced down to 300 or 400 nm [135].

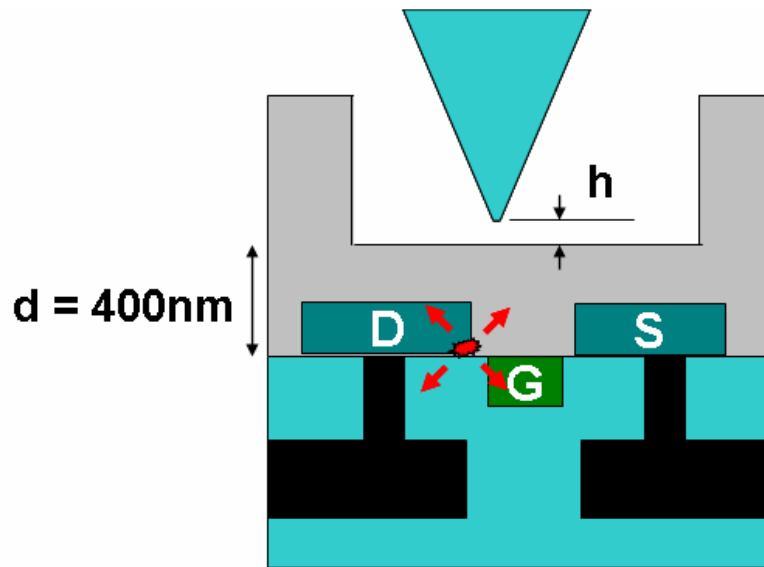


**Figure 3.9:** Schematic representation of the bulk silicon sample thinned down to nanometric level for back-side SNPEM analysis using FIB.

Two main disadvantages of the preparation method are clear. First, the method requires an expensive FIB tool equipped with the specific option of gas-assisted etching and specially designed infrared camera. Secondly, the etching is controlled by an operator, which makes the process unrepeatable and sensitive to human error. If the process is not terminated correctly, the etching will attack the active layer, altering or destroying the circuit of interest [138]. Although Quanta 3D FIB system from FEI is available for the purposes of SNPEM project, it does not have the gas precursor necessary for silicon etching and infrared camera. That is why the described sample preparation technique is not attempted.

#### 3.4.2.2. Selective chemical etching of SOI substrates.

The SOI substrates consist of three layers: i) thick silicon substrate; ii) buried oxide layer (BOX) and iii) thin silicon active layer or SOI. One can apply the chemical etching process with a high degree of selectivity between silicon and silicon dioxide, while BOX will play the role of a perfect etch-stop layer [139]. The expected final structure for SNPEM analyses is shown in Fig.3.10.

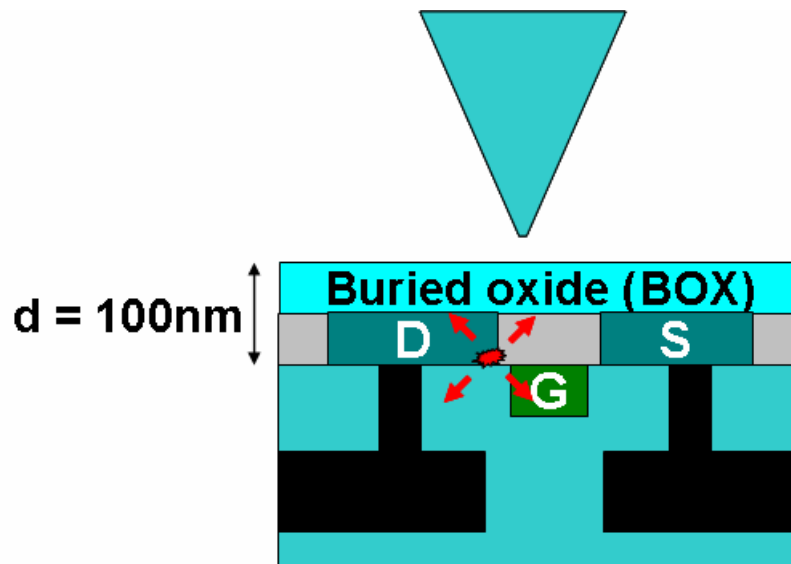


**Figure 3.10:** Schematic representation of the SOI sample thinned down to nanometric level for back-side SNPEM analysis using chemical etching.

The FIB technique described above can be applied for this purpose [139] but a simpler and cheaper method of wet chemical etching is available. In this method, a globally thinned substrate is subjected to tetra-methyl ammonium hydroxide (TMAH) solution with a selectivity of 3000:1 between Si and SiO<sub>2</sub> [136,140].



The self-termination of the etching process avoids human involvement. For SNPEM analysis, this process can bring the probe to a much closer distance because the thickness of BOX is already below 100 nm for modern technologies [5]. Such a preparation technique was already successfully employed for high-resolution back-side analysis using scanning capacitance microscopy [141].

Unfortunately, attempts to use such a method for SNPEM sample preparation were not successful. One of the results of SOI back-side deprocessing is shown in Fig.3.11. In Fig.3.11a, the sample is shown from the front-side before substrate deprocessing. In Fig.3.11b, it is clear that the TMAH solution has gone under the BOX and attacked the SOI layer. Even aluminium contacts and bondpads were etched away, exposing the wire bonds (Fig.3.11b). At the same time, the silicon substrate is only partly removed (Fig.3.11b).

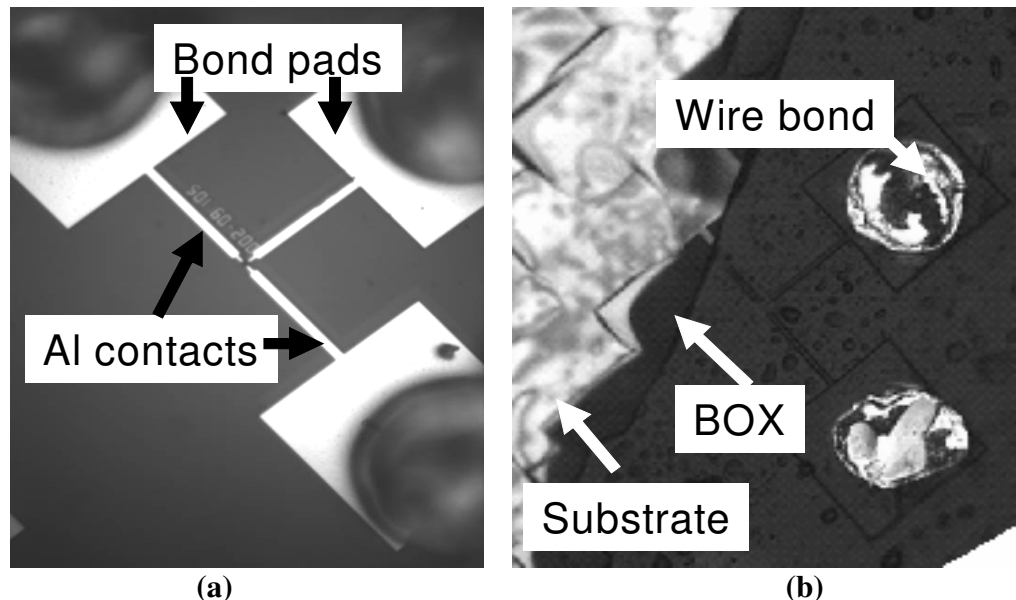


**Figure 3.11:** SOI sample deprocessing for back-side SNPEM analysis: a) front-side image of SOI device before deprocessing; b) back-side image of the device after substrate etching with TMAH solution.

There are a few factors that could be responsible for this problem. First, the planarity of the polishing was not good enough leading to considerable differences in thickness at different parts of the substrate. Secondly, the epoxy used for fixing the die could not withstand the elevated temperatures required for the etching process and this caused an under-etch to occur at the sides of the die.

### 3.5 Light sensitive detectors for SNPEM

The target wavelength range for SNPEM is from 400 nm to 1700 nm (see Appendix A). Two different detectors are used in the experiments to cover such a broad spectral range. The first to be used is a Photo Multiplier Tube (PMT) from Hamatsu H5783-20 which is sensitive mainly in the visible spectral range from 300 nm to 920 nm. The cathode radiant sensitivity curve for this detector is shown in Fig.3.12.

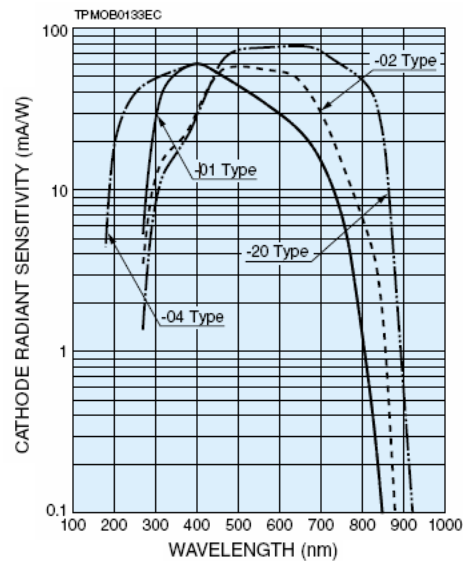


**Figure 3.12:** Spectral response of Hamamatsu H5783-20 [142].

The quantum efficiency of the detector is above 10% [142]. When this PMT is used in SNPEM measurements, the cleaved fiber is placed directly in front of the cathode, as shown in Fig.3.13.

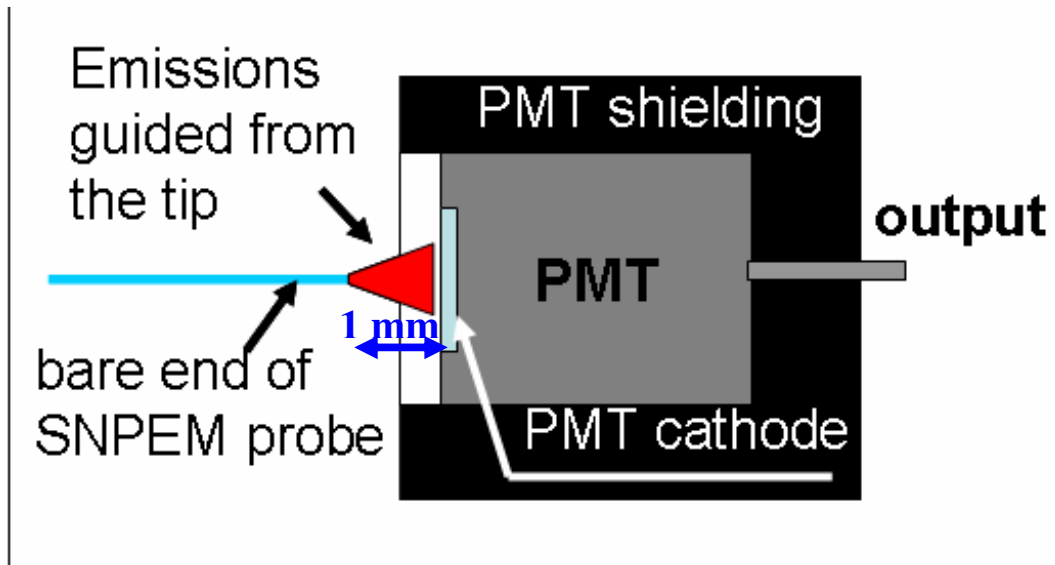


**Figure 3.13:** Connection between the bare end of the fiber and visible PMT.

The cathode has a diameter of 8 mm. This ensures that all the photons collected by the tip and ejected from the core at the bare end of the fiber are incident to the sensitive area of the cathode (Fig.3.13). The schematic representation in Fig.3.13 is provided in order to compare two different designs of fiber attachment to two PMTs used for SNPEM measurements.

The second detector is a liquid nitrogen cooled NIR-PMT from Hamamatsu R5509-42. The cathode radiant sensitivity of NIR-PMT (Fig.3.14) shows that this PMT is sensitive in a broad range - from 300 nm to 1400 nm. A trade-off for such a broad range is low quantum efficiency below 1 % (Fig.3.14). Another trade-off is a high dark current from the cathode. This is why liquid nitrogen cooling of the PMT is implemented.

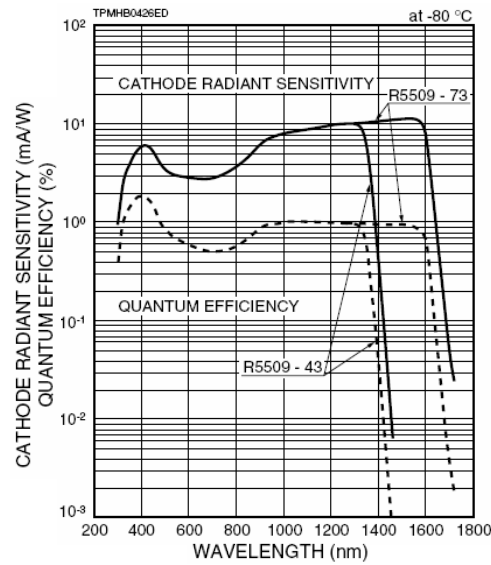


**Figure 3.14:** Spectral response of Hamamatsu R5509-42 [143].

For this model, the temperature is kept at  $-80^{\circ}\text{C}$  by placing PMT inside a special container as shown in Fig.3.15.

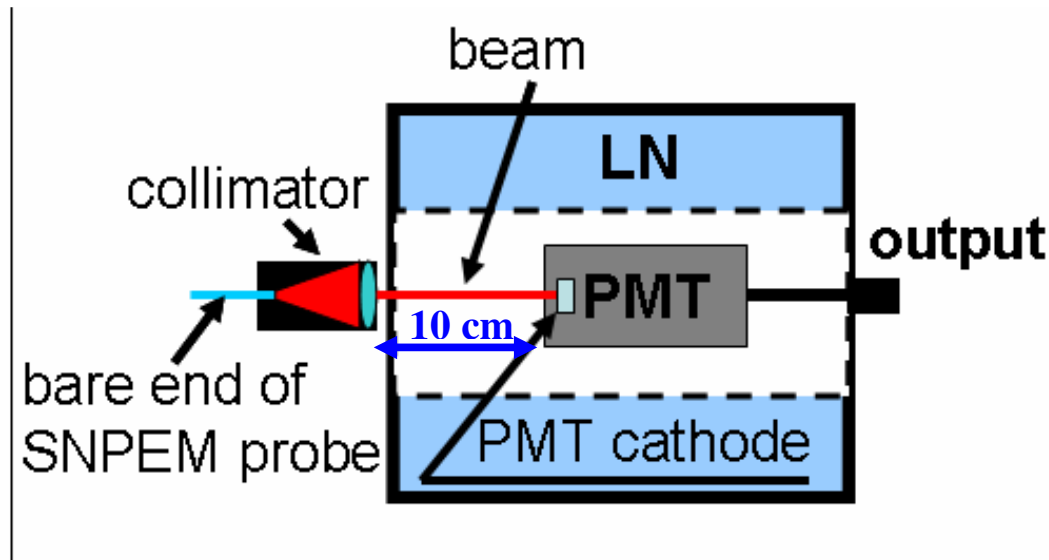


**Figure 3.15:** Connection between the bare end of the fiber and NIR PMT.

In order to achieve the desired temperature for the PMT, the sidewalls of the container are in constant contact with the liquid nitrogen. The design of the container is such that

the cathode of the PMT is placed 10 cm away from the entrance window inside the chamber, as shown in Fig.3.15.

The size of the cathode is 3 mm by 8 mm and thus, if the bare end of the fiber is placed in front of the window, a negligible portion of light ejected from its core will be incident on the cathode area. In order to improve the collection efficiency, a lens collimator [144] is used (Fig.3.15). This collimator is optimized for the spectral range from 1  $\mu\text{m}$  to 1.6  $\mu\text{m}$  and has a specified beam diameter of less than 1 mm. The collimation for the specified wavelength is preserved up to a distance of 10 cm. Other wavelengths are partially reflected back and are exiting the collimator in a diverging beam. The wavelength range of the system is expected to be from 1  $\mu\text{m}$  to 1.4  $\mu\text{m}$ . This assumption was confirmed by placing a long pass-edge filter with cut-on wavelength at 1  $\mu\text{m}$  in between the bare end of the fiber and the NIRPMT entrance window. With the filter in place, the probe was put in front of the 10W quartz tungsten halogen lamp and no change of the signal from PMT was observed in comparison to the measurements without the filter.

### **Summary.**

In this chapter, the SNPEM system set-up was described. There are five components critical for the SNPEM application: i) probe positioning; ii) probe-sample regulation; iii) required sample properties and iv) photon sensitive detectors; v) SNPEM probe. Probe positioning is performed with a piezo scanning stage in three directions with its resolution better than 1 nm. Probe-sample distance regulation is controlled using a quartz tuning fork within a distance of 10 nm. The methods of mechanical and direct driving of

the tuning fork are implemented. Different sample preparation techniques for back-side analysis are considered for the particular application in SNPEM. The chemical etching of SOI substrates creates an opportunity to bring the emission source to a distance below 100 nm. Unfortunately, attempts to use such a method for SNPEM sample preparation were not successful and further developments for this are beyond the scope of this thesis. The photon sensitive detectors available for SNPEM analysis cover a broad spectral range from 300 nm to 1400 nm, which practically overlaps the range of interest for photon emission microscopy. The fifth and final component – probe design – is discussed in the following chapter.

## **Chapter 4.**

### **Near-field probe for SNPEM**

In this Chapter, I propose a set of requirements imposed on the design of the NF probe for the particular SNPEM application introduced in the preceding chapters. A variety of existing designs are investigated and compared according to the formulated conditions. It is identified that uncoated dielectric probes are the most suitable for SNPEM applications. Dielectric probes are successfully applied to the investigation of the emission sources from several semiconductor devices. The resultant improved resolution capability in comparison with FFPEM is demonstrated. However, the demonstrated resolution is still insufficient for complying with the requirements for SNPEM application declared in Chapter 1. Poor contrast between the NF signal due to the tip interaction and the background is the main reason for such poor resolution capabilities.

#### **4.1 Requirements for SNPEM probe**

The goals of SNPEM applications, as declared in Section 1.4, require high resolution imaging with sufficient detection efficiency in terms of the minimum current passing through the active elements. Repeatability of the results along with applicability to a broad range of semiconductor devices is also required.

In order to insure usefulness of SNPEM in FA, I formulated the following requirements for the probe design:

- i. The probe should ensure the localization of photon emission sites with precision that is compatible with current technology node. This can be achieved by confining the interaction volume to the dimension of the order of 50 nm.
- ii. The probe should provide a sufficient detection efficiency of emissions at biasing levels close to its normal operating conditions. A high detection efficiency can be achieved through:
  - a. higher scattering efficiency of the probe interaction volume,
  - b. improved efficiency of collecting the scattered light.
- iii. The contrast of the recorded images should be sufficient to distinguish the high spatial frequency components of the signal on top of the background. The background due to NF and FF interactions of the probe body should be minimized and clearly distinguished from the NF interaction of the tip.
- iv. The probe should demonstrate the SNPEM results repeatedly. It includes the use of the same probe, meaning that it has high durability and does not change its properties during considerable number of measurements, and the use of different probes, implying that the fabrication methods should ensure a consistency of the critical properties of all the probes.
- v. The effect of the probe on a sample or its operating conditions should be avoided or minimized.
- vi. The NF detection should be applicable to a wide range of samples including structures, which are non-planar and can have a high aspect ratio. This condition can be achieved only if the collection of the scattered light is performed through the body of the same probe.



- vii. The topography artifacts should be avoided or clearly revealed, allowing the deduction of the actual PE distribution.
- viii. The results should be independent of the wavelength within the range of interest (400 nm - 1700 nm).

## 4.2 Evaluation of existing near-field probes

Several NF optical probe designs were discussed in Section 2.2. In Fig.4.1, these designs are summarized, while in the following sub-sections, they are discussed in terms of applicability to SNPEM analysis.

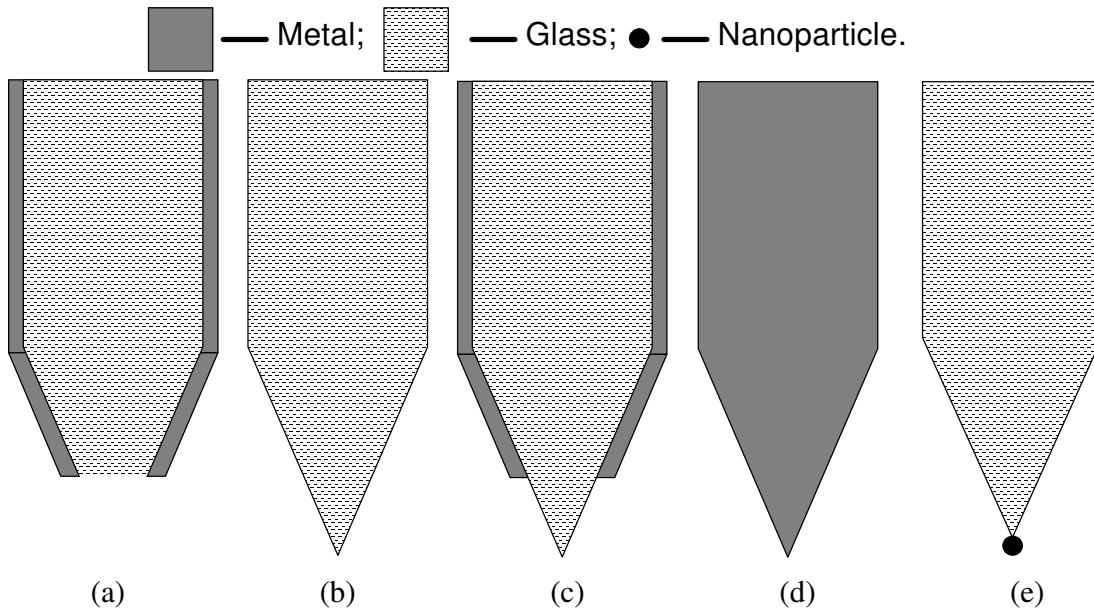


**Figure 4.1:** Schematic representations of existing probe designs based on: a) sub-wavelength aperture; b) uncoated dielectric tip; c) protrusion type probe (PTP); d) metal tip; e) metallic nanoparticle attached to the dielectric tip.

#### 4.2.1 Probes with sub-wavelength aperture

Previous attempts to use SNOM for collection of PEs from semiconductor devices were focused on the application of probes based on sub-wavelength aperture [36,51-57]. The signal was detected from devices biased up to several tens of milliamperes and in most cases, the devices were efficient light emitters, like laser diodes. A few aspects of these results show that aperture-based probes cannot comply with the requirement for detection efficiency (ii) proposed earlier. First, the detection capability of only milliamperic currents is more than three orders of magnitude worse than the desired detection capability for SNPEM analysis. Secondly, the variation of current that could be distinguished upon application of sub-wavelength apertures are also in the milliamperic regime and thus, the impact of leakage current is not revealed in such measurements. Third, laser diodes are made of direct bandgap semiconductors and are designed for efficient light emission. In contrast, silicon is an indirect bandgap semiconductor with low quantum efficiency and the design of the silicon-based devices is not intended for the efficient generation of photons (for more details see Appendix A). This means that for silicon based devices, higher biasing currents are generally required to generate the same number of photons. Hence, if for laser diodes the detection efficiency is on the level of milliamperic, then the application of sub-wavelength apertures for the detection of PE in silicon-based devices is even less practical. Fourth, silicon has a small bandgap corresponding to emissions at wavelengths beyond 1000 nm (Fig.A.3). Using Eqn.2.2, it is possible to estimate that detection at such wavelengths will degrade the detection efficiency by at least another order of magnitude. From the same Eqn.2.2, it is also clear

that, although the resolution of SNOM with aperture-based probes is independent of wavelength, the dependence of the measurements on the wavelength comes through transmission of the sub-wavelength aperture. This will make the interpretation of the results challenging.

It is clear from the discussion above that aperture-based probes cannot achieve a detection efficiency sufficient for benefiting from higher resolution capabilities. Apart from this, they have other disadvantages as well: 1) complicated and unrepeatable methods of fabrication [74,75]; 2) low topography resolution due to blunted probe apex and poor applicability to “real-world” samples [81]; 3) strong topographic artifacts [78]; 4) unpredictable shift between topography and optical images [78]; 5) unpredictable transmission properties of the aperture due to the grainy structure of the metal coating around the aperture (Fig.2.3b) and finite penetration depth of the field into the metal coating [64,65] and 6) metal coating of the probe can cause a short-circuit between the neighboring metal lines in highly integrated devices.

One clear advantage of the sub-wavelength aperture is a high level of image contrast. However, this factor is not sufficient to negate the effect of all the disadvantages highlighted above, clearly showing that the use of aperture based probes cannot offer any more benefits in applications like the NF characterization of PE sources.

#### 4.2.2 Dielectric probes

The ultimate spatial resolution achievable with the uncoated dielectric probes is defined by the scattering with the final tip [47], which can be made as small as possible. The second advantage of these probes is that they are based on glass optical waveguides. Hence, the collection of the scattered light is performed through the probe body, avoiding the need for any external optics. The sharp tip and collection of the scattered light through the same probe make it possible to collect emission even from structures with a high aspect ratio, thereby allowing access to “real-world” samples with arbitrary structures. The dielectric nature of the tip also implies that such probes should not affect the DUT, like causing a shortcircuit. The nearly constant dielectric function of the glass within the spectral range of interest (Fig.2.9), allows wavelength independent measurements. Also, the communication fibers used for probe fabrication have a very low absorption within the same spectral range. These properties make the performance of such probes potentially independent of the wavelength for SNPEM application.

The pitfall with this kind of probes is the poor scattering efficiency of the dielectric tip due to the positive real part of the dielectric function for glass (Fig.2.9). Another drawback is the poor imaging contrast because the near-field signal and the background light are collected simultaneously.

It is interesting to examine the origin of this background. The background is determined by two factors. The first factor is related to the coupling into the waveguide. The

coupling is equivalent to the collection of scattered light using a microlens formed by the body of the probe [98,124]. The second factor is the NF interaction of the emission source and the probe body above the tip [39]. This factor can be modeled through the NF scattering by another Sphere T shown in Fig.2.13. This contribution is given by Eqn.2.11. For dielectric probes, the materials of the tip and the body of the probe are the same and thus, the difference in scattering efficiency is determined mainly by the size of the tip  $a_P$  (Sphere P in Fig.2.13) and size of Sphere T  $a_T$ . As the  $a_T > a_P$  the NF interaction of the probe body is comparable or even higher than the NF interaction of the tip. And this will lead to the poor contrast of the image.

#### 4.2.3 Protrusion type probe

One effective method to improve the contrast is to limit the NF interaction of the probe body using the concept of protrusion type probe (PTP), shown in Fig.2.5. For PTP, the resolution is determined by the scattering volume of the final tip. The detection efficiency is controlled by the scattering efficiency of the tip and by the radius of the base aperture (Fig.2.5). This base aperture also controls the level of the background due to NF interaction of the probe body [39] and direct coupling [47]. Hence, the radii of the tip and the base aperture define the “band-pass” filter for spatial resolutions recorded by the system. That is why the PTP is capable of providing imaging with better contrast than uncoated dielectric tips.

The disadvantage of the PTP is that placing the base aperture close to the tip implies that the aperture has sub-wavelength dimensions. Hence, it is still characterized by a low transmission rate and will limit the detection efficiency of the probe. Another disadvantage is the complicated method of fabrication. Although a few self-terminating processes were developed for the base aperture formation [95,96], the overall multi-step procedure for probe fabrication does not guarantee the reproducibility of the probe properties.

#### 4.2.4 Scattering metallic probes

An approach based on aperturless or scattering metallic probes can currently achieve optical resolutions at the level of 10 nanometers [102]. In order to retrieve weak NF signal from the background, the detection is usually performed at first or higher harmonics of probe vertical oscillations [102,97].

One clear problem of this approach is the strict sample constraint. The sample has to be flat as the light detection is usually performed by the objective placed at an angle (Fig.2.6). However, semiconductor samples need biasing and thus, bulky structures with high aspect ratios are anticipated. Such structures will unavoidably shadow the emission area from proper observation, as shown in Fig.4.2. The interpretation of the recorded data at such geometry will not be reliable.

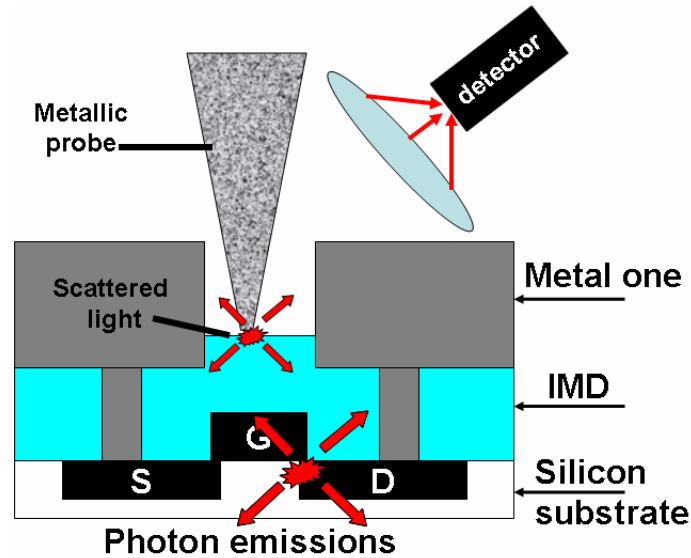


**Figure 4.2:** Schematic representation of SNPEM analysis with a metallic probe demonstrating the limitations due to external collection as well as danger to cause a short-circuit between the probe and the sample or between adjacent metal lines.

Another constrain is the fact that one cannot use a metallic tip for the analysis of biased circuits. For example, the technology node in ITRS roadmap [5] is defined as a half pitch between adjacent metal lines. Hence, for the advanced technology nodes, where distances between metal lines are less than 50 nm (Table 1.1), the body of the probe as well as the tip can cause a short-circuit between two adjacent metal lines. This makes any SNPEM analysis impractical. Short-circuit between one metal line and the probe will also affect the biasing conditions within the sample. With these problems, metal-based probes are not considered for SNPEM applications.

#### 4.2.5 Probes based on metallic nanoparticle attached to the dielectric probe

The PTP discussed earlier improves the contrast by reducing the impact of the probe body on the image formation. Another way to improve the contrast is to increase the

scattering efficiency of the probe tip and make it the main contributor in collecting the signal. The higher scattering efficiency will also lead to the higher detection efficiency of the probe.

This kind of enhancement can be achieved if a metallic nanoparticle is attached to the dielectric tip, as shown in Fig.2.7. The higher polarizability of the metal leads to a higher scattering efficiency, while the polarizability of the glass body is low. Such a composite tip also promises a much higher enhancement in comparison to metallic probes [101]. In principle, such a probe can overcome another drawback of metallic tips by collecting the scattered light through the dielectric part to which the metallic particle is attached. However, experimentally it is very hard to align the nanoparticle and the optical axis of the dielectric waveguide [98]. Also, only a small fraction of the scattered light will fall within the collection angle of the waveguide resulting in the inefficient collection of the scattered light and thus, low detection efficiency. These are the reasons why the collection of scattered light for such probes is still performed by external optics [45,46].

Three other disadvantages of such probes need to be highlighted. First, there is still the danger of causing a short-circuit within the DUT for small technology nodes. Second, there is a chance that the particle will be displaced from the tip during the scan. The attachment of the new nanoparticle cannot be repeated in terms of both the position and the amount of glue, thereby violating requirement iv stated before. Third, each metal is an efficient scatterer only in the narrow band of optical wavelengths and cannot cover the whole spectral range of interest. These problems place a considerable doubt on the



repeatability of the SNPEM results. Taking into account all these factors, the application of such probes for SNPEM analysis cannot comply with the requirements listed in Section 4.1.

#### 4.2.6 Ranking of existing probes

In Section 4.1, a list of the requirements for the NF optical probe was proposed. These requirements have to be fulfilled for the successful application of SNPEM. Using these requirements and the analysis in sub-sections 4.2.1-4.2.5, the existing probe designs are ranked in Table 4.1.

<b>Table 4.1:</b> Ranking of the existing probe designs.									
	<b>i</b>	<b>ii a</b>	<b>ii b</b>	<b>iii</b>	<b>iv</b>	<b>v</b>	<b>vi</b>	<b>vii</b>	<b>viii</b>
<b>Aperture probe</b>	+	-	--	++	--	-	--	-	-
<b>Dielectric probe</b>	+	-	++	-	+	+	+	+	++
<b>Protrusion type probe</b>	+	-	+	+	+	+	+	+	+
<b>Metallic probe</b>	++	+	-	+	+	--	--	+	--
<b>Nano-particle attached to dielectric probe</b>	++	++	-	++	--	--	-	+	--

The presence of the double minus “--” in any row is treated as a “show-stopper” for any of the probe designs. From Table 4.1, it is clear that aperture based probes should not be considered for SNPEM analysis due to their extremely low detection efficiency, low repeatability and blunt tips that prevent access to the structures with high aspect ratios.

Metallic tips, on the other hand, have the advantage of better resolution and a high scattering efficiency, but they put considerable restrictions on the sample and can affect the sample operating conditions. This makes them impractical for SNPEM applications.

Probes based on metallic nanoparticles attached to the dielectric tip promise even higher scattering efficiency and better contrast of the images. There is also a possibility, though still not realized, to collect the scattered light through the waveguide structure of the probe body. But low repeatability of probe properties as well as the remaining danger of causing short-circuits in the biased DUT, makes such probes also impractical for SNPEM application. The limited wavelength range of efficient scattering for such probes additionally degrades the usefulness of their application.

Thus, the best chances of achieving practical results can be expected from dielectric probes. However, they have the disadvantage of the poor scattering efficiency of the final tip. They also demonstrate a poor contrast of the recorded images. The application of the PTP concept might improve the contrast but at the expense of the degraded collection efficiency of the scattered light.

Using this ranking procedure, it is concluded that dielectric probes or PTPs are the only possible candidates for an SNPEM application and they will be considered in the following sections.

### 4.3 Applications of dielectric tips for SNPEM analysis

Before moving to the actual applications of the dielectric probe for an SNPEM analysis, it is important to consider the impact of the probe structure and the sample properties on the recorded signal.

#### 4.3.1 Dependence of intensity distribution on probe geometry and on emission source location below the surface

In section 2.4, it was suggested that Eqns.2.9-2.11 can be used to investigate the impact on the signal of the opening angle  $2\theta$ , tip radius  $a_p$  and the characteristic dimension of the emission source  $a_s$ , as defined in Fig.2.9. The final intensity distribution will be considered in terms of the interaction between the emission source or Sphere S and both Sphere P and Sphere T from Fig.2.9.

For simplicity sake, it will be assumed that there is only one emission source placed in the middle of the Sphere S (Fig.2.9). More complicated or extended emission sources can be modeled by a set of such point sources based on the assumption that each PE event in the semiconductor devices is independent from other emissions. This assumption is valid because, in biased semiconductor devices, different locations will be characterized with different electric fields. This determines the PE mechanism specific for each point.

The intensity distribution due to scattering with Sphere P is given by  $I_P(\mathbf{x})$  from Eqn.2.10. The dependence due to scattering with Sphere T is given by  $I_T(\mathbf{x})$  from Eqn.2.11. These quantities are visualized using Matlab 7.0 in Fig.4.3-4.6. In the following discussion, it is considered that the parameters  $\mathbf{g}_P = \mathbf{g}_T$  are the same. This is reasonable because only dielectric probes are considered. In Fig.4.3, the line profiles corresponding to  $I_P(\mathbf{x})$ ,  $I_T(\mathbf{x})$  and  $I_P(\mathbf{x}) + I_T(\mathbf{x})$  are presented as  $\mathbf{a}_S = 0\text{nm}$ ;  $\mathbf{a}_P = 10\text{nm}$  and for two different angles  $2\theta_1 = 20^\circ$  (Fig.4.3a) and  $2\theta_2 = 90^\circ$  (Fig.4.3b).

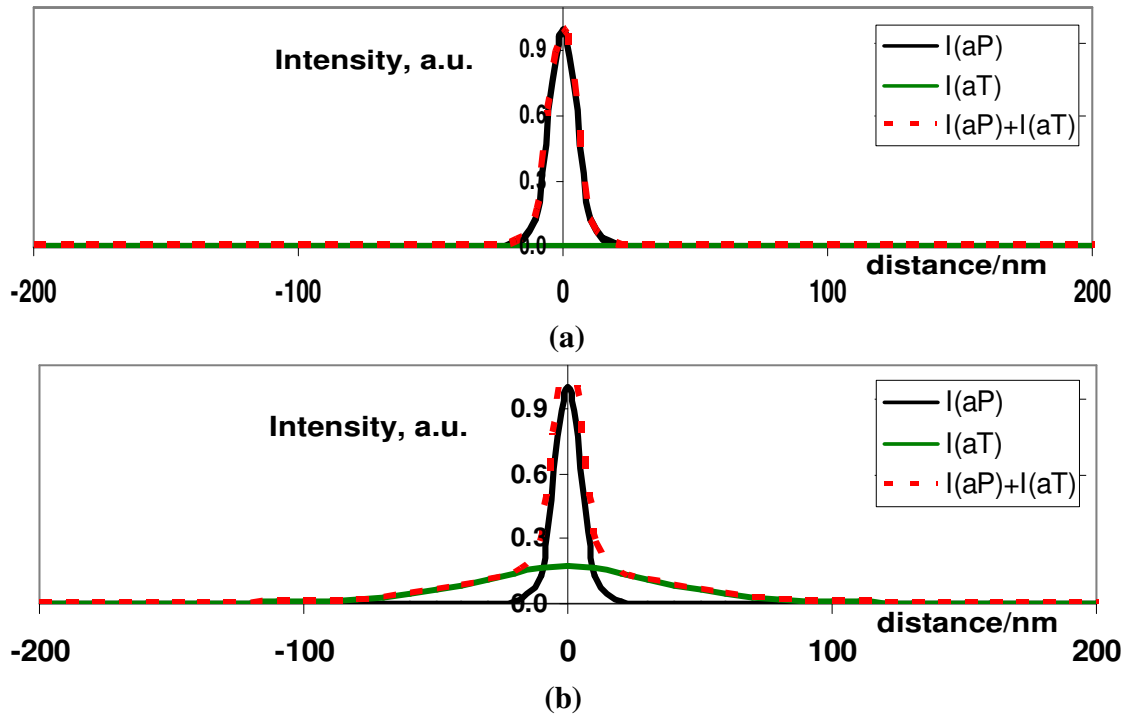


**Figure 4.3:** Calculation of point source emission profile detected with uncoated probe. Used parameters:  $\mathbf{a}_S = 0$ ,  $\mathbf{a}_P = 10\text{nm}$  and a)  $2\theta = 20^\circ$  and b)  $2\theta = 90^\circ$ .

It was already suggested in Section 2.4, that the center of Sphere S can be assumed as the position of the point emission source. Then the radius of the sphere  $\mathbf{a}_S$  represents the position of the source below the surface. Hence, the increasing  $\mathbf{a}_S$  simply means that the point emission source is pushed further below the surface of the sample. From Fig.4.3, it is clear that when the emission source is at the surface ( $\mathbf{a}_S = 0$ ), the increase in  $\theta$  has a marginal influence on the resolution and detection efficiency of the probe.

The impact of the angle becomes evident if the emission source is placed at 10 nm below the surface, as shown in Fig.4.4.

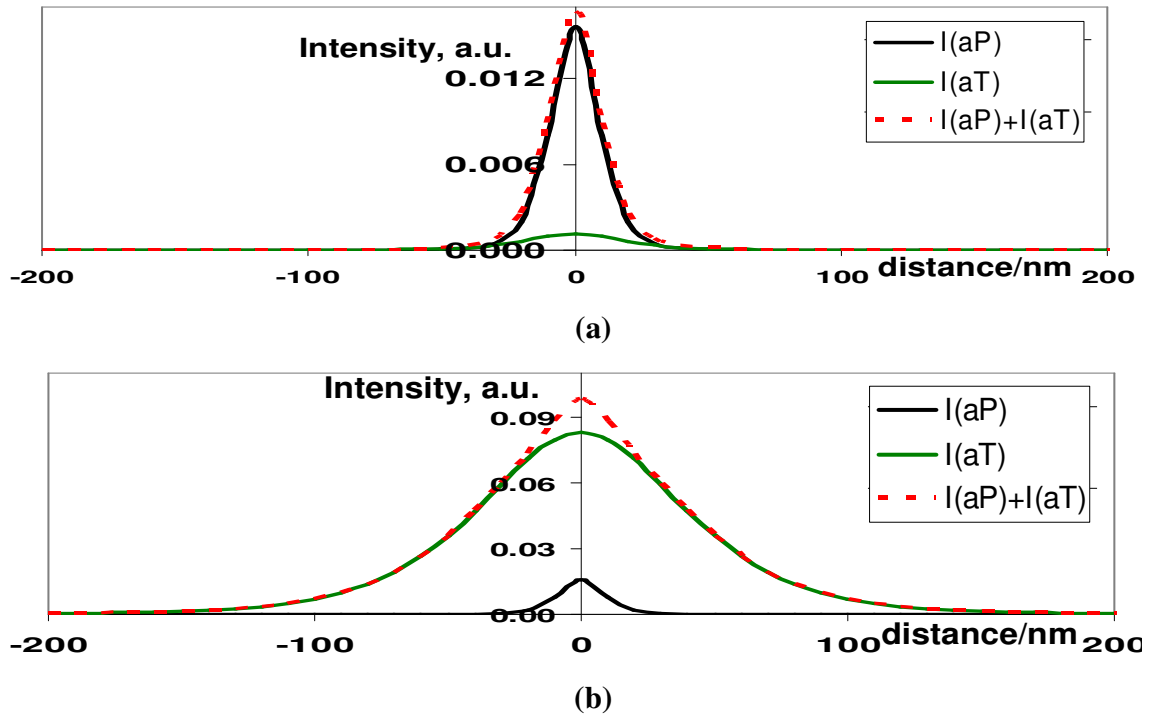


**Figure 4.4:** Calculation of point source emission profile detected with uncoated probe. Used parameters:  $\mathbf{a}_S = \mathbf{a}_P = 10\text{nm}$  and a)  $2\theta = 20^\circ$  and b)  $2\theta = 90^\circ$ .

For a small  $\theta_1$ , the signal scattered with Sphere P degrades by two orders of magnitude (Fig.4.4a). One order of magnitude can be regained when the angle is large  $\theta_2$  (Fig.4.4b). However, this improvement in detection efficiency is compromised by the contrast of the image. The signal due to Sphere P contributes to the intensity profile only 80% above the maximum level of the signal. The signal below this 80% level is contributed solely to the Sphere T.

The Full Width at Half Maximum (FWHM) of the curves can be used as a measure of spatial resolution. The FWHM increases from 10 nm in Fig.4.3a to 24 nm in Fig.4.4a, while in Fig.4.4b the FWHM = 80 nm. The larger FWHM in Fig.4.4b is mainly attributed to the background corresponding to scattering with the Sphere T (Fig.2.9). The strong degradation (by more than one order of magnitude) between situations described in Fig.4.3 and Fig.4.4, as well as the loss in resolution capabilities show that it is not reasonable to keep the size of the tip as sharp as possible if the source is placed below the surface. It is expected that in SNPEM application, the emission source is always below the surface. Fortunately, with the miniaturization of devices the active layer thickness is also decreasing [5], but in keeping a broader perspective, the emission source for all varieties of devices is expected to be deeper than 10 nm.

Taking into account this expectation  $a_p$  is increased to 50 nm in Fig.4.5. For small angle  $\theta_1$  this increase allows an improvement in the detection efficiency by more than one order of magnitude but at the expense of resolution degradation to 60 nm (Fig.4.5a). For larger angles, the increased  $a_p$  actually allows the resolution to improve from a FWHM

of 80 nm in Fig.4.4b to the value of 60 nm in Fig.4.5b. This occurs due to higher contribution of Sphere P. The detection efficiency also improves but only five times (Fig.4.5b).

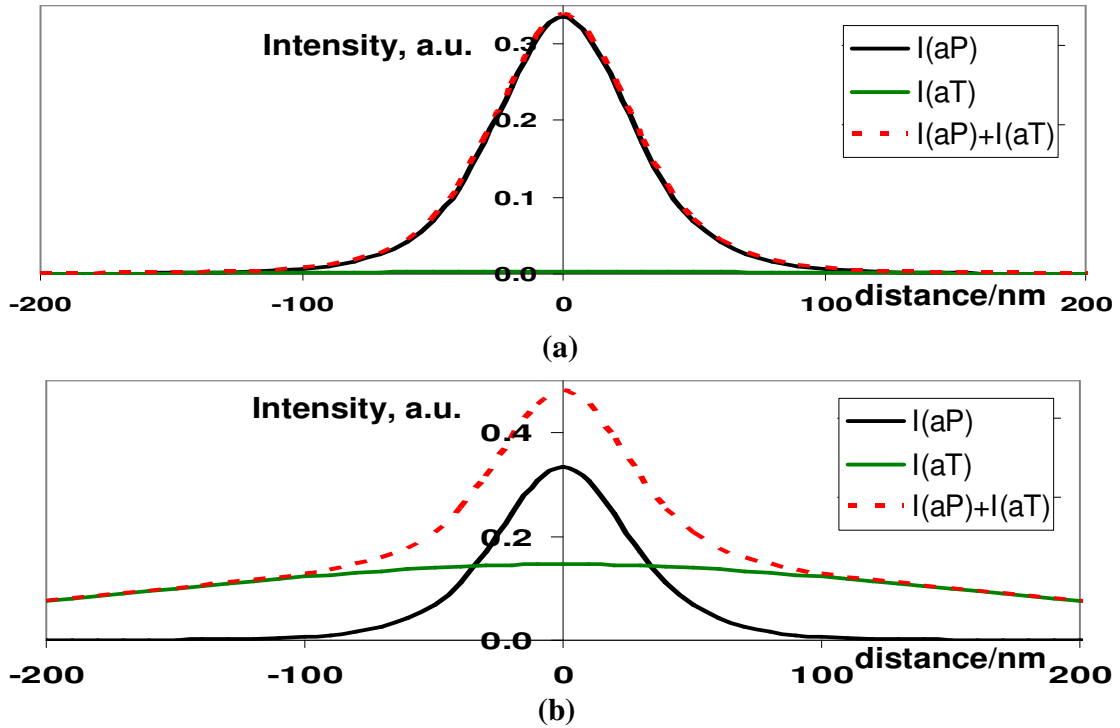


**Figure 4.5:** Calculation of point source emission profile detected with uncoated probe. Used parameters:  $a_S = 10\text{nm}$ ;  $a_P = 50\text{nm}$  and a)  $2\theta = 20^\circ$  and b)  $2\theta = 90^\circ$ .

In Fig.4.6, the analysis is continued with  $a_S = 100\text{ nm}$ . For a small angle, the impact of Sphere T is still small (Fig.4.6a). The FWHM is now mainly determined by  $a_S$  because  $a_S > a_P$ . That means that  $d = a_S$  starts to dominate in Eqn.2.1. For large cone angles, the impact of Sphere P becomes negligible as seen in Fig.4.6b and Sphere T with radius of 300 nm dominates the image properties.

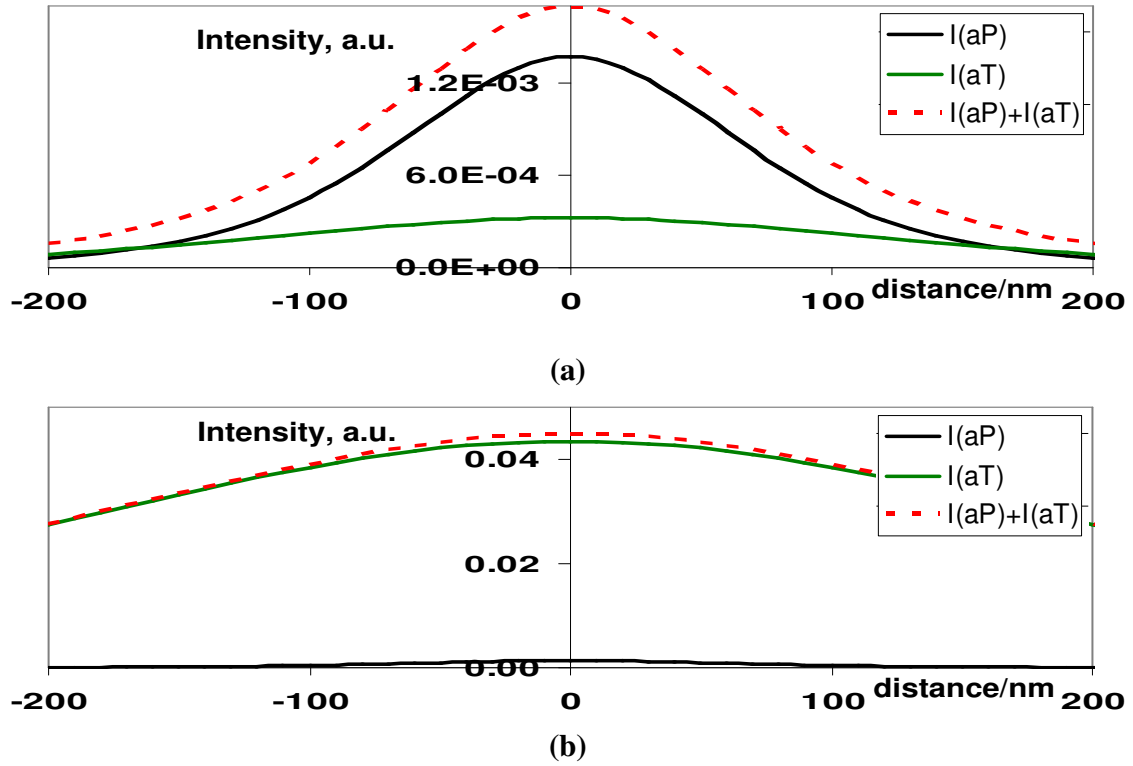


**Figure 4.6** Calculation of point source emission profile detected with uncoated probe. Used parameters:  $a_s = 100\text{nm}$ ;  $a_p = 50\text{nm}$  and a)  $2\theta = 20^\circ$  and b)  $2\theta = 90^\circ$ .

From Figs.4.3-4.6, it is clear that resolution, detection efficiency and contrast are interdependent in NF imaging with dielectric probes. Optimum parameters additionally depend on the properties of the emission source. The latter's dependence is attributed not only to the location of the source below the surface but also to the finite dimension of the source.

In the above analysis only uncoated dielectric probes were considered and this will be discussed further in Chapter 5. This means that  $g_p = g_T$ . The influence of direct coupling into the body of the probe was neglected. For uncoated probes, this coupling is not negligible and must be considered for actual application.



#### 4.3.2 Application of dielectric probe to emission source placed below the surface

The first probe used for SNPEM analysis is shown in Fig.4.7. It is similar to PTP, however the base aperture is kept relatively large. It is known that, for aperture diameters larger than the wavelength, the transmission is close to unity [66]. Hence, this aperture will not affect detection efficiency, but it still gives sufficient improvement in the contrast. The final tip radius is chosen to be relatively large, because it is expected that the probe cannot reach the actual NF condition of the emission source for the chosen samples.

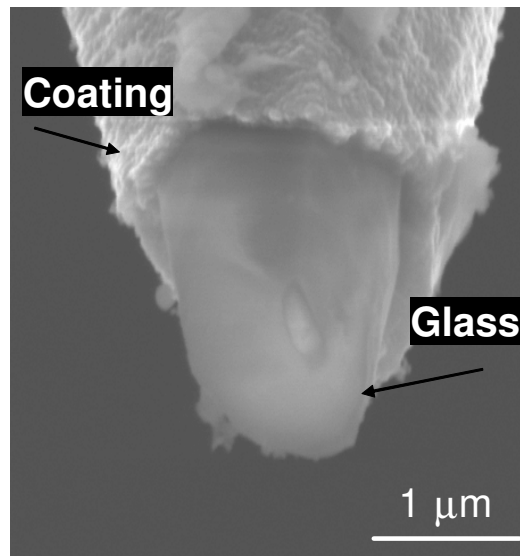


**Figure 4.7:** SEM image of PTP with large base aperture fabricated using FIB [145].

The bare end of the probe is attached to the visible PMT, which is sensitive in a spectral range from 300 nm to 900 nm (Fig.3.13). Most of the photons emitted from operating silicon devices are concentrated around 1.2 μm (Figs.A.3-A.4). Hence, in order to generate a sufficient amount of photons in the visible wavelength range, the DUTs are

subjected to biasing conditions that imply high electric fields, such as avalanche breakdown.

The first DUT is a silicon p-n junction subjected to ESD stress. After ESD stress the reverse breakdown voltage of the junction reduced by nearly 2V in comparison with a good unstressed device, as shown in Fig.4.8. This stressed junction is more preferable in comparison to a good device because it should have a single emission site at the weakest area after the ESD stress.

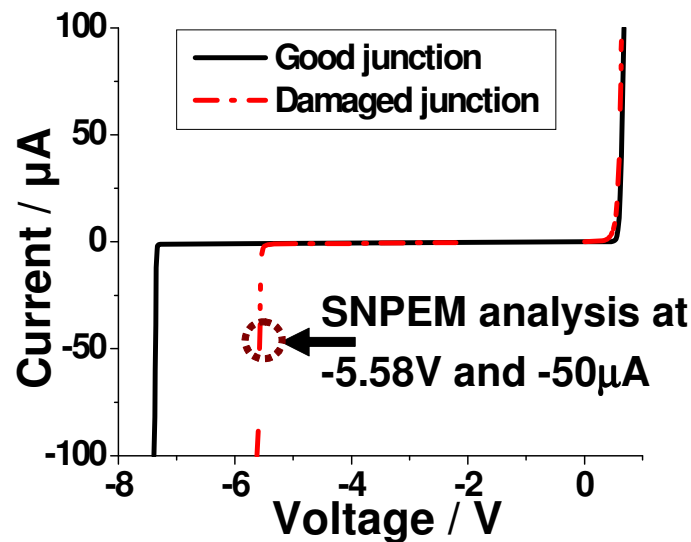


**Figure 4.8:** I-V characteristics of the good and stressed (damaged) device.

In Fig.4.9a, an overlay of the FFPEM image on the FF reflected image is shown. The emission distribution for the good device can be found elsewhere [169]. The color gradation in Fig.4.9 is optimized using Matlab 7.0.

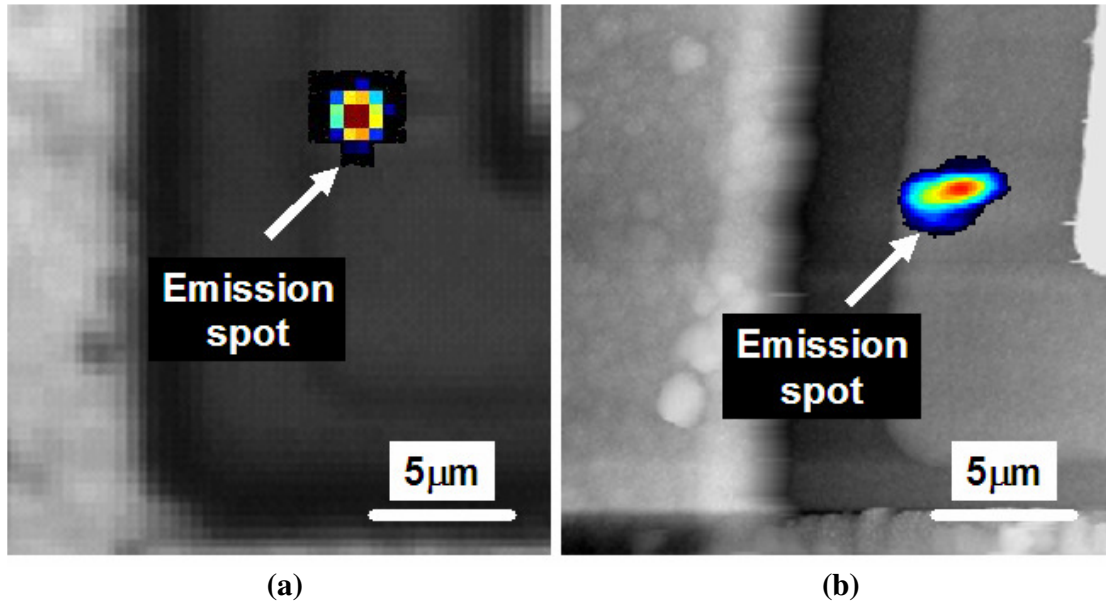


**Figure 4.9:** a) FFPEM of the leaking silicon p-n junction; b) SNPEM analysis of the same junction with PTP. Passivation layer thickness:  $\sim 1.5 \mu\text{m}$ ; avalanche current of  $50 \mu\text{A}$  [145].

The overlay of the SNPEM image on the topography image for the same area and biasing conditions is shown in Fig.4.9b. It may not be correct to make a direct comparison between the FF and NF images because the spectral sensitivity of the silicon CCD camera used in the FFPEM system extends to  $1100 \text{ nm}$  [12]. An analysis of the similar device cross-section using SEM revealed that the junction is covered with a passivation layer that has a thickness of approximately  $1.5 \mu\text{m}$ . This means that the collection is taking place in the NF of the sample surface but not in the NF of the emission source. However, it is evident that more details are revealed by the SNPEM image in comparison to the FFPEM image.

A 3D representation of the photon emission distribution detected by the FF and NF systems are shown in Figs.4.10a and 4.10b, respectively.

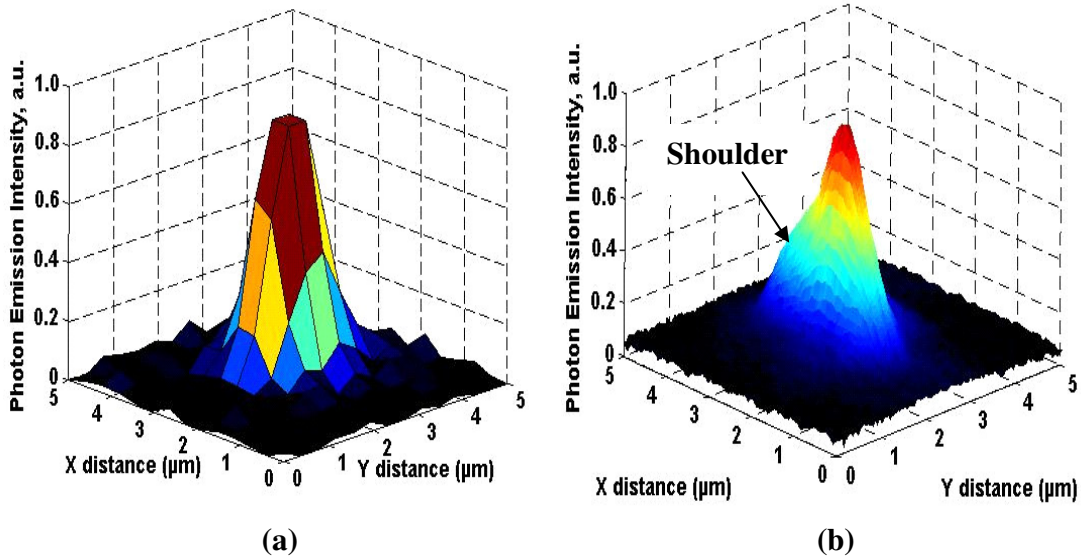


**Figure 4.10:** 3D representations of the a) FFPEM and b) SNPEM results in Fig.4.9 [145].

The Z-axis is attributed to the photon emission intensity in arbitrary units. From this 3D representation, one can clearly see that SNPEM provides a high level of detalization of the intensity profile. The SNPEM image also reveals a clear “shoulder” close to the peak with the maximum intensity (Fig.4.10b). It is hard, if possible at all, to deduce this shoulder from the FFPEM image (Fig.4.10a).

In spite of the fact that it is hard to define resolution capabilities of the system through the NF analysis of such samples, it is observed that the application of SNPEM can reveal finer details of the emission distribution in comparison with FFPEM.

#### 4.3.3 Application of dielectric probe to MOSFET with a short channel

Another sample that is analyzed using the SNPEM is a test structure of an n-MOSFET with 180 nm length and 20  $\mu\text{m}$  width. Fig. 4.11 shows a schematic representation of the MOSFET.

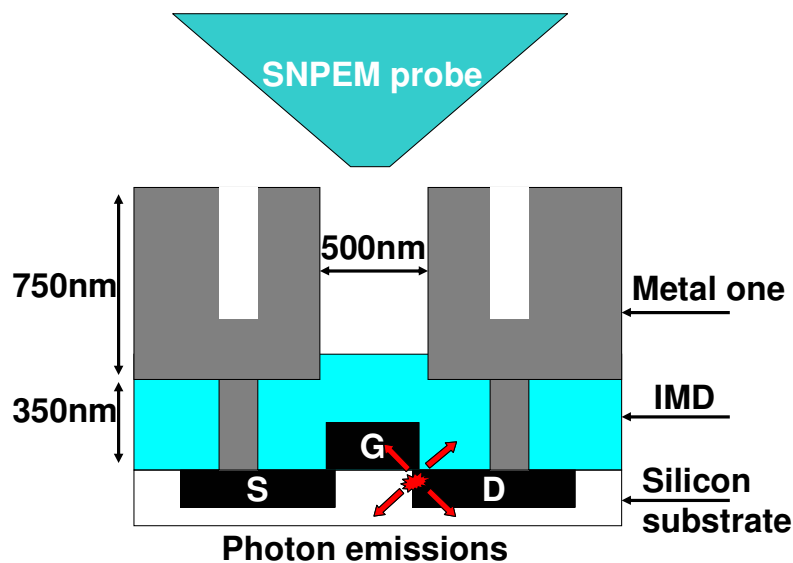


**Figure 4.11:** Schematic representation of the MOSFET test structure.

This sample is chosen because it reveals critical problems of SNPEM applications for the front-side analyses of samples even with one metal layer. The first problem is that metal lines always cover the emission source for such samples, as shown in Fig.4.11. Another problem appears due to the presence of a small gap of approximately 500 nm between the drain and source metal contacts. Such a narrow gap prevents the probe from penetrating the NF of the actual emission source. This should in turn affect both resolution and detection efficiency. However, the probe can reach the NF of the light distribution at the

gap (Fig.4.11). Hence, the known confinement of the emission distribution can provide an estimation of the resolution capabilities of the probe used

The PE distribution is recorded with both FFPEM and SNPEM systems (Figs.4.12-4.13). The color gradation in Figs.4.12-4.13 is again optimized using Matlab 7.0. As mentioned earlier, the spectral sensitivity of the Si CCD camera extends up to 1100 nm, while the PMT used in the SNPEM system is sensitive only up to 900 nm. So the SNPEM system relies heavily on the detection of photons in this range. Photons with such energies can be achieved only under elevated biasing conditions. That is why all the FFPEM images are recorded when the MOSFET is biased into a saturation with the drain current of 3 mA, while all SNPEM images are recorded when the MOSFET is biased into a breakdown with the drain current of 6 mA.

The FF reflection and FFPEM images are shown in Figs. 4.12a(i) and 4.12(ii), respectively. The topography and SNPEM images are shown in Figs.4.12b(i) and 4.12(ii). By comparing Figs.4.12a(ii) and Fig.4.12b(ii), it is concluded that in the case of low magnification, not much difference in PE distribution is observed for two techniques. Both techniques show that the emissions are concentrated within the gap between the drain and source metal contacts.

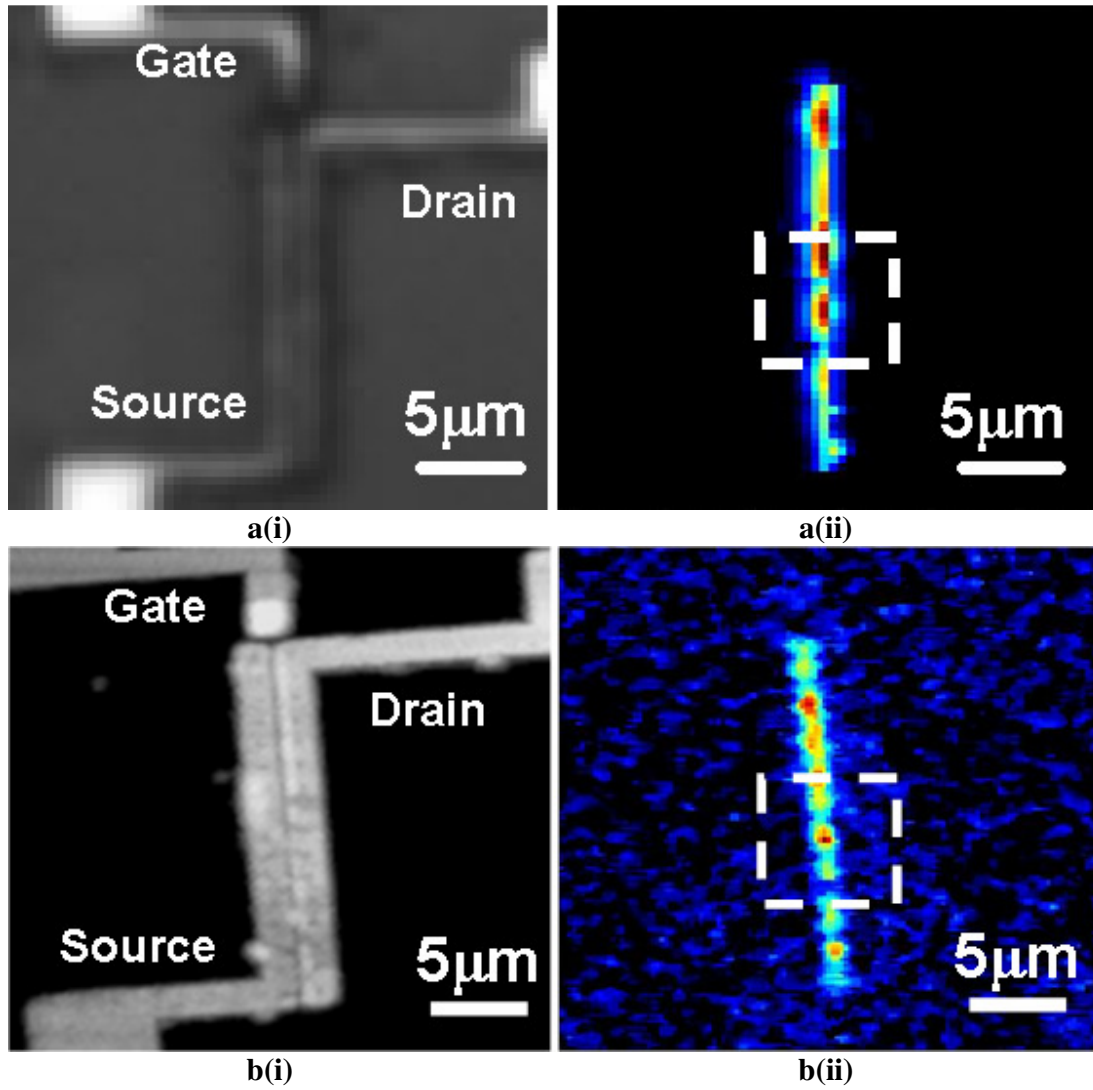


**Figure 4.12:** Low magnification images of the test MOSFET: a) (i) FF reflection and (ii) FFPEM; b) low magnification (i) topography and (ii) SNPEM images recorded with probe shown in Fig.4.7 [145].

For high magnification imaging, the regions highlighted in Figs.4.12 a(ii) and b(ii) with broken squares are chosen and are shown in Fig.4.13. It is worth noting that, in the case of SNPEM, a higher magnification means the reduction of the scan area keeping the number of pixels in the image the same. In Figs.4.12b and 4.13b, the SNPEM image

resolution is kept constant at 200 by 200 pixels. In the case of FFPEM (Figs.4.12a and 4.13a) the images are already recorded with an objective lens of the highest magnification available (100X) and any further magnification can be done only digitally by cutting out the corresponding pixels.

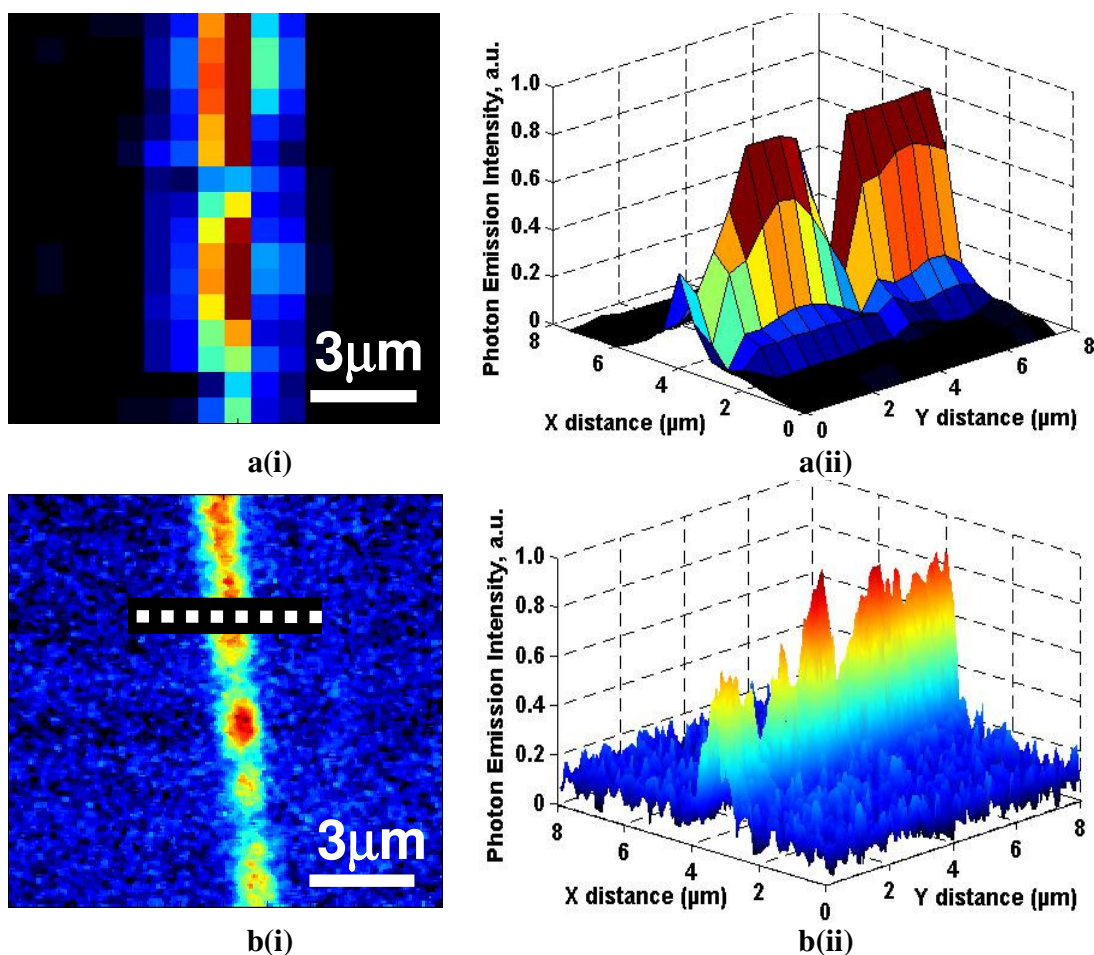


**Figure 4.13:** a) Digitally magnified (i) 2D and (ii) 3D FFPEM images of the test MOSFET (ii); b) High magnification (i) 2D and (ii) 3D SNPEM images of the test MOSFET recorded with PTP [145].

The FFPEM image in Fig.4.13a(i) has only 16x16 pixels for 8 by 8  $\mu\text{m}^2$  area, producing an image resolution of 500 nm per pixel. The SNPEM image of the same area has 200 by



200 pixels (Fig.4.13b(i)), producing the image resolution of 40 nm per pixel. Image resolution of 0.3 nm per pixel is available for the current set-up (Section 3.2).

From the 3D representation of FFPEM image shown in Fig.4.13a(ii), one can observe two distinct emission areas in the image. From the 3D representation of the SNPEM image (Fig.4.13b(ii)), a fine structure within those areas is revealed.

In order to assess the resolution of SNPEM, an emission intensity profile along the broken line in Fig.4.13b(i) is shown in Fig.4.14.

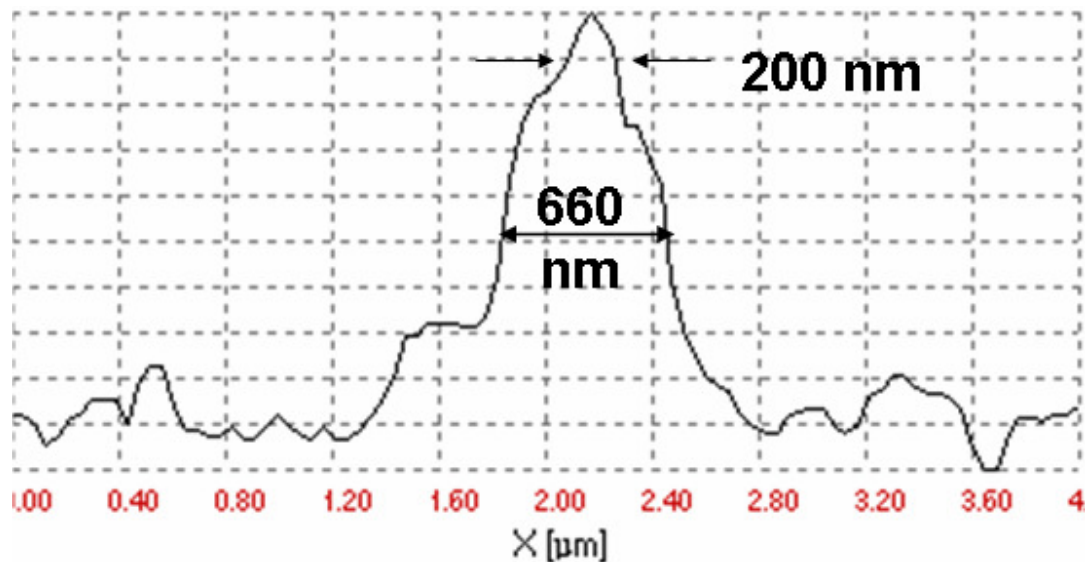


**Figure 4.14:** Emission intensity profile across the line marked in Fig.4.12b(i).

A 660 nm wide region of photon emission distribution is clearly revealed. This region corresponds to a 500 nm gap between the source and drain contacts. Within this region, it is also possible to recognize features smaller than 200 nm. This result is strongly correlated to the topography and practically represents the convolution between the probe and the side walls of the gap. This means that, within the 200 nm region, the probe is

getting closer to the emission source, permitting the NF interaction. Hence, this result provides an artificial value of the resolution. It is also possible to conclude that in terms of the emission localization, such probes achieve an accuracy comparable to the theoretical capabilities of SIL technology discussed in sub-section 1.3.1.

#### 4.3.4 Applications of dielectric probe to MOSFET with a long channel

In the following experiments, a test structure of an n-MOSFET with 5  $\mu\text{m}$  length and 10  $\mu\text{m}$  width (Fig.4.15) is chosen. A transistor with its length longer than the one shown in Fig.4.13 is chosen in order to bring the probe between two metal contacts and thus, get closer to the emission source.

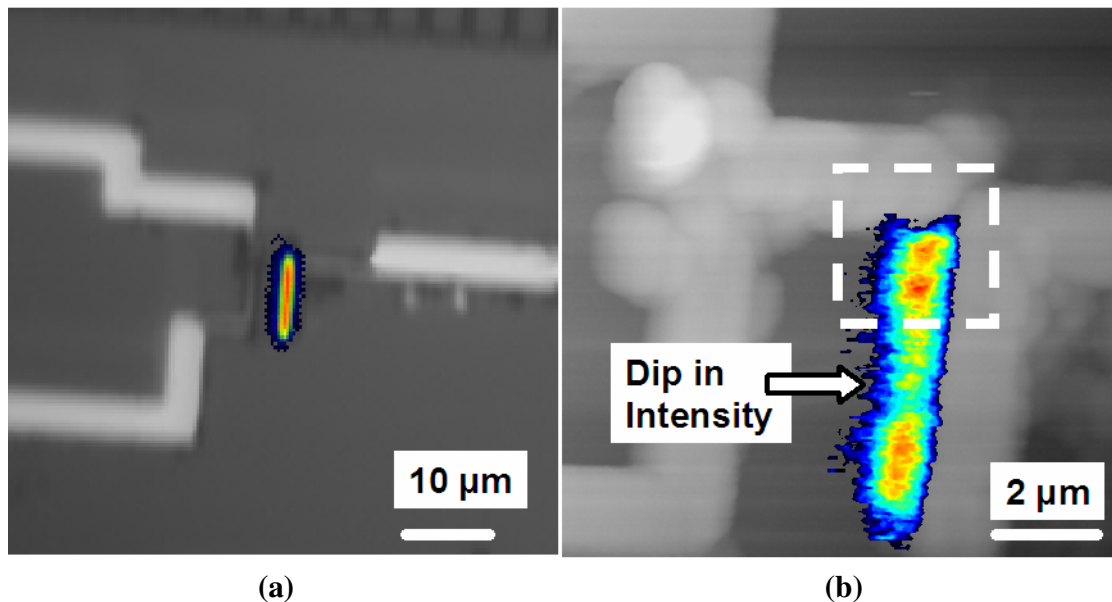


**Figure 4.15:** Investigation of PE distribution for n-MOSFET with 5  $\mu\text{m}$  gate length by a) FFPEM and b) SNPEM.

An uncoated commercial polymer probe from LovaLite [146] with an apex radius of 200 nm is applied. The taper of such a probe has a nearly parabolic shape. Such a taper is expected to provide a higher efficiency in the scattered light collection but at the expense of the- contrast.

The overlay of the FFPEM image on FF reflected images is shown in Fig.4.15a. No color optimization using Matlab 7.0 is applied. The intensity distribution is thresholded using the standard FFPEM software. The recorded image shows a commonly observed phenomenon: when the emissions are concentrated at the drain metal contact of the transistor. The overlay of the SNPEM image on the corresponding topography image is shown in Fig.4.15b. The dip in emission intensity (see Fig.4.15b) in the middle part of the transistor is caused by probe-sample regulation problems. From topography profiles, it is deduced that the expansion of the Z scanner is at least 50 nm less in this middle region with low intensity in comparison to neighboring regions at the top and lower parts of the image.

In Fig.4.16, the area within a broken square (marked in Fig.4.15b) is imaged at two different biasing conditions: a) drain current  $I_d = 30 \mu\text{A}$ , drain voltage  $V_d = 4.5\text{V}$ , gate voltage  $V_g = 2.5\text{V}$  and b)  $I_d = 40 \mu\text{A}$ ,  $V_d = 5.2\text{V}$ ,  $V_g = 2.5\text{V}$ . The limits for the fake color gradient are adjusted to the same values in both images. The intensity of the brightest pixel in Fig.4.16a(i) is approximately two times lower than the intensity of the brightest pixel in Fig.4.16b(ii). This result clearly demonstrates the possibility of distinguishing current variations at the level of at least  $10 \mu\text{A}$ . This result shows at least a

three orders of magnitude improvement in comparison to sensitivities reported in literature using sub-wavelength aperture-based probes [36,51-57]. Of course, 10  $\mu\text{A}$  is still a far from the desired nA regime, which should allow the detection of not only the drive current but also of the leakage current in the device.

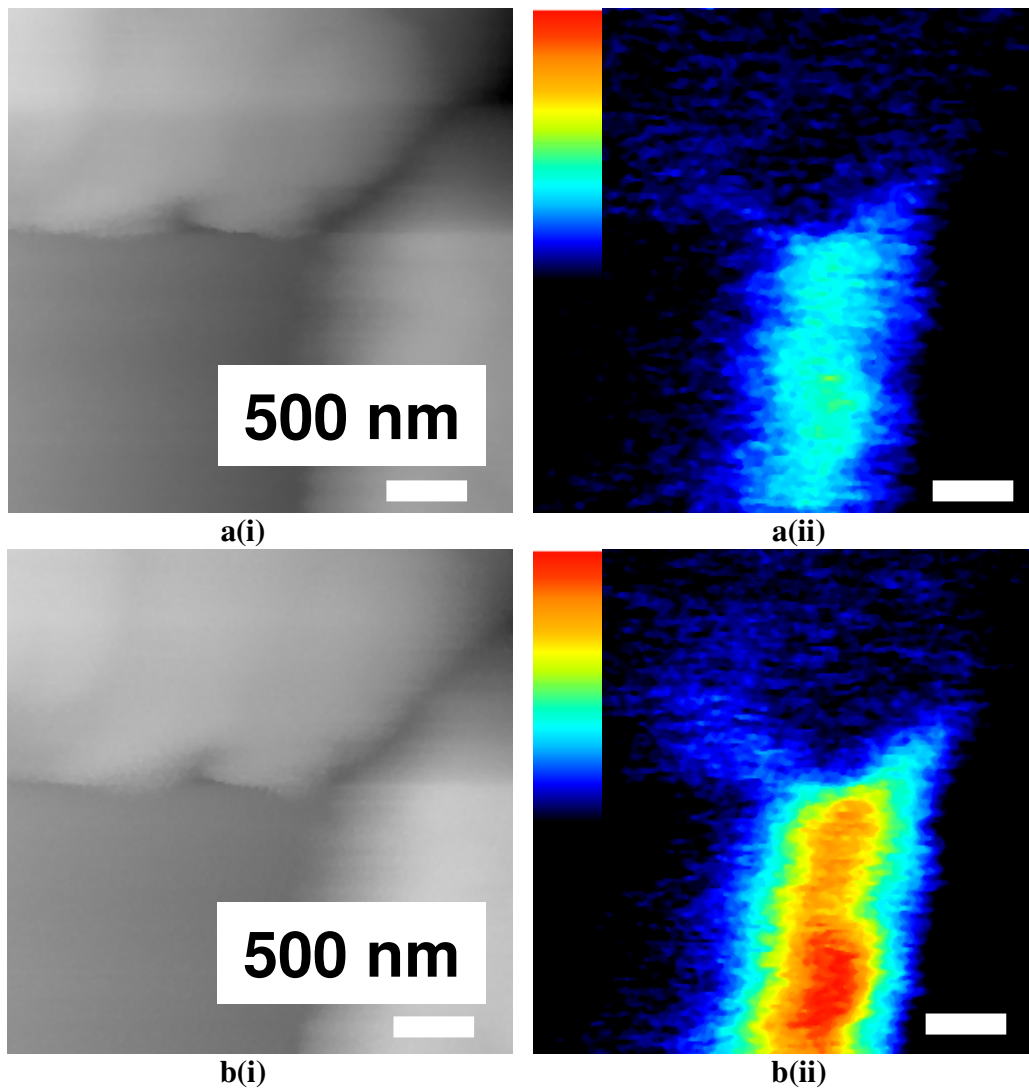


**Figure 4.16:** (i) topography and (ii) SNPEM images recorded at a)  $I_d = 30\mu\text{A}$ ,  $V_d = 4.5\text{V}$ ,  $V_g = 2.5\text{V}$  drain current and b)  $I_d = 40\mu\text{A}$ ,  $V_d = 5.2\text{V}$ ,  $V_g = 2.5\text{V}$ .

## Summary

In this chapter, different probe designs that could be used for an SNPEM project were analyzed. Using the ranking system, the uncoated dielectric probe proved to satisfy most of the demands imposed by the SNPEM application. It was shown that this probe can demonstrate better resolution capabilities in comparison to FFPEM detection. However, the demonstrated resolution capabilities are at the level of 200 nm, which is not sufficient for the SNPEM goals. The reason for such a poor resolution is the insufficient contrast between the NF signal, as defined by the final tip interaction and the background that appears due to FF collection with the probe body, as well as due to the NF interaction of the probe body with the same emission source. In terms of its detection efficiency, it was shown that such probes can distinguish variations in the supplied current to the order of 10  $\mu\text{A}$ , which shows at least three orders of magnitude improvement in comparison to the sensitivities reported in literature using sub-wavelength aperture-based probes. However, 10  $\mu\text{A}$  is still above the desired values that could make the SNPEM approach acceptable for FA. From the analysis and results in this Chapter, it is clear that none of the existing designs of the NF probes are capable of satisfying the demands of the SNPEM application.

## **Chapter 5.**

### **Scattering dielectric probe with embedded metallic scatterer**

This Chapter proposes a novel design for an NF optical probe with an embedded metallic scatterer in the nanometric tip of the dielectric probe. Placing the metallic nanoparticle inside the dielectric matrix allows us to combine the advantages of the dielectric probes and the probes with an externally attached metallic nanoparticle. At the same time, it avoids the disadvantages of these two designs. The proposed embedding process is based on an implantation using a focused ion beam of gallium (Ga) atoms. These atoms later form colloid nanoparticles within 60 nm of the probe's tip. This process also repeatedly forms a taper structure that can perform the role of an efficient collector of the scattered radiation and an efficient coupler into the guiding modes of the fiber. The unique optical properties of Ga suggest that the new probe can demonstrate the enhancement in the spectral range critical for a SNPEM application. The enhancement of at least 37 times is demonstrated for the probe enhanced with Ga, while being compared to a simple glass probe at the wavelength of 660 nm.

#### **5.1 Considerations for SNPEM probe optimization**

The main focus of this SNPEM project is to achieve a resolution compatible with the current and future technological nodes together with detection efficiency sufficient to analyze silicon-based devices at normal operation conditions (See Section 1.4). In Section 4.3 it was shown that the uncoated dielectric probes can be used to record photon emission (PE) distribution with lateral resolutions below 200 nm (Fig.4.13). The detection efficiency to drive a current variation of 10  $\mu$ A was also demonstrated

(Fig.4.17). The relatively poor resolution was attributed to the blunted tips used (Fig.4.7). Those tips also provided a poor contrast of the images, as a result of either the FF coupling into the waveguide structure of the probe or the NF interaction of the probe body with the emission source. Additionally, blunted tips prevent the probe from penetrating between the metal lines (Fig.4.11) and reaching the actual NF of the emission source.

In sub-section 2.2.4, it was proposed that the contrast can be improved by altering the scattering properties of the final tip. As was discussed in sub-section 2.3.1, if the probe tip can be represented by a nanoparticle, then the scattered intensity is proportional to the square modulus of the nanoparticle polarizability  $\alpha$ . In a simplest case of quasi-static approximation (QSA),  $\alpha$  is given by Eqn.2.5. In Eqn.2.5,  $\alpha$  is determined by the third order of the sphere radius  $a$  and the value of  $g = \frac{\epsilon - \epsilon_m}{\epsilon + 2\epsilon_m}$ , where  $\epsilon$  is the complex dielectric function of the nanoparticle and  $\epsilon_m$  is the dielectric function of the medium. For simplicity, let's assume that the nanoparticle is placed in air ( $\epsilon_m \approx 1$ ). For particular probe geometry, the value of  $a$  is fixed and it is preferable to keep it as small as possible for a higher resolution imaging. This higher resolution will come at the cost of much lower detection efficiency due to lower polarizability - according to Eqn.2.5. Hence, the only way to enhance the resolution (reduce  $a$ ) without compromising on the detection efficiency, is to increase the value of  $g$  by optimizing the sign and absolute value of  $\epsilon$ .

In Chapter 4, the uncoated dielectric probe made of silica ( $\text{SiO}_2$ ,  $\mathbf{g} \approx 0.3$ ) was considered. Several strategies can be considered for increasing the value of  $\mathbf{g}$  and thus, optimizing the scattering efficiency of the dielectric probes. In Fig.2.10, the impact of the sign of the real part of the dielectric function  $\mathbf{Re}(\epsilon)$  was already analyzed. From Fig.2.10, it is possible to deduce that one strategy to improve the scattering efficiency is to use dielectric or semiconductor tips with large positive values of  $\epsilon$  [39]. Silicon tips can provide approximately 5 times higher scattering efficiency in comparison to silica tips (Fig.2.10). However, for dielectric tips, the value of  $\mathbf{g}$  is smaller than unity and the scattering efficiency saturates at  $\epsilon \rightarrow \infty$  as shown in Fig.2.10. Hence, a further increase in the dielectric function will provide a marginal improvement in the scattering efficiency.

The second strategy is to use a metal tip with the negative real part of the dielectric function  $\mathbf{Re}(\epsilon)$ . For such a tip in air, the value of  $\mathbf{g}$  is more than unity, which causes a substantial increase in the scattering efficiency (Fig.2.10). At certain wavelengths, the condition when  $\mathbf{Re}(\epsilon) = -2$  can be satisfied. This will lead to a theoretically infinite value of  $\mathbf{g}$  [41]. This condition corresponds to the plasmonic resonance in metals at a specific wavelength. Such a strategy is applied when the scattering probes based on metal tips or metallic particles attached to dielectric tips are chosen [97,97]. However, as it was already discussed in sub-sections 4.2.4 and 4.2.5, such tips have the potential of affecting the biased devices. They also require a complicated optics design to detect the scattered light (Figs.2.6-2.7). Such constraints restrict the application of such probes in an SNPEM project and thus are not considered in this thesis.



In order to overcome these constraints, an alternative solution is proposed in this Chapter. Here, a metallic nanoparticle is embedded into the tip of the tapered optical fiber, as schematically shown in Fig.5.1.

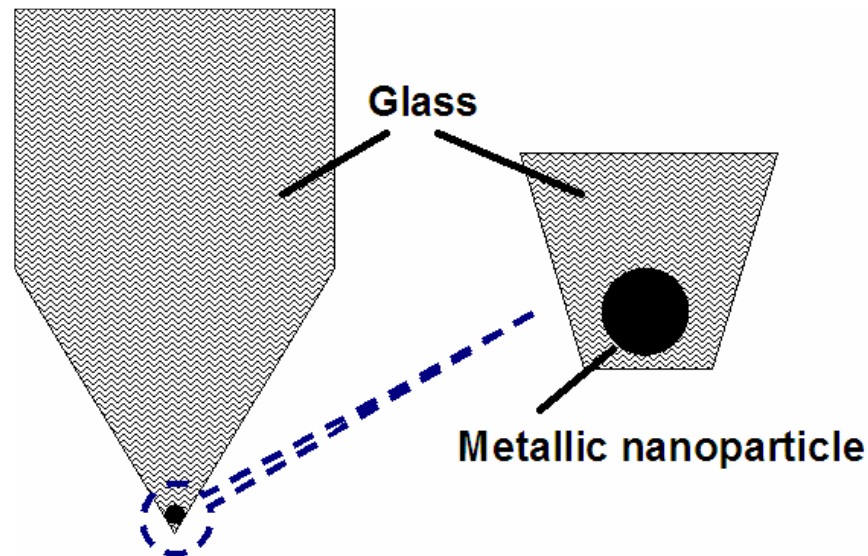


**Figure 5.1:** Schematic representation of proposed dielectric probe with embedded metallic scatterer.

Placing the metallic nanoparticle inside the dielectric matrix combines the advantages of dielectric probes (Fig.4.1b) and probes with externally attached metallic nanoparticle (Fig.4.1e). At the same time, it avoids the disadvantages of these two designs. In comparison to a dielectric probe, the new design provides a higher scattering efficiency due to its modified dielectric function. It also allows a better definition of the scattering volume that will lead to the enhanced contrast of the images. In comparison to probes with an externally attached metallic nanoparticle, several advantages can be highlighted. First, such an arrangement prevents any possible contact between the metallic nanoparticle and the biased DUT. Second, the scattering volume is placed within the dielectric waveguide. This should allow a larger fraction of the light to be coupled into

the waveguide. The idea can be linked to the scattering by dopants and other inhomogeneities in the optical fiber discussed in sub-section 2.2.2. However, metallic inhomogeneities provide a higher scattering efficiency. Ultimately, the metallic nanoparticle in Fig.5.1 will determine the scattering volume responsible for the NF interaction and thus, resolution [47]. Third, the nanoparticle is an integral part of the tip and it cannot detach from the tip during the scanning, unless the whole tip is broken.

As a result of these advantages, the proposed probe can achieve a high resolution, high detection efficiency and a good contrast. It also has the ability to collect light through the same probe while possessing a more rigid design. It can also be applied to biased samples without running the danger of causing a short circuit within the semiconductor device.

The introduction of the embedded scatterer has a certain similarity to the idea described in sub-section 2.3.3, where accelerated ions are bombarding the surface of the dielectric. This bombardment leads to the formation of a layer of nanoparticles embedded at distance less than 100 nm below the surface (Fig.2.11). However, it is important to design a method for embedding the metallic nanoparticles not just into the surface of a dielectric but to confine them to the nanometric tip of the SNPEM probe. In order to accommodate the above consideration, a novel approach is proposed in this thesis. In this approach, metallic gallium (Ga) is implanted into the tip of a multi-mode optical fiber (MMF) tapered by a three step process [147].

## **5.2 Tapering of the optical fiber by three step process**

The choice of the new probe design is restricted by the requirement of manufacturability as well as the ability to reproduce probes with the desired parameters. Following these conditions, it is reasonable to introduce the new design in parallel with the fabrication method. The method consists of 3 major steps: i) reduction of the fiber diameter down to a few micrometers; ii) sharpening the tip down to nanometric dimensions; and iii) implantation of Ga into the tip. In the proposed method, steps ii) and iii) take place simultaneously, making the method simpler and allowing more reproducible results. In this section only steps i) and ii) will be analyzed, while step iii) will be discussed in Section 5.3.

### **5.2.1 Reduction of fiber diameter using heat-drawing method**

It is important to achieve sufficient detection efficiency for SNPEM applications. This requires a high scattering efficiency of the tip. It also requires that the probe taper performs the dual role of an efficient collector of the scattered radiation and an efficient coupler into the guiding modes of the optical fiber. Such a taper should allow the maximum scattered intensity to reach the detector at the bare end of the fiber. Following the discussion in Sections 2.4 and 4.1, the taper optimal for an SNPEM application should satisfy the following conditions: i) the final taper should consist of only one material leading to a high collection efficiency due to the higher capture fraction (Fig.2.12); ii) the final taper should be a direct extension of the core of the optical fiber, so that all the light guided by the taper is naturally coupled into the guiding mode of the

fiber core; iii) the surface of the final taper should be smooth, preventing the leakage of light out of the waveguide; and iv) the aspect ratio (AR= length/width) of the taper should be large enough for the SNPEM probe to analyze samples with complicated topographic features. The design of the taper that complies with all four conditions is proposed in Fig. 5.2.

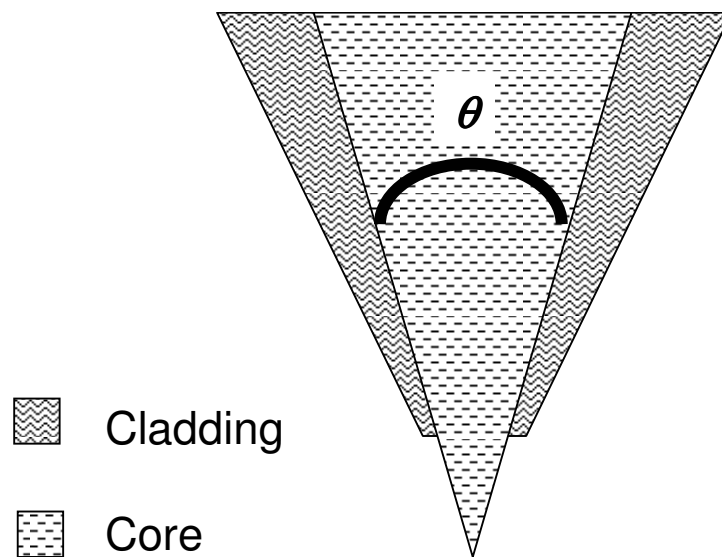


**Figure 5.2:** The design of the taper optimum for SNPEM application.

Probes tapered only by a heat-drawing method have a disadvantageous geometry, as shown in Fig.5.3a and 5.3b for a single mode fiber (SMF) and a multi mode fiber (MMF), respectively. In the heat-drawing method, the cladding stays around the core, reducing the capture fraction as was discussed in sub-section 2.4.1. The advantageous geometry (Fig.5.2) can be achieved naturally by the chemical removal of the cladding [123]. However, the chemical etching strongly depends on the environmental conditions. For example, vibrations can cause uneven etching [122]. Unevenness of the etching results in the poor quality of the probe surface and makes it impossible to satisfy condition iii). Also, in spite of a theoretical capability of mass production, the chemically etched probes

are more expensive than probes made by the heat-drawing method. The probable reason is that only a very experienced person manning only one probe at a time can ensure the ideal conditions for the etching. Many disadvantages of the etched probes can be minimized by the implementation of a hybrid pull-etch method [123]. In the hybrid method, the etching step is performed on a tip with a reduced diameter. In this case, the etching step takes a much shorter time, thereby reducing the impact of the environment. These probes are also attractive due to high AR. Hence, they comply with condition iv). The problem with the hybrid pull-etch method is that the tip is still made of a dielectric material, reducing the scattering efficiency (Fig.2.10).

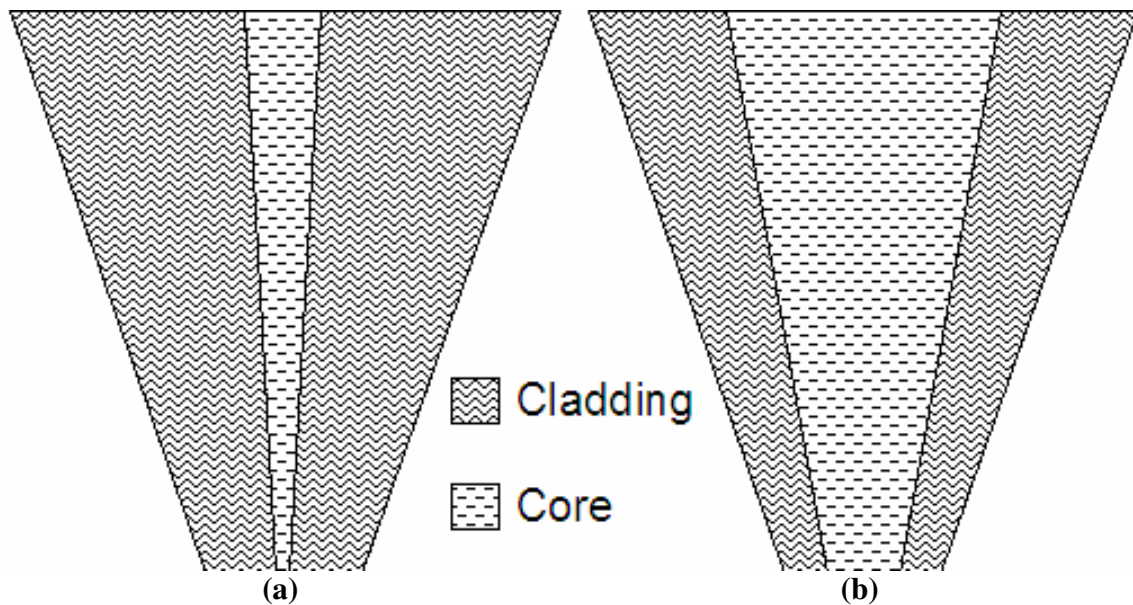


**Figure 5.3:** Probes tapered by heat-drawing method: a) SMF; b) MMF.

In this chapter, a new approach is proposed. In this approach, the heat-drawing method is first implemented in order to comply with requirements iii) and iv) discussed above. A standard optical MMF with a core diameter of  $50\text{ }\mu\text{m}$  and fiber diameter of  $125\text{ }\mu\text{m}$  is used. The choice of the MMF is based on the analogy to the conventional optical fiber

fabrication [148], in which the core diameter decreases proportionally in relation to the fiber diameter. The resulting taper should be similar to the one shown in Fig.5.3b. Following this assumption, it is possible to estimate that the core diameter reduces to  $0.8\ \mu\text{m}$  when the fiber diameter is reduced to  $2\ \mu\text{m}$ . Such a waveguide will still be able to guide the fundamental mode [47]. On the other hand, if the SMF (core diameter -  $10\ \mu\text{m}$ , fiber diameter -  $125\ \mu\text{m}$ ) is subjected to the same tapering down to  $2\ \mu\text{m}$ , the core diameter will reduce to  $0.16\ \mu\text{m}$  (Fig.5.3a), which will in turn lead to a considerable leaking of the fundamental mode into the cladding [47] causing an attenuation of the guided signal.

The heat-and-pull procedure is performed using a commercial Fusion Splicer Unit (FSU) 995 PM from Ericsson. During the process, an electrical arc heats a region of the fiber, while both ends of the fiber are pulled in opposite directions, as shown in Fig.5.4a.

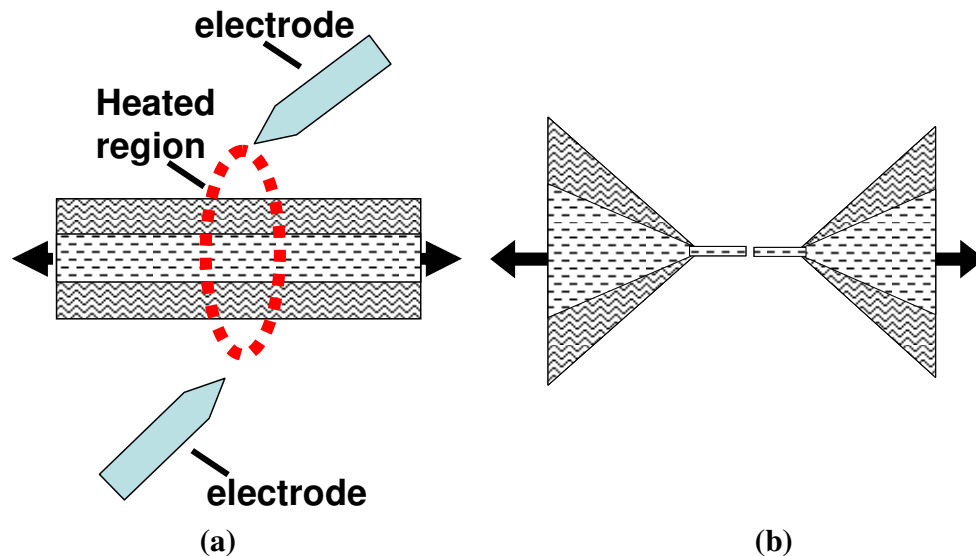


**Figure 5.4:** Heat-drawing method applied to MMF: a) heating and simultaneous pulling of MMF; b) hard pull.

The heating of the fiber is stopped manually when the diameter reaches a value below 5  $\mu\text{m}$ . This parameter is controlled by visual observation using an inbuilt CCD camera. This approach is inaccurate at the moment leading to the final diameter of the tips in the range from 2  $\mu\text{m}$  to 5  $\mu\text{m}$ , but certain improvement can be achieved through automation.

The reason for making the hard pull is to prevent the melting of the taper-end after the breakage. The melting leads to the formation of a blunt parabolic tip, as shown in Fig.5.5a. This kind of blunt tip is unsuitable for the next step of probe sharpening, which will be considered in sub-section 5.2.2.

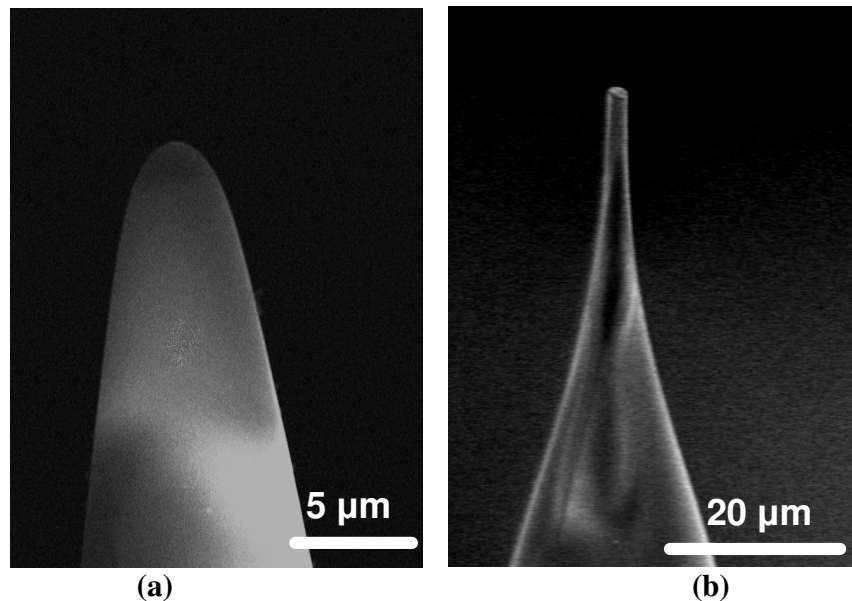


**Figure 5.5:** The effect of hard pull on the probe shape: a) parabolic shape achieved with heating; b) shape after hard pull.

The final shape of the probe after the hard pull is shown in Fig.5.5b. The shape consists of conical and cylindrical parts. The presence of the cylindrical part makes the probe look different from the solely conical shape expected earlier (Fig.5.3b). This shape is achieved

because of the dependence of the fiber temperature on the fiber diameter. Hot fiber loses heat through the surface and when the fiber necks, the surface to volume ratio increases and it cools more rapidly [69]. Lower temperatures increase the viscosity of the glass. Due to this, the elongated portion of the fiber reduces its diameter slower [69]. That is why a nearly cylindrical shape is observed.

Another observation for the hard pulled tips is that the cylindrical facet is very rough (Figs.5.6a and b). This can become a problem if the second step of tip sharpening, which will be discussed in the next sub-section 5.2.2, is applied directly. The problem is overcome by slicing the end of the tip using Focused Ion Beam (FIB) perpendicular to the probe axis as identified with a dotted line in Fig.5.6a. A very smooth surface can be achieved by this step, as shown in Fig.5.6c.

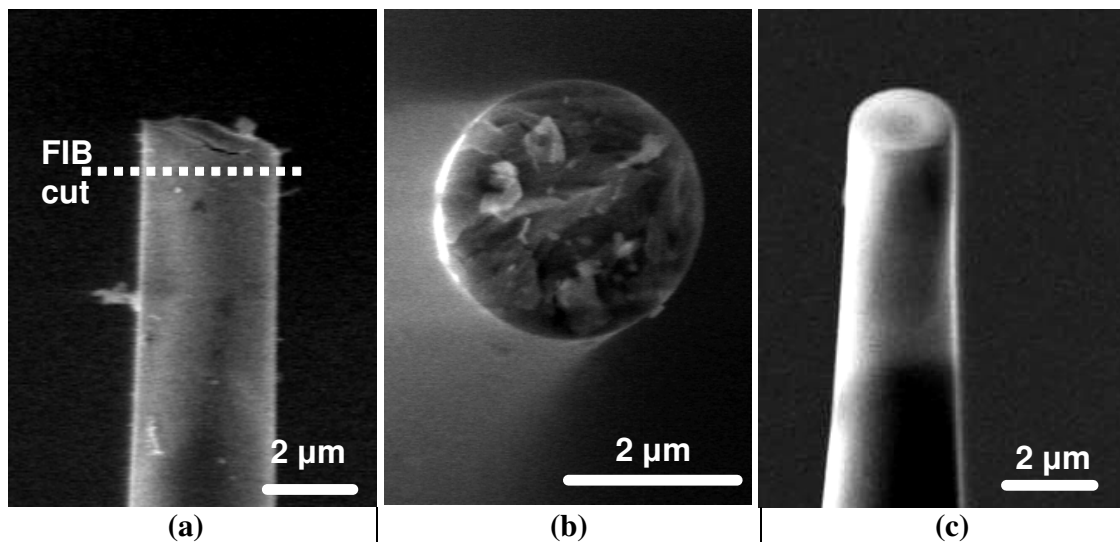


**Figure 5.6:** Tip quality after hard pull: a) side view; b) facet view; c) tip after FIB cut.



### 5.2.2 Sharpening the tip down to nanometric dimensions

The pulling procedure described above is very convenient for reducing the diameter of the probe from 125  $\mu\text{m}$  down to a few micrometers. Further reduction of the probe diameter using this method will lead to the deterioration of the guiding properties similar to the case of the SMF (Fig.5.3a). In this thesis, a novel method of nanometric tip formation using FIB is proposed.

For the sharpening process, a FEI “Quanta 3D” FIB system is applied. This system consists of both electron beam and ion beam columns. This allows us to control the geometry of a manufactured probe in-situ. According to specifications, the FIB resolution is 10 nm, making the FIB an attractive tool for fabrication of a NF probe with desired properties. Unfortunately, this resolution capability is achievable only on a limited number of samples. The sample should, preferably, be a flat (2D) conductor. In the case of a dielectric 3D probe, the accuracy of FIB-processing may degrade to a few hundreds of nanometers. Hence, micromachining of the tip using FIB cannot ensure high repeatability. It only adds a considerable cost to the final product. It is clear that a different approach is required if FIB is going to be used for the probe fabrication. Such an approach should imply the minimum interaction of an operator with a system in order to bring repeatability allowing batch fabrication.

The proposed approach is based on an observation that the edges of an object illuminated with the beam of high-energy ions are sputtered much faster than the inner parts [149].

For the same reason, it is critical to additionally treat the tip shown in Fig.5.6b with FIB because the edges on the defective surface cause accelerated etching. Such accelerated etching leads to an unpredictable shape and quality of the final tip, as shown in Fig.5.7.

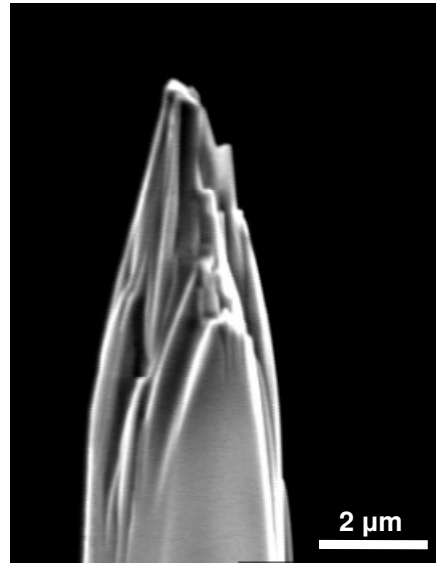


**Figure 5.7:** The effect of the defective primary surface on the final result of FIB based sharpening.

In regard to the FIB-treated probe (Fig.5.6c), the sharpening process is described in Fig.5.8. The front-side of the cylindrical tip (Fig.5.8a) is raster-scanned with a focused beam of Ga ions (Fig.5.8b). For a beam with an accelerating voltage of 30 keV and at a beam current of 1 nA, the cylinder reduces to a sharp cone with its base equal to the original cylinder diameter of approximately 2 μm (Fig.5.8d). The process takes approximately one minute. The schematic representations on the left side of images show how the shape of the probe affects the properties of the waveguide in terms of core exposure. By the end of the sharpening process, the final tip consists of only the core material (Fig.5.8d), making the probe very similar to the ideal shape proposed in Fig.5.2.

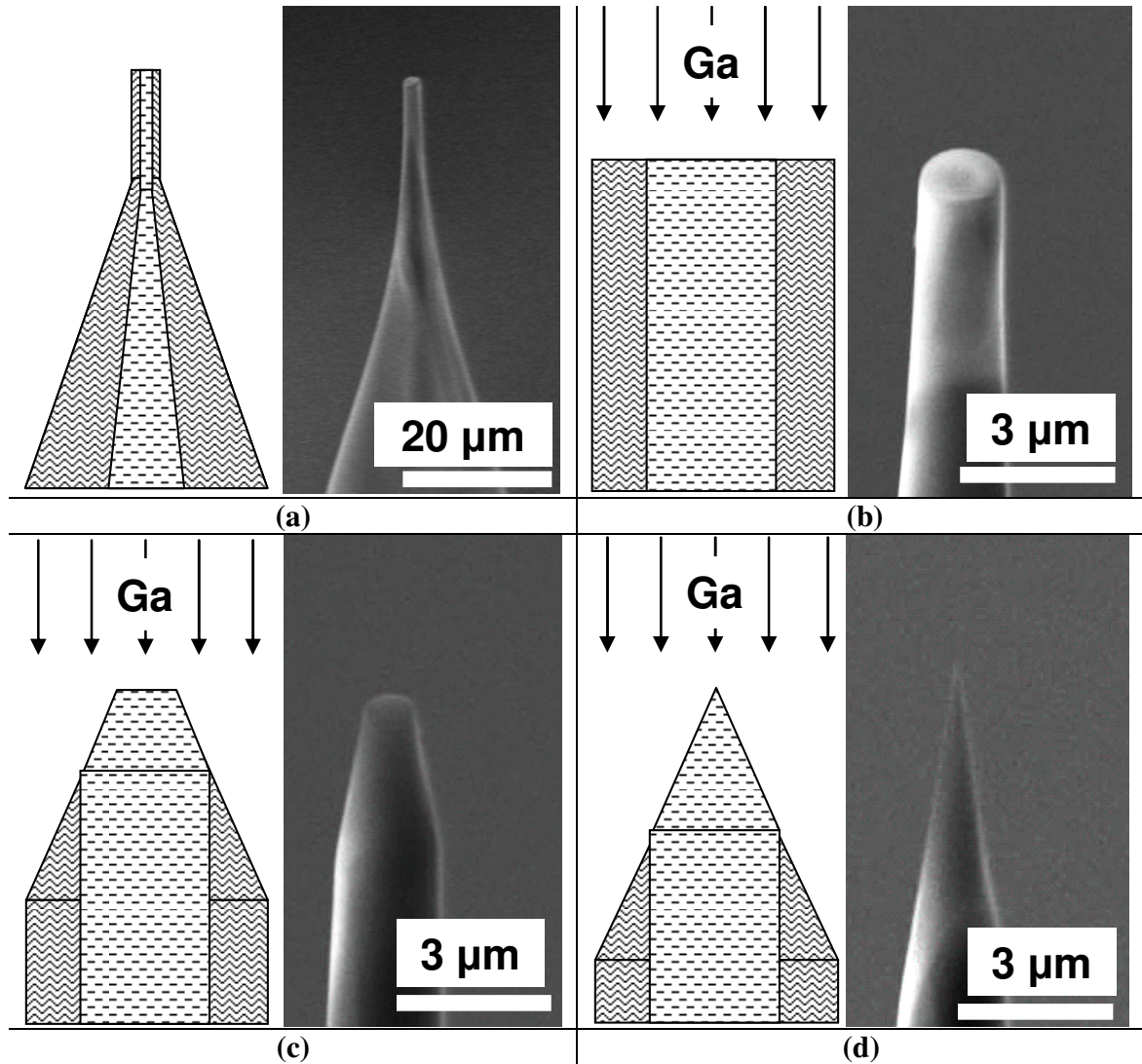


**Figure 5.8:** Formation of the sharp dielectric tip: a) shape of the probe after heat and pull method; b) shape of the probe tip before application of FIB; c) tip shape after 30 sec of FIB illumination; d) tip shape after 60 sec of FIB illumination [147].

This core-cladding profile is confirmed using the Energy Dispersive X-ray (EDX) analysis. The EDX spectra are recorded from three separate locations on the taper (Fig.5.9a). The recorded spectra are shown in Figs.5.9b-d.

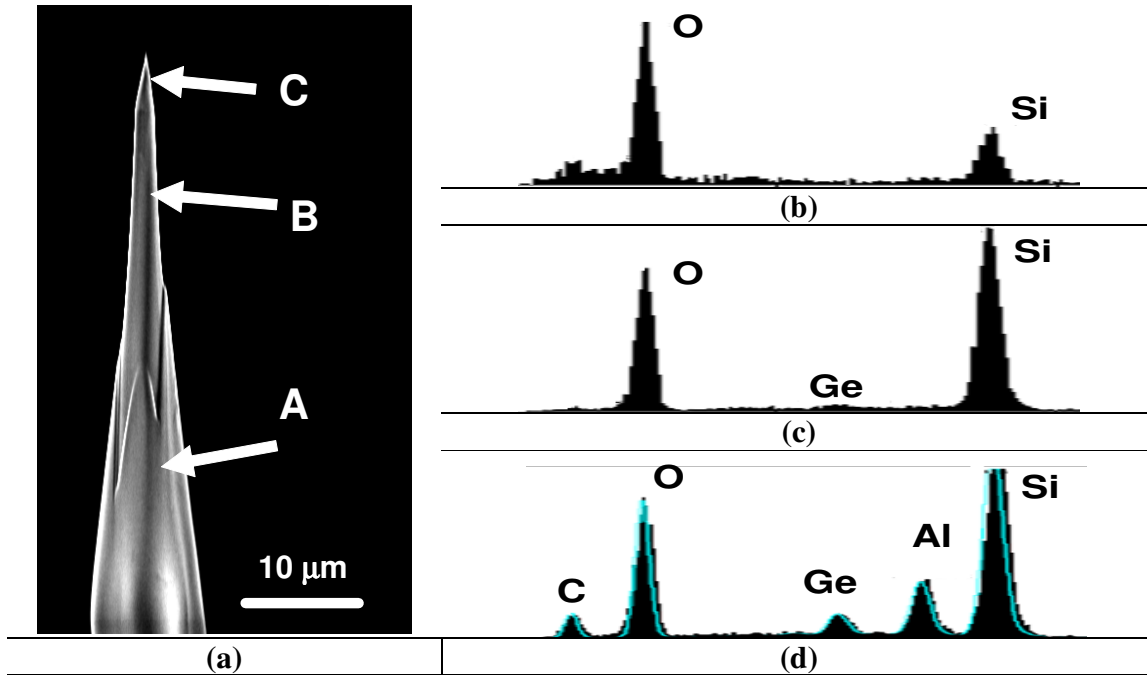


**Figure 5.9:** Evaluation of the core/cladding profile using EDX characterization at different regions of the probe: a) SEM image; b) region A; c) region B; d) region C.

The spectrum in Fig.5.9b is recorded from the first conical taper marked A in Fig.5.9a. It shows that within the electron beam penetration depth, the only material present is silica with an atomic concentration corresponding to  $\text{SiO}_2$ . Pure silica is commonly used in MMF to form the cladding [148]. The spectrum from the cylindrical part (Fig.5.9c) reveals a considerable change in the atomic weights between silicon and oxygen as well as traces of germanium. The drastic change in relation between the atomic concentrations of silicon and oxygen is not clear at the moment and will not be considered in this thesis. The presence of germanium is expected because it is a common implant used to increase the refractive index of the core material. The MMF used for fabrication has a refractive index different between the core and the cladding of 1%, which corresponds to the  $\text{GeO}_2$  mole fraction of 14% [148]. A lower fraction observed in the spectrum might indicate that the original cladding is still present (Fig.5.8b). This cladding limits the number of

electrons, that can reach the core material and at the same time have sufficient energy to excite the X-ray photon. The spectrum taken at the final taper (Fig.5.9d) revealed a much higher amount of Ge. The observed value is roughly equal to the expected 14 % in relation to Si. Hence, it confirms that in this region the core is exposed, as shown in the schematic part of Fig.5.8d. The aluminium and carbon peaks appearing in the spectrum are attributed to the aluminium holder covered with carbon tape placed below the probe. They are subjected to bombardment with electrons passing through the thin part of the probe.

In order to confirm the repeatability of the sharpening process, the same ion beam parameters are used for two different probes as shown in Fig.5.10.

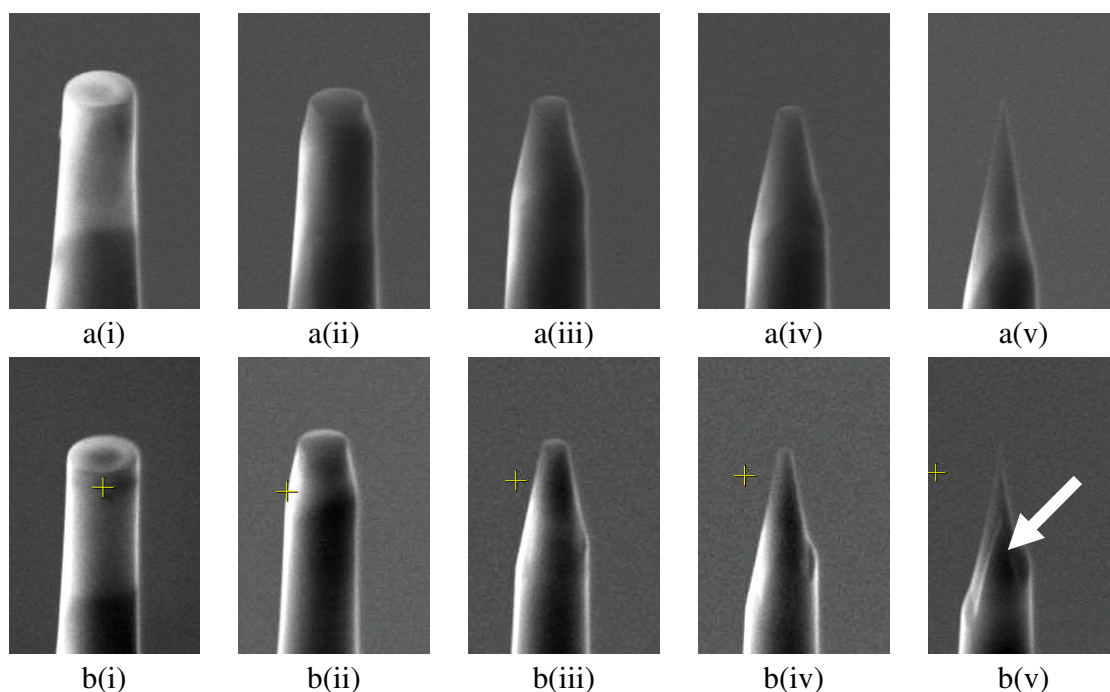


**Figure 5.10:** Confirmation of repeatability of the sharpening process for two different probes. a) and b) are SEM images of the probes at different points of time : i) starting point; ii) 15 sec; iii) 30 sec; iv) 45 sec; v) 60 sec.

The similarity of the shapes of two probes confirms that the result is repeatable. However, there is an additional structure at the side of the probe, indicated by the arrow in Fig.5.10b(v). This structure appears due to a misalignment between the probe and the beam.

The taper angle for both probes is approximately  $20^\circ$ . It is observed that the final shape is affected by the beam parameters (like accelerating voltage and current), alignment and the probe diameter before sharpening. A thorough investigation of these dependences is required in order to ensure the repeatability of the probe fabrication. Such an investigation goes beyond the scope of this thesis because the primary goal here is to prove the feasibility of the method for achieving a tip of sizes below 100 nm.

### **5.3 Dielectric probe with embedded gallium scattering center**

One of the major factors that influenced the choice of FIB for the probe fabrication was the unavoidable implantation of Ga into the object subjected to ion bombardment [150]. Another reason is that FIB became a common tool in most of the failure analysis labs around the world.

Schematically the process is represented in Fig.5.11. The bombarding ions are concentrated at the center of the probe within the implantation range. The implantation range of Ga atoms can vary from 10 nm down to 100 nm for different materials and accelerated voltages [149]. Although the consecutive sputtering process removes the implanted atoms, new Ga atoms are implanted into the material below the surface. The

atoms on the side should be removed at a much higher rate and thus, the considerable concentration of Ga should be observed only at the final tip, as shown in Fig.5.11.

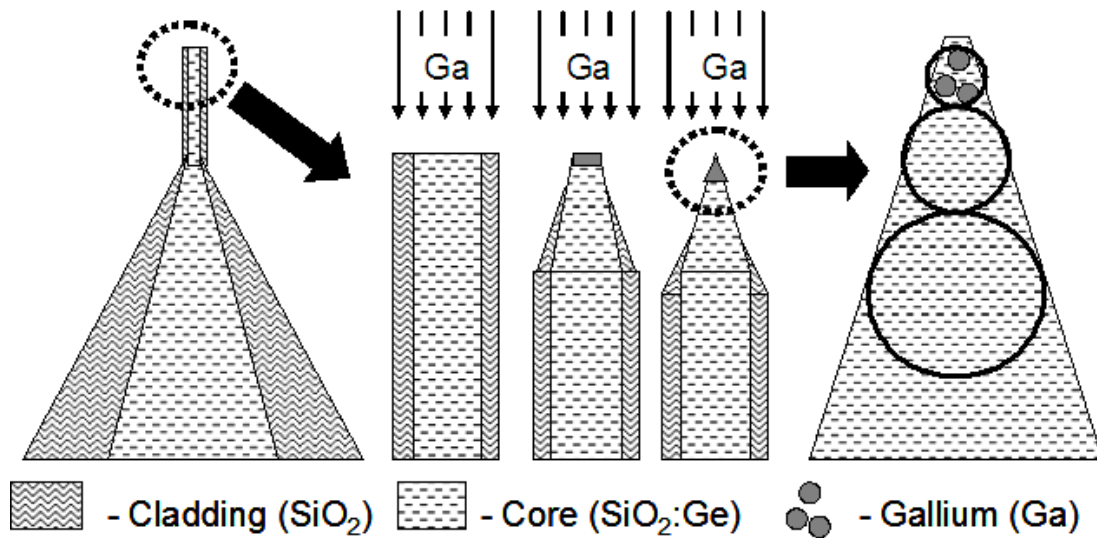


**Figure 5.11:** Formation of embedded scatterer by Ga ion implantation using FIB.

In order to confirm the occurrence of such processes, the freely available software The Stopping and Range of Ions in Matter (SRIM) developed by James F. Ziegler [151] is used. Figure 5.12a shows the simulated trajectories of 2000 Ga ions inside glass slide. The ions bombard the surface at one spot, at normal incidence and with a kinetic energy of 30 keV. Figure 5.12b shows the distribution of the implanted Ga atoms. It is found that most of the atoms are concentrated around the implantation range at a value of 27 nm. This value is close to the 30 nm demonstrated in literature [112]. It is also known that the implanted Ga tends to form colloids of nanoparticles within this distance [112], similar to other metals. For example, in Fig.2.11, the result of Cu implantation into silica was shown. Figure 5.12b shows that colloid nanoparticles should be confined within 60 nm of

the probe's tip. And we can expect a high concentration of the metallic colloids at the tip of the fiber embedded into the dielectric matrix.

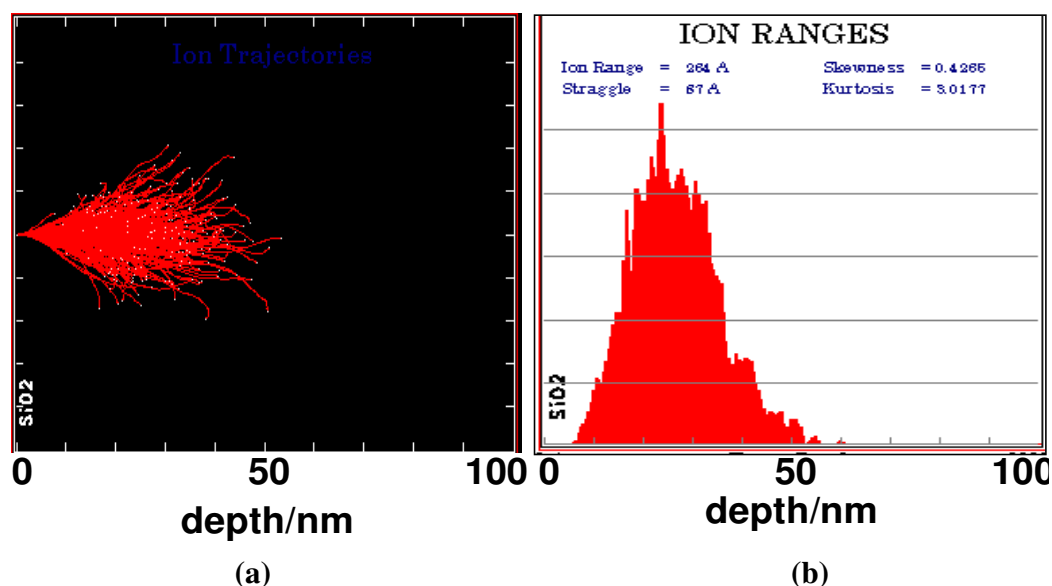


**Figure 5.12:** Implantation of 2000 Ga ions into silica at normal incidence with energy of 30keV: a) Trajectories inside the target; b) distribution of implanted Ga below silica surface.

Contrary to the implantation into the tip, much lower levels of Ga concentration are expected at the slanted sides. Using the same SRIM [151] software, it is possible to estimate the sputtering rate at different incidence angles. The incidence angle can be defined through the probe cone half-angle  $\theta$ , as schematically shown in Fig.5.13. It is found that the sputtering yield at the normal incidence is approximately one magnitude lower than the sputtering yield at an angle of  $80^\circ$  from the normal. In the case of illuminating a conical tip, this angle corresponds of the tip with  $\theta = 10^\circ$ , as shown in Fig.5.13. Hence, the sputtering process dominates at the sides and should lead to a 5-10 times smaller concentration of Ga in comparison to the normal-incidence [149]. This can explain why the Ga peak (expected at 1 keV) did not appear in the EDX spectra shown in



Fig.5.9d. Unfortunately, it was not possible to perform an EDX analysis at the tip because the focused beam of electrons caused the tiny glass to melt, preventing the illumination of the tip for a sufficiently long time.

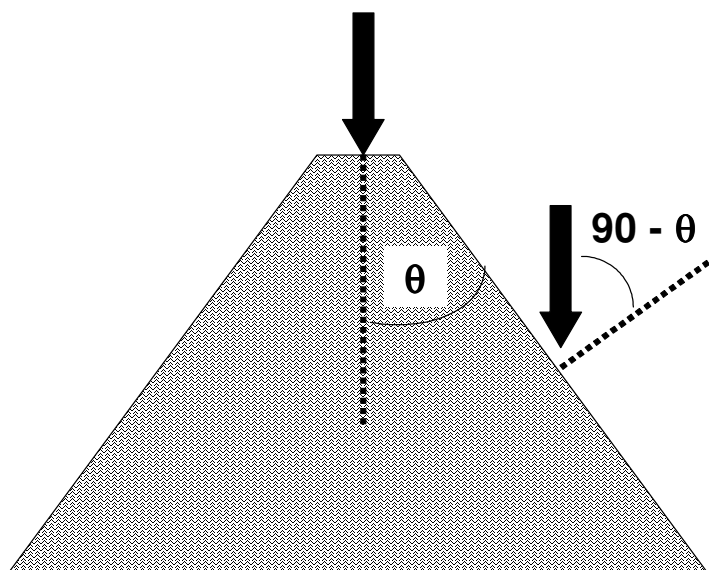


**Figure 5.13:** Sputtering yield at different incidence angles: a) normal incidence  $0^\circ$ ; b)  $80^\circ$ .

The presence of Ga in the tip is confirmed by measuring the number of transmitted electrons when a 30keV electron beam is scanned across the tip. Figure 5.14a shows the secondary electron micrograph of the probe tip. The tip was deliberately subjected to a longer illumination with the ion beam in order to reach a sharper cone angle. A sharper tip allows better contrast in the transmission image. In Fig.5.14b, the transmission image is overlaid on the SEM image from Fig.5.14a. The red and blue limits of the color bar in Fig.5.14b represent a low and high number of transmitted electrons, respectively. It is clear that there is higher electron attenuation at the tip. This attenuation indicates that in the last 40 nm of the tip there is a presence of a dense material. The only possible reason

for the denser material to occur is presence of Ga, while the value of 40 nm is close to the value predicted in Fig.5.12b.

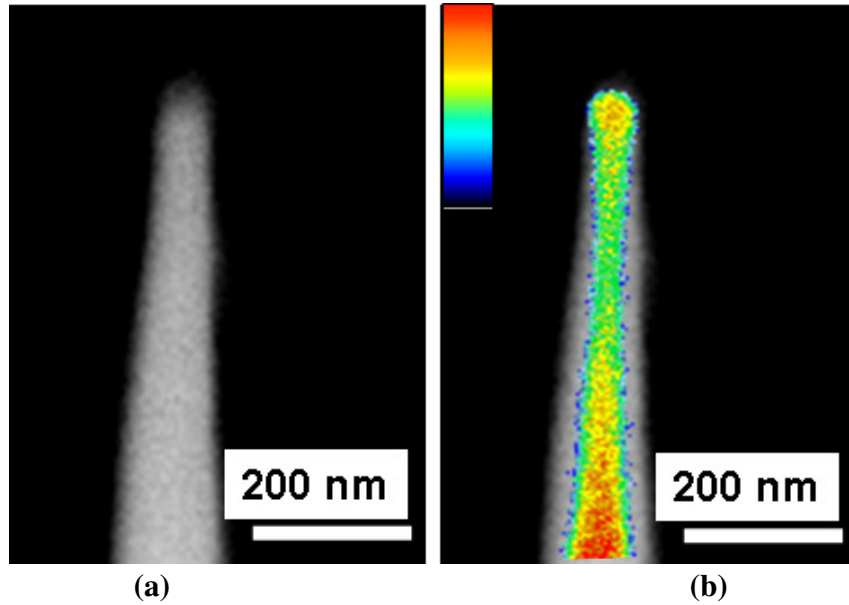


**Figure 5.14:** Observation of Ga “drop” in the tip: a) SEM image of the probe tip; b) visualization of the material density by measuring the number of transmitted electrons when 30 keV electron beam is scanning across the tip [147].

As a result of the sharpening process described above, it is possible to achieve the embedded scattering center inside the probe. This has several advantages. First, such an embedded center minimizes the scattering volume of the tip, which is responsible for resolution. Second, the higher polarizability of Ga in comparison to glass allows higher detection efficiency (see the following Section 5.4). Third, it improves the contrast of emission detection due to the considerable difference in interaction properties between the tip and the body of the probe. Forth, the embedment of the metallic nanoparticle prevents the detachment of the scatterer from the tip during the scanning. Fifth, such an embedment also prevents the direct contact between the metallic nanoparticle and the biased sample. Sixth, placing the scatterer inside the dielectric waveguide structure

allows more efficient coupling into the propagating modes for the scattered light in comparison to the metal particles placed outside the probe body. This arrangement also ensures a much better alignment of the nanoparticle in relation to the waveguide axis. The simplicity of the fabrication method and its repeatability demonstrated in Fig.5.10, suggest that the method can be scaled into mass production using area implantation systems. In order to emphasize the scattering due to the presence of Ga and the impact of the dielectric nature of the probe, this system shall be referred to as a ‘Ga-based scattering dielectric probe’ (Ga-SDP) for future reference. The highlighted advantages make the Ga-SDP the best candidate for a SNPEM application in comparison to other existing probe designs.

## 5.4 Optical characterization of the probe with embedded Ga

One of the intentions of implanting the metallic scatterer into the tip of the dielectric probe is to enhance its scattering efficiency. In this Section, the influence of the optical properties of Ga on the probe scattering efficiency will be analyzed, both theoretically and experimentally.

### 5.4.1 Optical properties of Ga

The scattering efficiency of the Ga-SDP has to be analyzed through the specific optical properties of Ga. One reason why Ga is chosen for SNPEM application because this metal has a unique property of having the real part of the dielectric function  $\text{Re}(\epsilon_{\text{Ga}})$

which is approximately constant within a broad spectral range of 500 nm to 1300 nm [152]. Using Eqn.2.5, it is possible to compare the scattering properties of Ga nanoparticle with the properties of nanoparticles made of gold (Au) and glass (SiO<sub>2</sub>).

Assuming nanoparticles have the same radius, it is possible to calculate the relation **K(λ)** between the scattering intensity from Ga nanoparticle, and the scattering intensities from Au and glass nanoparticles in air.

$$\mathbf{K}(\lambda) = \frac{I_{\text{Ga}}}{I_{\text{j}}} \propto \frac{|\alpha_{\text{Ga}}|^2}{|\alpha_{\text{j}}|^2} \propto \frac{|g_{\text{Ga}}|^2}{|g_{\text{j}}|^2} = \left| \frac{\epsilon_{\text{Ga}} - 1}{\epsilon_{\text{Ga}} + 2} \right|^2 \bigg/ \left| \frac{\epsilon_{\text{j}} - 1}{\epsilon_{\text{j}} + 2} \right|^2 \quad (5.1)$$

where **j** is either Au or SiO<sub>2</sub>.

In Eqn.5.1, the square moduli of the polarizabilities are compared and it is necessary to take into account the imaginary part of the dielectric function for a correct calculation. In Fig.5.15, **log(K)** is plotted versus the photon energy, where the values of the dielectric constant for Au and SiO<sub>2</sub> are taken from Refs. 107 and 109.

The calculations are performed using Matlab 7.0. It is clear that throughout the broad range of photon energies, the scattering efficiencies of Ga and Au are comparable. However, when Ga is compared to SiO<sub>2</sub>, the difference in the scattering efficiencies is at least one order of magnitude. It ranges from 15 to 20 times in a spectral range from 0.5 eV (2.5 μm) to 2.5 eV (0.5 μm). This wavelength range generally covers the entire region important for photon emission detection from silicon-based devices [12].

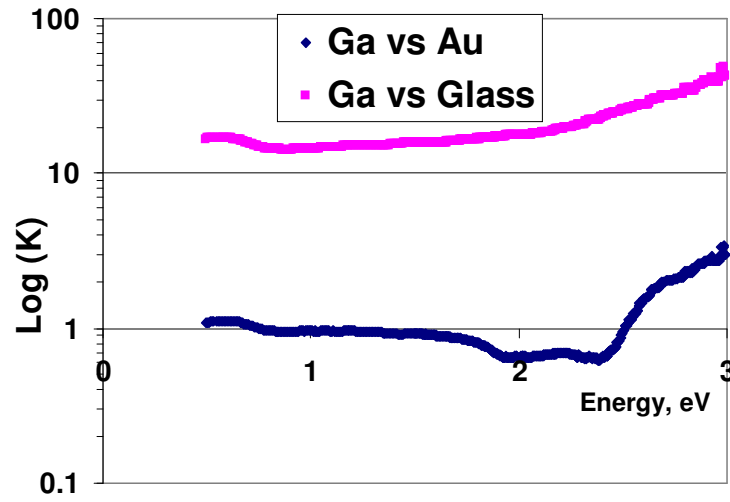


**Figure 5.15:** Comparison of scattering efficiencies for Ga vs. Au and SiO<sub>2</sub> nanoparticles.

#### 5.4.2 Characterization of Ga impact on the probe scattering efficiency

The intensity scattered by the proposed probe should be proportional to a square modulus of the nanoparticle polarizability  $\alpha$ . According to Fig.5.15, the probe with an implanted Ga should demonstrate at least one order of magnitude improvement in its scattering efficiency in comparison to a glass probe without Ga. This assumption is verified by imaging a polished waveguide using probes with and without implanted Ga, as shown in Fig.5.16a and 5.16b, respectively. In this experiment, a laser diode emitting at 660 nm wavelength is used to launch light into the waveguide. The optical images are recorded at the same amplification parameters for the detector sensitive in the visible spectral range (Fig.3.13). The images in Fig.5.16 contain 100 by 100 pixels and the dwell time for each pixel is approximately 25 milliseconds. The color gradients in Fig.5.16 are optimized for each individual image. The numbers at gradient bars indicate the maximum intensity within the images. From Fig.5.16, it is possible to conclude that both probes reveal the

waveguide location as well as a small bright spot. This bright spot appears due to the surface defect, which allows a strong leakage of light from the waveguide.

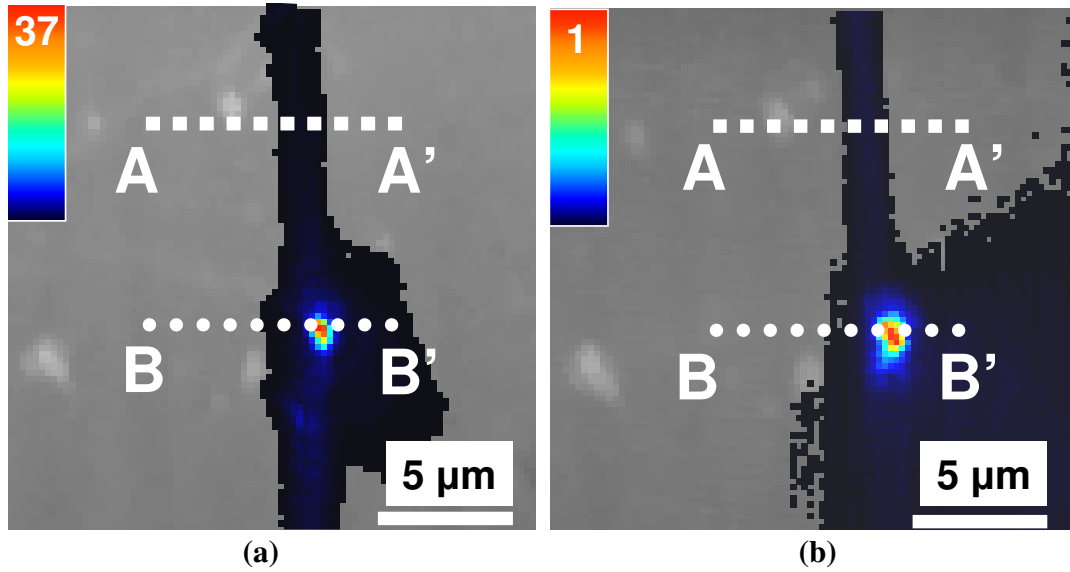


**Figure 5.16:** Overlaid optical and topography images of the polished waveguide recorded with different probes: a) SDP-Ga; b) simple tapered glass tip [147].

The maximum intensity level recorded by Ga-SDP (Fig.5.16a) is 37 times higher in comparison to the maximum intensity recorded by the probe without Ga (Fig.5.16b). This value is approximately two times larger than the enhancement factor predicted for the Ga tip in Fig.5.15. A probable explanation for higher enhancement is that the enhancement should be calculated using an effective dielectric constant of a composite structure made of Ga embedded into the glass (Eqns.2.6 or 2.7). Depending on the metal fraction in the composite, the real part of the effective dielectric function comes closer to the resonance value of -2, leading to a stronger scattering efficiency.

In Figs.5.17a and 5.17b, the line profiles recorded with different probes across lines AA' and line BB' are compared. Line AA' is relatively far from the defect and represents mainly the evanescent field from the waveguide. The intensity profile recorded with a glass tip has to be amplified 25 times in order to match the intensity level of the Ga tip. The Signal to Noise Ratio (SNR) can be used for comparison between two probes. It is defined as the ratio of the signal mean to the background noise standard deviation. The SNR for the Ga tip at the brightest point of line AA' is more than 250, while for a glass tip SNR is less than 10. When the probes are scanning across the defect, the SNRs are around 24000 and 600, respectively.

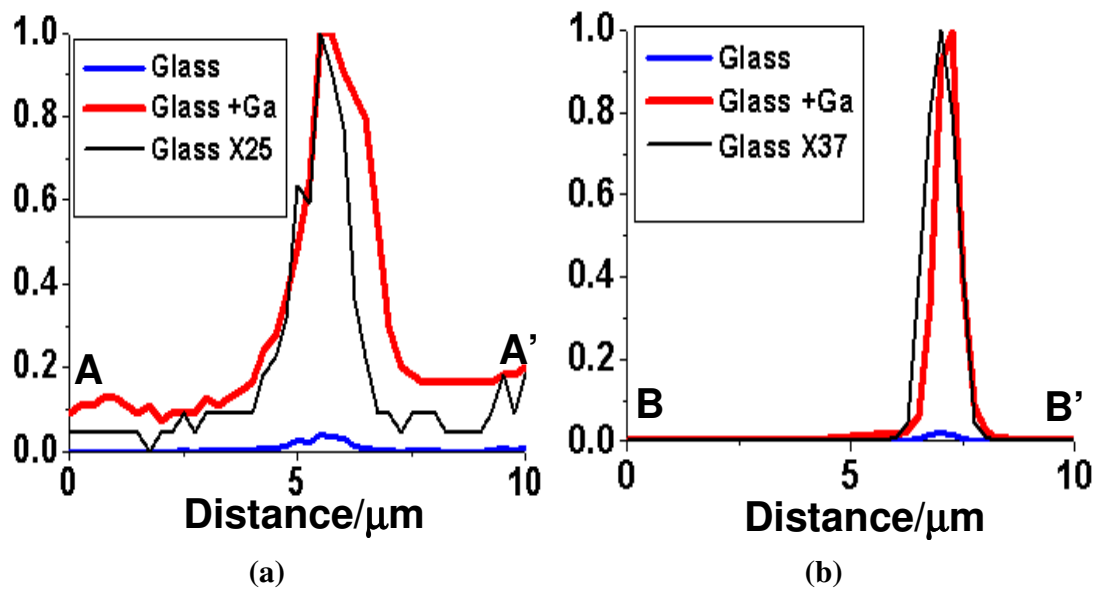


**Figure 5.17:** Line profiles of the waveguide across with different tips: a) line AA' shown in Fig.5.16a; b) line BB' shown in Fig.5.16b. For the simple glass tip the amplified line profiles are also presented for comparison [147].

It can be noticed that the FWHM of the intensity profile depends on both the location of the scan and on the probe. When the waveguide is scanned, the FWHM recorded with the

simple glass tip is smaller than that for the Ga-SDP (Fig.5.17a), while for the defect site the opposite is observed (Fig.5.17b). The size of the waveguide core is approximately 3  $\mu\text{m}$ . The apparent “better” resolving power of the simple glass tip is just determined by the poor detection efficiency of the probe. This probe can detect only the signal from the center of the waveguide. On the contrary, Ga-SDP is more efficient and it allows recovering the actual intensity profile of the waveguide. When detection efficiency is not a limiting factor, as in the case of the defect (Fig.5.17b), the better resolving power of the Ga-enhanced probe becomes clear.

In spite of the improvement of the detection efficiency of imaging using Ga-SDP, it is worth noting that the images presented in Fig.5.16 are made with fresh probes. The consecutive scan showed a gradually decreasing maximum intensity within the images for both probes. The reason to this degradation is a considerable build-up of dust at the tip and on the body of the probe, as shown in Fig.5.18. Ga-SDP is made of silica, which easily attracts dust particles from the surroundings and sample surface due to electrostatic forces. The dust particles will affect the quantity  $h$  from Eqn.4.1 and also will cause the collected light to leak from the taper of the probe. All these effects deteriorate the detection efficiency.



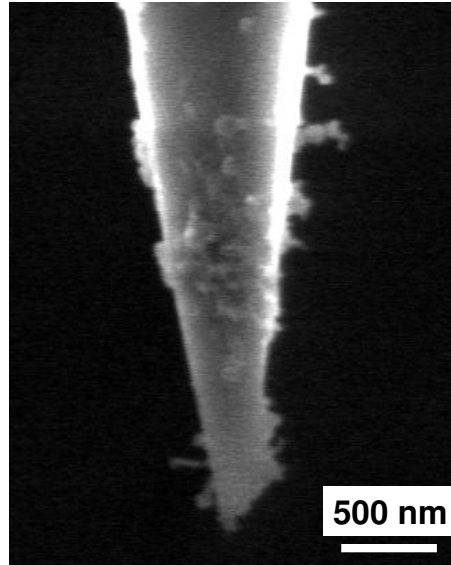


**Figure 5.18:** Dust build up on SDP-Ga probe after SNPEM measurements.

## Summary

In this chapter, I proposed a novel concept of a scattering dielectric probe with an embedded metallic nanoparticle was proposed. The concept is implemented through a Ga implantation into the nanometric tip of the tapered glass fiber using FIB. The optical properties of Ga and the embedment of the metal inside the dielectric, enhances the scattering efficiency of the dielectric tip. Such a design also avoids the limitations faced by metallic probes or probes based on metallic nanoparticles attached to the dielectric tips. In order to achieve the desired design I proposed a unique fabrication method. The method also creates a taper structure, which is beneficial in terms of the capture fraction for the light scattered at the tip. The simplicity and repeatability of the method suggest that it can be scaled up for mass production. The critical challenge of dust build-up on the probe is identified to be a limiting factor for repeatable imaging with Ga-SDP.

## **Chapter 6**

### **Photon emission detection with Ga-SDP**

This Chapter demonstrates the results of a Ga-SDP application in SNPEM analysis. The advantages of Ga-SDP make it an attractive solution for the effective detection of photon emissions with a superior resolution and detection efficiency. By applying the Ga-SDP to the front-side analysis of a nanometric Fin Field Effect Transistor, a lateral resolution of 50 nm is demonstrated. Also, a detection efficiency capable of reversing currents as small as 2  $\mu\text{A}$  across the silicon p-n junction is achieved. The detected signal is strongly affected by the probe and sample properties as well as by the distance regulation accuracy. The impact of these parameters on the SNPEM performance is revealed in subsequent sections of this chapter. The possibilities and importance of NF spectroscopic measurements are demonstrated.

#### **6.1 Estimation of lateral resolution for Ga-SDP**

A novel concept of a Ga-SDP was introduced in Chapter 5 with the aim of achieving high resolution and high detection efficiency in the measurements of photon emission (PE) spots in biased semiconductor devices. In this chapter, the Ga-SDP is applied to a variety of semiconductor devices in order to evaluate its capabilities.

For a demonstration of the resolution capability of the SNPEM system with a Ga-SDP, a Fin Field Effect Transistor (FinFET) test structure [153] is investigated. The FinFET has a fin length of 10  $\mu\text{m}$  and width of 60 nm. Figure 6.1a shows the FFPEM image overlaid with the FF reflection image of the FinFET, indicating that the highest intensities of photon emission are localized at the drain metal contact.

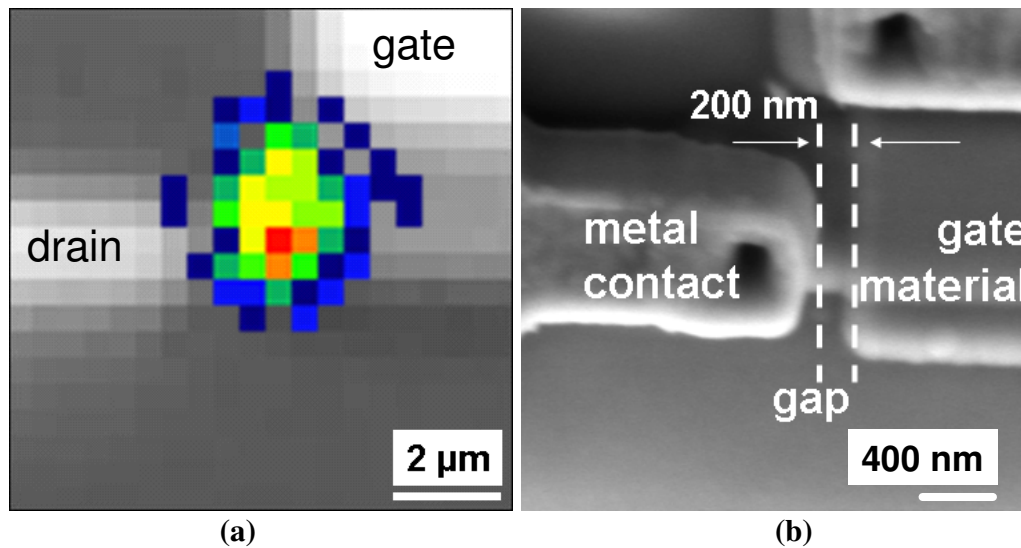


**Figure 6.1:** FinFET test structure: a) FFPEM image; b) SEM image of the drain metal contact area [137].

The image is recorded with a 100X objective lens having a numerical aperture of 0.55. The detector used for FFPEM imaging is a Si-CCD camera, sensitive from 400 nm to 1100 nm. The pixel size of the digitally magnified image is equal to approximately 500 nm. Smaller pixel sizes can be used but it will not improve the resolution, because the resolution of a FF system is always determined by the highest value between the pixel resolution and the optical resolution [13]. The later is limited by diffraction (Eqn.1.1). A SEM analysis of the drain region, shown in Fig.6.1b, reveals that there is a 200 nm-wide

gap between the drain metal contact and the gate material. This gap can serve as a window for guiding photons from the active area at the drain side of the transistor.

The topography images of the FinFET recorded with SNPEM system at two different magnifications are shown in Figs.6.2a(i) and 6.2a(ii).

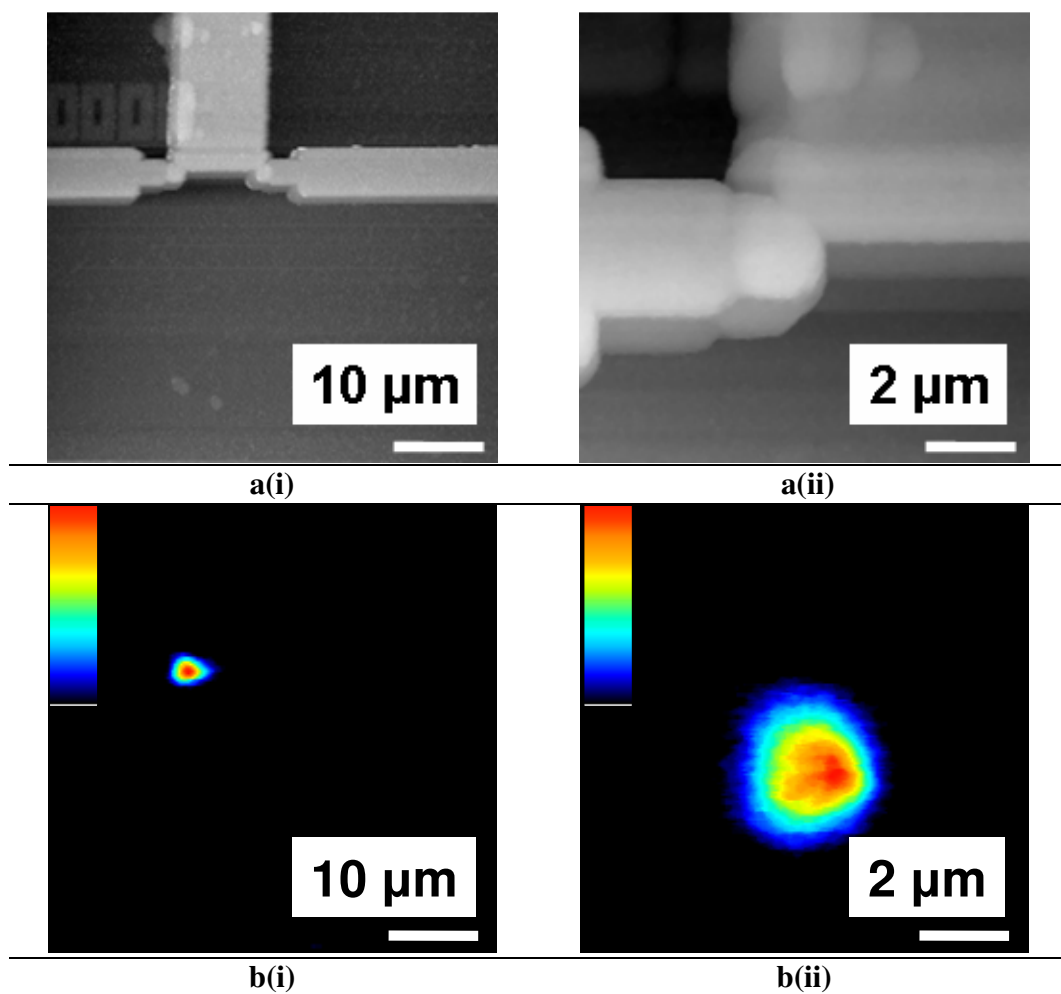


**Figure 6.2:** Images of the Fin-FET test structure at different magnifications: a) topography and b) SNPEM [137].

The corresponding PE distributions are shown in Figs. 6.2b (i) and 6.2b (ii). The detection is performed using Hamamatsu's NIR-PMT module that has its sensitivity in the wavelength range of 1000 nm to 1400 nm (see explanation for Fig.3.16).

The PE spot of approximately 2  $\mu\text{m}$  in diameter is evident in both images. Some of the emissions are recorded when the probe is placed on top of the metal contact. Under such conditions, every part of the probe is far enough from the emission source to prevent any NF interaction. Hence, the FF collection of PEs with the glass body of the probe strongly contributes to the recorded image in Fig.6.2b. The observed PE spot roughly correlates with the spot recorded by the FFPEM (Fig.6.1a).

In the background of this 2  $\mu\text{m}$  spot, high spatial frequencies in the PE distribution can be distinguished. They are expected to represent the interaction of the Ga-implanted tip with the NF of the emission source. In Fig.6.3, the region with the highest intensity is further magnified so that only an area of 1  $\mu\text{m}$  by 1  $\mu\text{m}$  is scanned by the probe. Imaging within such a small area means that we are looking at details much smaller than any wavelength detectable by the NIR-PMT module. The pixel size is just 5 nm, while the dwell time for each pixel is approximately 30 msec. On the left side of Fig.6.3b, it is easy to recognize the profile of the topographic image of the metal line, shown in Fig.6.3a. Hence, it is possible to use the optical image of the opaque metal for the estimation of the lateral resolution [102]. The resolution is estimated by the distance between the points with 10% and 90% of the total intensity.

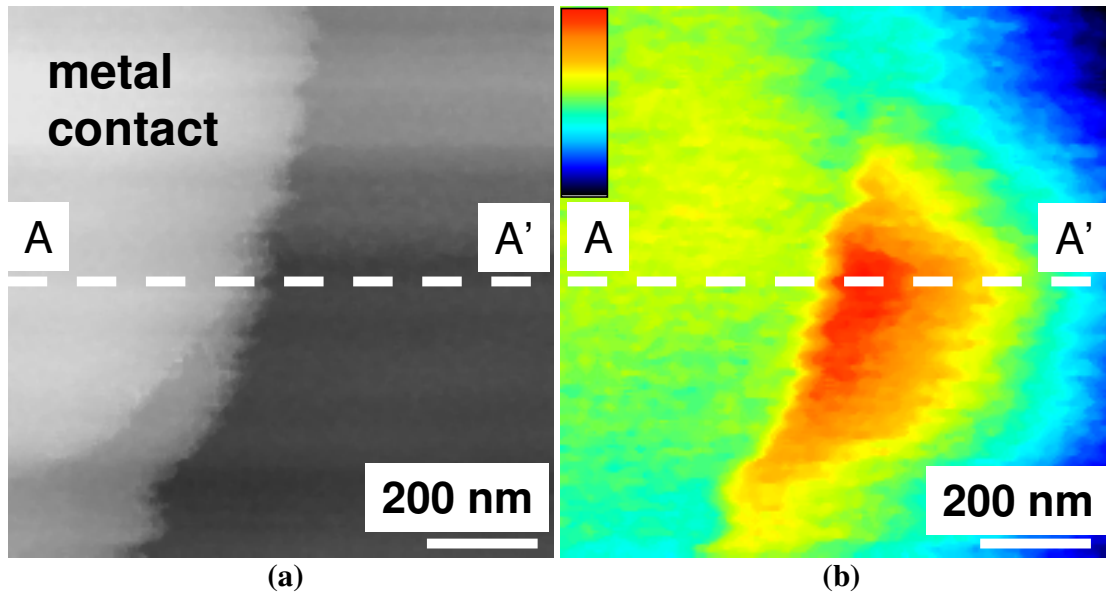


**Figure 6.3:** High magnification (a) topography and (b) SNPEM images of the PE spot in the location of highest intensities [137].

The line profiles (line AA') across the topography (Fig.6.3a) and the SNPEM images (Fig.6.3b) are shown in Fig.6.4.

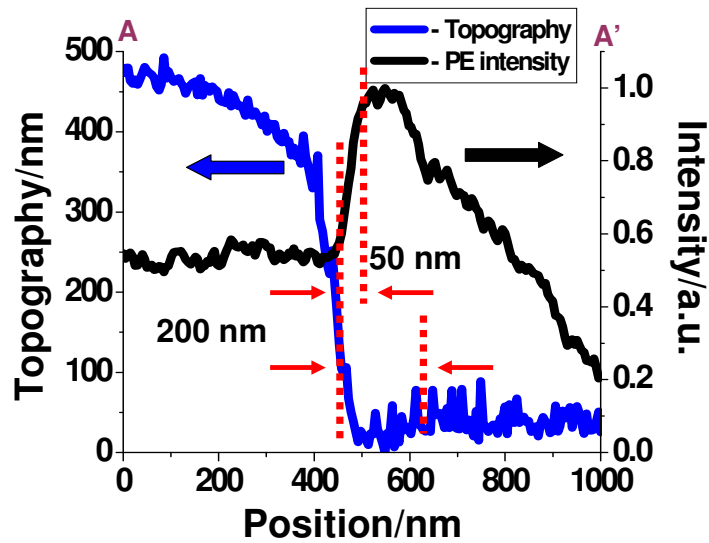


**Figure 6.4:** Topography and intensity profiles across AA' lines in Fig.6.3 [137].

A clear correspondence between the edge of the metal line and the point from where of the PE intensity begins to show a sharp increase is observed.

It is important to note here that the variation in height is not the major contributor to the contrast. One can see in the left part of the graph in Fig.6.4, that the primary reduction in the topography signal - from approximately 500 nm values down to 250 nm - does not affect the intensity value. This behavior indicates that the variation of intensity is determined primarily by the interaction of the tip with the emission source. The interaction starts taking place only when the tip passes the edge of the metal contact. Hence, in the proximity of the edge, the observed contrast is not a topographic artifact but the indication of the tip-emission source interaction.

The knife-edge criterion gives the resolution value of 50 nm (Fig.6.4) – which is at least 20 times smaller than any wavelength detectable by the NIR-PMT module. Of course, this value is affected by the exponential decrease of the NF interaction with the distance from the surface, as well as by the finite penetration (skin depth) of the radiation into the aluminum contact. Hence, it might not adequately represent the true optical resolution of the system. Nevertheless, this value can be used as an indicator of the spatial resolution because one should not forget that the highest signal will be detected only at those locations where there is an emission source.

In order to get a clearer understanding of the system capabilities in terms of the NF resolution, the region on the right side of the metal edge is considered. It is evident that

the highest 20% of the photon emission intensity, i.e. intensity above an 0.8 level, are confined within a 200 nm distance from the metal edge (Fig.6.4). This region should correspond to the gap between the metal contact and the gate material in Fig.6.1b. Following the discussion in sub-section 4.3.1, a probe with an opening angle of  $20^\circ$  – like the Ga-SDP shown in Fig.5.8d – should have minimal background caused by the interaction of the probe taper with the NF signal (Fig.4.3a-4.6a). Then the intensity profile in Fig.6.4 should mainly consist of two components: the signal scattered by the Ga enhanced tip in the NF of the emission source; and the FF signal collected by the body of the probe. As an approximation, the intensity profile on the right side of the metal edge is fitted with two Gaussian Curves representing the NF and FF interactions, respectively (Fig.6.5).

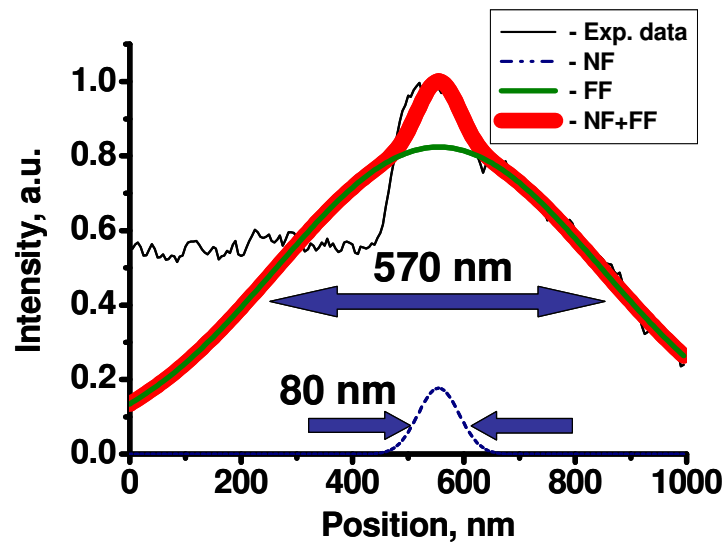


**Figure 6.5:** Curve fitting of the intensity profile in Fig.6.5 with two Gaussian curves corresponding to NF and FF interactions of the emission source and the probe [137].

For the curve fitting procedure, the following assumptions are made: i) the area of interest is from 500 nm to 1000 nm of the intensity profile as shown in Fig.6.4; ii) there is



only one emission source; and iii) the maxima of the two curves coincide. During the curve fitting process, the number of peaks and the position of their maxima are fixed, while amplitudes and FWHMs are varied. The fitted curve in Fig.6.5 is obtained within 20 iterations, using the data analysis software Origin 7.0. The resulting values of the FWHM for two curves are 80 nm and 570 nm respectively (Fig.6.5). The larger value of FWHM is approximately equal to half of the wavelength corresponding to the silicon bandgap energy ( $\lambda_{\text{Si}} = 1170 \text{ nm}$ ). This result shows that this curve represents the diffraction-limited image of the PE spot in the FF. The FWHM of 80 nm for the second curve is larger than the resolution value determined by the knife-edge criterion in Fig.6.4. However, in Fig.6.5, this value should be treated as the sum of the system NF optical resolution and the effective size of the emission source.

From the results of the curve fitting in Fig.6.5, it is possible to ignore PE intensities below a 0.8 level of the maximum intensity, because those photons are mainly attributed to the FF collection by the probe body. Using this assumption, it should be possible to extract the NF signal from the image in Fig.6.3b. With this purpose, the distribution of the highest 20% of PE intensities is overlaid with the topography image in Fig.6.3a, as shown in Fig.6.6. This SNPEM image clearly demonstrates a higher spatial resolution in comparison to the FFPEM image in Fig.6.1a and shows the exact location of the emission source with respect to the metal contact. Of course, the criterion of 20% is an approximation, which cannot be taken as a rule.

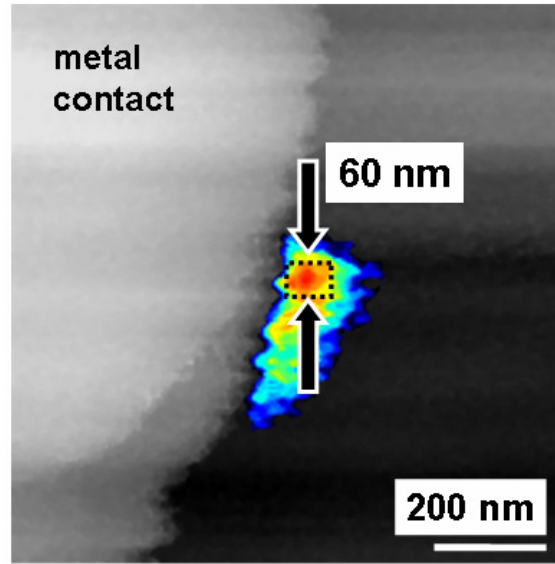


**Figure 6.6:** Localization of photon emission spot with 50 nm resolution. Highest 20% of PE intensities in Fig.7.4b is overlaid with the topography image in Fig.6.4a [137].

One can notice that the actual brightest area is contained within a region with dimensions of approximately 80 nm by 60 nm, as marked by a dotted square in Fig.6.6. The vertical dimension of this square actually corresponds to the designed FinFET width of 60 nm. The rest of the photons outside the dotted square are likely to represent the background due to the NF interaction with the probe body (Sphere T) considered in Figs. 4.3-4.6.

## 6.2 Sensitivity of SNPEM system

The sensitivity of the whole SNPEM is a complex function of multiple parameters, including the probe scattering efficiency; probe distance separation, collection efficiency of the probe taper, emission source efficiency, location of the emission source below the surface, geometry of the source, emission wavelength, and the sensitivity of the detector to the particular wavelength. In this thesis, the sensitivity of the SNPEM is evaluated in terms of its detection efficiency. The detection efficiency is determined by the minimum

current or minimum variation due to the leakage current that can be detected by the SNPEM system. The achieved result is benchmarked against those from aperture-based SNOM (a-SNOM) systems that were already tried for PE detection. Such benchmarking gives an estimate of the level of improvement that the Ga-SDP provides in comparison to the state of the art approach. As was highlighted in sub-section 2.2.1, the reported images using a-SNOM do not amply demonstrate the sub-wavelength resolution. At the same time, a-SNOM displayed a capability to detect emissions at drive currents only at several tens of mA from the laser diodes [36,51-57]. At such biasing conditions, the emission can be observed with the naked eye.

In semiconductor ICs, the generation of photons is a byproduct of their original purpose. They are, thus, not optimized for an efficient light generation. Hence, it is reasonable to conclude that the detection of emissions from silicon-based devices with uncoated probes at  $\mu\text{A}$  range, as demonstrated in Fig.4.9 and Fig.4.16, was already a substantial improvement in comparison to aperture-based probes. Another simple indicator of the detection efficiency during most of SNPEM measurements shown in this thesis can be provided. The applied biasing conditions generated emissions that were visible neither by the naked eyes nor by the in-built CCD camera of the system used for probe monitoring. The detection efficiency demonstrated in Fig.4.9 and Fig.4.16 was partly enhanced due to the use of the blunt tip (tip of large radius) as shown in Fig.4.7. Such large tips enhance the scattering efficiency according to Eqn.2.4. At the same time, they degrade the resolution capability due to a large scattering volume. However, for SNPEM, it is

desirable to achieve a higher scattering efficiency without a compromise in the resolution. And that is why a Ga-SDP was introduced in Chapter 5.

### 6.2.1 Detection efficiency of the Ga-SDP for an SNPEM application

For a demonstration of the detection efficiency capabilities, a leaking silicon p-n junction is imaged at different biasing conditions. The junction is biased with a square wave at a frequency of 800 Hz and the signal from the photon sensitive detector is amplified using the lock-in technique. The lock-in technique is adopted in order to improve the Signal-to-Noise Ratio (SNR) of the SNPEM imaging. The SNR is defined as the ratio of the signal mean to the background noise standard deviation. The oscillation frequency is chosen arbitrarily. The amplitude is chosen to be 1 V while the offset voltage is varied.

In Fig.6.7, the magnified area of the leaking site of the junction is recorded at different biasing conditions with a step for offset voltage of 20mV. The images in Fig.6.7 are detected using visible a PMT (Fig.4.13) and are indicative of the hot carrier emissions (see Appendix A). The size of the emission spot is relatively large due to the sub-surface location of the actual emission source (see discussion for Fig.4.6). The shift in the image is caused by the hysteresis in the scanner stage or sample drift. These effects prevent the probe from returning to the same location for different scans. However, it is not critical for the SNPEM imaging as long as the topographic features can be used for reference.

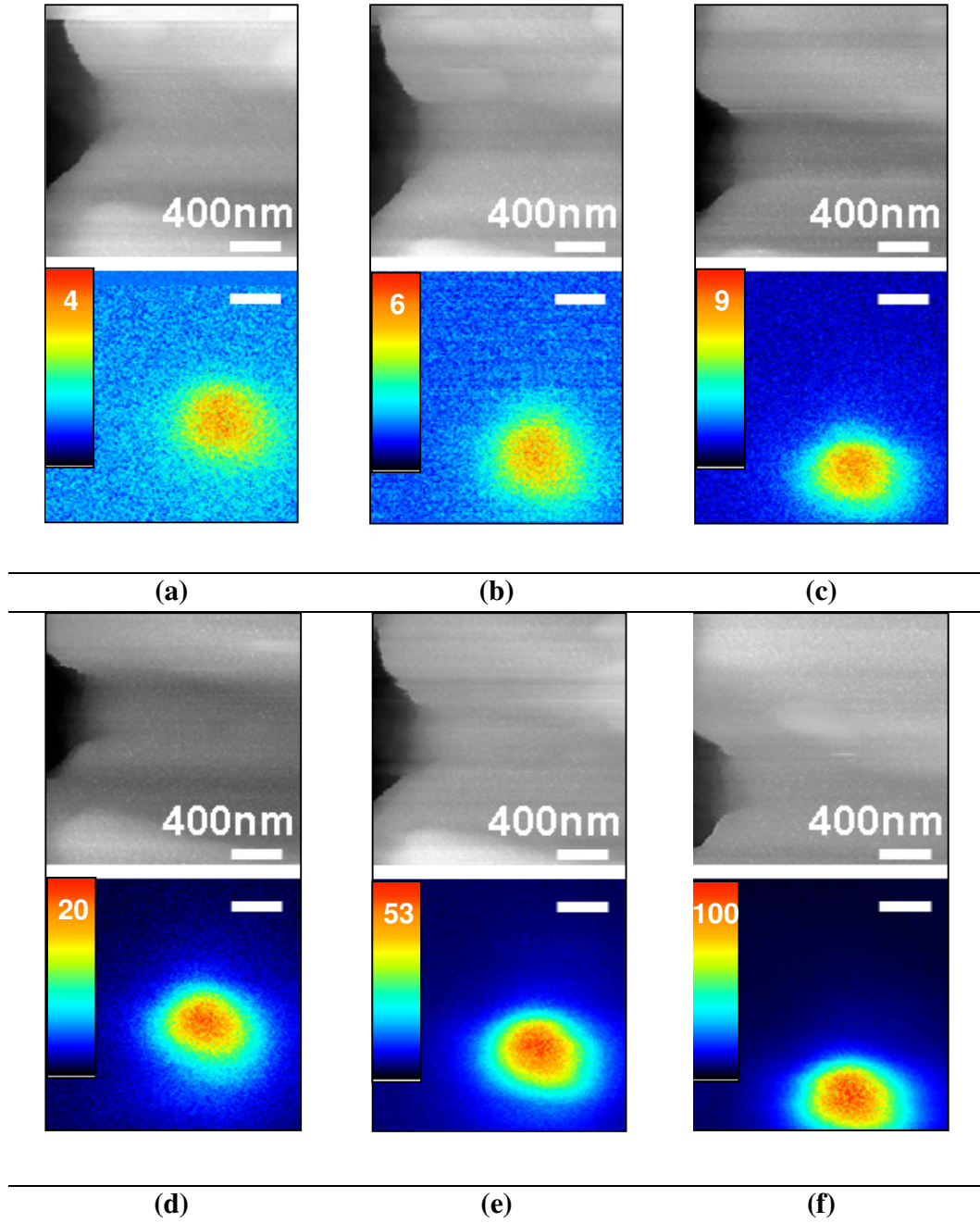


**Figure 6.7:** Visible emission distribution in the NF of the sample surface at different reverse bias of the p-n junction: a) 5.50V, 1.6 $\mu$ A; b) 5.52V, 2.3  $\mu$ A; c) 5.54V, 7.5 $\mu$ A; d) 5.56V, 27 $\mu$ A; e) 5.58V, 60 $\mu$ A; f) 5.60V, 100 $\mu$ A.

The color gradation for all images is stretched to maximize the visibility and demonstrate the SNR. For each image, the SNR is indicated at the color bar. The noise value is mainly governed by the signal amplification circuit and, for the same amplification parameters, this value is constant. Hence, a change in the SNR represents the signal evolution due to a variation in the biasing conditions. For a clearer representation, all the SNRs are normalized to the maximum value in Fig.6.7f and later multiplied by 100. The lowest detected leakage current is just 1.6  $\mu\text{A}$ , as shown in Fig.6.7a. At the same time the lowest variation of current is below 1  $\mu\text{A}$ . This result shows that the capabilities of the SNPEM equipped with a Ga-SDP satisfy the second goal of this thesis as stated in Section 1.4.

Similar types of measurements are performed in the NIR spectral range, as shown in Fig.6.8. The measurements are shown starting with the biasing voltage of 5.58V, which corresponds to the biasing current of approximately 60  $\mu\text{A}$ . However, the actual measurements were extended down to a voltage of 5.52 V, corresponding to the current of approximately 3  $\mu\text{A}$ . The lower values are not shown in Fig.6.8 due to much stronger distortions in the images that can already be observed in the presented images. This distortion can be attributed to the probe quality or to the presence of dust particles attached at the tip, as was observed in Fig.5.18. The presence of loosely attached dust particles is likely to introduce substantial variations in the distance regulation. In spite of the distortion in Fig.6.8, it is still possible to conclude that the emission spot is elongated in a certain direction, while in Fig.6.7 it had a circular shape. The elongation effect can be attributed to the different physical mechanism of photon emission in the NIR spectral range.

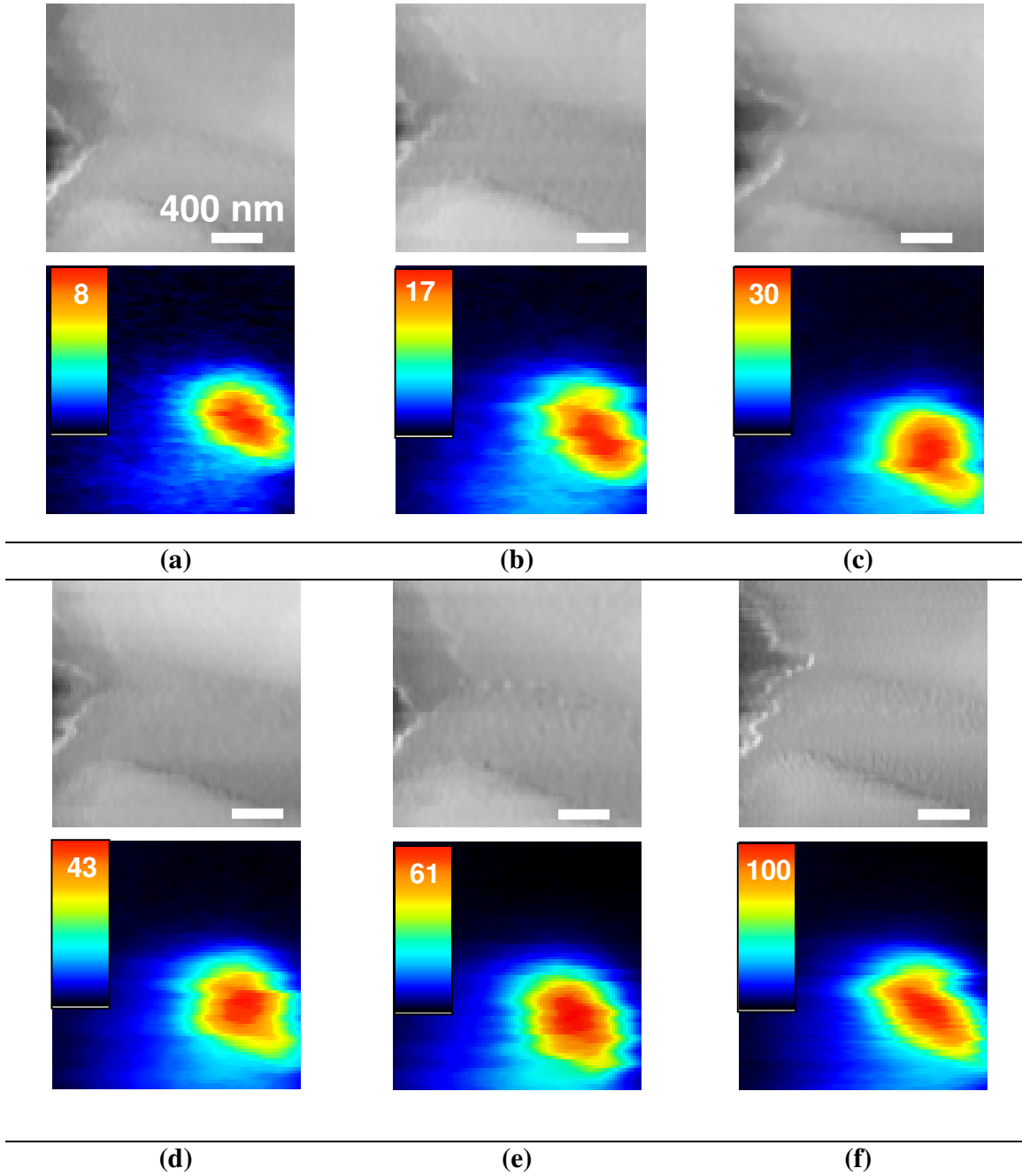


**Figure 6.8:** NIR emission distribution in the NF of the sample surface at different reverse bias of the p-n junction: a) 5.58, 60 $\mu$ A; b) 5.62V, 123  $\mu$ A; c) 5.66V, 186 $\mu$ A; d) 5.68V, 218 $\mu$ A; e) 5.72V, 281 $\mu$ A; f) 5.76V, 345 $\mu$ A.

In order to identify the possible mechanism, Fig.6.9 compares the I-V characteristic of the p-n junction with the SNR, which is plotted as a function of the maximum voltage, supplied to the junction during the oscillation period (offset + amplitude).

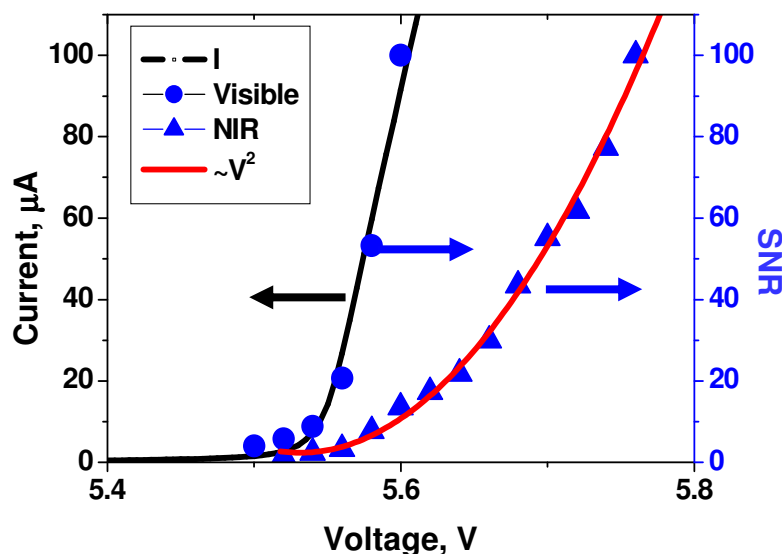


**Figure 6.9:** Comparison of I-V characteristic of the p-n junction at a reversed bias with SNR dependence on supplied voltage in Visible and NIR spectral ranges. The dependence of NIR signal is fitted with a parabolic function.

For the visible spectral range, the SNR approximately follows the value of the current (Fig.6.9). In Fig.6.10, the SNR is plotted versus the value of the current deduced from the I-V characteristic in Fig.6.9. The linear dependence between the SNR and the reverse current can be observed in Fig.6.10. This result is similar to observations in literature (See Appendix A) and confirms the direct carrier involvement in the emission process.



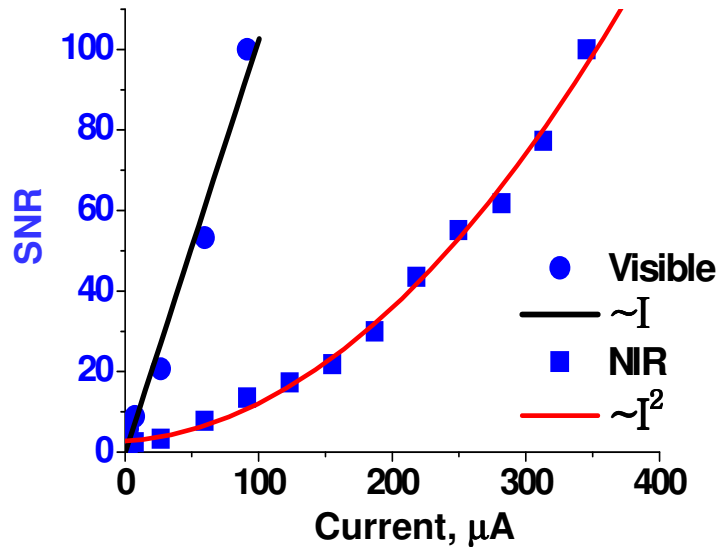


**Figure 6.10:** Comparison of SNR dependences on supplied current in Visible and NIR spectral ranges. The corresponding fitting functions for both spectral ranges are provided.

Surprisingly, for the NIR spectral range, the dependence on the supplied voltage is quadratic, as shown in Fig.6.9, and it is similarly quadratic for the current values, as shown in Fig.6.10. This dependence shows that the emission is proportional to the power dissipated in the device, as would be expected for a conductor subjected to Joule heating [180]. This heating can occur when a high resistive path is subjected to the conduction of substantial current densities [165]. The observed defect is the reason behind such a high resistive path. This result indicates that the PE in the NIR spectral range is determined by heat generation within the defect. Hence, the elongation noticed in Fig.6.8 represents the image of the actual length of the defect heated by the current. This result also demonstrates the power of wavelength-selective SNPEM imaging for identifying the different PE mechanisms in semiconductor devices. Such a capability can help resolve the arguments about PE mechanisms, which are highlighted in Appendix A.

### 6.3 Impact of the detection condition on SNPEM analysis

This Section analyses the impact of two important detection conditions determining the SNPEM performance. The first condition is the location of the emission source below the surface. The second condition is the distance between the probe and the sample surface. These two conditions practically represent values **d** and **h** in left side of Eqn.3.1.

#### 6.3.1 Impact of emission source location below the surface

In sub-section 4.3.3, it was shown that there is a clear limitation to the SNPEM application for a front-side analysis due to the presence of the metal line. Metal contacts either prevent the probe from reaching the emission source or partly block the source from observation. In order to remove the impact of the metal lines, a back-side analysis is preferred. However, as it was discussed in Section 3.4, it is likely that for back-side analysis the emission source can be several hundred nanometers below the surface (quantity **d** in Eqn.3.1). The importance of **d** is demonstrated using the same leaking p-n junction, which was investigated in Fig.4.9. However, this junction originally had a passivation layer, as schematically shown in Fig.6.11, with a thickness of approximately ~1.5  $\mu\text{m}$ . It is clear from Eqn.3.1 that such a layer will negate any impact of the NF detection and thus, both the resolution and detection efficiency of SNPEM will degrade. In order to overcome this problem, the passivation is removed using buffered hydrofluoric acid (HF).

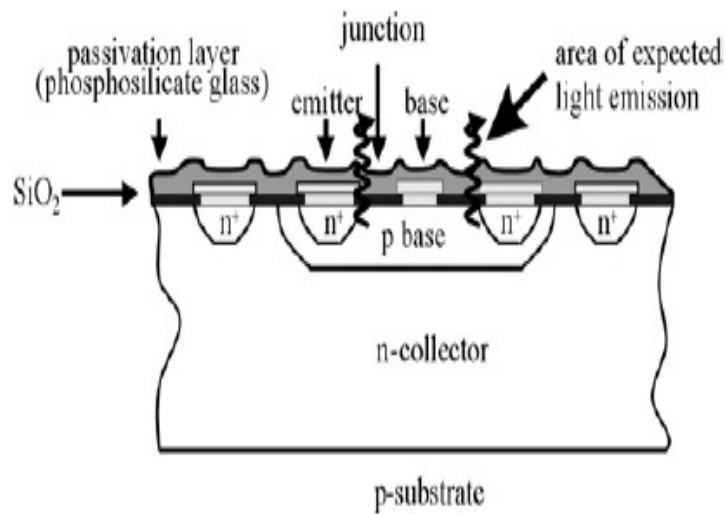


**Figure 6.11:** Schematic representation of the base-emitter junction [57].

In Fig.6.12a, an optical image of the passivated junction is shown; while Fig.6.12b shows the same junction after the passivation is removed.

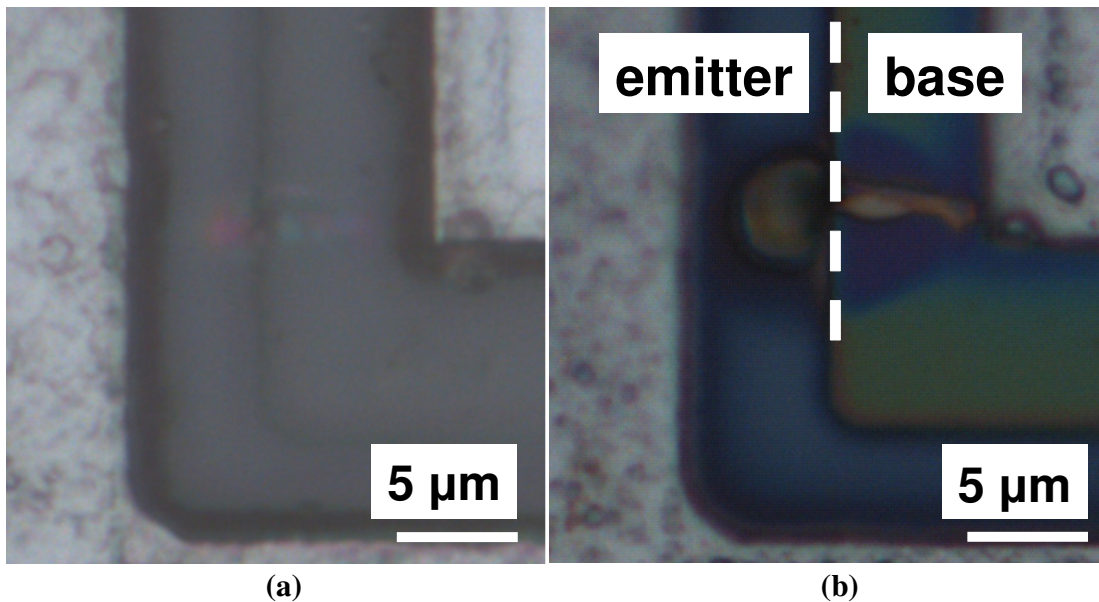


**Figure 6.12:** A reflection image of the leakage area of the p-n junction a) before and b) after passivation is removed.

Considerable structural damage to the junction is evident at the location corresponding to the leakage emission spot, detected in Fig.4.9. A defect in the same location of a similar device was previously introduced by Electrostatic Discharge (ESD) stressing [154]. The ESD is known to cause crystalline defects in semiconductor devices, like dislocations [155]. Hence, the detected spot is likely to indicate a defect of the same origin. It is important to note that the removal of the passivation did not affect the I-V characteristic of the junction.

In Fig.6.13a, the p-n junction is imaged with FFPEM at a reversed bias, while in Fig.6.13b the junction is imaged at a forward bias.

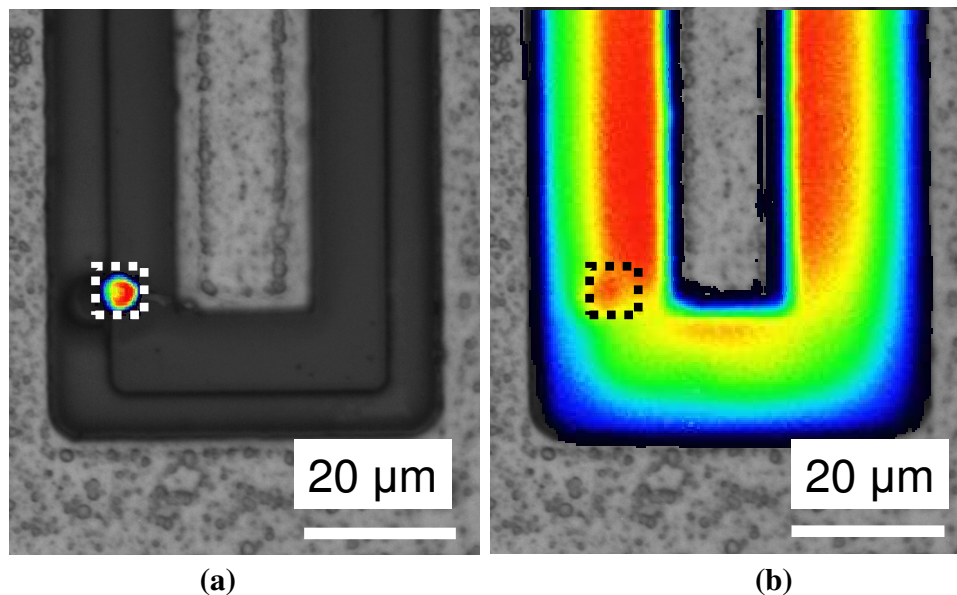


**Figure 6.13:** FFPEM images of the p-n junction at a) reverse and b) forward bias.

In the case of the reversed biased junction, the PE is determined by the presence of a high electric field in the depletion region. In the presence of the dislocation across the junction, a current crowding occurs through the leakage path (Appendix A). Hence, the PE

generation will also be confined to this leakage path. This explains why the emission is localized at one spot in Fig.6.13a.

For the forward bias, the PE distribution is reasonably uniform within the diffusion length from the junction (Fig.6.13b). This distribution is governed by the recombination of opposite carriers. These carriers have to travel a considerable distance before they recombine, which manifest in a large area of emission. The spectral distribution of the emitted photons is concentrated at the silicon band-gap peak (Appendix A). This peak is within the spectral range of the Si-CCD and thus, the distribution of the corresponding photon can be detected.

The topography and SNPEM images of the areas inside the dotted squares in Fig.6.13 are recorded using the NIR-PMT module and shown in Fig.6.14. The recorded distributions generally coincide with the FF images in Fig.6.13, for both the forward and reverse biasing conditions. In chapter 5, this junction was not imaged at the forward bias condition because the visible PMT used for SNPEM measurements was insensitive above 900 nm (Fig.4.13). Using the NIR-PMT module sensitive to photons above 1000 nm (Fig.4.16), it is possible to image the leakage site not only in a reversed bias (Fig.6.14b) but also at a forward bias (Fig.6.14d).

Using the feature on the left side of the topography images in Fig.6.14 as a reference, it is possible to conclude that emissions at the forward and reversed biasing conditions are taking place at different locations that do not overlap. Such a conclusion could hardly be

done using the FFPEM images in Fig.6.13. This conclusion also means that the path for the reversed current is not taking part in the forward current conduction and vice versa.

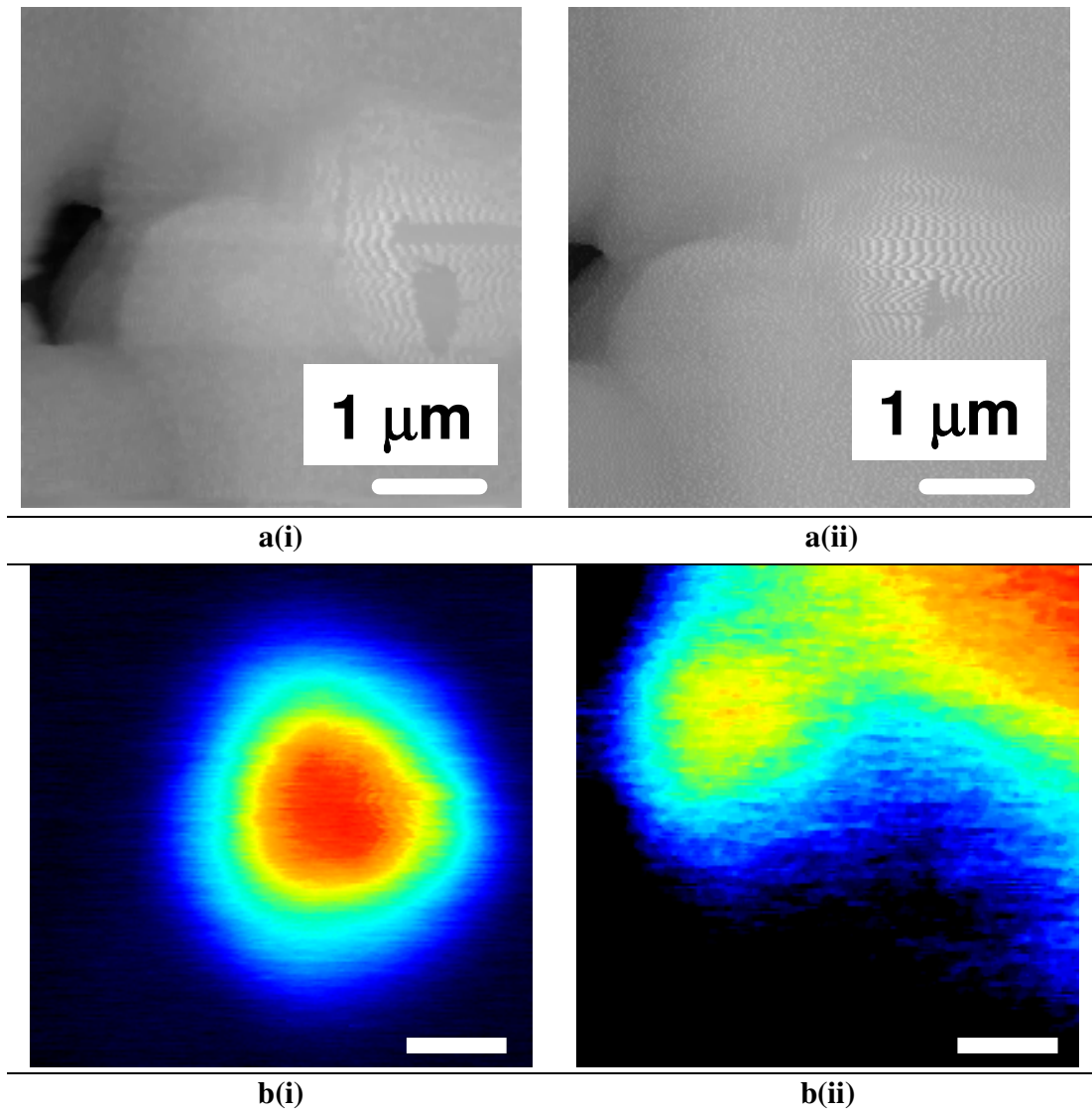


**Figure 6.14:** a) Topography and b ) SNPEM images of a leaking p-n junction at reverse and forward biasing conditions: i) -5.56V, -50μA; ii) 0.89V, 9 mA.

The reason for this behavior can be explained by a simplified representation shown in Fig.6.15. When the defective junction is biased in the forward direction, the depletion

region is reduced and the defect is more resistant than the junction area. However, at the reversed bias condition, the increased depletion region prevents any current from passing through the junction, while the defect becomes the path with a lower resistance and the preferential site for the junction leakage. Dislocations are commonly linked to this phenomenon (Appendix A).

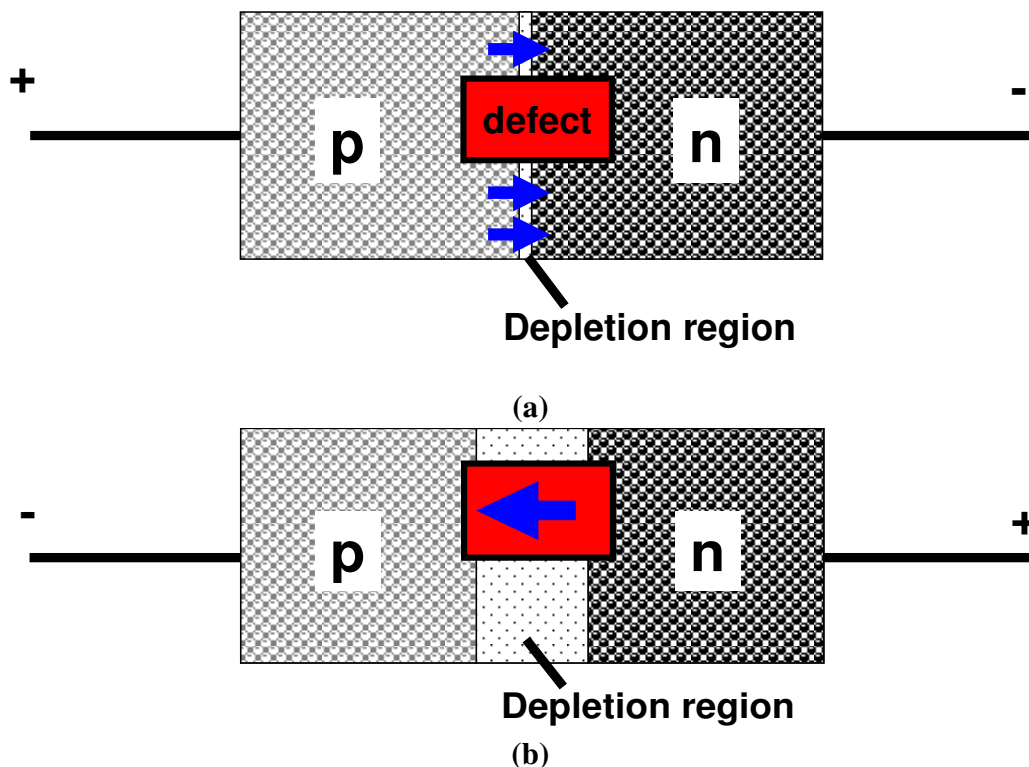


**Figure 6.15:** Difference in current paths (indicated by arrows) for a) forward and b) reverse biased junction with defect.

In Fig.6.14, a much clearer picture of the current distribution in the junction was provided in comparison to the FF imaging shown in Fig.6.13. However, the SNPEM technique cannot demonstrate superior resolution capabilities on this sample. The reason for this is the remaining SiO<sub>2</sub> layer above the junction, as well as the relatively deep location of the junction in such devices, as indicated in Fig.6.11.

Such a conclusion brings us to the main focus of this section: which is the analysis of the impact of the quantity **d** from Eqn.3.1. Such an analysis became possible due to the degradation of the junction surface at the emission spot location after several hours of imaging at a reversed biasing condition. The progress in SiO<sub>2</sub> degradation is shown in Fig.6.16. The temperatures inside the p-n junction are not expected to be above the melting points of both Si and SiO<sub>2</sub>. However, elevated temperatures at the leakage site could affect the interface between these two materials. In the situation of a weakened interface, a possible cause of the material removal could be the numerous SNPEM scans. The exact process of removal can be explained in the following way. The shear-force mechanism based on a quartz tuning fork should ensure the non-contact mode of operation. However, this mechanism did not perform satisfactory for all the probes. As was discussed in Section 3.3.2, even for good probes, the mechanism performance could deteriorate with time. This deterioration led to a direct contact between the probe and the sample. In this case, the glass tip will be scrubbing the surface and can potentially remove the weakened material.

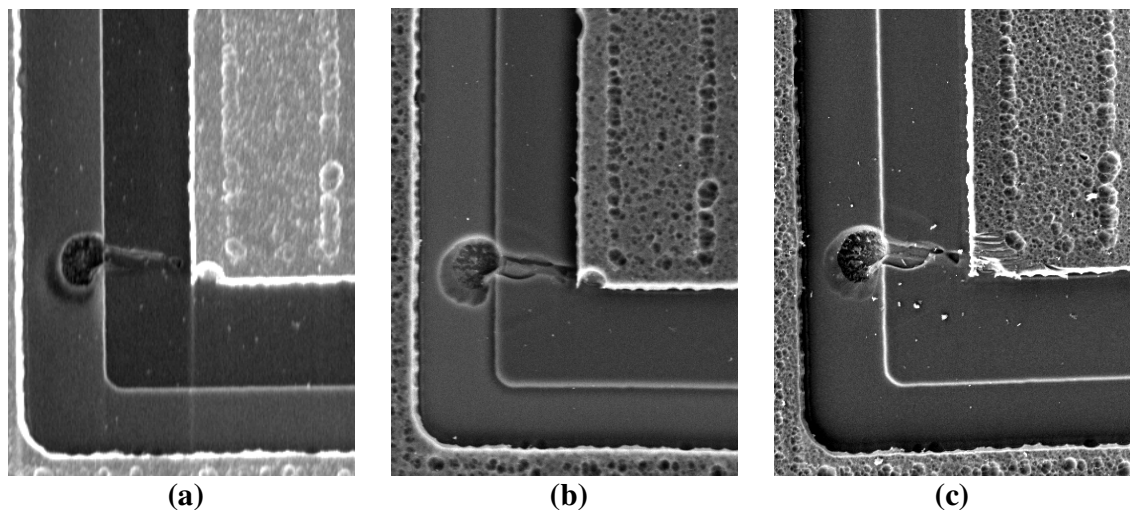


**Figure 6.16:** Degradation of the oxide layer on top of the leakage site of the junction.



In Fig.6.17 the topography of the damaged area and the emission spot detected with the NIR-PMT are shown. The images are recorded at the degradation state of SiO<sub>2</sub> layer shown in Fig.6.16c.

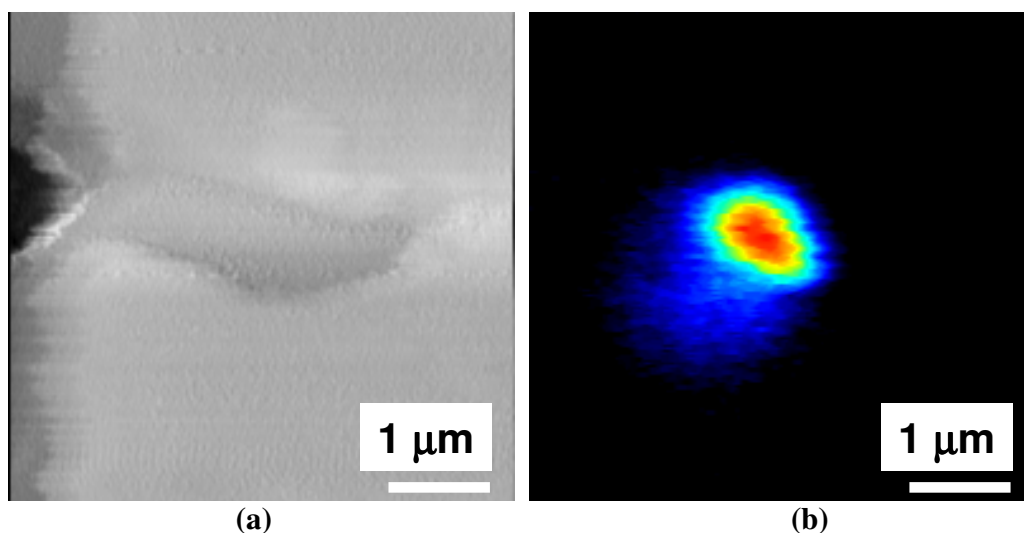


**Figure 6.17:** a) Topography and b) NIR SNPEM images of reverse biased p-n junction with locally removed SiO<sub>2</sub> layer.

From the topography profile (demonstrated later in Fig.6.21a), the thickness of the removed SiO<sub>2</sub> layer is estimated to be approximately 100 nm. The emission spot in Fig.6.17b is smaller than the emission spot detected from the same sample just after the passivation removal (Fig.6.14b (i) ).

In Fig.6.18, the emission profiles from Fig.6.14b (i) and Fig.6.17b are compared. The former has a FWHM of 2 μm, while the later has a FWHM of 0.8 μm. This proves that the resultant curve from Fig.6.17b with a smaller FWHM is reasonable because the SNPEM probe is placed closer to the emission spot.

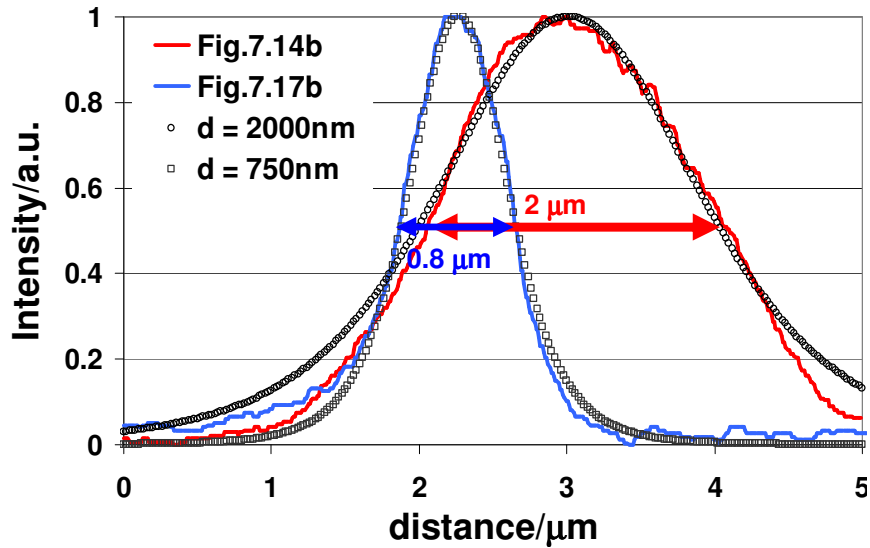


**Figure 6.18:** Variation of the intensity profiles of the emission spot recorded at different  $d$ .

In sub-section 4.3.1, it was already discussed that the impact of the emission source location can be approximated by inserting the value of  $\mathbf{a_s} \neq \mathbf{0}$  in Eqn.2.10. In this case  $\mathbf{a_s}$  corresponds to the distance between the source and the sample surface or  $\mathbf{d}$  in Eqn.3.1. Hence, using Eqn.2.10, it is possible to fit the curves in Fig.6.18 and deduce the value of  $\mathbf{d}$ . The value of  $\mathbf{d} = 750$  nm used for fitting the curve, as observed from Fig.6.17b, is an expected result because this p-n junction is based on old technology with deep junction profiles. Two other parameters in Eqn.3.1 ( $\mathbf{a}$  and  $\mathbf{h}$ ) are still much smaller than the wavelength and thus, the resolving capabilities of SNPEM should be determined mainly by the value of  $\mathbf{d}$ . The value of 2000 nm recovered from Fig.6.14b(i) is more surprising on closer examination.. The thickness of the removed  $\text{SiO}_2$  layer is approximately 100 nm and thus, the value of  $\mathbf{d}$  should be closer to 900 nm. The observed discrepancy can be understood by taking into account the refraction at the Si-SiO<sub>2</sub> interface, as shown in Fig.6.19.

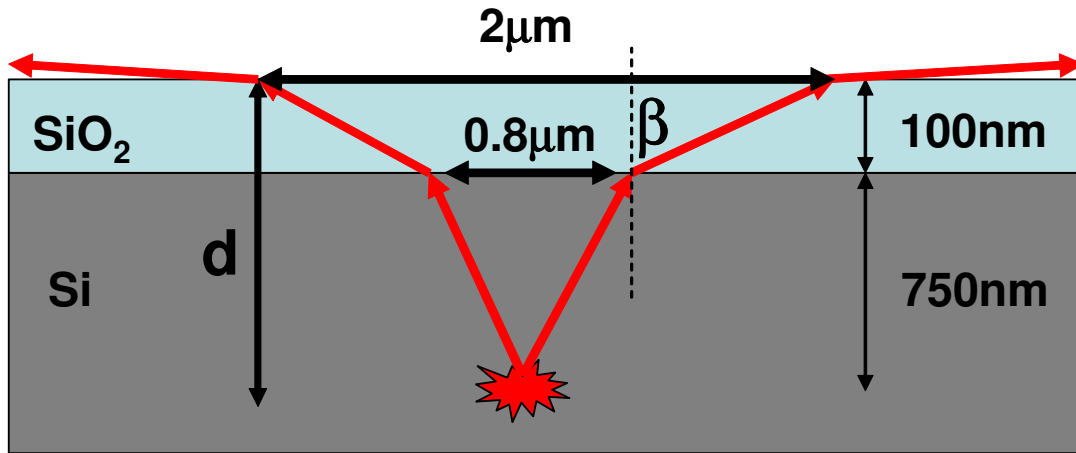


**Figure 6.19:** Expansion of the emission spot due to the refraction at Si-SiO<sub>2</sub> interface.

The refractive index of Si is more than two times larger than that for SiO<sub>2</sub>. From Snell's Law (Eqn.1.2), it is easy to find that the refracted light travels at a higher angle  $\beta$  from the interface normal and thus, expands the emission spot image at the SiO<sub>2</sub>-air interface even within a distance of 100nm. This result is important from the point of the back-side analysis of SOI structures considered in Fig.3.11. It is clear that such a multilayer structure will unavoidably expand the emission spot even for thicknesses as small as 100 nm.

In spite of this issue, these results show that the SNPEM can provide an opportunity to deduce the location of the point emission source below the surface in all three dimensions. The deduction is possible if the sample structure is known. This is usually the case because the thickness of the layers is fixed for every technology. The lateral position is determined by the location of the emission spot maximum, while the depth is determined by the observed FWHM of the emission spot.

### 6.3.2 Impact of probe positioning above the surface

In this section, the impact of the quantity  $h$  from Eqn.3.1 is considered. For this purpose, the same leaking p-n junction is imaged in the following fashion. After the location of the damaged region (Fig.6.16) using the topography image shown in Fig.6.20a, a set of SNPEM images are recorded at different distances  $h$  from the sample surface (Fig.6.20 b-g). The SNPEM in Fig.6.20g is recorded in a regular fashion with a TF-based distance regulation. The images away from the sample surface are recorded when the distance regulation is switched off. The value of  $h$  is changed from 4  $\mu\text{m}$  down to 500 nm using the step motor of the z-positioning stage (Fig.3.2b). The exact value of  $h$  is determined each time before running the scan by using the approach curve (Fig.3.5). Scanning without regulation is not performed below 500 nm due to the danger of crashing the probe into the sample with such a complicated topography.

From Fig.6.20, it is clear that the quality of the collected information improves drastically in the NF showing the exact location of the emission source. The numbers at the color bars in Fig.6.20b-g indicate the highest intensities within the images normalized to the highest value in Fig.6.20b. It is observed that, when the probe scans at distances above 500 nm (Fig.6.20b-f), the value of the maximum intensity within the image is increasing gradually with a decreasing  $h$ . This kind of behavior can be explained by the change of the numerical aperture of the collecting probe placed in the FF ( $h > \lambda/2$ ) from the sample.

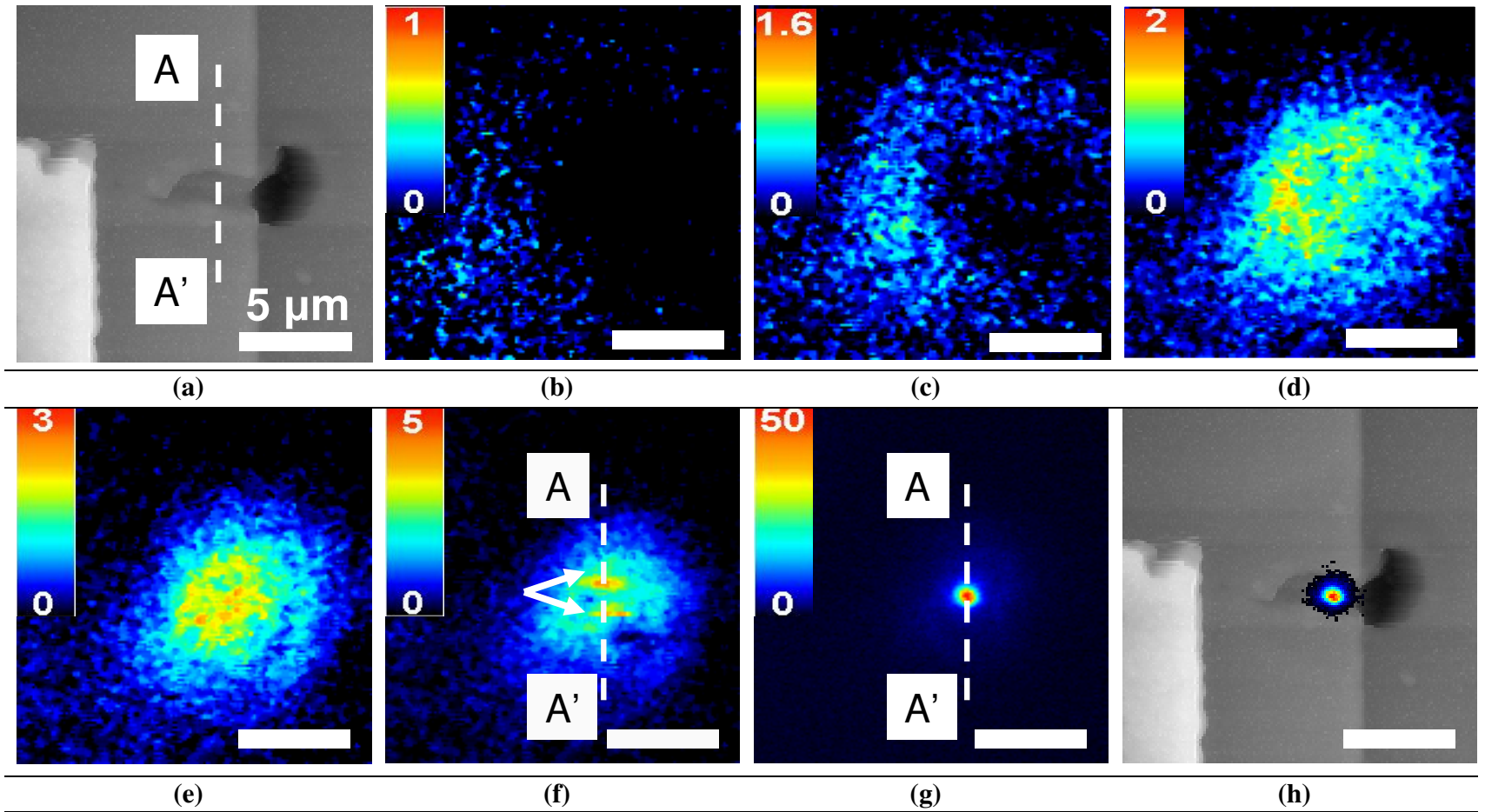


**Figure 6.20:** Images of the leakage site in the silicon p-n junction acquired with SDP-Ga at different distances  $h$  from the sample surface: a) topography; b)  $h = 4 \mu\text{m}$ ; c)  $h = 2.6 \mu\text{m}$ ; d)  $h = 1.5 \mu\text{m}$ ; e)  $h = 1 \mu\text{m}$ ; f)  $h = 0.5 \mu\text{m}$ ; g)  $h \approx 10 \text{ nm}$ ; h) image g) overlaid on image a).

The results observed in Fig. 6.20 are similar to the collection efficiency of the microlens which does not have any scattering center at the end of the probe. An increase of just 30% in signal intensity was reported when the microlens with a  $90^\circ$  cone angle approached the sample from a distance of  $4\text{ }\mu\text{m}$  to the NF distances below  $100\text{ nm}$  [124]. However, in the case of the Ga-SDP, the intensity increases by at least one order of magnitude when the probe is brought from the FF (Fig.6.20f) into the NF (Fig.6.20g) condition with the sample surface. This result is indicative that the scattering of the NF is the dominant contributor to the intensity and also confirms the importance of the Ga implantation for the performance of the Ga-SDP. It is important to note that the enhancement factor of 50, as shown in Fig.6.20g, is calculated from the comparison of the intensity values corresponding to pixels with the maximum intensity anywhere in the image. If one confines the analysis only to pixels within the area of the emission spot, the enhancement factor will reach even higher values.

Another interesting observation from this experiment is the presence of two bright horizontal lines recorded at  $500\text{ nm}$  distance from the sample surface (marked with arrows in Fig.6.20f). In Fig.6.21, the profiles across lines AA' in the topography (Fig.6.20a); the SNPEM image at a  $500\text{ nm}$  distance (Fig.6.20f); and the SNPEM image in the NF of the emission source (Fig.6.20g) are compared. It is clear that the two peaks in Fig.6.21b correspond to the edges in the topography profile shown in Fig.6.21a. This phenomenon can be explained by the enhancement of the light at the sharp edges of the sample seen in Fig.6.16c. Nevertheless, even such an enhancement makes only a small

contributes to the background in the NF image (Fig.6.21c). A direct NF interaction of the probe tip enhanced with Ga is still the strongest contributor.

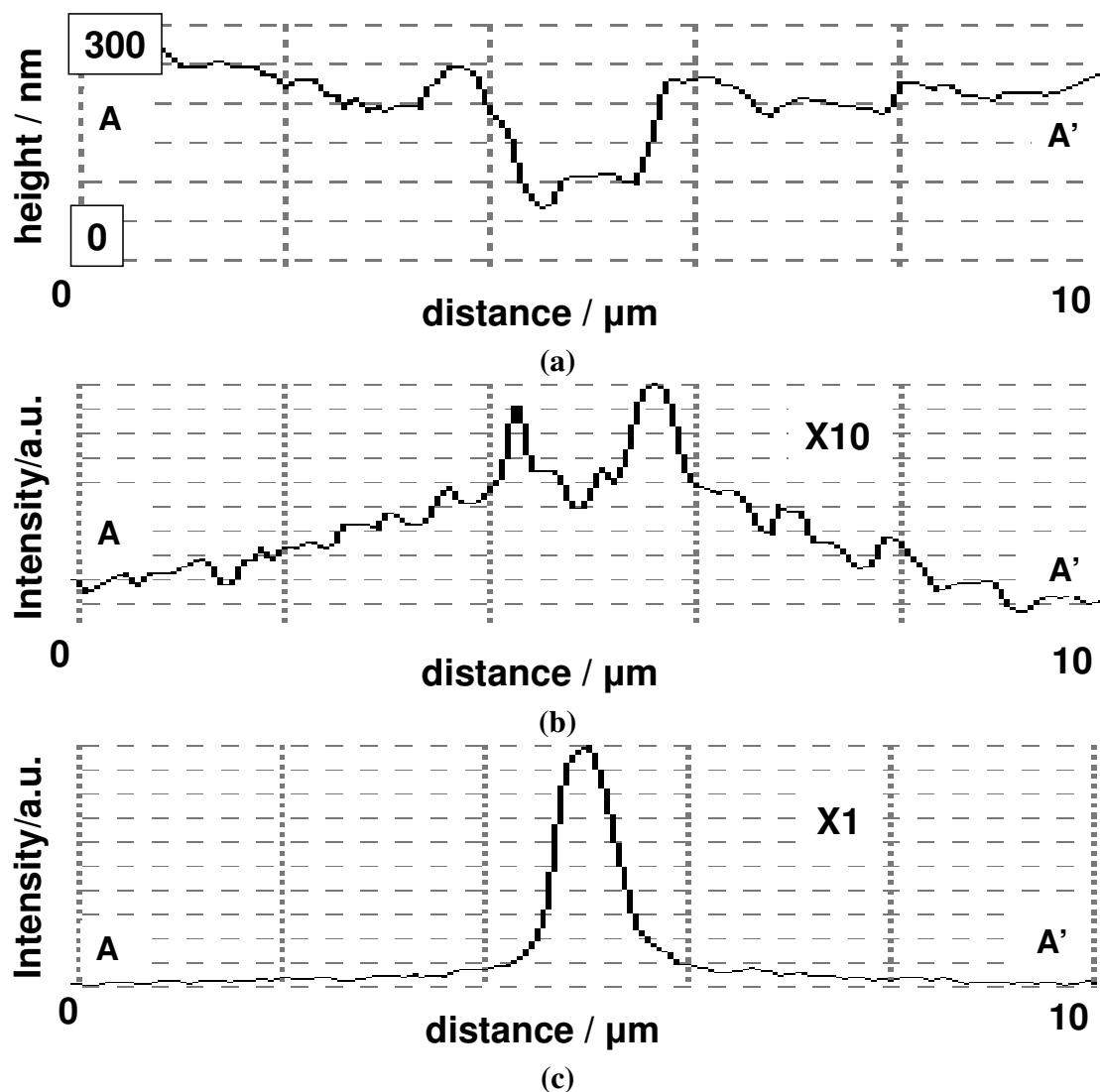


**Figure 6.21:** Comparison of profiles across line AA' in a) Fig.6.20a; b) Fig.6.20c; c) Fig.6.20b.

## Summary

In this chapter, the Ga-SDP was applied to the PE detection from a silicon-based semiconductor device. A lateral resolution value of 50 nm was demonstrated. These

results clearly indicate the improved resolution capability of the SNPEM in comparison to FFPEM. At the same time, the detection efficiency of currents as small as 2  $\mu\text{A}$  was achieved, which showed the improved capability of the SNPEM equipped with a Ga-SDP as opposed to a-SNOM approach. The impact of several limiting parameters related to SNPEM imaging was investigated. These factors were found to be: a) the metal contacts covering the emission source; b) the location of the emission source below the surface; and c) the probe-sample separation distance. It is clear that these parameters have to be tightly controlled in order to perform meaningful SNPEM measurements. The possibility and importance of spectroscopic SNPEM measurements was also demonstrated, revealing the dominance of field induced photon emissions in the visible spectral range and thermal emissions in the NIR spectral range for the ESD stressed silicon p-n junction.



## **Chapter 7.**

### **Conclusions and future work**

In this research, a novel process of Scanning Near-Field Photon Emission Microscopy (SNPEM) is developed for the characterization of photon emission sites in biased semiconductor devices with lateral resolutions compatible to 65 nm technology nodes and beyond. The SNPEM detection efficiency equipped with a novel Ga-SDP is several orders of magnitude better than the detection efficiency demonstrated by other techniques based on Near-Field (NF) optical detection. The following section lists the conclusions achieved along with suggestions for future work drawn from the results of this thesis:

#### **7.1 Conclusions**

1. This thesis demonstrated the detection of photon emissions from biased semiconductor devices in the near-field of the emission source. The lateral resolution of 50 nm for the photon distribution detected in the wavelength range above 1000 nm was demonstrated. This resolution value is one order of magnitude better than a theoretically achievable resolution for conventional air-gap far-field system and three times better in comparison to the theoretical value achievable by a system equipped with the Solid Immersion Lens.
2. This thesis achieved the detection of variation in the reverse current across a silicon p-n junction below 1  $\mu\text{A}$ . This level of detection capability was

demonstrated for wavelengths emissions generated in the visible (300 nm - 900 nm) and near-infrared (1000 nm – 1400 nm) spectral ranges.

3. The detection efficiency in the  $\mu\text{A}$  range is superior to the sensitivities demonstrated in literature using other approaches based on a near-field optical detection. At the same time, the demonstrated spatial resolutions are comparable.
4. The SNPEM application puts several requirements on the design of the near-field probe. This thesis proposed eight requirements for the design and showed that that all designs proposed prior to this work cannot comply with these requirements (Chapter 4).
5. In order to comply with the requirements imposed by an SNPEM application, I proposed a new concept for the near-field probe design (Chapter 5). In this concept, a metallic nanoparticle is embedded into the nanometric tip of the dielectric probe. This design has several advantages. First, the embedded nanoprticle minimizes the scattering volume, which is responsible for resolution. Second, the higher polarizability of metal in comparison to glass allows a higher detection efficiency. Third, it improves the contrast of the emission detection due to a considerable difference in the interaction properties between the tip and the body of the probe. Forth, the embedment of the metallic nanoparticle prevents the detachment of the scatterer from the tip during the scanning. Fifth, such an embedment also prevents the direct contact between the metallic nanoparticle and

the biased sample. Sixth, placing the scatterer inside the dielectric waveguide structure allows a more efficient coupling into the propagating modes for the scattered light in comparison to the metal particles placed outside the probe body. This arrangement also ensures a superior alignment of the nanoparticle in relation to the waveguide axis. The simplicity of the fabrication method and its demonstrated repeatability, suggest that the method can be scaled into mass production using area implantation systems.

6. In order to achieve such probe, I proposed and implemented a three-step fabrication method (Chapter 5). In the first step, the multi-mode optical fiber is tapered down to a diameter of a few microns. In the second step, the tapered end of the fiber is sharpened using raster scanning with a Focused Ion Beam of the front-side of the tip for approximately one minute. In the third step, gallium atoms from the ion beam are implanted into the final tip of the probe. In actuality, the second and third steps are performed simultaneously. The method is relatively simple, fast and repeatable. I confirmed the repeatability of the method on different probes. Due to the particular use of gallium, the probe was given the name of 'Ga -based Scattering Dielectric Probe (Ga-SDP).
7. I compared the performance of the Ga-SDP with a dielectric probe that did not have any implanted Ga (Chapter 5). By scanning the polished waveguide, I was able to demonstrate that the Ga-SDP can achieve up to 37 times better detection efficiency.

8. I simulated the ion implantation range for Ga ions in silica (Chapter 5). The simulated result showed that Ga should be confined to a distance of 60 nm below the surface. A value of at least 40 nm was observed using Scanning Transmission Electron Microscopy with a 30keV electron beam.
9. The application of the proposed fabrication method to the multi-mode fiber ensured that the final taper of the probe consists of only the core material. Such geometry ensured the efficient collection of the light scattered by the tip and the practically lossless guiding of the collected radiation towards the distant photon sensitive detector. I confirmed this advantageous geometry of the probe taper using an Electron Dispersive X-Ray analysis (Chapter 5).
10. The superior sensitivity allowed me to perform bias-dependent SNPEM measurements in two different spectral ranges– Visible and NIR (Chapter 6). The resolution of the images was compromised due to the sub-surface location of the emission source and variations in the probe properties, as well as in the distance regulation. However, the results clearly revealed that photons in the Visible and NIR spectral ranges are generated by two different photon emission mechanisms. The visible photons were linked to the high energetic hot-carriers present in the conduction path of the reverse current through the defect, which had been confirmed by the linear dependence between the photon intensity and supplied current. At the same time, NIR photons were linked to Joule heating across the

conduction path. The Joule heating was confirmed by the quadratic dependence between the photon intensity and the supplied current.

11. The efficiency of the SNPEM application is determined by the near-field condition. The near-field condition is defined through the distance between the emission source and the probe. This distance depends on the probe-sample separation and on the location of the emission source below the surface. I performed theoretical and experimental evaluations of these dependences (chapter 4). I demonstrated that by bringing the Ga-SDP from a distance of 4  $\mu\text{m}$  down to the near-field of the emission source, an increase in the signal of approximately 50 times can be achieved (chapter 6). Also only at such distance, can the location of the source be identified. Better localization was also achieved through a decrease in the thickness of the layer separating the emission source and the sample surface.
12. I also discussed the applicable configurations of the sample for front and back-side analysis with SNPEM (Chapter 3). For front-side analysis, the application could be performed to a test structure with only one metal layer. The back-side sample preparation techniques appropriate for a SNPEM application to a variety of semiconductor devices were found in literature. However, I was not successful with the implementation of these preparation techniques and thus, no back-side SNPEM analysis was performed.

## 7.2 Future work

- i. The results presented in this thesis present an opportunity to get new information about the physics of semiconductor devices at different biasing conditions. SNPEM has the potential to visualize the leakage paths in semiconductor devices, as well as identify regions with the highest electric field. Such information will be invaluable for the future development of the semiconductor industry.
- ii. The main concern for the adoption of the SNPEM technique in failure analysis is the repeatability of the results. The main sources of repeatability degradation are:
  - i) the amount of Ga implantation; ii) the consistence of the SDP-Ga shape and the taper structure; iii) the distance regulation; iv) the probe degradation during scan; v) environmental issues, including the build-up of dust particles at the tip and along the taper; and vi) the alignment of the probe and photon sensitive detector.These issues must be addressed for the future development of the SNPEM.
- iii. The contrast of the images detected with Ga-SDP is still quite poor. In the future, more sophisticated methods can be applied for background removal. For now, the adoption of the PTP concept described in sub-section 2.2.3 can improve the contrast due to the stronger dependence of direct coupling on the base aperture diameter. A second approach is a deconvolution of the image using prior knowledge about the probe and the emission source. However, this technique requires a precise measurement of the Ga-SDP parameters, especially the Ga implantation volume and the Ga fraction within the SDP, which are critical for the

estimation of the actual scattering efficiency. The development of methods for such measurements will be considered in future works. Also the correct deconvolution requires a better understanding of the probe-sample interaction, especially the contribution of the topography to the recoded intensity distribution. This will imply that the distance regulation between the probe and the sample is controlled with high precision and repeatability. This is not the case in the current set-up. In a third approach, one can capitalize on the methods developed for aperturless microscopy with metallic tips. In these methods, vibrating the probe in the vertical direction and detecting the signal at the same or higher harmonics removes the strong background. Following the result shown in Fig.6.20, one can use the strong dependence of the scattered signal on the separation distance. It is clear from Fig.6.20, that the far-field component is only slightly affected by the vibration. Hence, this far-field signal will not be amplified by the lock-in technique. This approach shows a lot of promise, but will require considerable modifications to the current set-up.

- iv. One of the major drawbacks of the current probe attachment is the manual gluing of the probe to the tuning fork. For future applications of SNPEM, it is preferable to shift towards glue-free approaches, like the one proposed in Ref.133.
- v. Back-side preparation techniques were proposed in Chapter 3 for bringing the emission source closer to the sample surface. More development in this direction is required in order to bring the SNPEM probe to the actual near-field of the emission source.

- vi. In spite of the back-side techniques being successfully developed, another problem can be anticipated. Samples prepared for the back-side analysis will not have any topography features that can be used for reference in an SNPEM analysis. A laser or a FIB marking might be needed for solving this problem. An illumination mode of the SNOM can also be implemented for identifying the area of the analysis as was shown in Ref. [156].
- vii. In Chapter 6, the use of the SNPEM data for the determination of the emission source location in all three coordinates was proposed. This approach has interesting opportunities and thus, it is worth further study.
- viii. A characterization technique for SNPEM probe is required. A far-field characterization is preferable to prevent any possible damage to the probe prior to the actual SNPEM analysis. A near-field standard sample can also be developed similar to the waveguide used in Fig.5.16.



## **Appendix A**

### **Photon Emission mechanisms**

#### **A.1 Radiative transitions**

Generation of PEs requires a transition of a charged carrier from a higher energy state to a lower state. The excitation process can be different but transitions which follow the excitation are in general the same [157]. These transitions can be either radiative [158] or nonradiative [159]. Radiative transitions are those in which the energy of the carrier is reduced via generation of electromagnetic radiation or photons [158]. Generation of photons is a statistical process having a probability that is dependent on carrier life time [160], which in its turn depends on the semiconductor material and device structure. There are three main groups of radiative transitions [157], shown in Fig.A.1a. The first group consists of interband transitions between conduction and valence bands. PE occurs due to intrinsic recombination (1a) with energy transition close to bandgap energy or (1b) higher energy transitions involving a hot electron or (1c) a hot hole. The second group consists of transitions involving chemical impurities or physical defects. These transitions include: (2a) conduction band to acceptor impurity level, (2b) donor level to valence band, (2c) donor level to acceptor level, (2d) conduction band to deep trap level and (2e) deep trap level to valence band. The third group consists of intraband transitions involving the (3a) deceleration of hot electron or (3b) hot hole. It should be noted that not all transitions can occur in the same material or under the same conditions [157].

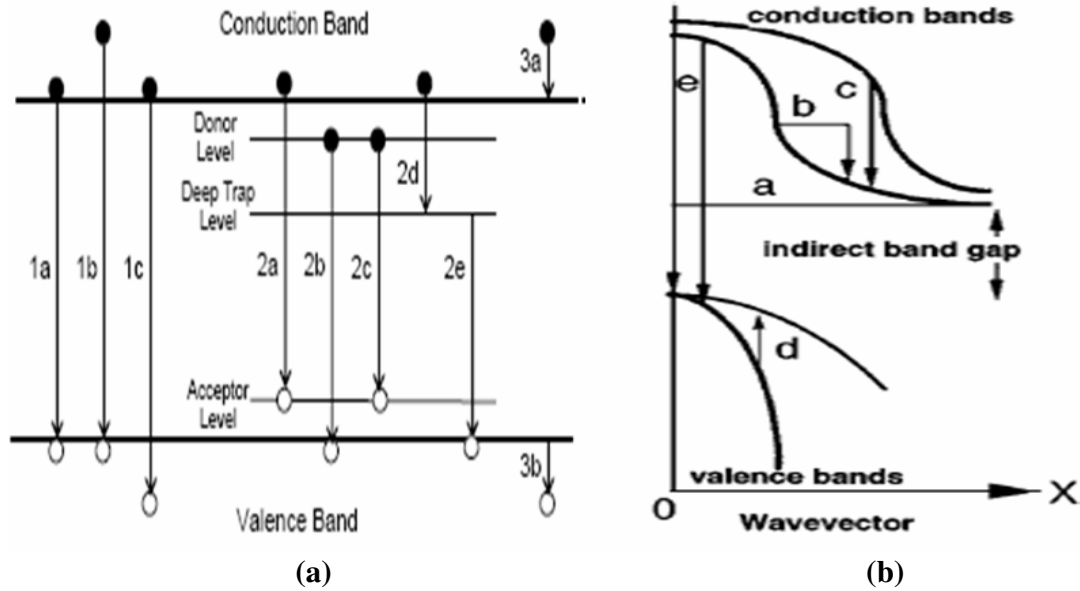


**Figure A.1:** a) Radiative transition processes in silicon devices [12]; b) Distinction of various radiation transition mechanisms in a realistic band structure of silicon [14].

Radiative processes in an indirect bandgap semiconductor, like silicon, can be further divided into direct and indirect transitions, as shown in Fig.A.1b. Direct transitions, in which both energy and momentum conservation are provided by a single photon, are marked as (c), (d), and (e). Indirect transitions, in which energy is emitted with a photon and momentum is transferred to an ionized impurity or lattice vibrations known as phonons, are marked as (a) and (b). The need for three “particles” (electron, photon and phonon) to meet at the same location as well as a relatively high momentum that should be conserved through phonons makes the probability of the radiative transition many orders of magnitude smaller than for non-radiative transition [161]. Hence, silicon based devices should demonstrate much lower efficiency of PE generation, limiting the detection efficiency of PEM [158].

## A.2 Photon emission from silicon based ICs

Most of the semiconductor devices are constructed using two major elements: p-n junctions and metal-oxide-semiconductor (MOS) structures. In silicon based devices the term PE is usually related to the wavelength range from 400 nm to approximately 2  $\mu\text{m}$  [12]. Photons with wavelengths below 400 nm have energies above the direct band-gap of silicon (3.4eV) and thus have a negligible probability to be emitted [162]. The upper boundary is less strict. Indeed even far-infrared emissions from hot electrons were observed from Si-MOSFET's [162]. The upper boundary of 2  $\mu\text{m}$  is given in order to avoid the strong contribution of thermal radiation background. In Fig.A.2 the spectra of black body radiation at different temperatures are shown. The efficiencies of commonly used FFPEM detectors are also presented in Fig.A.2.

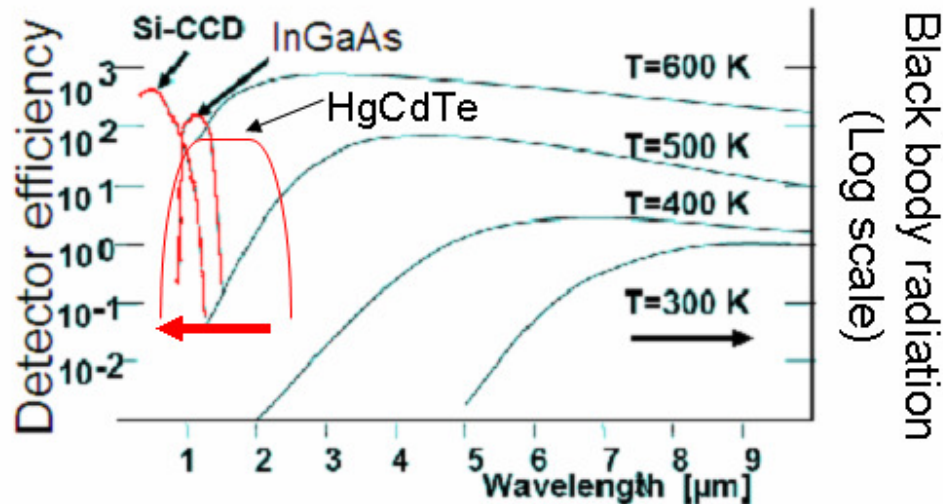


**Figure A.2:** Qualitative spectral range comparison of black body and PEM detectors [adopted from 164]

It should be noted that, although most of the silicon based devices are designed to work at temperatures below 100°C (373°K), locally the temperatures can rise above 350°C (623°K) and photons with wavelength down to 700 nm were attributed to the presence of

such hot spots [165]. Hence, the value of 2  $\mu\text{m}$  is chosen as a figure of merit combining the boundary of spectral detection efficiency of commonly used detectors and the onset of thermal background from the operating ICs.

#### A.2.1 Photon emission from forward biased silicon p-n junction

Silicon p-n junctions are the most common sources of PE from biased ICs which have been investigated since 1955 [162,166]. The emission phenomenon happening within a biased p-n junction is controlled through a depletion region formed between adjacent n (donor) and p (acceptor) doped semiconductors. At forward bias width of the depletion region reduces [167]. This leads to a lower electric field across the depletion region leaving little excess energy (energy greater than the bandgap energy) for carriers to gain [168]. In such conditions the emission is generated mainly due to interband transitions represented by group (1) in Fig.A.1a [157]. The emission is very weak due to the indirect mechanism of transition. The internal quantum efficiency is estimated to be one photon per  $10^6$  electron-hole pair recombination in standard silicon forward biased p-n junction [160]. That is why high currents have to be supplied in order to detect sufficient amount of photons [162,164]. The spectrum of the emitted photons has a distinct peak at the wavelength slightly longer than wavelength corresponding to the energy level of silicon indirect bandgap (Fig. A.3). This shift is attributed to the involvement of phonon in the recombination process [169].

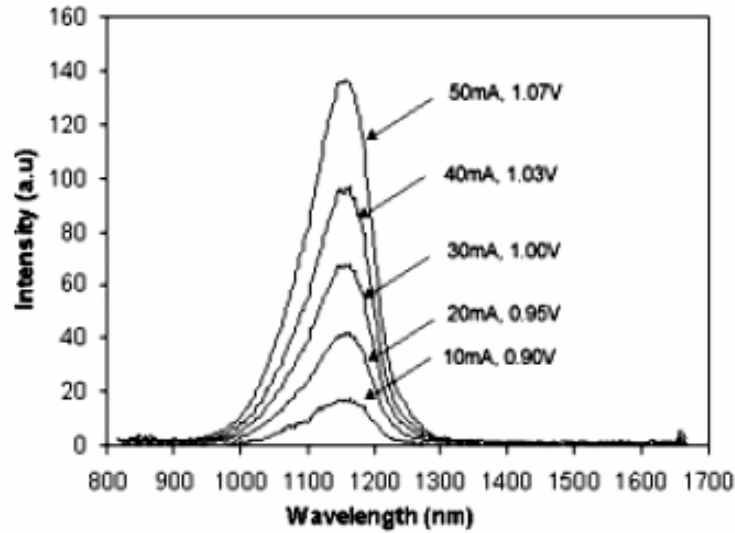


**Figure A.3:** Emission spectrum of forward biased p-n junction [169].

The presence of the one peak in Fig.A.3 confirms that recombination is the main mechanism [158]. The broadening of the peak is due to several reasons: phonon involvement and recombination through donor and acceptor levels (Fig.A.1a transitions (2a) and (2b)) [158] and still present electric field induced by few tenths of the volt of the forward bias [167]. Due to this field the peak is asymmetrical with larger broadening at shorter wavelengths [160]. From Fig.A.3 it can be also deduced that the intensity is increasing linearly with current. The distribution of PE is uniform within the diffusion length from the junction because the recombination in forward biased p-n junction is mainly governed by majority carrier diffusion [170].

#### A.2.2 Photon emission from reverse biased silicon p-n junction

For reverse biased p-n junction the phenomenon of PE is less understood and probably involves multiple mechanisms [171]. The distribution of photons in Visible and Near

Infra-Red (NIR) spectral regions from a commercial junction is shown in Fig.A.4. The significant tail in the spectrum extending into the visible range of wavelengths is observed (Fig.A.4a). It is attributed to the presence of high electric field across the depletion region [168,161]. The additional peak just below 1000 nm can be attributed to specific regions of weakness where a high concentration of high energy carriers can recombine [169]. At low reverse bias the value of reverse current is practically zero [172]. At sufficiently high bias the reverse current exponentially increases, which is attributed to direct tunneling or to impact ionization [157]. Spatial distribution of PE at avalanche breakdown is usually non-uniform because the weak points, like defects, are distributed randomly within the junction [170].

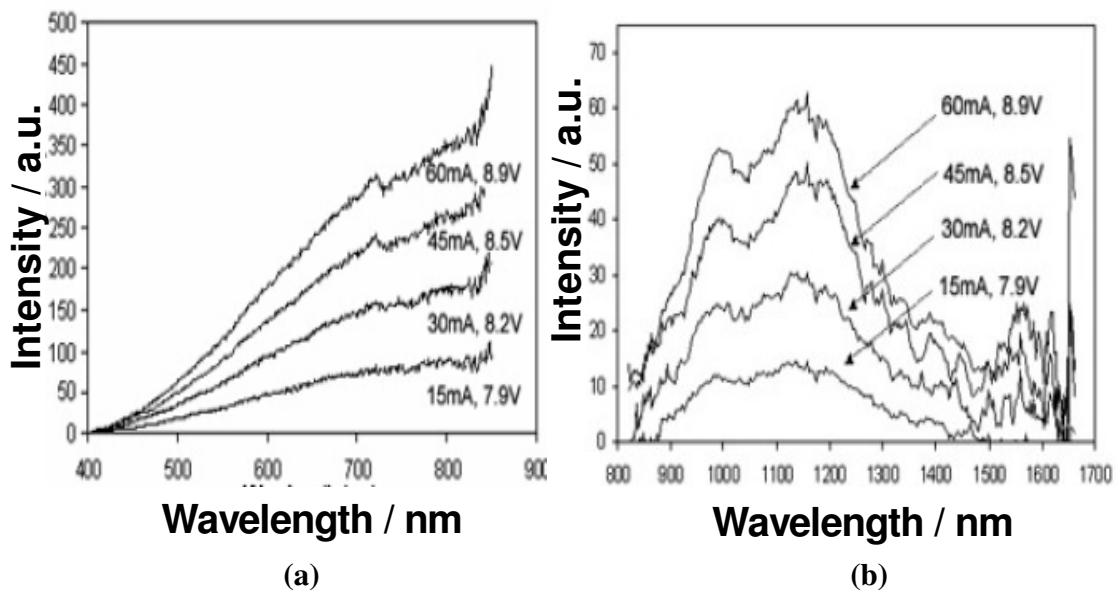


**Figure A.4:** Emission spectrum of reverse biased p-n junction a) visible and b) NIR spectral range [169].

The dominant mechanism responsible for photon generation at such extreme conditions is less understood and it is still debated in literature. The debate is focused on the nature of the transitions responsible for the PE in different spectral ranges. For the visible spectral

range the argument is between explanations using intraband transitions of hot electrons [173] and hot holes [174] within their respective bands (group 3 in Fig. A.1a) or using interband recombination [162] of energetic electrons in the conduction band with holes in the valence band (group 1 in Fig. A.1a). Also a combination of different transitions can be considered [164]. The dependence between PE intensity and reverse current is linear in visible spectral range [175-179]. The linear dependence can be also deduced from the Fig.A.4a.

In the NIR range of wavelengths the spectrum can contain different peaks from intrinsic transitions and transitions involving trap levels (group 2 in Fig.A.1a) [158]. These transitions are superimposed on a background provided by the deceleration of hot-carriers with low energies (group 3 in Fig.A.1a) [173]. The thermal radiation from a heated junction can also contribute into the spectrum [165]. Hence, spectra from junction with different structure and material properties should have quite different signatures. This makes it hard to compare the experimental data available in literature. However, it is interesting to note that in NIR spectral range shown in Fig.A.4b the overall intensity is linearly dependent on the current, similarly to visible spectral range shown in Fig.A.4a. This indicates that thermal emissions due to Joule heating, characterized by the square law [180], are not present in the spectrum.

### A.2.3 Photon emission from MOSFET

The origin of PEs in MOSFETs is even harder to deduce due to a more complicated structure involved. Fig.A.5 schematically shows the distribution of just a few possible PE phenomena within MOSFET. Information about the location, intensity and spectral signature of a particular emission spot is required in order to identify the underlying phenomenon. Unfortunately, the capability of FFPEM to pin-point the exact location of PE spot within a transistor is insufficient even for the technologies with large dimensions [181], while for the today's technologies (table 1.1) one cannot identify not only the emitting transistor but also the functional block where the transistor is placed (Fig.1.4).

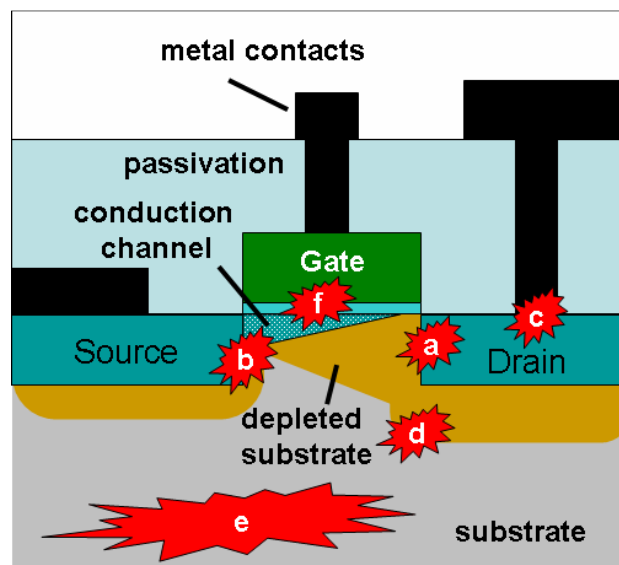


**Figure A.5:** Occurrence of photon emissions in MOSFETs: a) hot carrier effects; b) junction leakage; c) contact spiking; d) junction avalanche; e) latch-up; f) oxide current leakage.

### A.3 Confusion on the origin of hot carrier emission

It is interesting to note that there is an argument in literature in regard to the origin of hot carrier emission. The term “hot” here is used by convention, and does not literally mean



hot from a thermodynamic perspective [178]. A hot carrier is defined as a free carrier with considerably more kinetic energy than expected from the temperature of the lattice surrounding the carrier [14]. There are three main mechanisms of hot carrier related PE in MOSFET structures (excluding mechanisms related to oxide breakdown): a) interband transition through recombination [164,182-187]; b) intraband transitions assisted by impurity or defect, usually referred as Bremstrahlung radiation [171,183,188,189]; c) intraband transitions assisted by phonons [173,190-196]. At the same time there are papers that claim the disproval of one particular mechanism responsible for emission during MOSFET operation: a) recombination [173,188,189]; b) Bremstrahlung [173,182,184,190,192]; c) phonon assisted [171]. Of course, the list of papers is not complete but there is a trend to use a third mechanism of phonon assisted intraband transitions for PE analysis.

It is also important to note that papers about PEM applied for failure analysis often ignore the development in silicon based photonics. However, it is obvious that the effects of photon generation in both cases should be similar. Recent developments towards silicon based light emitters showed that the emission efficiency can be improved by introduction of defects into the bulk silicon, like dislocations [179,197], porous silicon [198,199] or nanocrystalline structures [200,202]. These defects are nanometric and ensure strong confinement of charged carriers [179,197,203]. Such confinement will smear the momentum of the carrier and thus permit direct interband recombination [160,204].

## Appendix B

### Quasi-static approximation (QSA)

In sub-section 2.3.1 it was stated that the use of Eqn.2.5 for calculating polarizability is valid only in the QSA. This approximation is valid if three conditions are satisfied [105]. These conditions are based on the assumption that the field at the boundaries of the particle is equal to the value of the external field, meaning that  $\mathbf{E}(+\mathbf{a}) \approx \mathbf{E}(-\mathbf{a}) \approx \mathbf{E}_0$ .

First, this assumption is valid only when

$$\mathbf{ka} = 2\pi\mathbf{a} / \lambda \ll 2\pi \quad (\text{B.1})$$

where  $\mathbf{k}$  is the wave number. Here it is also worth noting that Eqn. A.1 is similar to the right side of the NF condition (Eqn. 2.1).

The second and the third condition can be defined through the complex refractive index of the sphere:  $\mathbf{n} = \mathbf{n}' + i\mathbf{k}'$ . The second condition is that the time  $\tau^* = 2\mathbf{an}' / \mathbf{c}$  required for the field to propagate across the sphere is much smaller than the characteristic time of the field  $\tau = (2\pi\omega)^{-1}$ . This condition is satisfied when

$$2\mathbf{an}' / \lambda \ll 1 \quad (\text{B.2})$$

where  $\mathbf{c}$  is substituted with  $2\pi\omega\lambda$ .

The third condition is that the absorption of propagating field should be negligibly small, which is satisfied when

$$\mathbf{ak}' / \lambda \ll 1 \quad (\text{B.3})$$

The conditions in Eqn.B.1-B.3 have to be verified for every particular case, if quantitative result is required. In Table 6.1 this conditions are summarized for glass (SiO<sub>2</sub>) and gold (Au) particles with radius of  $a = 30$  nm.

**Table 6.1:** Validity of the assumptions for quasi-electrostatic approximation for SiO<sub>2</sub> and Au nanoparticles with radius of 30 nm.  $n'$  and  $k'$  are real and imaginary parts of the refractive indexes of SiO<sub>2</sub> and Au at particular wavelength.

$a = 30$ nm	SiO <sub>2</sub> [109]		Au [107]	
$\lambda/\text{nm} (n_1; k_1)$	600 (1.45;0)	1000 (1.5;0)	600 (0.3;2.9)	1000 (0.2;7)
$a/\lambda$	0.05	0.03	0.05	0.03
$2an'/\lambda$	<b>0.14</b>	0.09	0.03	0.01
$ak'/\lambda$	0	0	<b>0.14</b>	0.2

The conditions are satisfied if the values given in the first column of Table 6.1 are much smaller than unity. The corresponding relations are calculated for both materials at two different wavelengths of 600 nm and 1000 nm. The values in brackets, shown in the second row of Table 6.1, represent real and  $n'$  imaginary  $k'$  parts of the refractive index of corresponding materials at these wavelengths.

From Table B.1 it is clear that, while all the conditions are satisfied to a large extent, the second condition (Eqn.B.2) for SiO<sub>2</sub> and the third condition (Eqn.B.3) for Au are not strictly satisfied (highlighted in red color in Table 6.1). This means that the prediction on the value  $\alpha$  using Eqn.2.5 is only qualitative.

### B.1 Influence of the sample on QSA

The assumption of the plane wave is valid for any wave in a free space because any electromagnetic wave can be represented as a superposition of plane waves [205].

However, in the NF optics the probe is usually brought close to the surface of the sample, thus the plane wave assumption is not strictly valid. However, the conditions Eqn.B.1-B.3 can still be satisfied if the probe-surface system is illuminated by the plane wave [206,97]. Hence, the particle is still assumed to be placed into the uniform field. In this case the effect of the surface on particle polarizability can be taken into account by mirror (image)-dipole model [207]. In this model the dipole representing the particle at the end of the tip induces polarization effects on the sample surface that can be accounted for by placing the mirror dipole below the surface as shown in Fig.B.1.

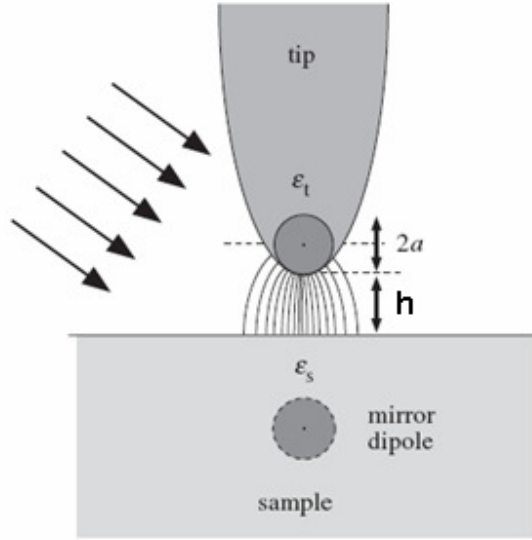


**Figure B.1:** The mirror-dipole induced by the tip in the proximity of the sample surface [206].

This effect leads to the appearance of substrate dielectric function  $\epsilon_{\text{sub}}$  in the expression for polarizability [97, 207]

$$\alpha_{\text{eff}} = \frac{\alpha(1 + \beta)}{1 - \alpha\beta/16\pi(h + a)^3} \quad (\text{B.4})$$

where  $\beta = (\epsilon_{\text{sub}} - \epsilon_m)/(\epsilon_{\text{sub}} + \epsilon_m)$ .

Considering that the substrate is silicon ( $\epsilon_{\text{Si}} = 13$ ) and for  $\mathbf{h} \rightarrow 0$  in the near-field the new value of polarizability is given by

$$\alpha_{\text{eff}} = \frac{7.6\pi a^3 (\epsilon - \epsilon_m)}{0.8\epsilon + 1.2\epsilon_m} \quad (\text{B.5})$$

The difference between Eqn.B.5 and Eqn.2.5 is confined to the numerical coefficients. Hence, the search for the particle with maximum scattering efficiency is still confined to the materials with negative  $\text{Re}(\epsilon) \approx -2\epsilon_m$ , which is similar to the result using QSA [208-209].

## B.2 Influence of the near-field of the emission source on QSA

Additional restriction on the validity of the QSA comes when the nanoparticle is illuminated not by the plane wave but by the NF of the emission source [46]. In the case of SNPEM application the NF probe is interacting with sub-wavelength emission sources. The emission properties of these sources in the NF might be very complicated in nature. However, some basic properties can be deduced from examples of an oscillating electric dipole and the evanescent field existing at the interface of two materials.

The electric dipole fields at distance  $\mathbf{r}$  from the dipole are given by [210]

$$\begin{aligned} \bar{H} &= \frac{ck^2}{4\pi} (\bar{n} \times \bar{p}_d) \frac{e^{ikr}}{r} \left(1 - \frac{1}{ikr}\right) \\ \bar{E} &= \frac{1}{4\pi\epsilon_0} \left\{ k^2 (\bar{n} \times \bar{p}_d) \times \bar{n} \frac{e^{ikr}}{r} + [3\bar{n}(\bar{n} \cdot \bar{p}_d) - \bar{p}_d] \left( \frac{1}{r^3} - \frac{ik}{r^2} \right) e^{ikr} \right\} \end{aligned} \quad (\text{B.6})$$

where  $\mathbf{c}$  is the speed of light,  $\mathbf{k} = \omega/\mathbf{c}$  is the wave number,  $\bar{\mathbf{n}}$  is the propagation direction and  $\epsilon_0$  is vacuum permittivity.

If the dipole dimensions are of the order of  $\mathbf{L}$  and for wavelengths  $\lambda \gg \mathbf{L}$  the radiation pattern can be divided into three spatial regions [210]: near zone; intermediate zone and far zone. The near (static) zone is determined by:

$$\mathbf{L} \ll \mathbf{r} \ll \lambda \quad (\text{B.7})$$

While the far (radiation) zone is determined by:

$$\mathbf{L} \ll \lambda \ll \mathbf{r} \quad (\text{B.8})$$

In the near zone the higher orders of  $\frac{1}{\mathbf{r}}$  are dominating, while Eqn.B.7 is equivalent to  $\mathbf{kr} \ll 2\pi$ . This allows for the replacement of the exponential term in Eqn.B.6 with unity. Hence, the fields are practically static in the near-zone [210]. These static fields are given by

$$\begin{aligned} \bar{H} &= \frac{i\omega}{4\pi} (\bar{\mathbf{n}} \times \bar{\mathbf{p}}_d) \frac{1}{\mathbf{r}^2} \\ \bar{E} &= \frac{1}{4\pi\epsilon_0} [3\bar{\mathbf{n}}(\bar{\mathbf{n}} \cdot \bar{\mathbf{p}}_d) - \bar{\mathbf{p}}_d] \frac{1}{\mathbf{r}^3} \end{aligned} \quad (\text{B.9})$$

From Eqn.B.9 it is also clear that in the limit of  $\mathbf{r} \rightarrow 0$  the magnetic field is always smaller than the electric field and can be ignored.

In the far zone  $\frac{1}{\mathbf{r}}$  terms are dominant in Eqn. (3.6) reducing it to

$$\begin{aligned}\bar{H} &= \frac{ck}{4\pi}(\bar{n} \times \bar{p}_d) \frac{e^{ikr}}{r} \\ \bar{E} &= \frac{1}{c\epsilon_0} \bar{H} \times \bar{n}\end{aligned}\tag{B.10}$$

Eqn. B.10 shows the typical behavior of radiation fields [210].

Combining the results from Eqn.B.9 and B.10 it is possible to specify that in the near zone the field will decay with distance as  $\frac{1}{r^3}$ , while in the far zone the term  $\frac{1}{r}$  should be dominant.

Another example of NF source is the evanescent field arising from the interaction of light with inhomogeneities or interfaces [211]. Evanescence field can be described in a form  $\bar{E}e^{i(\bar{k}\bar{r}-\omega t)}$ . This form is similar to the plane wave representation, but in this case at least one component of the wavevector  $\bar{k}$  is imaginary [212]. The existence of evanescent fields was first demonstrated by I. Newton in his famous “two prism experiment”, in which a light beam undergoes TIR at a face of the first prism, while the second prism is brought into contact with this face [213]. Newton noticed that light start to propagate inside the second prism before the contact is achieved. This occurs due to the presence of evanescent field above the face of the first prism. And this effect was used by A. Einstein to rule out the original idea proposed by E.H. Synge (see Section 2.1).

In general, amplitudes and directions of the reflected and the transmitted waves are described using Fresnel coefficients [212] and Snell’s law (Eqn.1.2). The transverse  $\mathbf{k}_t$  and longitudinal  $\mathbf{k}_z$  wavenumbers for waves reflected back into the first medium with

refractive index  $n_1$  and refracted into the second medium with refractive index  $n_2$  can be written as

$$\begin{aligned} k_{t1} &= k_{t2} = \frac{2\pi}{\lambda} n_1 \sin \vartheta \\ k_{z1} &= \frac{2\pi}{\lambda} n_1 \sqrt{1 - \sin^2 \vartheta} \\ k_{z2} &= \frac{2\pi}{\lambda} n_2 \sqrt{1 - \left(\frac{n_2}{n_1}\right)^2 \sin^2 \vartheta} \end{aligned} \quad (\text{B.11})$$

where  $\vartheta$  is the incident angle of the light beam.

Now, when we consider TIR inside the prism we observe that  $n_1 > n_2$ . Hence, at certain angles (  $\vartheta > \arcsin(\frac{n_2}{n_1})$  ) the wavenumber of the refracted beam  $k_{z2}$  becomes

imaginary and the field takes a form

$$\bar{E} \propto e^{i(k_t x - \omega t)} e^{-\gamma z} \quad (\text{B.12})$$

where the decay constant  $\gamma$  is defined by

$$\gamma = \frac{2\pi}{\lambda} n_2 \sqrt{\left(\frac{n_1}{n_2}\right)^2 \sin^2 \vartheta - 1} \quad (\text{B.13})$$

This field propagates along the surface of the prism but decays exponentially into the second medium. The  $\gamma$  determines the distance at which the time averaged field reduces by a factor of  $e$  and it is usually in the range of several hundreds of nanometers [49].

For both dipole and evanescent field models the field is non-uniform on the scale comparable or smaller than particle radius. Hence, at least one of the conditions in Eqn.

B.1-B.3 is not satisfied and QSA is not valid. In spite of this problem multiple



experimental results [97,206,209,214,215] have demonstrated that Eqn.2.5 can qualitatively explain the observed phenomena. It can be speculated that in this case the induced dipole is still determined by Eqn.2.4 but the constant field has to be substituted by a spatially varying field, given either by Eqn.B.9 or by Eqn.B.12.

## References:

1. Moor G.E., interview, 2003,  
<http://www.intel.com/technology/silicon/mooreslaw/eml02031.htm>
2. Moor G.E., "Cramming more components onto integrated circuits" *Electronics*, Vol. 38, Number 8, April 19, 1965.
3. Moor G.E., "Progress in digital integrated electronics" *International Electron Devices Meeting*, Vol. 21, pg. 11- 13, 1975.
4. Kuhn K., Kenyon C., Kornfeld A., Liu M., Maheshwari A., Shih W.K., Sivakumar S., Taylor G., Van Der Voorn, P. Zawadzki K., "Managing Process Variation in Intel's 45nm CMOS Technology", *Intel Technology Journal*, Vol. 12, pg. 93-109, 2008.
5. Semiconductor Industry Association, "International Technology Roadmap for Semiconductors, 2007 Edition, <http://public.itrs.net/>
6. Iwai H., "Logic LSI Technology roadmap for 22 nm and beyond", *Proceedings of 16th International Symposium on the Physical and Failure Analysis of Integrated Circuits (IPFA2009)*, pg. 7-10, 2009.
7. Lee D.H., Kwak D.K., Min K.S., "Comparative Study on Leakage Current of Power-Gated SRAMs for 65-nm, 45-nm, 32-nm Technology Nodes", *Journal of Computers*, Vol. 3, pg. 39-47 (2008).
8. Vallett D.P., "Probing the Future of Failure Analysis", *Electronic Device Failure Analysis*, Vol 4, No 4, pg. 5-9, 2002.
9. Wagner L., "A Product Analysis Forum Roundtable Discussion", *Electronic Device Failure Analysis*, Vol. 4, pg. 23-25, 2002.
10. Kudva S.M., Clark R., Vallett D., Ross D., Hasegawa T., Gilfeather G., Thayer M., Pabbisetty S., Shreeve R., Ash B., Serpiello J., Huffman K., Wagner L., Kazmi S., "The SEMATECH Failure Analysis Roadmap", *Proceedings of the 21st International Symposium for Testing and Failure Analysis*, pg. 1-5, 1995.
11. Tosi A., Stellari F., Pigozzi A., Marchesi G., Zappa F., "Hot-carrier photoemission in scaled CMOS technologies: a challenge for emission based testing and diagnostics", *Proceedings of the International Reliability Physics Symposium*, pg. 595-601, 2006.
12. Phang J.C.H., Chan D.S.H.B24, Tan S.L. , Len W.B., Yim K.H., Koh L.S., Chua C.M., Balk L.J., "A review of near infrared photon emission microscopy and spectroscopy", *Proceedings of International Symposium on the Physical & Failure Analysis of Integrated Circuits*, pg.275-281, 2005.

13. McDonald J., "Optical Microscopy", Microelectronic Failure Analysis, edited by Electronic Device Failure Analysis Society Desk Reference Committee, 5th Edition, Chapter 12, pg. 541-559, 2004.
14. Tsang J.C., Kash J.A., Vallett D.P., "Time-resolved Optical Characterization of Electrical Activity in Integrated Circuits," Proceedings of the IEEE, Vol. 88, no. 9, pg. 1440-1459, 2000.
15. Knauss L.A., Cawthorne A.B., Lettsome N., Kelly S., Chatrathorn S., Fleet E. F., Wellstood F.C. and Vanderlinde W.E., "Scanning SQUID microscopy for current imaging", Microelectronics Reliability, Vol. 41, pg. 1211-1229, 2001.
16. Chatrathorn S.; Fleet E.F.; Wellstood F.C.; Knauss L.A., "Noise and spatial resolution in SQUID microscopy", IEEE Transactions on Applied Superconductivity, Vol. 11, pg. 234 – 237, 2001.
17. Vallet D.P., "Why waste time on roadmaps when we don't have cars?", IEEE Transactions on Device and Materials Reliability, Vol 7, pg. 5-10, 2007.
18. Cole A.I., Barton D.L. "Failure Site Isolation: Photon emission microscopy, optical/electron beam techniques", in "Failure Analysis of Integrated Circuits: Tools and Techniques" edited by Wagner L.C., Springer, pg. 87-112, 1999.
19. Lamy M., De la Bardonnie M., Lorut F., Ross R., Ly K., Wyon C., Kwakman L.F.Tz., "How Effective Are Failure Analysis Methods for the 65nm CMOS Technology Node?", Proceedings of International Symposium on the Physical & Failure Analysis of Integrated Circuits, pg. 32-37, 2005.
20. Vallet D.P., "From Microns to Molecules – Can FA Remain Viable Through the Next Decade?", Proceedings of the 28th International Symposium for Testing and Failure Analysis, pg. 11-20, 2002.
21. Murphy D.B., "Fundamentals of light microscopy and electronic imaging", John Wiley & Sons, New-York, pg.61-84, 2001.
22. Hicks J. Bergstrom D. Hattendorf M., Jopling J., Maiz J., Pae S., Prasad C., Wiedemer J., "45nm Transistor Reliability", Intel Technology Journal, Vol. 12, pg.131-144, 2008.
23. Lammers D. "Thin SOI devices Shine at VLSI Symposium", Semiconductor International (e-magazine), 18 June 2009.
24. Source: Chipworks  
<http://www.chipworks.com/blogs.aspx?blogmonth=11&blogyear=2008&blogid=86>
25. De Wolf I., Groeseneken G., Maes H.E., Bolt M., Barla K., Reader A., McNally P.J., "Micro-Raman spectroscopy evaluation of the local mechanical stress in shallow trench isolation CMOS structures: correlation with defect generation and diode leakage", Proceedings of the International Symposium for Testing and Failure Analysis, pg 11-15, 1998.
26. Eiles T., Pardy P., "Liquid Immersion Objective for High-Resolution Optical Probing of Advanced Microprocessors", Proceedings of the International Symposium for Testing and Failure Analysis, pg 167-170, 2001.

27. Murphy D.B., " Fundamentals of light microscopy and electronic imaging ", Wiley-Liss, New-York, Chapter 6, pg.85-96, 2001.
28. Kino G.S., "The solid immersion lens," Far- and Near-Field Optics: Physics and Information Processing, SPIE -the International Society for Optical Engineering, pg. 2-5, 1999.
29. Ippolito S. B., Goldberg B. B., and Ünlü M. S., "Theoretical analysis of numerical aperture increasing lens microscopy", Journal of Applied Physics 97, 053105, 2005.
30. Mansfield S.M., Kino G.S., "Solid Immersion Microscope", Applied Physics Letters, Vol. 57, pg 2615-2616, 1990.
31. Zachariasse F., Goossens M., "Diffractive Lenses for High Resolution Laser Based Failure Analysis", Proceedings of the International Symposium for Testing and Failure Analysis, pg 1-7, 2005.
32. Goh S.H., Quah A.C.T., Sheppard C.J.R., Chua C.M., Koh L.S., Phang J.C.H., "Effect of Refractive Solid Immersion Lens Parameters on the Enhancement of Laser Induced Fault Localization Techniques", Proceedings of the International Symposium for Testing and Failure Analysis, pg 1-6, 2008
33. Koyama T., Yoshida E., Komori J., Mashiko Y., Nakasuji T., Katoh H., "High resolution backside fault isolation technique using directly forming Si substrate into solid immersion lens", Proceedings of the International Reliability Physics Symposium, pg. 529-535, 2003.
34. Luo Z.: "Method and apparatus for isolating defects in an integrated circuit near field scanning photon emission microscopy", US Patent Reference 5,981,967, 1999.
35. Pohl D.W., Denk W. and Lanz M., "Optical Stethoscopy: Image recording with resolution  $\lambda/20$ ," Applied Physics Letters, Vol. 44, p. 651-653, 1984.
36. Ackland M.P., Dunstan P.R., Rees P., "Near-field scanning optical microscopy and near-field induced photocurrent investigations of buried heterostructure multiquantum well lasers", Journal of Microscopy, vol 220, pg. 229–235, 2005.
37. Novotny L., "Progress in Optics", E. Wolf (ed.), Elsevier, Amsterdam, The Netherlands, Vol. 50, Chapter 5, pg. 137-184, 2007.
38. Balk L.J., Heiderhoff R., Phang J.C.H, Thomas C.: "Characterization of electronic materials and devices by scanning near-field microscopy", Applied Physics A, Vol. 87, pg. 443-449 (2007).
39. Ohtsu M., Kobayashi K., "Optical Near Fields: Introduction to Classical & Quantum Theories of Electromagnetic Phenomena at the Nanoscale", Springer, Chapter 4, pp. 53-76, 2003.
40. Synge E. H., "A suggested model for extending microscopic resolution into the ultra-microscopic region," Philosophical Magazine, Vol. 6, pg. 356–362, 1928.
41. Pohl D. W., "Optics at the nanometre scale", Philosophical Transactions of the Royal Society A, Vol. 362, pg. 701-717, (2004).

42. McCutchen C. W., "Superresolution in microscopy and the Abbe resolution limit," *Journal of Optical Society of America*, Vol. 57, pg. 1190-1192, 1967.
43. Vigoureux J. M. and Courjon D., "Detection of nonradiative fields in light of the Heisenberg uncertainty principle and the Rayleigh criterion", *Applied Optics*, Vol. 31, pg. 3170-3177, 1992.
44. Jackson J.D., "Classical Electrodynamics" 3rd edition, John Willey and Sons, Chapter 10, pg. 456-513, 1998
45. Kalkbrenner T., Ramstein M., Mlynek J., Sandoghdar V., "A single gold particle as a probe for apertureless scanning near-field optical microscopy", *Journal of Microscopy*, Vol. 202, pg. 72-76 (2001).
46. Anger P., Bharadwaj P., Novotny L., "Enhancement and quenching of single molecule fluorescence", *Physical Review Letters*, Vol. 96, p. 113002, 2006.
47. Buckland E.L., Moyer P.J., Paesler M.A., "Resolution in collection-mode scanning optical microscopy", *Journal of Applied Physics*, Vol. 73, pg. 1018-1028, 1993.
48. Courjon D., "Near-field Microscopy and Near-field Optics", Imperial College Press, New York, Chapter 4, pg. 57-92, 2003.
49. Novotny L., Hecht B., "Principles of Nano-Optics", Cambridge University Press, New York, Chapter 5, pg.134-172, 2006.
50. Hecht B., Sick B., Wild U.P., Deckert V., Zenobi R., Martin O.J.F., Pohl D.W., "Scanning near-field optical microscopy with aperture probes: Fundamentals and applications", *Journal of Chemical Physics*, Vol 112, pg.7761-74, 2000.
51. Buratto S. K., Hsu J. W. P., Trautman J. K., Betzig E., Bylsma R. B., Bahr C. C., Cardillo M. J., "Imaging InGaAsP quantum-well lasers using near-field scanning optical microscopy", *Journal of Applied Physics*, Vol.76, pg. 7720-7725, 1994.
52. Lienau Ch., Richter A., Elsaesser T., "Light-induced expansion of fiber tips in near-field scanning optical microscopy", *Applied Physics Letters*, Vol.69, pg.325-327, 1996.
53. Ben-Ami U., Tessler N., Ben-Ami N., Nagar R., Fish G., Lieberman K., Eisenstein G., Lewis A., Nielsen J. M., Moeller-Larsen A., "Near-infrared contact mode collection near-field optical and normal force microscopy of modulated multiple quantum well lasers", *Applied Physics Letters*, Vol. 68, pg. 2337-2339, 1996.
54. Herzog W. D., Unlu M. S, Goldberg B. B., Rhodes G. H., Harder C., "Beam divergence and waist measurements of laser diodes by near-field scanning optical microscopy", *Applied Physics Letters*, Vol. 70, pg. 688-690, 1997.
55. DeAro J.A., Westony K.D., Herrickzx R.W., Petroffzk P.M., Burattoy S.K., "Near-field scanning optical microscopy of cleaved vertical-cavity surface-emitting lasers", *Semiconductor Science and Technology*, Vol. 13, pg. 1364-1367, 1998.
56. Chen S.-H., Tsai D.P., Chen Y.-F., Ong P.-M., "True near-field optical characters of a GaAlAs semiconductor laser diode", *Review of Scientific Instruments*, Vol.70, pg 4463-4465, 1999.

57. Balk L.J., Cramer R.M., Heiderhoff R., Phang JCH, Sergeev O., Tiedemann A.-K., 'Dedicated Near-Field Microscopies for Electronic Materials and Devices', SPIE proceedings of International Symposium on Optical Metrology, Vol. 5856, Part One, pg. 1-13, 2005.
58. Bethe H.A., "The Theory of Diffraction by Small Holes", Physical Review, Vol. 66, pg. 163-182, 1944.
59. Bouwkamp C.J., "On Bethe's Theory of Diffraction by Small Circular Disks and Holes", Philips Research Reports, Vol. 5, pg. 321-332, 1950.
60. Labeke D. V., Barchiesi D., Baida F., "Optical characterization of nanosources used in scanning near-field optical microscopy", Optical Society of America, Vol 12, pg. 695-703, 1995.
61. Dunn R., "Near-Field Scanning Optical Microscopy", Chemistry Review, Vol. 99, pg. 2891-2927, 1999
62. Kavaldjiev D.I., Toledo-Crow R., Vaez-iravani M., "On the heating of the fiber tip in a near-field scanning optical microscope", Applied Physics Letters, Vol. 67, pg.2771-2773, 1995.
63. Stahelin M., Bopp M.A., Tarrach G., Meixner A. J., and Zschokke-Granacher I., "Temperature profile of fiber tips used in scanning near-field optical microscopy", Applied Physics Letters, Vol. 68, pg. 2603-2605, 1996.
64. Novotny L., Hecht B., "Principles of Nano-Optics", Cambridge University Press, New York, Chapter 6, pg.173-224, 2006.
65. Aeschimann L., Akiyama T., Staufer U., De Rooij N.F., Thiery L., Eckert R., Heinzelmann H., Characterization and fabrication of fully metal-coated scanning near-field optical microscopy SiO<sub>2</sub> tips", Journal of Microscopy, Vol. 209, pg. 182-187, 2003.
66. Saiki T., Mononobe S., Ohtsu M., Saito N., Kusano J., "Tailoring a high-transmission fiber probe for photon scanning tunneling microscope", Applied Physics Letters, Vol. 68, pg. 2612-14, 1996.
67. Yatsui T., Kourogi M. and Ohtsu M., "Increasing throughput of a near-field optical fiber probe over 1000 times by the use of a triple-tapered structure", Applied Physics Letters, Vol 73, pg. 2090-2092, 1998.
68. Nakamura H, Sato T, Kambe H, Sawada K, Saiki T. "Design and optimization of tapered structure of near-field fibre probe based on finite-difference time-domain simulation", Journal of Microscopy, Vol. 202, pg. 50-52, 2001.
69. Garcia-Parajo M. Tate T, Chen Y., "Gold-coated parabolic tapers for scanning near-field optical microscopy: fabrication and optimization", Ultramicroscopy, Vol. 61, pg. 155-163, 1995.
70. Arslanov N.M., "The optimal form of the scanning near-field optical microscopy probe with subwavelength aperture", Journal of Optics A: Pure and Applied Optics, Vol. 8, pg. 338-344, 2006.

71. Ecoffet C., Bachelot R., Deloeil D., Royer P., Lougno D.J., "Integration of polymer elements at the end of optical fibers by free-radical photopolymerization" *Synthetic Metals*, Vol. 124, pg. 29-31, 2001.
72. Hocine M., Fressengeas N., Kugel G., Carré C., Lougno D.J., Bachelot R., Ecoffet C., Royer P., "Modeling the growth of a polymer microtip on an optical fiber end", *Journal of Optical Society of America B*, Vol. 23, pg. 611-620, 2006.
73. Betzig E, Trautman JK, "Near-field optics: microscopy, spectroscopy, and surface modification beyond the diffraction limit," *Science*, Vol. 257, p. 189-195, 1992.
74. Heinzelmann H, Freyland JM, Eckert R, Huser T, Schürmann G, Noell W, Staufer U, De Rooij NF., "Towards better scanning near-field optical probes – progress and new developments", *Journal of Microscopy*, Vol. 194, pg. 365-368, 1999.
75. Kim G.M., Kim B.J., Ten Have E.S., Segerink F., Van Hulst N.F., Brugger J, "Photoplastic near-field optical probe with sub-100 nm aperture made by replication from a nanomould", *Journal of Microscopy*, Vol. 209, pg. 267–271, 2003.
76. Valaskovic G.A., Holton M., Morrison G.H., "Parameter control, characterization, and optimization in the fabrication of optical fiber near-field probes, *Applied Optics*, Vol. 34, pg. 1215-1228, 1995.
77. Hsu J.W.P., "Near-field scanning optical microscopy studies of electronic and photonic materials and devices", *Materials Science and Engineering*, Vol 33, pg. 1-50, 2001.
78. Hecht B., Bielefeldt H., Inouye Y., Pohl D. W., Novotny L., "Facts and artifacts in near-field optical microscopy", *Journal of Applied Physics*, Vol. 81, pg.2492-2498, 1997.
79. Veerman J.A., Otter A.M., Kuipers L., van Hulst N.F., "High definition aperture probes for near-field optical microscopy fabricated by focused ion beam milling", *Applied Physics Letters*, Vol. 72, pg. 3115-3117, 1998.
80. Pilevar S., Edinger K., Atia W., Smolyaninov I., Davis C. "Focused ion-beam fabrication of fiber probes with well-defined apertures for use in near-field scanning optical microscopy", *Applied Physics Letters*, Vol. 72, pg. 3133-3135, 1998.
81. Kim J.H., Song K.-B., "Recent progress of nano-technology with NSOM", *Micron*, Vol. 38, pg. 409–426, 2007.
82. Courjon D., Sarayeddine K., Spajer M., "Scanning tunneling optical microscopy", *Optics Communications*, Vol.71, pg. 23-28, 1989.
83. Reddick R.C., Warmack R.J., Ferrell T.L., "New form of scanning optical microscopy", *Physical Review B*, Vol. 39, pg. 767-770, 1989.
84. de Fornel F., Goudonnet J. P., Salomon L., Lesniewska E., "An evanescent field optical microscope", *Proceedings SPIE*, vol. 1139, pp. 77-84. 1989.
85. Buchler B. C., Kramer P., Kafeski M., Soukoulis C.M., Sandoghdar V., "Near-field optical investigations of photonic crystal microresonators", *The Institute of*

- Electronics, Information and Communication Engineers (IEICE) Transactions, Vol.E85–A, pg. 1-7, 2002.
86. Gersen H., Karle T. J., Engelen R. J. P., Bogaerts W., Korterik J. P., van Hulst N. F., Krauss T. F., Kuipers L., “Real-Space Observation of Ultraslow Light in Photonic Crystal Waveguides”, *Physical review letters*, Vol. 94, 073903, 2005.
  87. Fillard J. P., Castagne M., Prioleau C., “Atomic force microscopy silicon tips as photon tunneling sensors: a resonant evanescent coupling experiment”, *Applied Optics*, Vol. 34, pg. 3737-3742, 1995
  88. Von Freymann G., Wegener M., Schimmel Th., “Depolarization Near-Field Scanning Optical Microscopy: Influence of Wavelength and Tip Shape on the Lateral Resolution”, *Surface Interface Analysis*, Vol. 27, pg. 499-502, 1999.
  89. Gregersen N., Tromborg B., Bozhevolnyi S. I., “Vectorial modeling of near-field imaging with uncoated fiber probes: transfer function and resolving power”, *Applied Optics*, Vol. 45, pg. 8739-8747, 2006.
  90. Weeber J.C., Bourillot E., Dereux A., Goudonnet J.P., Chen Y., Girard C., “Observation of Light Confinement Effects with a Near-Field Optical Microscope”, *Physical review letters*, Vol. 77, pg. 5332-5335, 1996.
  91. Krenn J.R., Dereux A., Weeber J.C., Bourillot E., Lacroute Y., Goudonnet J. P., Schider G., Gotschy W., Leitner A., Aussenegg F. R., Girard C., “Squeezing the Optical Near-Field Zone by Plasmon Coupling of Metallic Nanoparticles”, *Physical review letters*, Vol. 82, pg. 2590-2593, 1999.
  92. Li T., “Optical Fiber Communications: Fiber Fabrication”, Academic Press, Orlando, Vol. 1, pg. 305-363, 1985.
  93. Hosaka S., Shintani T., Kikukawa A., Itoh K., “Evaluation of nano-optical probe from scanning near-field optical microscope images”, *Journal of Microscopy*, Vol.194, pg. 369-373, 1999.
  94. Ohtsu M., Kobayashi K., “Optical Near Fields: Introduction to Classical & Quantum Theories of Electromagnetic Phenomena at the Nanoscale”, Springer, Chapter 2, pp. 11-25, 2003.
  95. Ohtsu M., Hori H., “Near-field nano-optics: from basic principles to nano-fabrication and nano-photonics”, Kluwert Academic, New York, Chapter 4, pg.113-142, 1999.
  96. Haefliger D., Stemmer A., “Subwavelength-sized aperture fabrication in aluminium by self-terminated corrosion process in the evanescent field”, *Applied Physics Letters*, Vol. 80, pp. 3397-3399, 2002.
  97. Brundermann E., Havenith M., “SNIM: Scanning near-field infrared microscopy”, *Annual Reports on the Progress of Chemistry, Section C*, Vol. 104, pg. 235–255, 2008.
  98. Eah S.K., Jaeger H.M., Sherer N.F., Weiderrecht G.P., Lin X.M., “Plasmon scattering from a single gold nanoparticle collected through an optical fiber”, *Applied Physics Letters*, Vol. 86, 031902, 2005.



99. Brehm M., Frey H. G., Guckenberger R., Hillenbrand R., Kazantsev D., Keilmann F., Ocelic N., Taubner T., "Consolidating Apertureless SNOM", Journal of the Korean Physical Society, Vol. 47, pg. S80-S85, 2005.
100. Gomez L., Bachelot R., Bouhelier A., Wiederrecht G. P., Chang S.H., Gray S. K., Lerondel G., Hua F., Jeon S., Rogers J., Blaize S., Stefanon I. and Royer P., "Apertureless scanning Near-field Optical Microscopy: a comparison between homodyne and heterodyne approaches," Journal of Optical Society of America B, Vol 23, pg. 823-833, 2006.
101. Martin Y.C., Hamann H.F.; Wickramasinghe H. K., "Strength of the electric field in apertureless near-field optical microscopy", Journal of Applied Physics, Vol. 89, pg. 5774-5778, 2001.
102. Hillenbrand R. and Keilmann F., "Material-specific mapping of metal/semiconductor/dielectric nanosystems at 10 nm resolution by back-scattering near-field optical microscopy", Applied Physics Letters, Vol. 80, pg. 25-27, 2002.
103. Yang G., "A review of techniques for attaching micro- and nanoparticles to a probe's tip for surface force and near-field optical measurements", Review of Scientific Instruments, Vol. 78, pg. 081101, 2007.
104. Jackson J.D., "Classical Electrodynamics" 3rd edition, John Willey and Sons, Chapter 4, pg. 145-173, 1998.
105. Bohren C.F. and Huffman D.R., "Particles Small Compared with the Wavelength", Wiley, New York, Chapter 5 pg. 130-165, 1983.
106. Bohren C.F. and Huffman D.R., "Absorption and Scattering of Light by Small Particles", Wiley, New York, Chapter 9 pg. 227-267, 1983.
107. Lynch D.W., Hunter W.R., "Comments on the optical constants of metals and an introduction to the data for several metals" in "Handbook of optical constants of solids", eddited by Palik E.D., Ghosh G., Academic Press, pg.275-368, 1998.
108. Amekura H., Takeda Y., Kishimoto N., "Criteria for surface plasmon resonance energy of metal nanoparticles in silica glass", Nuclear Instruments and Methods in Physics Research B, Vol. 222, pg. 96-104, 2004.
109. Philipp H.R., "Silicon Dioxide (SiO<sub>2</sub>) (Glass)" in "Handbook of optical constants of solids", eddited by Palik E.D., Ghosh G., Academic Press, pg.749-764, 1998.
110. Mitra S.S. "Optical properties of nonmetallic solids for photon energies below the fundamental band gap" in "Handbook of optical constants of solids", eddited by Palik E.D., Ghosh G., Academic Press, pg.213-270, 1998.
111. Aigouy L., Mortier M., Gierak J., Bourhis E., De Wilde Y., Corstjens P., Tanke H.J. "Field distribution on metallic and dielectric nanoparticles observed with a fluorescent near-field optical probe", Journal of Applied Physics, Vol. 97, 104322, 2005.
112. Hole D.E., Townsend P.D., Barton J.D., Nistor L.C., Van Landuyt J., "Gallium colloid formation during ion implantation of glass", Journal of Non-Crystalline Solids, Vol. 180, pg. 266-274, 1995.

113. Townsend P.D., Hole D.E., "Optical responses of ion implanted nanoparticles in silica and glass", *Vacuum*, Vol. 63, pg. 641-647, 2001.
114. Kishimoto N., Umeda N., Takeda Y., Gritsyna V.T., Renk T.J., Thompson M.O., "In-Beam Growth and Rearrangement of Nanoparticles in Insulators Induced by High-Current Negative Copper Ions", *Vacuum*, Vol.58, pg. 60-78, 2000.
115. Tsuji H., Kurita K., Gotoh Y., Kishimoto N., Ishikawa J., "Optical absorption properties of Cu and Ag double negative-ion implanted silica glass", *Nuclear Instruments and Methods in Physics Research Section B*, Vol. 195, Issues 3-4, pg. 315-319, 2002.
116. Takeda Y., Lu J., Okubo N., Plaksin O., Suga T., Kishimoto N., "Optical Properties of metal nanoparticles synthesized in insulators by negative ion implantation", *Vacuum*, Vo. 74, Issues 3-4, pg. 717-721, 2004.
117. Choy T.C., "Effective medium theory: principles and applications", Oxford University Press, New York, Chapter 1, pg.1-23, 1999.
118. Aspens D.E. "The accurate Determination of Optical Properties by Ellipsometry" in "Handbook of optical constants of solids", edited by Palik E.D., Ghosh G., Academic Press, pg.89-134, 1998.
119. Kofman R., Cheyssac P., Richard J., "Optical properties of Ga monocrystal in the 0.3-5-eV range", *Physical Review B*, Vol.16, pg. 5216- 5224, 1977.
120. Betzig E., Trautman J. K., Harris T. D., Weiner, J. S.; Kostelak, "Breaking the diffraction barrier: optical microscopy of a nanometric scale," *Science*, Vol. 251, pg. 1468-1470, 1991.
121. Shi J., Qin X.R., "Formation of glass fiber tips for scanning near-field optical microscopy by sealed- and open-tube etching", *Review of Scientific Instruments*, Vol.76, 013702, 2005.
122. Courjon D., "Near-field Microscopy and Near-field Optics", Imperial College Press, New York, Chapter 7, pg. 139-174, 2003.
123. Moar P, Ladouceur F, and Cahill L, "Numerical analysis of the transmission efficiency of heat-drawn and chemically etched scanning near-field optical microscopes.", *Applied optics*, Vol.39, Issue 12, pg.1966-1972, 2000.
124. Paesler M.A., Moer P.J., "Near Field Optics: theory, instrumentations and applications", John Willey & Sons, New-York, Chapter 3, pg. 33-66, 1996.
125. Yu Y.-J., Noh H., Hong M.-H., Noh H.-R., Arakawa Y., Jhe W., "Focusing characteristics of optical fiber axicon microlens for near-field spectroscopy: Dependence of tip apex angle", *Optics Communications*, Vol. 267, pg. 264–270, 2006.
126. Feige V.K.S., Balk L.J., "Calibration of a scanning probe microscope by the use of an interference–holographic position measurement system", *Measurement Science and Technology*, Vol. 14, pg.1032-1039, 2003.

127. Novotny L., Hecht B., "Principles of Nano-Optics", Cambridge University Press, New York, Chapter 7, pg.225-249, 2006.
128. Karrai K., Grober R., "Piezoelectric tip-sample distance control for near-field optical microscopes", Applied Physics Letters, Vol 66, pg. 1842-1844, 1995.
129. Karrai K., Grober R., "Piezo-electric tuning fork tip-sample distance control for near field optical microscopes", Ultramicroscopy, Vol. 61, pg. 197-205, 1995
130. Ruiter A.G.T., "Near-field Optical Microscopy", Dissertation, University of Twente, Chapter 3, pg.33-54 1997.
131. Karrai K., "Lecture Notes on Shear and Friction Force Detection with Quartz Tuning Forks", Proceedings of Ecole Thématique de CNRS on near-field optics, La Londe les Maures, France, 2000.
132. Grober R.D., Asimovic J., Schuck J., Hessman D., Kindlemann P. J., Hespanha J., Morse S., Karrai K., Tiemann I., and Manus S., "Fundamental limits to force detection using quartz tuning forks". Review of Scientific Instruments, Vol. 71, pg. 2776-2780, 2000.
133. Mühlischlegel P., Toquant J., Pohl D.W., Hechta B., " Glue-free tuning fork shear-force microscope", Review of Scientific Instruments, Vol. 77, 016105, 2006.
134. Calibration sample TGX1, [http://www.ntmdt-tips.com/catalog/gratings/afm\\_cal/products/TGX1.html](http://www.ntmdt-tips.com/catalog/gratings/afm_cal/products/TGX1.html)
135. Boit C., Schlangen R., Kerst U., Lundquist T., "Physical Techniques for Chip-Back-side IC Debug in Nanotechnologies", IEEE Design & Test of Computers, Vol.25, pg. 250-257, 2008.
136. Prejean S., Bruce V., Burke J., "CMOS Back-side Deprocessing With TMAH / IPA as a Sample Preparation Procedure for Failure Analysis", Proceedings of the International Symposium for Testing and Failure Analysis, pg. 317-324, 2002.
137. Isakov D.V., Tan B.W.M., Phang J.C.H., Yeo Y.C., Tio A.A.B., Zhang Y., Geinzer T., Balk L.J., "Applications of Scanning Near-field Photon Emission Microscopy" 34rd International Symposium for Testing and Failure Analysis (ISTFA), pg. 25-29, 2008.
138. Shlangen R., Leihkauf R., Lundquist T., Egger P., Boit C., "RF performance increase allowing IC timing adjustments by use of backside FIB processing", International Symposium on the Physical and Failure Analysis of Integrated Circuits (IPFA), pg. 33-36, 2009.
139. Herschbein S., Rue C., Scrudato C., "The Joy of SOI: As Viewed from a Back-side FIB Perspective", Proceedings of the International Symposium for Testing and Failure Analysis, pg.78-83, 2005.
140. Prejean S., Shannon J., "Back-side Deprocessing of CMOS SOI Devices for Physical Defect and Failure Analysis", Proceedings of the International Symposium for Testing and Failure Analysis, pg. 99-104, 2003.

141. Narang V., Lim V., Muthu P., Chin J.M., "Development of Back-side Scanning Capacitance Microscopy Technique for Advanced SOI Microprocessors", Proceedings of International Symposium for Testing and Failure Analysis, pg. 94 - 97, 2006.
142. Hamamatsu H5783-20 datasheet, <http://sales.hamamatsu.com/en/products/electron-tube-division/detectors/photomultiplier-modules/part-h5783-20.php>
143. Hamamatsu R5509-42 datasheet, <http://sales.hamamatsu.com/en/products/electron-tube-division/detectors/photomultiplier-tubes/part-r5509-42.php>
144. Thorlabs F230FC-C datasheet, <http://www.thorlabs.com/catalogPages/1010.pdf>
145. Isakov D., Tio A.A.B., Geinzer T., Phang J.C.H., Zhang Y., Balk L.J.: "Scanning Near-field Photon Emission Microscopy", Proceedings of International Reliability Physics Symposium (IRPS), Phoenix, Arizona, USA, pg. 575-579, 2008.
146. LovaLite Optical Micro Tip Catalogue, <http://www.lovalite.com/EN/tips.php>
147. Isakov D.V., Zhang Y., Balk L.J., Phang J.C.H., "Optical near-field probe with embedded gallium scattering center", Applied Physics Letters, Vol. 94, 253108, 2009
148. Keiser G., "Optical Fiber Communications", 4d ed., New York: McGraw-Hill, pg. 29-89, 2007.
149. Volkert C.A., Minor A.M., "Focused Ion Beam Microscopy and Micromachining", MRS Bulletin, Vol 32, pg. 389-395, 2007.
150. Reiner J.C., Nellen P., Sennhauser U., "Gallium artefacts on FIB-milled Silicon Samples", Microelectronics Reliability, Vol.44, pg.1583-1588, 2004.
151. James F. Ziegler, <http://www.srim.org/>
152. Kofman R., Cheyssac P., Richard J., "Optical properties of Ga monocrystal in the 0.3-5-eV range", Physical Review B, Vol.16, pg. 5216- 5224, 1977.
153. Liow T.Y. Tan K.M. Lee R.T.P., Du A., Tung C.-H., Samudra G.S., Yoo W.-J., Balasubramanian N., Yeo Y.-C., "Strained N-channel FinFETs with 25nm gate length and silicon-carbon source/drain regions for performance enhancement", Symposium on VLSI Technology, pg. 68-69 (2006).
154. Chin J.M., Phang J.C.H., Chan D.S.H., Soh C.E., Gilfeather G., "Single contact optical beam induced currents (SCOBIC) -Technique and Applications", International Symposium on the Physical and Failure Analysis of Integrated Circuits (IPFA), pg. 42-49, 2001.
155. Hashimoto C., Okuyama K., Kubota K., Ishizuka H., "Degradation of I/O devices due to ESD-induced dislocations," in Technical Digest of international Electron Devices Meeting, pg.459-462, 1994.
156. Cramer R.M., Chin R., Balk L.J., "Reflection mode scanning near-field optical microscopy analyses of integrated devices", Journal of Microscopy, Vol. 194, p.542, 1999.

157. Ivey H.F., "Electroluminescence and semiconductor lasers", IEEE Journal of Quantum Electronics, QE-2, pg. 713-726, 1966.
158. Pankove J.I., "Optical Processes in Semiconductors", Dover Publications, New York, Chapter 6, pg. 107-159, 1971.
159. Pankove J.I., "Optical Processes in Semiconductors", Dover Publications, New York, Chapter 7, pg. 160-169, 1971.
160. Ossicini S., Pavesi L., and Priolo F., "Light Emitting Silicon for Microphotonics", Springer, Berlin, Chapter 1, pg. 1-36, 2003.
161. Anderson B.L., "Fundamentals of semiconductor devices", McGraw Hill, New York, Part 1, Supplement 1B, pg.215-234, 2005.
162. Chynoweth A.G., McKay K.G., "Photon emission from avalanche breakdown in silicon", Physical Review, Vol. 102, pg. 369-, 1956.
163. Gornik E., Tsui D.C., "Far infrared emission from hot electrons in Si-inversion layers", Solid-state Electronics, Vol.21, pg.139-142, 1978.
164. Boit C., "Fundamentals of photon emission (PEM) in silicon – electroluminescence for analysis of electronic circuit and device functionality ", Microelectronic Failure Analysis, Desk Reference, 5th Edition, ASM International, pg. 356-368, 2004.
165. Rasras M., De Wolf I., Bender H., Groeseneken G., Maes H. E., Vanhaeverbeke S. and De Pauw P., " Analysis of Iddq failures by spectral photon emission microscopy", Microelectronics Reliability, Vol. 38, pg. 877-882, 1998.
166. Newman R., "Visible Light from a Silicon p-n Junction", Physical Review, Vol 100, No 2, pg 700-703, 1955.
167. Pankove J.I., "Optical Processes in Semiconductors", Dover Publications, New York, Chapter 8, pg. 170-212, 1971
168. Barton D.L., Tangyunyong P., Soden J.M., Henderson C.L., Cole E.I., Danz R., Steiner R., Iwinski Z., "Light Emission Spectral Analysis: The Connection between the Electric Field and Spectrum", Proceedings of the International Symposium for Testing and Failure Analysis, pp 57–67, 1999.
169. Len W.B., Liu Y.Y., Phang J.C.H., Chan D.C.H., "Near IR Continuous Wavelength Spectroscopy of Photon Emissions from Semiconductor Devices", Proceedings of the International Symposium for Testing and Failure Analysis, pg. 311-316, 2003
170. Chim W.K., "Semiconductor device and failure analysis: using photon emission microscopy", Wiley, England, Chapter 1, pg. 1-26, 2000.
171. Akil N., Kerns S. E., Kerns D. V., Hoffmann A., Charles J.-P., "A multimechanism model for photon generation by silicon junctions", IEEE Transactions on Electron Devices, Vol. 46, pg. 1022-1028, 1999.
172. Chynoweth A.G., McKay K.G., "Internal Field Emission at Narrow Silicon and Germanium p-n Junctions", Physical review, Vol.106, pg. 418-427, 1957.
173. Bude J., Sano N., Yoshii A., "Hot-carrier luminescence in Si", Physical Review B, Vol. 45, p.5848-5856, 1992

174. Haecker W., "Infrared radiation from breakdown plasmas in Si, GaSb, and Ge: Evidence for direct free hole radiation," *Physica Status Solidi (a)*, Vol. 25, pp. 301–310, 1974.
175. Lacaita A.L., Zappa F., Bigliardi S., Manfredi M., "On the bremsstrahlung origin of hot-carrier-induced photons in silicon devices". *IEEE Transactions on Electron Devices*, Vol. 40, pg. 577 – 582, 1993.
176. Swoger J.H., Kovacic S.J., "Enhanced luminescence due to impact ionization in photodiodes", *Journal of Applied Physics*, vol. 74, pg. 2565-2571, 1993.
177. Deboy G., Kölzer J., "Fundamentals of light emission from silicon devices," *Semiconductor Science and Technology*, Vol. 9, pg. 1017–1032, 1994.
178. Teh G.L., Chim W.K., Swee Y.K., Co Y.K., "Spectroscopic photon emission measurements of n-channel MOSFETs biased into snapback breakdown using a continuous-pulsing transmission line technique", *Semiconductor Science and Technology*, Vol. 12, pg. 662–671, 1997.
179. Morschbach M., Oehme M., Kasper E., "Visible Light Emission by a Reverse-Biased Integrated Silicon Diode", *IEEE Transactions on Electron Devices*, Vol. 54, pg. 1091 - 1094, 2007.
180. Pollock D., "Physical properties of materials for engineers", CRC Press, Florida, Chapter 7 pg.227-268, 1993.
181. Herzog M., Schels M., Koch F., "Electromagnetic radiation from hot carriers in FET-devices" *Solid-State Electronics* Vol. 32, No. 12, pg. 1765-1769, 1989.
182. Tsuchiya T., Nakajima S., "Emission mechanism and bias-dependent emission efficiency of photons induced by drain avalanche in Si MOSFET's", *IEEE Transactions on electron devices*, Vol. ED-32, N. 2, pg. 405-412, 1985
183. Herzog M., Koch F., "Hot-carrier emission from silicon metal oxide semiconductor devices", *Applied Physics Letters*, Vol. 53, pg. 2620-2622, 1988.
184. Wong H.-S., "Experimental Verification of the Mechanism of Hot-Carrier-Induced Photon Emission in N-MOSFET's Using an Overlapping CCD Gate Structure" *IEEE Electron Device Letters*, Vol. 13, pg. 389-391, 1992.
185. Selmi L., Lanzoni M., Bigliardi S., Sangiorgi E., "Photon emission from sub-micron p-channel MOSFETs biased at High Fields", *Microelectronic Engineering*, Vol. 19, pg. 747-750, 1992.
186. Muniandy R., "Sub-0.25 $\mu$ m MOSFET impact ionization and photon generation dynamics based on high-resolution photo-emission spectrum analysis", *Proceedings of the International Reliability Physics Symposium*, pg. 427 – 428, 2002.
187. Asli N., Vexler M. I., Shulekin A. F., Seegebrecht P., "Hot-electron-induced luminescence of metal–oxide–semiconductor tunnel devices", *Semiconductor Science and Technology*, Vol.18 pg.147–153, 2003.

188. Tam S., Hu C., "Hot-electron-induced photon and photocarrier generation in Silicon MOSFET's", IEEE Transactions on electron devices, Vol. ED-31, N. 9, pg. 1264-1273, 1984.
189. Toriumi A., Yoshimi M., Iwase M., Akiyama Y., Taniguchi K., "A Study of Photon Emission from n-Channel MOSFET's", IEEE Transactions of electron devices, Vol. ED-34, N.7, pg. 1501-1507, 1987.
190. Das N.C., Arora B.M., "Luminescence spectra of an n-channel metal-oxide-semiconductor field-effect transistor at breakdown", Applied Physics Letters, Vol. 56, pg. 1152-1153, 1990.
191. de Kort K., Damink P., Boots H., "Spectrum emitted by hot electrons in p-i-n cold cathodes", Physical review. B, vol. 48, pg. 11912-20, 1993.
192. Chan D.S.H., Phang J.C.H., Chim W.K., Liu Y.Y., Tao J.M., "Design and Performance of a New Spectroscopic Photon Emission Microscope System for the Physical Analysis of Semiconductor Devices", Review of Scientific Instruments, Vol 67, pg. 2576-2583, 1996.
193. Carbone L., Brunetti R., Jacoboni C., Lacaita A., Fischetti M., "Polarization analysis of hot-carrier light emission in silicon", Semiconductor Science and Technology, Vol. 9, pg. 674-676, 1994.
194. Villa S., Lacaita A. L., Pacelli A., "Photon emission from hot electrons in silicon", Physical review B, Vol. 52, pg. 10993-9, 1995.
195. Pavese M., Rigolli P. L., Manfredi M., Palestri P., Selmi L., "Spontaneous hot-carrier photon emission rates in silicon: Improved modeling and applications to metal oxide semiconductor devices", Physical review B, Vol. 65, pg. 195209 (1-8), 2002.
196. de Luna N.C., Bailon M.F., Tarun A.B., "Analysis of Near-IR Photon Emissions From 50-nm n- and p-Channel Si MOSFETs", IEEE Transactions on Electron Devices, Vol. 52, pg. 1211-1214, 2005.
197. Ng W.L., Lourenco M.A., Gwilliam R.M., Ledain S., Shao G., and Homewood K.P., "An efficient room-temperature silicon based light-emitting diode," Nature, Vol. 410, pg. 192-194, 2001.
198. Richter A., Steiner P., Kozlowski F., Lang, W., "Current Induced Light Emission from a Porous Silicon Device", IEEE Electron Device Letters, Vol.12, No. 12, pg. 691-692, 1991.
199. Lang W., Steiner P., Kozlowski F., Sandmaier H., "Porous silicon light-emitting p-n junction", Journal of Luminescence, Vol. 57, pg. 169-173, 1993.
200. Cloutier S.G., Kossyrev P.A., and Xu J., "Optical gain and stimulated emission in periodic nanopatterned crystalline silicon," Nature Materials, Vol. 4, pg. 887-891, 2005.
201. Chen M.J., Yen J.L., Li J.Y., Chang J.F., Tsai S.C., Tsai C.S., "Stimulated emission in a nanostructured silicon pn junction diode using current injection," Applied Physics Letters, Vol. 84, pg. 2163-2165, 2004.

202. Pavesi L., Dal Negro L., Mazzoleni C., Franzo G., and Priolo F., "Optical gain in silicon nanocrystals," *Nature*, Vol. 408, pg. 440–444, 2000.
203. El-Tahchi M., Nassar E., Mialhe P. "Study and Development of a Silicon Infrared Diode Operating Under Forward Bias", *Microelectronics Journal*, Vol. 36, pg. 260-263, 2005.
204. Saito S., Hisamoto D., Shimizu H., Hamamura H., Tsuchiya R., Matsui Y., Mine T., Arai T., Sugii N., Torii K., Kimura S., Onai T., "Electro-Luminescence from Ultra-Thin Silicon", *Japanese Journal of Applied Physics*, Vol. 45, pg.L679–L682, 2006.
205. Bohren C. F. and Huffman D. R., "Absorption and Scattering of Light by Small Particles", Wiley, New York, Chapter 3 pg. 57-81, 1983.
206. Keilmann F., Hillenbrand R., "Near-field microscopy by elastic light scattering from a tip" *Philosophical Transactions of the Royal Society A*, Vol. 362, pg. 787-805, 2004.
207. Knoll B., Keilmann F., "Near-field probing of vibrational absorption for chemical microscopy" *Nature*, Vol.339, pg. 134-137, 1999.
208. Labeke D.V., Barchiesi D., "Theoretical problems in Scanning near-field optical microscopy" in "Near Field Optics" edited by D. W. Pohl and D. Courjon, NATO ASI Series E, Kluwer, Dordrecht, The Netherlands, Vol. 242, pg. 157-178, 1993.
209. Hillenbrand R., Keilmann F., "Complex optical constants on a subwavelength scale", *Physical Review Letters*, Vol. 85, 3029-3032, 2000.
210. Jackson J.D., "Classical Electrodynamics" 3rd edition, John Willey and Sons, Chapter 9, pg. 407-455, 1998
211. Wolf E., Nieto-Vesperinas, "Analyticity of the angular spectrum amplitude of scattered fields and some of its consequences", *Journal of Optical Society of America A*, Vol. 2, pg. 886-889, 1985.
212. Novotny L., Hecht B., "Principles of Nano-Optics", Cambridge University Press, New York, Chapter 2, pg.13-44, 2006.
213. Courjon D. "Near-field Microscopy and Near-field Optics", World Scientific, Singapore, Chapter 1, pg. 1-16, 2003
214. Maier S.A., Atwater H.A., "Plasmonics: Localization and guiding of electromagnetic energy in metal/dielectric structures", *Journal of Applied Physics*, Vol. 98, 011101, 2005.
215. Kuwata H., Tamaru H., Esumi K., "Resonant light scattering from metal nanoparticles: Practical analysis beyond Rayleigh approximation", *Applied Physics Letters*, Vol. 83, pg. 4625-4628, 2003.



## Publication list:

1) A.C.A. Tan, **D.V. Isakov**, C.T. Au, J.C.H. Phang, Y. Zhang, Y.C. Soh, L.J. Balk, “Aperture Probe Tips for Near-Field Scanning Optical Microscopy by Focused Ion Beam Micro-Nano Machining”, presented at the Asia-Pacific Conference of Transducers and Micro-Nano Technology, Singapore, 2006.

2) S. L. Tan, K. W. Ang, K. H. Toh, **D. Isakov**, C. M. Chua, L. S. Koh, Y.-C. Yeo, D. S. H. Chan, J. C. H. Phang, “Near-IR photon emission spectroscopy on strained and unstrained 60 nm silicon nMOSFETs” 33rd International Symposium for Testing and Failure Analysis (ISTFA) San Jose, CA, pg. 81-85, 2007.

3) S.L. Tan; J.K.J. Teo; K.H. Toh; **D. Isakov**; D.S.H. Chan; L.S. Koh; C.M. Chua; J.C.H. Phang, “Near-infrared spectroscopic photon emission microscopy of 0.13  $\mu\text{m}$  silicon nMOSFETs and pMOSFETs”, 15th International Symposium on the Physical and Failure Analysis of Integrated Circuits (IPFA), pg. 1-5, 2008.

4) **D. Isakov**, A.A.B. Tio, T. Geinzer, J.C.H. Phang, Y. Zhang, L.J. Balk: “Scanning Near-field Photon Emission Microscopy”, Proceedings of International Reliability Physics Symposium (IRPS), Phoenix, Arizona, USA, pg. 575-579, 2008.

5) **D. Isakov**, A.A.B. Tio, T. Geinzer, J.C.H. Phang, Y. Zhang, L. J. Balk, “Near-field detection of photon emission from silicon with 30 nm spatial resolution”, Microelectronics Reliability, Vol. 48, pg. 1285-1289, 2008.

*reprinted* from 19th European Symposium on Reliability of Electron Devices, Failure Physics and Analysis (ESREF), Maastricht, Netherlands, pg 1285–1288, 2008.

6) **D. V. Isakov**, B. W. M. Tan, J.C.H. Phang, Y. C. Yeo, A. A. B. Tio, Y. Zhang, T. Geinzer, L. J. Balk, “Applications of Scanning Near-field Photon Emission Microscopy” 34rd International Symposium for Testing and Failure Analysis (ISTFA), pg. 25-29, 2008.

*Invited Paper* presented at 16th IEEE International Symposium on the Physical and Failure Analysis of Integrated Circuits (IPFA), pg.631-634, 2009.

7) **D. V. Isakov**, Y. Zhang, L. J. Balk, and J. C. H. Phang, “Optical near-field probe with embedded gallium scattering center”, Applied Physics Letters, Vol. 94, 253108, 2009.

*selected for the* July 6, 2009 issue of Virtual Journal of Nanoscale Science & Technology

8) **D.V. Isakov**, Y. Zhang, L. J. Balk and J. C. H. Phang, "Scanning near-field photon emission microscopy for failure analysis of advanced semiconductor devices", The Second International Competition of Scientific Papers in Nanotechnology for Young Researchers at The Second Nanotechnology International Forum (RusNanoTech2009), Moscow, Russia, pg. 271-272, 2009.